SEISMICITY, TECTONICS, AND SURFACE WAVE PROPAGATION IN THE CENTRAL ANDES

by

GERARDO SUAREZ

Ingeniero Geofísico, Universidad Nacional Autónoma de México
(1976)

SUBMITTED TO THE DEPARTMENT OF
EARTH AND PLANETARY SCIENCES
IN PARTIAL FULFILLMENT
OF THE REQUIREMENTS
FOR THE DEGREE OF

DOCTOR OF PHILOSOPHY

at the

MASSACHUSETTS INSTITUTE OF TECHNOLOGY

December 1982

Signature of Author _____
Department of Earth and Planetary Sciences
December, 1982

Certified by _____
Keiiti Aki
Thesis Supervisor

_____
Peter Molnar
Thesis Supervisor

Accepted by _____
Theodore R. Madden
Chairman, Department Committee

SEISMICITY, TECTONICS, AND SURFACE WAVE PROPAGATION IN THE CENTRAL ANDES

by

GERARDO SUAREZ

SUBMITTED TO THE DEPARTMENT OF EARTH AND PLANETARY SCIENCES ON DECEMBER 1,1982 IN PARTIAL FULFILLMENT OF THE REQUIREMENTS FOR THE DEGREE OF DOCTOR OF PHILOSOPHY

Abstract

The objectives of this thesis may be divided into two parts: In the first part a seimotectonic study is undertaken to try to determine the seismicity and the style of tectonic deformation of the central Andes of Peru, Ecuador, and southern Colombia. The second part consists of a study of surface wave propagation. A new technique is presented to obtain the moment-tensor from the amplitude spectra of Rayleigh waves and we explore the possibility of routinely applying the linear-moment tensor inversion to seven earthquakes in the central Andes.

The intracontinental seismicity of the central Andes of Peru, and those of Ecuador and southern Colombia, is concentrated along the easternmost flank of the Cordillera beneath the western margin of the sub-Andes. The focal depths and fault-plane solutions of all the events within the Andes for which a fault-plane solution could be obtained were constrained by comparing the observed long-period P waves with theoretical waveforms. In general, the fault-plane solutions show reverse faulting on steeply dipping planes striking northwest-southeast. Therefore, reflecting crustal shortening perpendicular to the range, probably in response to the horizontal stress applied to the South American plate by the subduction of the Nazca plate. Earthquakes in the sub-Andes occur at depths of between 8 and 38 km indicating that much of the crust deforms in a brittle manner. The style of deformation depicted by these earthquakes does not resemble closely, either, a thin-skinned tectonic regime as that of the Canadian Rockies for example, or a broad zone of deformation with faults extending through the crystallinte basement, as that in the Laramide province of Colorado and Wyoming in the western United States. The deformation here seem to reflect the antithetic underthrusting of the

created farther east, and the deformation in the Andes apparently becomes progressively younger towards the east. In contrast with the sub-Andes, the high Andes are characterized by normal faulting on planes parallel to the axis of the range. Thus, there seems to be a delicate balance between the compressive stress, which is applied to the mountain belt in the direction of subduction causing thrust faulting in the sub-Andes, and the gravitational body force acting on the topographically higher parts and the crustal root of the Andes, which may cause normal faulting in the High Andes.

A microseismicity study conducted in the central Andes of Peru, east of the city of Lima also reveals the same tectonic fabric. Even though most of the stations forming our temporary seismographic network were located on the high plateaus, the vast majority of the microearthquakes recorded occurred on a fault in the Eastern Cordillera or in the western margin of the sub-Andes. Thus, the western part of the sub-Andes appears to be the physiographic province subjected to the most intense brittle deformation. Focal depths for these crustal earthquakes are as deep as 50 km, and the fault-plane solutions, as in the case of the teleseismic data, show thrust faulting on steep planes oriented roughly north-south. The Huaytapallana fault in the Cordillera Oriental also shows relatively high seismicity along a northeast-southwest trend that agrees with the fault scarp and the east-dipping nodal plane of two large earthquakes that occurred on this fault on July 24 and October 1, 1969. Microearthquakes of intermediate depth recorded during the experiment show a flat seismic zone about 25 km thick at a depth of 100 km. This agrees with the contention of Hasegawa and Sacks (1981) who suggest that beneath Peru the slab first dips at an angle of 30° to a depth of 100 km and then flattens. Fault-plane solutions of intermediate-depth microearthquakes have horizontal T axes oriented east-west.

The first part of the surface wave analysis presents a method to invert for the moment tensor using only the amplitude spectra of Rayleigh waves. The method is inspired from a similar approach suggested by Romanowicz (1982a) to invert for the moment tensor from the complex spectra and presents some distinct advantages to the method originally proposed by Mendiguren (1977). It eliminates some biases and errors in the data arising, for example, from inaccurate propagation corrections. In addition, it is substantially faster computationally and permits one to study separately the dependence of each of the moment tensor components as a function of depth, resulting in better focal depth resolution. The method is applied to three earthquakes in New Brunswick, Canada, the Gibbs transform fault in the north Atlantic, and the Hindu-Kush in central Asia.

In order to test the feasibility of routinely using the linear moment-tensor inversion method, phase velocities from an earthquake in the central Andes to various WWSSN stations around the world were calibrated using the results of moment-tensor inversion on the amplitude spectrum of this reference event. Using these phase velocities the observed source spectrum of another earthquake occurring closeby was corrected for propagation effects and its moment tensor and focal depth determined using a linear moment-tensor inversion. The source parameters for this new event were used to calculate a theoretical source spectrum and the phase velocities were upgraded and refined using a maximum-likelihood estimator (Pisarenko, 1970). This process was repeated anew for a third event and the final phase velocity measurements were used to correct the observed spectra of other events away from the reference point in an effort to study how far away these corrections could be used and still be able to successfully retrieve the focal parameters of other events in South America. The results in South America show that if the distances between the reference point and the earthquake of interest is less than about 800 km, the moment-tensor inversion yields source mechanisms that agree to within 20° with the nodal planes determined using first motion data and long-period body-wave modelling. The estimated focal depths appear to be within 8 km to those obtained from body-wave studies, and the uncertainty increases with increasing depth. One event studied that was located at a distance of about 1400 km from the reference event shows a marginal residual reduction for inversions at different trial depths, and the dips of the nodal planes of the resulting mechanism differ by over 30° with those determined from the first motion data.

Prof. Keiiti Aki

Professor of Geophysics

Prof. Peter H. Molnar

Professor of Earth Sciences

ACKNOWLEDGEMENTS

I would like first to thank my advisors, Kei Aki and Peter Molnar, for the amount of time and advice they so freely contributed towards the completion of this thesis. I would like to specially acknowledge Kei Aki who, with a proverbial patience, allowed me the freedom to work on other research projects and summer field work during my tenure as a graduate student. Peter Molnar suggested studying the crustal seismic activity in the Central Andes and his broad view and enthusiasm towards the earth sciences have been a source of inspiration during my formative years at MIT. Thanks are also due to Clark Burchfiel and John Sclater for encouragement and criticism of my research while at MIT.

My fellow graduate students have provided me with a continuous and friendly sounding board. I would like to thank specially my croonies in the 521 dungeon. Dan Davis read the first draft of most of this thesis and suggested many changes and improvements. I learned a great deal from Dan through many late night (and late morning) discussions on practically everything -from the mechanics of fold-and-thrust belts to nuclear proliferation. Mark Willis endured with me the painful task of deciphering esoteric IBM documentation, and together with Rob Comer and Roger Buck provided me with many helpful discussions and suggestions at various stages of my research. I thank Jim

Muller for the seismograms of the Gibbs transform fault earthquake and for encouragement during the long and final weekends.

John Nabelek, one of the last of the dying breed of observational earthquake seismologists at MIT, allowed me to use his programs to synthesize body waves and has spent countless hours discussing the results with me. I look forward to continue studying other interesting earthquakes together. Steve Roecker, my favorite Georgian, and Denis "Le Chef des Chefs" Hatzfeld taught me the Zen of seismograph maintenace. Howard Patton helped me during the early stages of my work on surface waves and introduced me to the method of moment tensor inversion. Among many others whom I am unwillingly excluding, thanks are also due to Mike Fehler, Paul Huang, Fico "El Loco" Pardo, Rob Stewart, Steve Taylor, Brian Tucker and Cliff Thurber.

I thank Debby Roecker for her friendship and her assistance in guiding me through the bureaucratic maze. Jean Titillah, Jan Nattier-Barbaro, and Sharon Feldstein paid the bills of my computer accounts and other expenses, and provided occasional typing. Donna Hall ably drafted most of the figures.

I would not have been able to do any of this without the constant support, encouragement, and unfailing confidence in my efforts provided by my parents and family.

Finally, but most importantly I want to thank my wife Patricia who has graciously endured the thankless role of being the wife of a graduate student. She has helped maintain my sanity and together with my son Gerardo has made it all worthwhile.

This research was supported by grants from the National Science Foundation number 7713632-EAR and 8115538-EAR, and by NASA's Geodynamics Program under contract NAG5-19. I thank the Organization of American States for financial support during my first two years at MIT and CONACYT (Consejo Nacional de Ciencia y Tecnologia, Mexico) for partial support.

TABLE OF CONTENTS

Chapter 1

Introduction

It is generally accepted that the Andes were formed as a result of the subduction of the oceanic Nazca plate beneath the western margin of the South American plate. Furthermore, the Andean Cordillera is frequently used as a currently active example of the tectonic scenario that is presumed to have existed in other mountain belts of the world, e.g. along the western coast of North America and in the Alpine-Himalayan belt prior to the collision of continental terranes. The evolution of the Andes, however, is as yet poorly known. Details of the style and rate of crustal deformation responsible for the formation of the mountain belt are hampered by the fragmented and scanty knowledge of the gelogical record and the lack of geophysical data in many parts of the cordillera.

Review of Geophysical Data in the Andes

Seismicity

Studies of the spatial distribution of the best located earthquakes in South America indicate that these events may be explained by a segmented oceanic lithosphere subducted beneath the South American plate (Barazangi and Isacks, 1976; 1979; Hasegawa and Sacks, 1981). Two of these segments, beneath central and southern Peru (2° to 15°) and beneath central Chile and Argentina (27° to 33°), have a very shallow dip. Hasegawa and Sacks suggest the slab lies almost horizontally beneath central Peru. The other three segments, beneath Ecuador, northern Chile, and south-central Chile have a steeper and more "normal" subduction dipping at about 30° A correlation exists between the two regions in central Peru and central Chile and Argentina, where shallow subduction occurs, and an absence of Quaternary volcanism on the South American plate.

Fault-Plane Solutions

Fault-plane solutions of the larger earthquakes under Chile and Peru (Stauder, 1973; 1975) can be grouped into four categories: (1) Earthquakes along the coast ranging in depth from 30 to 70 km marking the main thrust contact between the Nazca and the South American plate.

(2) Intermediate-depth earthquakes showing normal faulting in which the T axes are parallel to the dip of the plate. They range in depth from 80 to 220 km. (3) Deep earthquakes that have focal depths of between 500 and 630 km. The fault-plane solutions for these events show P axes parallel to the dip of the plate. (4) Shallow seismic activity occurring within the South American plate. Most of these earthquakes show P axes oriented in an east-west direction and suggest deformation of the overlying continental plate due to the compressive stress produced by the subduction of the Nazca plate.

Crustal Thickness and Seismic Wave Attenuation

Geophysical data in the central Andes provide us with a general view of the structure of the cordillera. One of the features that consistently emerges from these studies is the fact that the crust is thick. Very large Bouguer gravity anomalies in the order of about 400 mgals are observed in the Andes (eg James, 1971; Ocola and Meyer, 1973) implying a deep crustal root beneath the mountain belt. James (1971) studied the phase and group velocities of Love and Rayleigh waves propagating in the central Andes and shows that they are generally low. Based on these observations, James (1971) suggests that crustal thickness reaches a depth of 70 km beneath the high Andes and that the shear-wave velocity of the upper mantle beneath the

Moho is very low, in the order of between 4.3 and 4.45 km/sec. Surface wave data alone cannot uniquely determine the thickness of the crust. If the crust is thinned, the data can be fit using a lower shear velocity for the upper mantle. Likewise, using a higher mantle velocity would produce a thicker crust. Thus, a thickness of about 70 km appears to be an adequate lower bound for the thickness of the crust because it is unlikely that shear velocities of the upper mantle can be reduced further from the already low values estimated by James (1971).

Although several refraction lines have been shot in the central Andes (Ocola et al, 1971; Ocola and Meyer, 1973; Tatel and Tuve, 1958), none of these experiments have recorded Pn waves refracted at the Moho. This evidence for high seismic wave attenuation at depth has been confirmed by other studies of seismic wave propagation in the Andes (Barazangi et al, 1975; Chinn et al, 1980). A high topographic relief on the surface and the evidence of large attenuation of seismic waves suggests a regime of high temperature and possibly partial melting at depth. The only published heat flow measurement in the central Andes that I know of, however, show a mean value of 1.3 HFU (Sclater et al, 1970), only slightly higher than that of the Eastern United States.

Description of the Work

This thesis consists broadly of two sections. The first part of the work deals primarly with the seismotectonics of the Andes of Peru, Ecuador, and southern Colombia. The second part uses the vertical-component Rayleigh waves to invert for the moment tensor of some of these events and studies the propagation of surface waves from these sources to stations in Africa, North America, Europe, and the western Pacific.

In the first two chapters of this thesis my objective has been to understand the tectonic deformation currently taking place in the central Andes through the study of the seismicity, fault-plane solutions of earthquakes, and evidence of recent faulting observed in the geologic record. To understand how the deformation of the Andes occurs today and how they might have evolved through time, one would like to answer the following questions: Is most of the topography we observe today the product of extensive crustal shortening? Are the faults in the Andes shallow-dipping faults tapering at depth suggesting a style of deformation similar to the large decollements present in the Canadian Rockies or are they steep faults similar to those in the Colorado-Wyoming Rockies? Where in the Cordillera does faulting occur today? To what depth do these faults extend?

Chapter 2 attempts to answer some of these questions by studying all of the large teleseismic events occurring within the continental plate in Peru, Ecuador, and southern Colombia. The focal depths and fault-plane solutions of these large events were constrained by comparing the observed long-period P waves to synthetic waveforms at teleseismic distances. Based on the scalar seismic moment obtained from the comparison of observed versus synthetic waveforms, rates of crustal shortening during the last 17 years were estimated for the central Andes. This chapter also summarizes all available data (to our knowledge) of recent faulting in the central Andes and attempts to integrate the results of the seismic investigation with observations of the geologic record in an effort to interpret these data in light of plausible mechanisms of how the Andes might have formed and evolved.

Chapter 3 presents the results of a microseismic experiment conducted in the Andes of central Peru. A subset of what are considered accurately located events are screened and used to discuss the tectonic regime of the Altiplano, the Eastern Cordillera, and the sub-Andes. A number of intermediate-depth events recorded during the field experiment are also used to determine the depth and the dip of the subducted slab beneath central Peru.

In the second part of this work we investigate the use of the technique of moment tensor inversion from

vertical-component Rayleigh waves (Gilbert, 1970; McCowan, 1976, Mendiguren, 1977). In Chapter 4 a new method is proposed to invert for the seismic moment tensor using only the amplitude spectra. The proposed method offers some advantages over the one originally proposed by Mendiguren (1977) and is shown to be an efficient method to determine the focal depth and seismic moment tensor of earthquakes when the phase velocities from the source to the stations are not accurately known. The technique was applied to three earthquakes in Central Asia, a transform fault in the North Atlantic, and the 1982 New Brunswick earthquake with positive results.

Chapter 5 investigates the source and propagation effects of surface waves from earthquakes in the Central Andes. The source mechanism and focal depth of one of the large crustal earthquakes occurring in central Peru are obtained using the moment tensor inversion from the amplitude spectra of Rayleigh waves described in Chapter 4. Phase velocities to stations around the globe are then calculated using this earthquake as the reference event. Using a reference point equalization scheme (Patton, 1978), the source mechanism and focal depth of other earthquakes close to our reference event are determined and the estimates of phase velocity improved using a stacking technique. Finally, the feasibility of using the phase velocities estimated from these cluster of events to routinely apply

the linear moment tensor inversion on earthquakes located at greater distances from the reference point (500 to 1300 km) is investigated.

Chapter 2

Introduction

The Andes are important as a contemporary example of a mountain belt formed as a result of subduction of oceanic lithosphere beneath a continental plate. They are frequently used as the type example of a tectonic environment in which many ancient orogenic belts formed (eg. Dewey and Bird, 1970). "Andean margins" are characterized by a voluminous magmatic arc bounded on one side by a trench, and on the other side by a fold and thrust belt. They are inferred to have been present along some continental margins during the closing of oceanic terranes that ultimately led to continental collisions.

Western North America is interpreted to have been an "Andean margin" during the late Mesozoic and early Tertiary, when the Farallon plate or other oceanic plates were subducted beneath it (Burchfiel and Davis, 1972; 1975; Hamilton, 1969), much as the Nazca plate presently plunges beneath western South America. The variability of structural development along strike in both North and South America, however, allows the generic term "Andean margin" to embrace a broad spectrum of tectonic styles. Specif-

ically, differences between the tectonic development of western Canada, with its classic thin-skinned fold and thrust belt (Bally et al, 1966; Price and Mountjoy, 1970) , and the broad zone of late Cretaceous-early Tertiary Laramide deformation with faults extending through the crystalline crust of the western United States in Colorado and Wyoming (eg. Burchfiel and Davis, 1972; 1975; Sales, 1968; Stearns, 1978), are as great as the differences, for instance, in the tectonic style of the Alps, a collisional orogen, and the High Atlas, an intracontinental zone of deformation. Yet, the late Cretaceous and early Tertiary structures in both Canada and the United States formed in a setting typically classified as an "Andean margin". Moreover, the structure and history of the Andes shows similar and equally large variations in tectonic style along strike. Even though knowledge of Andean geology is still limited, it is clear that the Pampean ranges in central Argentina, represent a broad zone of deformation characterized by faults that extend into crystalline basement. They are clearly different from the wide belt of folds and thrust faults that appear to affect only the Paleozoic sedimentary cover in Bolivia in what can be interpreted as a thin-skinned tectonic style (Jordan et al, 1982). Accordingly, before the concept of "Andean margin" can contribute more to the understanding of older belts than simply to suggest cartoon-like analogies, a more comprehen-

sive understanding of the tectonics of different parts of the Andes is required.

The purpose of this paper is to contribute some new data bearing on the active tectonics of the Central Andes (Peru, Ecuador and southern Colombia), and to summarize these data in light of plausible mechanisms of how the Andes might have formed and evolved. We are concerned primarily with evidence of recent faulting, particularly reflected by intracontinental earthquakes and geologic evidence of Quaternary faulting.

In the Central Andes, local seismic station coverage is scanty and routine determination of hypocentral depths are frequently grossly in error (eg. James et al, 1969). Using synthetic seismograms of long period body waves, we revise published fault plane solutions (Pennington, 1981; Stauder, 1975; Wagner, 1972) and determine both focal depths and fault plane solutions for others. At epicentral distances of between 30° and 80°, the shape of long period body waves depends upon both the depth of the hypocenter and the orientation of the nodal planes, and is not very sensitive to changes in the local structure of the upper mantle. Thus, focal depths and fault plane solutions can be constrained by a visual comparison between observed long period P waves and synthetic waveforms on a trial-and-error basis.

The Central Andes: an Overview

The main morphological units in the Central Andes are, from the trench eastward: the coastal plains, the Cordillera Occidental, the Altiplano, the Cordillera Oriental, and the sub-Andes (Figure 1). A brief description of the geology and tectonic evolution of each region is taken from recent reviews of central Andean geology (Audebaud et al, 1973; Dalmayrac et al, 1980; Gansser, 1973; Megard, 1978; Zeil, 1979).

The Coastal Plains

In northern Peru, the coastal plain is a narrow and arid strip of land not wider than 40 km. Limited on the west by the coastline and to the east by the Cordilleran batholith, it is formed mainly of gently folded volcanic and sedimentary rocks of Mesozoic age. In southern Peru, the coastal plains widen and strongly folded crystalline basement rocks crop out. The Precambrian coastal massif in southern Peru, generally called the Arequipa block, contains rocks as old as 1.8 to 2.0 b.y. (Cobbing et al, 1977; Dalmayrac et al, 1977) and was subjected to deformation in Precambrian, Paleozoic and Mesozoic times (Shackleton et al, 1979).

The Cordillera Occidental

The western Cordillera consists mainly of volcanic and plutonic rocks of Mesozoic and Cenozoic age and shallow water marine deposits of Mesozoic age. It forms a continuous and impressive structural entity parallel to the coast and is the locus of most of the late Cenozoic volcanism. The main structural unit is the immense Coastal Batholith extending from about 6° to 16° S parallel to the coast (Figure 2). Plutons ranging in composition from gabbro to syenogranite (Cobbing and Pitcher, 1972; Cobbing et al, 1977) were emplaced episodically from 100 to 30 m.y. ago (Pitcher, 1975). The plutons become younger and show an increase in silicic content eastward (Bussel et al, 1976; Stewart et al, 1974). Cenozoic volcanic rocks are widespread in the western Cordillera and massive ignimbrites of Neogene age are present (Dalmayrac et al, 1980). Volcanic activity began to wane about 11 m.y. ago and stopped rather abruptly 5 m.y. ago (Noble and McKee, 1977). This cessation of Quaternary volcanism has been interpreted as marking the begining of shallow plate subduction under Peru (Barazangi and Isacks, 1976;1979; Megard and Philip, 1976). East and north of the Cordillera Blanca, structures developed in the Mesozoic rocks are similar to those of a foreland fold and thrust belt. The folds and thrusts in this region are generally of flexural-slip type with both broad-rounded hinges and chevron geometry. The Mesozoic limestones were thrust

eastward on gentle west-dipping faults, while the underlying Jurassic shales formed tight flexural-slip folds (Dalmayrac, 1978; Dalmayrac et al, 1980; Wilson et al, 1967). The tectonic style implies detachment of the Mesozoic cover from an older substratum and extensive east-west shortening (Coney, 1971). In the western part of the belt, volcanic rocks of Oligocene-Miocene age unconformably overlie deformed Mesozoic rocks and limit the age of deformation to late Cretaceous and early Cenozoic time (Dalmayrac, 1978; Wilson et al; 1967). The folded belt is truncated and limited on its western side by the granitic plutons of the Cordillera Blanca emplaced 3 to 12 m.y. ago (Stewart et al, 1974).

In central Peru, the Mesozoic sedimentary rocks east of the coastal batholith are tightly folded in chevron folds. Fracture cleavage present in the late Cretaceous red beds is absent in the overlying Tertiary volcanic rocks indicating a late Cretaceous to early Tertiary age of deformation (Megard, 1978).

In southern Peru, the Mesozoic sedimentary rocks are almost completely covered by Cenozoic volcanic rocks and the amount and age of deformation of the Mesozoic rocks is not well known. Recently, Vicente et al (1979) mapped a sub-horizontal east-directed thrust fault with a minimum displacement of 15 km, in the area near Arequipa (Figure 2). The thrust fault places rocks as old as Precambrian on

Mesozoic sedimentary rocks. Although this thrust fault is now west of the active volcanoes, when thrusting occurred during the late Cretaceous, it lay east of the volcanic arc active then.

The Altiplano and Central High Plateau

The high plateau of central Peru and the Altiplano in southern Peru are bounded to the west by the coastal batholith,and to the east by the Cordillera Oriental. North of about 10° S, the central high plateaus disappear and the western and eastern Cordillera are adjacent. The width of the high plateau in central Peru is 10 to 50 km wide and increases considerably in the south to nearly 200 km near Lake Titicaca in the Altiplano. The thick sequences of Paleozoic and Mesozoic marine sedimentary rocks that are present in the high plateau and the Altiplano apparently were deposited in deep, northwest-trending basins (eg. Harrington, 1962; Lohman, 1970; Wilson, 1963) and later were capped by late Cretaceous to late Eocene red beds.

The tectonic style in the central high plateaus is variable along strike. In the region around Huancayo in central Peru (Figure 2), zones of tight folds and thrust faults form narrow belts (10 to 30 km wide) that are separated by zones of open folds and undeformed rocks of similar width (Lepry and Davis, 1982; Megard, 1978). These belts of intense deformation anastomose along strike. The

geometry of folds and some faults suggests local detachment from their substratum (Lepry and Davis, 1982). Where exposed, Paleozoic or Precambrian rocks appear to be involved in some of the structures.

Much of the Altiplano in southern Peru is covered by a thick sequence of mildly deformed continental molasse deposited during the Oligocene and Miocene (eg. Newell, 1949). Folding is less severe than in central and northern Peru and the Tertiary sedimentary rocks are generally deformed in broad concentric folds cut by reverse faults (eg. Chanove et al, 1969). Northwest of Lake Titicaca, the thrust faults suggest that the sedimentary cover was detached from its underlying basement and deformed during late Cretaceous and early Cenozoic time (Chanove et al, 1969; Laubacher, 1978).

Cordillera Oriental

The eastern Cordillera is a broad zone underlain largely by pre-Mesozoic rocks located east of the central high plateaus. Precambrian crystalline rock and Paleozoic plutonic rocks crop out in large areas of the eastern Cordillera, particularly in central Peru. The sedimentary rocks are composed of a thick section of mainly Paleozoic shallow marine and continental strata that are folded and frequently cut by reverse faults.

Precambrian rocks are generally low-grade meta-sedimentary rocks (phyllites or fine-grained schists) that are weakly to strongly foliated (Dalmayrac et al, 1980; Megard, 1978). Only locally do the Precambrian crystalline rocks reach amphibolite to granulite grade. Lower Paleozoic rocks range from Ordovician to Devonian in age, and are generally unmetamorphosed to weakly metamorphosed. The upper Precambrian and lower Paleozoic rocks are the oldest rocks exposed in the eastern Andes, and they form a very anisotropic and weak upper crust. Published material (eg. Dalmayrac et al, 1980; Megard, 1978) attributes deformation of these rocks to a middle to late Paleozoic ("Hercynian") event. The presence of this deformation and the existence of Paleozoic batholiths suggests subduction along the western margin of South America was active at this time.

The sub-Andes

The sub-Andean zone consists of a belt of folded sedimentary rocks parallel to the mountain chain between the high Andes and the Brazilian shield. The limit between the Cordillera Oriental and the sub-Andes is generally shown to be formed by a zone of west-dipping thrust or reverse faults (Ham and Herrera, 1963). The rocks consist of shallow water and continental sedimentary rocks deposited intermittently from Paleozoic to Pliocene time. No

evidence of Andean magmatism has been found in the sub-Andes. The thickness of the sedimentary cover is not well known. In northern Peru, where exploration for oil has been active, depths of up to 10 km have been reported in some basins (Audebaud et al, 1973; Rodriguez and Chalco, 1975).

The upper-Tertiary sedimentary rocks are poorly dated and the deformation of the sub-Andes is difficult to date precisely (eg. Audebaud et al, 1973). In Peru, the sub-Andes are formed by a series of folds and faults active from at least the Pliocene to the present. Deformation is usually interpreted as the result of crustal shortening expressed by cylindrical folds cut by steep, west-dipping reverse faults that pass from the sedimentery rocks into the underlying basement (eg. Audebaud et al, 1973; Megard, 1978). The age and intensity of tectonic deformation is typically shown to decrease steadily to the east (eg. Dalmayrac et al, 1980). Published cross sections are mostly schematic because data from drill holes or seismic profiles have not generally been available. Dense vegetation limits the exposure; the outcrops are small and fault planes commonly are not exposed well enough to determine their dips. In northern Peru, oil exploration has produced a more detailed three dimensional picture of the structure of the sub-Andes (Rodriguez and Chalco, 1975;

Touzett, 1975). Here, the sub-Andes can be interpreted as a thin-skinned fold-and-thrust belt.

Shallow Seismicity in South America

Epicenters of well located shallow earthquakes (less than 50 km deep) occurring along the western margin of South America in the last 20 years or so define two distinct loci of seismic activity (Barazangi and Isacks, 1976;1979) To the west, one belt lies parallel to the coastline and marks the boundary where the Nazca plate subducts under South America (Stauder, 1975). The other belt of seismic activity occurs within the overriding continental plate and follows a trend parallel to the mountain chain. The majority of these crustal events take place in the transition zone between the eastern Cordillera and the western margin of the sub-Andes. The distribution of epicenters of crustal events shows a remarkable quiescence of seismic activity in the high Andes and in the eastern part of the sub-Andes (Figure 3). There is also a paucity of seismic activity in the forearc region, a feature commonly observed in other areas of the world (eg. Yamashina et al, 1978).

The spatial distribution of intracontinental seismicity shows variations along strike as well (Jordan et al, 1982).

The most seismically active areas occur under Peru and southern Ecuador, between 2° and 13° S, and under northern Argentina, between 28° and 33° S (Figure 3). These regions correspond roughly to the two areas where telesesmic data suggest that subduction of the Nazca plate under South America takes place at the unusually shallow dip of about ten degrees (Barazangi and Isacks, 1976; 1979; Megard and Philip, 1976). In the Central Andes most of the intracontinental earthquakes occur in the eastern part of the Cordillera, beneath the western sub-Andes (Figure 4). Seismicity along the eastern margin of the Altiplano and the Argentinian Puna, beneath which subduction of the Nazca plate occurs at a steeper angle (~30°), also shows the existence of a seismic sub-Andean margin, though less active than the two regions mentioned above (Figure 3). A remarkable segment of quiesence is found along the eastern margin of the Altiplano of southern Peru and northern Bolivia, between 13° and 18° S (Figure 4).

Fault Plane Solutions and Depth of Foci

Data and Method of Analysis

We studied all intracontinental events in the cen-

tral Andes sufficiently large that a fault plane solution could be obtained with data from the World Wide Seismographic Station Network (WWSSN) between 1962 and 1978 (Table 1). Constraints on the fault plane solutions and the depths of foci were obtained synthesizing long period P waves for a spectrum of solutions and focal depths, and comparing them to the observed waveforms, as others have done elsewhere (eg. Jackson and Fitch, 1981; Kanamori and Stewart, 1976; Rial, 1978; Trehu et al., 1981).

In this study, a point source embedded in semi-infinite half space was used to synthesize all available long period P waves at WWSSN stations within an epicentral distance of 30° to 80°. Body waves at these distance ranges have paths that lie almost entirely within the lower mantle and are not affected by the local structure of the upper mantle (eg. Langston and Helmberger, 1975). At epicentral distances between 30° and 80°, P waves do not experience triplification or diffraction near the core-mantle boundary that severely complicate the observed waveforms.

Synthetic seismograms were computed in the time domain by convolving the response of a shear dislocation in a semi-infinite half space with a far field source time function, an attenuation operator, and the instrument response. The far-field source time function was assumed to be a symmetric trapezoid for both direct and reflected phases and was adjusted in an ad-hoc manner to fit the observed P

waves. Plots of the fault plane solutions and waveforms used in the analysis are shown in Appendix 1. Synthesized waveforms are also shown at several hypocentral depths for a few selected stations spanning a range of azimuths. This will permit the reader to judge the uncertainty in the estimates of focal depth (Appendix 1).

Constraints on the Fault Plane Solution

The determination of fault plane solutions for earthquakes in the Andes suffers from a dearth of WWSSN stations to the west. Only a few stations on islands in the Pacific, with low magnifications, sometimes yield reliable first motions. Thus, since most of the events in the area show reverse faulting, the dip of nodal plane dipping west is generally very poorly constrained (Appendix 1).

A clear example illustrating this problem is the earthquake of May 15,1976 (event 16). First motions for this earthquake are scarce and allow two different families of fault plane solutions (Figure 5). The solid line depicts an almost pure dip-slip solution with reverse faulting, while the dotted line indicates nearly pure strike-slip motion. Only two stations, WES and OGD in the eastern United States, produced long period P waves large enough to be useful in the visual comparison with synthetic waveforms. WES and OGD are stations in close proximity and rays to them leave the source with similar take-off angles. Thus,

the orientation of the fault planes cannot be resolved well. Synthetic waveforms, however, allow us to determine which of the two alternative types of faulting is likely (eg. Langston, 1979). The strike-slip solution does not produce waveforms that resemble the observed P waves, but synthetic P waves corresponding to the dip-slip mechanism closely resemble the observed wavetrains (Figure 6). It should be pointed out, however, that varying the strike or dip of the nodal planes of the dip-slip solution by as much as 15 degrees will not change appreciably the shape of the synthetic waveforms observed at these two stations.

Errors in Depth Determination

A comparison of focal depths reported in the ISC catalog and those determined in this study using synthetic waveforms shows large discrepancies in many cases (Tables 1 and 2). The problem stems in part from the sparse coverage of the local networks and the poor azimuthal distribution of the WWSSN stations. One of the primary objectives in this paper is the accurate determination of the focal depths of these events.

To illustrate the accuracy of focal depth estimates, Figure 7 shows that for the earthquake of March 20, 1972 (event 13), focal depths shallower than 36 km are clearly unacceptable, for the average crustal velocity used in the calculation. Similarly, for depths larger than about 42

km, the interval between the direct and reflected phases is too large, and the synthetic P waves are too broad (Figure 7). Thus, we consider the focal depth in this case to be 38±2 km, if the average crustal velocity were 6.0 km/sec This would be equivalent to an error in focal depth of about 5%. It is noteworthy that the focal depth reported by ISC was 52 km. The inferred depth is proportional to the assumed velocity of P waves in the crust. Using velocities of 5.5 or 6.5 km/sec, which span the range of plausible crustal velocities, synthetic seismograms for a given depth at these three stations are not significantly different from one another (Figure 8). Thus, our ignorance of the crustal velocity adds roughly another 5 to 10 % uncertainty to the estimated focal depth.

Discussion of Results

Of the seventeen earthquakes studied, ten occurred along the transition zone between the sub-Andes and the Cordillera Oriental. The rest are distributed among the high Andes (four), the forearc in Ecuador (two), and the Brazilian shield in Colombia (one).

Events in the Forearc

As discussed above, the forearc in the Central Andes

is, in general, seismically quiet. Of the events studied only two earthquakes beneath the coast of Ecuador occured in the forearc. They are two of the largest earthquakes studied. The focal depth of event 15 is about 22 km. Therefore, this event probably occurred above the inclined seismic zone, which lies at a depth of about 35 km in the region just south of where event 16 occurred (Barazangi and Isacks, 1979). The fault plane solution for this event shows thrust faulting on a north or northeast trending plane. This event reflects crustal shortening along the western margin of the Andean cordillera and not simple underthrusting of the Nazca plate beneath the arc, as most events along the margin do. Thus, it might be part of a process of tectonic erosion of the continental margin due to subduction (eg. Plafker, 1972).

The solution for event 10 also shows thrust faulting on a north trending plane that dips approximately 45° either east or west. The focal depth of event 10 is 32 km, and it is not clear if it lies within or above the inclined seismic zone. The dip of 45° of the east-dipping nodal plane appears to be too steep for this event to occur along the shallow-dipping plate boundary (Figure 10). This zone appears to be shallower beneath Ecuador than it is farther south, but it is very poorly defined by teleseismic data (see Figure 5 in Barazangi and Isacks (1979)). Thus, the depth of event 10 (30 km) is sufficiently deep that it is

difficult to ascribe it to internal deformation of the overriding plate or attribute it to slip on the main inclined seismic zone.

The Brazilian Shield

The fault plane solution of event 14 in the Brazilian shield indicates strike-slip motion with the P axis oriented in an east-west direction. The orientation of the P axis parallel to the direction of subduction suggests that the Brazilian shield experiences compression in that direction and in response to convergence. This is consistent with the solutions of 5 shallow events in cratonic South America showing P axes oriented approximately east-west (Mendiguren and Richter, 1978).

Tectonics of the sub-Andes

Most of the earthquakes studied are concentrated along the eastern flank of the Andes on the western edge of the sub-Andes. They occur beneath regions of low topographic elevation and consistently show thrust faulting approximately parallel to the mountain belt (Figure 9). In most cases, the nodal planes dip at steep angles, between 30° and 60° (Figure 12), and we cannot determine which of the two nodal planes was the fault plane. The events are too small for the body waves to show azimuthal differences in pulse shapes due to the finiteness of the source that could

be used to select the fault plane. Moreover, the lack of local stations did not permit the recording and accurate locating of aftershock sequences. Nevertheless, because most of the thrust faults in the sub-Andes dip west (Dalmayrac, 1978; Dalmayrac et al, 1980; Megard, 1978), we presume that the west dipping nodal planes are the fault planes (Figures 10 and 11). Although west dipping nodal planes are usually the more shallow dipping of the two nodal planes, the dips are still much steeper than those associated either with decollement in a thin-skinned tectonic environment as in the Canadian Rockies (Bally et al, 1966; Price and Mountjoy, 1970), or with surface exposures of large crystalline nappes, such as those in Norway (Gee, 1975). At first glance, the steep dips appear to be more reminiscent of faults active in the early Tertiary (Laramide) in the Rocky Mountains of Colorado and Wyoming (eg. Brewer et al, 1979; Smithson et al, 1979), or of those deduced from fault plane solutions of earthquakes in the Tien Shan (eg. Tapponnier and Molnar, 1979) or the Zagros Mountains (Jackson and Fitch, 1981; McKenzie, 1972).

The earthquakes studied in the sub-Andes are relatively deep, ranging in depth from 8 to 38 km, compared with those in the Zagros Mountains with focal depths of 10 to 15 km (Jackson and Fitch, 1981). Thus, they indicate that most of the crust and possibly the uppermost mantle are involved in the deformation. The inferred depth of the deepest event

is between 36 and 40 km. Unfortunately, we are not aware of any studies of crustal thickness in the sub-Andes that resolves the question of whether these deeper events occurred in the uppermost mantle or in the lower crust. None of those studied here, however, occurred as deep as 80 km, as suggested by Stauder (1975). Regardless of the depth of the Moho, it is clear that the earthquakes occurred in the crystalline basement and not in the overlying sedimentary cover. This fact is consistent with the inference that the earthquakes do not result from slip along a decollement between the crystalline basement and overlying sedimentary strata.

Relating the earthquakes to specific faults identified from geologic field work is difficult, both because of inaccuracies in the locations of the earthquakes and because of a lack of detailed geologic studies of the sub-Andes. The best studied segment of the the sub-Andes is in Central Peru (Audebaud et al, 1973; Dalmayrac, 1978; Megard, 1978). Numerous west dipping thrust, or reverse, faults can be inferred from the juxtaposition of rocks of different ages. Typically, faults are drawn dipping at steep angles (60° to 70°). The descriptions of these regions are not sufficiently detailed, however, for us to know why steep instead of shallow dips have been inferred. In the regions that we have seen, albeit only during a cursory field reconnaissance, the fault planes generally were

not exposed and faults could be inferred only from the juxtaposition of rocks of very different ages. The style of internal deformation of the rocks near the faults suggested that they are thrust faults. From the gentle west-dipping cleavage present in Mesozoic and Cenozoic limestones and red sandstones and from the shallow west dips of some minor faults, we suspect that many of the thrusts dip at more shallow angles (less than 20°) than are shown in published cross sections.

One of the basic questions to be addressed by this study is to what extent does the deformation in the sub-Andes resemble that of the Canadian Rockies during the late Cretaceous in one extreme, or the Colorado-Wyoming Rockies during the early Tertiary in the other. The steep-dipping faults that cut the basement of the sub-Andes resembles the type of faulting in the Colorado-Wyoming Rockies, where the basement is clearly involved and some fault planes are quite steep (≥30°) (Brewer et al, 1980; Smithson et al, 1979). Nevertheless, the similarity is far from perfect. In particular, whereas the ranges in Colorado and Wyoming apparently are bounded and uplifted by one or two faults, the sub-Andes seem to be cut by numerous faults over a broad zone that has experienced deformation in the late Cenozoic. More importantly, the earthquakes in the sub-Andes occur only in the western margin of the province, while at the surface the most recently deformed rocks

appear to be on the eastern side. Thus, while the basement beneath the transition from the Cordillera Oriental and the sub-Andes undergoes crustal shortening, the youngest deformation of the cover occurs some 50 to 100 km to the east.

To reconcile these two observations, one can infer that the cover is, in fact, detached, so that the relatively steep thrusts in the basement flatten when they reach the overlying sedimentary rocks. In this respect, the style of deformation would resemble that of the Canadian Rockies. In the Canadian Rockies, faults dipping steeply at the surface flatten with depth and detach the sedimentary cover from the underlying basement. The earthquakes in the central Andes give no hint of a similar process; the nodal planes are too steep and the events are too deep, clearly having occurred within the basement. Moreover, there is no obvious systematic change with depth of the dips of the nodal planes as might be expected if fault surfaces curved smoothly with depth. It is also possible that shortening on steep faults in the basement is decoupled along a gently dipping decollement from the shortening in the sedimentary cover rocks; displacement in the decollement would then be largely aseismic. Thus, the earthquakes and brittle deformation of the basement in Peru may occur in a setting different from the wide zone of detached sedimentary rocks in the Canadian Rockies.

Perhaps, the earthquakes indicate deformation of the basement below and west of a detached sub-Andean terrane, and if there were a sequence of thick and competent sedimentary rocks in the sub-Andes of central Peru, they would show a style of deformation similar to that of the Canadian Rockies. Thus, the shortening in the basement would occur west of the surficial expression of shortening in the sedimentary cover, and the two areas would be related by a gently dipping aseismic(?) decollement. Considering the weak and foliated nature of the Precambrian crystalline rocks that crop out in the Cordillera Oriental, it is possible that part of this crystalline basement is also detached from a deeper and more rigid substratum. Alternatively, one can infer that some of the faults active in the basement continue into the overlying cover so that the eastward progression of deformation is then only approximate. Regardless, despite some similarities to both, the style of deformation in the Peruvian sub-Andes as a whole seems to differ from that of both the Colorado-Wyoming Rocky Mountains and the Canadian Rockies.

The present regime of steep basement-involved thrust faults is similar to the style of basement deformation that probably prevailed in the high Andes during their formation. Throughout much of Peru, the sedimentary cover is tightly folded, sometimes in localized zones of concentrated deformation and with occasional steep faults (eg.

Coney, 1971; Lepry and Davis, 1982; Megard, 1978). Except for a portion in north-central Peru, neither a preferred vergence nor large overthrusts can be recognized. Therefore, it is appropriate to suggest that the active tectonic regime that we observe today in the sub-Andes is similar to the process that produced extensive crustal shortening and is responsible for the formation of the Central Andes.

Rate and amount of crustal shortening. This interpretation motivates a comparison of the rate of crustal shortening obtained by adding the seismic moments of earthquakes with that implied by the geologic history. The definition of seismic moment is:

$$M_o = \mu \cdot S \cdot u \qquad (1)$$

(Aki, 1966), where Mo is the scalar seismic moment, S is the surface area of the fault, u is the average slip of the fault, and μ the shear modulus. Thus, the cumulative slip on a single fault can be estimated by simply summing the seismic moments of earthquakes causing slip on the fault (eg. Brune, 1968; Davies and Brune, 1968). In the central Andes, however, seismic energy release does not take occur along a single major fault. Instead, earthquakes occur on fault planes with different orientations distributed over a large seimogenic volume. In this case, it is more appropriate to follow Kostrov (1974) and use the seismic moment tensors to calculate the strain resulting from the motion

of all the faults in the region (eg. Wesnousky et al, 1982; Chen and Molnar, 1977).

The seismic moment tensor for an arbitrary shear dislocation may be expressed as,

$$M_{ij} = \mu A(u_i \eta_j + u_j \eta_i) \qquad (2)$$

where η_i are the direction cosines of the vectors normal to the fault plane, and u_i is the average slip in vectorial form. The principal values of the moment tensor, -Mo,0, and +Mo, correspond to the P, B, and T axes of fault plane solutions (Gilbert, 1970). Kostrov (1974) showed that the mean rate of irrotational strain in a volume, V, over a period of time, t, due to slip on N different faults within that volume is,

$$\dot{\epsilon}_{ij} = \frac{1}{2\mu Vt} \sum_{n=1}^{N} M_{ij}^{n} \qquad (3)$$

In the Central Andes, tha areal dimensions of the deformed volume are about 2000 km in length and 250 km in width. We assume a thickness of 35 km corresponding to the deepest intracontinental earthquake studied.

Diagonalizing $\dot{\epsilon}_{ij}$ yields the principal directions of the average strain rate. Crustal shortening is computed by multiplying the horizontal component of the maximum compressive strain rate times the width of the deformed body in the direction of maximum compressive strain. In the Central Andes, the principal value of compressive

strain rate is $6x10^{-9}$ yr^{-1} oriented about N85°E. This orientation is consistent with the direction of subduction of the Nazca plate beneath South America. The average rate of crustal shortening is between 1.0 and 1.7 mm/yr. The smaller figure is obtained by not including event 10 in the calculations. As discussed above, it is possible that event 10 occurs in the main thrust contact between the Nazca and South American plate and not be the result of crustal deformation of the continental plate. These rates of crustal shortening are lower bounds since they assume that the deformation is being taken up only by brittle fracture, and disregard the possibility of fault creep and viscoelastic deformation. The rates also include only contributions from earthquakes with magnitudes between 5.4 and 6.3. Combining the frequency-magnitude ($\log N=a-b\bullet M_s$) and moment-magnitude ($\log M_o=1.5\bullet M_s+16$) (Hanks and Kanamori, 1979) relations, where N is the number of earthquakes, Ms is the surface wave magnitude, and Mo the seismic moment, the contribution due to earthquakes smaller that magnitude 5.4 can be estimated (eg. Molnar 1979). Assuming a value of b equal to 1, the contribution to the total moment by events with Ms < 5.4 is only 37% of that of events with magnitudes between 5.4 and 6.3. Thus, average crustal shortening rates would be in the order of 1.4 to 2.1 mm/yr.

The total amount of crustal shortening can be estimated assuming that crustal volume is conserved, and excess mate-

rial beneath the mountainous topography and in the root of the Andes correspond to South American crust that subsequently has been substantially shortened. Assuming an average elevation of 4 km and a crustal thickness of 60 km (James, 1971), then for a crust originally 35 km thick, we obtain 190 km of crustal shortening. This estimate neglects the loss of crustal material through erosion or addition by magmatic processes. Even if 10 km of material had been eroded from the top of the Andes over a width of 250 km, these estimates of crustal shortening would increase by only 35%. Thus, we do not consider ignoring erosion to be important for the significance of the following calculations. More problematic is the quantity of mantle-derived plutonic rocks in the Andes. To our knowledge there are no reliable estimates of the amount of such rocks in the Peruvian Andes, and we simply ignore them, recognizing that the amount of crustal shortening estimated here is an upper bound. For contrast, from the structures and style of deformation in a geologic cross section traversing the Central Andes, Megard (1978) suggests crustal shortening to be of the order of 100 km.

Shortening of 190 km of Andean crust at a rate of 1.4 to 2.1 mm/yr would require 90 to 135 m.y. Although, subduction probably occurred throughout most of the Mesozoic (eg. Helwig, 1973), paleogeographic interpretations have indicated the presence of a major transgression ending in the

late Cretaceous (eg. Audebaud et al, 1973; Zeil, 1979). Therefore, much of the present Andes were at sea level about 70 to 80 m.y. ago and the present topography and thickened crust must have formed since then.

Because of the short record of seismicity, our ignorance of recurrence rates, and the unavoidable approximate assumptions made in estimating the rate and amount of crustal shortening, the agreement between the average rates of shortening inferred from the seismic moments of 17 years of seimicity and from about 70 m.y. of geologic history is not a strong argument that the present tectonics of the sub-Andes are similar to those of the Andes as a whole throughout the last 70 my or so. However, agreement within order of magnitude suggests that if most of the topography, and implicitly the associated crustal root as well, developed in latest Cenozoic time as often presumed (eg. Audebaud et al,1973), then the Andes must have been built by some process other than crustal shortening.

Earthquakes in the High Andes

Thrust faulting at high elevation. Only four large earthquakes occurred in the high Andes in the last twenty years: event 17, in Ecuador, events 7 and 8 in the Cordillera Oriental of southern Peru, and event 11 in the northern Altiplano (Figure 9). These earthquakes are shallow; focal

depths are not deeper than 20 km. In fact, among all of the earthquakes studied here only event 7 is known to have produced a surface break in the Andes. Events 7 and 8 occurred near the Huaytapallana fault, which crops out at an elevation of about 4600 m above sea level. The fault scarp indicates reverse faulting with a component of left-lateral strike-slip motion on a plane dipping about 60°NE and striking N50°W (Philip and Megard, 1976). In the basins just west of this fault, Dollfus and Megard (1968) reported folding of Quaternary glacial terraces. The strike of the folds is in a direction N30°W and is consistent with the strain pattern deduced from the fault.

Event 11 is the only large earthquake in the Altiplano large enough to be studied. It has a focal depth of 8 km and the fault plane solution indicates almost pure strike-slip motion with north-south oriented T axes. In Ecuador, event 17 occurs at a depth of 16 km. Event 17 shows a thrust mechanism with the P axes oriented approximately east-west.

Normal faulting in the high Andes. Although thrust faulting is the prevalent style of deformation throughout much of Andes, normal faulting has been documented in a number of localities in the high Andes. Normal faults clearly offset Quaternary glacial moraines along the eastern margin of the Cordillera Blanca of central Peru (Dalmayrac, 1974;

Yonekura et al, 1979). Yonekura et al (1979) recognize a system of normal faults on the satellite imagery more than 100 km long (Figure 13). The strike of the faults is roughly parallel to the Andes indicating a component of extension perpendicular to the mountain range. Furthermore, in the Altiplano of southern Peru and northern Bolivia, normal faults offset Quaternary sediments (Lavenu, 1979; 1980; Mercier, 1981). During field work in the summer of 1980, we discovered another clear, recently active normal fault near the northern edge of the Altiplano. The fault scarp is not prominent on satellite imagery, but it is clear on aerial photographs (Figure 14), and from the ground (Figure 15).

The only large earthquake recorded in areas where normal faulting has been reported is the 1946 Ancash earthquake (Richter, 1958). The epicenter is located about 100 km east of the Cordillera Blanca. Silgado (1951) described the scarps produced by this event and concluded that normal faulting occurred on a plane dipping west at about 45 degrees. Moreover, the fault plane solution (Figure 16) (Hodgson and Bremner, 1953) shows normal faulting with one of the nodal planes parallel to the strike of the fault scarps observed by Silgado (1951). It has also been suggested that normal faulting was also the cause of both the 1949 Ambato earthquake in the high Andes of Ecuador (B.

Foxall personal communication, 1982) and the 1958 Maipu earthquake in Chile (Jordan et al, 1982).

Implications of Normal and Thrust Faulting in the High Andes. The coexistance of normal faulting at high elevation and thrust faulting at the eastern edge of the mountain belt, within a few tens of kilometers of each other, can be explained by variations in the stress field that must balance the gravitational body force acting on the regions of high elevation and their associated crustal roots (Dalmayrac and Molnar, 1981). To balance the lateral variations in the gravitational body force, there must be a gradient in stress. This balance can be maintained if the horizontal compressive stress exceeds the vertical stress in regions of low elevation, where thrust faulting prevails. Alternatively, the vertical compressive stress can exceed the horizontal stress in regions of high altitude (and thickened crust), where normal faulting occurs. In portions of the central Andes both seem to occur concurrently. For topography in the form of a ridge on an elastic half space, the horizontal compressive stress induced by gravity acting on the ridge approaches a maximum on the flanks of the ridge and is mimimum at the peak (McTigue and Mei, 1981). For large characteristic slopes, the horizontal stress can become purely tensile at the peak of the ridge (Figure 17).

The two segments of the Central Andes where thrust faulting and crustal shortening are observed in the high Andes coincide with the regions where aseismic oceanic ridges are being subducted: the Galapagos-Carnegie ridge in Ecuador and the Nazca ridge in southern Peru. It is qualitatively easy, to ascribe an excess horizontal compressive stress to resistance to subduction of the buoyant ridges beneath these portions of the Andes as has been suggested before to explain other phenomena (eg. Kelleher and McCann, 1976; Pilger, 1981; Vogt et al, 1976).

Implications For Andean Evolution

In some ways, the active tectonics and tectonic setting are analogous to those present in the Himalaya and Tibet (Molnar and Tapponnier,1975; 1978; Molnar et al, 1977). Thrust faulting on the margins of Tibet occurs concurrently with normal faulting in the highest part of the plateau. The stress needed to cause slip on a thrust fault at low elevations apparently is less than that required to uplift the topography beyond a certain elevation. Consequently, the region of elevated topography seems to grow laterally instead of increasing its elevation.

The near absence of thrust faulting, and in some cases extension along much of the high Andes, suggest that no

significant amount of crustal shortening is taking place there. Unless deformation occurs in a ductile fashion, the active tectonic regime of the High Andes is mild compared to that in the sub-Andes, and the rates of extension or shortening are probably low. This tectonic style comprising extension in some areas and shortening in others, suggests a delicate balance between the compressive forces applied to the flanks of the Andes by the converging Nazca plate and Brazilian Shield and the gravitational force applied to the elevated crust and its thickened root. It appears that the Andes transmit the stresses applied by one side to the other, much as Tibet seems to do between India and Eurasia (Molnar and Tapponnier, 1978). Thus, the forces driving the plates together apparently are not elevating the portion of the Andes that is already at high altitudes, increasing the large amount of gravitational potential energy already stored there. Instead, they seem to do work breaking the crust where it is thinner and underthrusting the Brazilian shield beneath the eastern margin of the mountain belt. This has the effect of thickening the crust where it is thin and causing topographic relief to grow progressively towards the east. In this manner, when the elevation reaches a critical height, faults are progressively created farther east and new material is constantly appended to the central Andes along their eastern margin, maintaining an average equilibrium topography (Figure 18).

This mode of tectonic evolution would reconcile two important observations: 1) The eastward migration of deformation inferred from the geologic record, and 2) the alignement of the majority of the intracontinental earthquakes along a narrow zone of deformation beneath the western edge of the sub-Andes, in the transition zone to the Cordillera Oriental. Crustal earthquakes in other tectonically active areas of the world usually occur at depths of less than 15 km (eg. Chen and Molnar, 1981; Meissner and Strelhau, 1982) with the lower crust apparently deforming in a ductile manner. The presence of earthquakes in the lower crust beneath the sub-Andes, at depths of 20 to 38 km, indicates the presence of cold crustal material subject to brittle deformation. The existence of cold and brittle material at these depths suggests the presence of an abnormally low geothermal gradient in the sub-Andes, which in turn, is probably due to the underthrusting of shallow and cold basement rocks from the Brazilian shield under the eastern margin of the Andes.

Extension in the high Andes is probably due to body forces produced by gravity and to buoyancy forces exerted by the crustal root of the Andes (Dalmayrac and Molnar, 1981) . This delicate balance of thrust faulting along the eastern piedmont and extension in the highest part of the Cordillera helps maintain an average equilibrium topography. In this scenario, one can imagine that the

cessation of subduction along the western margin of the mountain belt may reduce the horizontal compressive stress required to support the topography. The Andes might then collapse by extensive normal faulting.

Summary

Comparing synthetic and observed long period P waves we determined fault plane solutions and depths of foci of all earthquakes occuring in the central Andes of Peru, Ecuador, and southern Colombia, sufficiently large to be studied with data form the WWSSN. In general, fault plane solutions indicate thrust faulting along nodal planes striking northwest-southeast in a direction parallel to the mountain belt. Nodal planes dip at high angles of about 30° to 60° degrees. The fault plane solutions of these intra-continental earthquakes seem to reflect deformation of the South American plate that is probably due to the convergence with the Nazca plate. Most of the earthquakes occur on the western margin of the sub-Andes, in the transition zone from the sub-Andes to the Cordillera Oriental, beneath regions of low elevation (~1000 m). The focal depths of earthquakes range from 10 to 38 km, suggesting the lower crust and possibly the uppermost mantle are involved in the deformation. The earthquakes in the sub-Andes are too deep,

and their nodal planes are too steep, to associate them with decollement of the sedimentary rocks from the underlying basement in a thin-skinned tectonic environment. A few earthquakes occur in the Cordillera Oriental. Earthquakes there are shallow with the focal depths of none of the four events studied exceding about 16 km. Two events that occurred in the Cordillera Oriental in southern Peru are the only two earthquakes in the last 20 years associated with surface fault breaks (Philip and Megard, 1976). With only two large earthquakes in the coastal region of Ecuador, the forearc in the central Andes appears to be relatively aseismic. The thrust solutions for these indicate that the crust is undergoing east-west shortening that may be associated with tectonic erosion of the western margin of the South American plate.

While thrust faulting at high angles is prevalent on the eastern side, normal faulting has been documented in a number of localities in the High Andes. The normal faults trend in a direction parallel to the mountain belt, suggesting some extension takes place in a direction normal to the strike. They occur in areas of high topographic relief and faulting associated with one earthquake (the 1946, Ancash earthquake) reflects this extensional regime.

Excess crustal material in the topography and the root of the Andes indicates that as much as 190 km of crustal shortening may have taken place. A summation of the seis-

mic moment of earthquakes in the sub-Andes yields a rate of shortening of 1.4 to 2.1 mm/yr. If these rates were comparable to those in the geologic past, the formation of the Andean topography and crustal root would have occurred in the last 90 to 135 my. Unless the deformation is aseismic and presumably ductile, no significant amount of crustal shortening is taking place in the High Andes. Most of the shortening, as reflected by the seismicity, takes place in the western sub-Andes. We infer that underthrusting of the Brazilian shield along the eastern side of the massif thickens the crust and creates topographic relief. New faults are successively created farther east when the topography reaches a critical height, so that the mountain belt grows eastward in areal extent.

TABLE 1

LIST OF EARTHQUAKES STUDIED

DATA FROM THE I.S.C. CATALOG

Event	Date	Latitude	Longitude	Origin Time	Depth	Magnitude
1	May 10, 1963	-2.20	-77.60	22^h 22' 42.0"	33	6.7
2	Nov 3, 1963	-3.50	-77.80	3^h 10' 12.7"	33	6.7
3	Feb 9, 1967	2.93	-74.83	15^h 24' 45.3"	36	6.3
4	Jun 19, 1968	-5.55	-77.20	8^h 13' 35.6"	33	6.1
5	Jun 20, 1968	-5.51	-77.30	2^h 38' 38.7"	33	5.8
6	Dec 1, 1968	-10.54	-74.81	13^h 14' 55.0"	33	5.4
7	Jul 24, 1969	-11.84	-75.10	2^h 59' 20.9"	1	5.9
8	Oct 1, 1969	-11.75	-75.15	5^h 5' 50.0"	43	5.8
9	Feb 14, 1970	-9.84	-75.55	11^h 17' 16.4"	36	5.8
10	Dec 10, 1970	-3.97	-80.66	4^h 34' 38.0"	15	6.3
11	Oct 5, 1971	-14.20	-73.45	10^h 33' 46.3"	54	5.7
12	Mar 20, 1972	-6.79	-76.76	7^h 33' 48.7"	52	6.1
13	Feb 23, 1973	-2.16	-78.33	4^h 26' 21.1"	44	5.7
14	Sep 27, 1974	2.72	-71.37	4^h 9' 1.6"	44	5.5
15	Apr 9, 1976	0.85	-79.63	7^h 8' 50.0"	19	6.0
16	May 15, 1976	-11.62	-74.45	21^h 55' 55.0"	5	5.9
17	Oct 6, 1976	-0.76	-78.75	9^h 12' 39.0"	33	5.7

TABLE 2

Source Parameters

Event Number	Date	P axis		T axis		Depth (km)	Seismic Moment M_o (dyne-cm)	Number of Stations Used to Estimate M_o
		Trend	Plunge	Trend	Plunge			
1	May 10, 1963	95.4	4.2	5.0	1.42	16	8.85×10^{25}	16
2	Nov. 3, 1963	90.0	5.0	270.0	85.0	18	2.73×10^{25}	24
3	Feb. 9, 1967	260.2	8.7	353.8	22.26	32	3.60×10^{26}	20
4	June 19, 1968	284.3	11.4	150.2	73.8	20	1.96×10^{26}	19
5	June 20, 1968	82.8	12.5	330.4	60.8	16	4.95×10^{24}	16
6	Dec. 1, 1968	80.8	5.0	260.0	85.0	18	5.75×10^{24}	3
7	July 24, 1969	77.0	23.0	205.8	55.9	6	1.81×10^{25}	14
8	Oct. 1, 1969	52.6	21.9	207.4	66.1	5	9.84×10^{25}	17
9	Feb. 14, 1970	260.0	9.0	80.0	81.0	28	9.71×10^{24}	9
10	Dec. 10, 1970	73.0	10.0	253.0	80.0	32	6.76×10^{26}	15
11	Oct. 15, 1971	264.1	0.1	174.1	14.1	8	2.98×10^{24}	6
12	March 20, 1972	267.0	10.0	87.0	80.0	38	4.23×10^{25}	26
13	Feb. 23, 1973	97.8	22.5	321.9	60.0	10	9.47×10^{24}	13
14	Sept. 27, 1974	285.0	5.3	194.8	1.76	6	3.67×10^{25}	1
15	April 9, 1976	264.0	33.0	84.0	57.0	22	9.69×10^{25}	12
16	May 15, 1976	16.5	9.1	281.2	25.4	18	1.25×10^{26}	23
17	Oct. 6, 1976	274.4	24.2	145.2	54.6	16	5.24×10^{24}	2

Figure Captions

Figure 1. Physiographic provinces of the Andes of Peru and northern Bolivia. (1) Coastal Plains, (2) Cordillera Occidental, (3) Altiplano, (4) Cordillera Oriental, (5) Sub-Andean zone. Dark areas indicate plutonic bodies and hachured areas the volcanic rock cover (after Dalmayrac et al, 1980).

Figure 2. Main structural features of the central Andes (after Audebaud et al, 1973).

Figure 3. Shallow focus seismicity in western South America from 1962 to 1979. Squares show the epicenters of earthquakes shallower than 70 km and registered by more than 40 stations reporting P waves to the International Seismological Catalog. Shown also is the 3000 m elevation contour.

Figure 4. Earthquakes shown in Figure 3 plotted on a physiographic map of the Central Andes. Intracontinental seismicity concentrates along the western margin of the sub-Andes in central and northern Peru.

Figure 5. Lower hemisphere equal area projection of the focal sphere for the May 15, 1976 earthquake (event 17). Open circles indicate dilatational first motions and closed circles indicate compressions. Two alternative pairs of nodal planes satisfying the data are shown.

Figure 6. Observed and synthetic long period P waves at stations WES and OGD for the two alternative fault plane solutions shown in Figure 5. The observed P waves are matched better by the dip-slip solution. Each of the strike, dip, and rake of the nodal planes, however, may be varied as much as 10° without changing appreciably the shape of the synthetic pulses.

Figure 7. Comparison of the recorded P waveforms from the event of March 20, 1972 with a suite of synthetic waveforms for different focal depths using the fault plane solution shown in Appendix 1. Synthetic P wavesforms for depths shallower than 36 km or deeper than 40 km do not match the observed waveforms as well as those for 38 km.

Figure 8. Comparison of synthetic P waveforms using mean crustal velocities of 5.5, 6.0, and 6.5 km/sec with the observed P waveforms from the earthquake of March 20, 1972 at the same stations shown in Figure 7.

Figure 9. Map of the central Andes summarizing fault plane solutions and focal depths. Dark areas indicate quadrants with compressional first motion in lower hemispheric projections of focal spheres. Epicenters are plotted as stars and the numbers beside them indicate estimated focal depths in km. Numbers next to balloons correspond to those in Table 1 and Appendix 1.

Figure 10. Cross section of seismicity accross Ecuador. Black dots show position of earthquakes selected by Barazangi and Isacks [1979] in cross section B-B^1 These events determine the dip of the slab. The east-dipping nodal plane of event 10 in the forearc, is too steep to be associated with slip on the main-inclined seismic zone. The west-dipping nodal planes of earthquakes in the sub-Andes are also projected on the cross section. The position of the Moho beneath the Andes is drawn so as to maintain approximate isostatic equilibrium but is not constrained by other data.

Figure 11. Cross section of seismicity through central Peru (symbols as in Figure 10). The dip of the slab is determined by the earthquakes selected by Barazangi and Isacks [1979] in cross section C-C^1. West dipping nodal planes of two of the earthquakes studied here from sub-Andes are projected onto the cross section. The fault

plane of the earthquakes in the high Andes is known to dip east, as observed in the field (Philip and Megard, 1976)

Figure 12. Histogram of the dips of the nodal planes of the earthquakes studied.

Figure 13. LANDSAT image 2194-14345-7 of the area north of the Cordillera Blanca (snow capped range). Steep escarpment to the west of the range defines zone of normal faulting.

Figure 14. Aerial photograph of an active normal fault in the Altiplano of southern Peru. Arrow points to the fault scarp (scale 1:20,000).

Figure 15. Photographs of normal fault shown in figure 14 taken from the ground at a distance of two kilometers south southwest of the fault. Arrow in Figure 15 shows position of main river valley in left third of photo. The fault scarp clearly offsets Quaternary sediments and moraines.

Figure 16. Fault plane solution of the November 10, 1946 Ancash earthquake. Open circles indicate dilatational and closed circle compressional first motions (from data collected by Hodgson and Bremner [1953]).

Figure 17. Stress in and near an elastic, two-dimensional ridge subjected to horizontal compression perpendicular to it. The horizontal compressive stress reaches a maximum at the edges of the ridge. At the center of the ridge the value of the horizontal stress decreases, and for large characteristic slopes it may become purely tensile (positive) (after McTigue and Mei, 1981).

Figure 18. Sequence of idealized cross sections across the Central Andes through time. (a) Underthrusting of the Brazilian shield east of the incipient mountain belt. (b) and (c) The crust thickens and uplifts the topography to an equilibrium height and a new fault breaks to the east. (d) Present day topography and crustal thickness. Circles indicate earthquakes plotted in Figure 10.

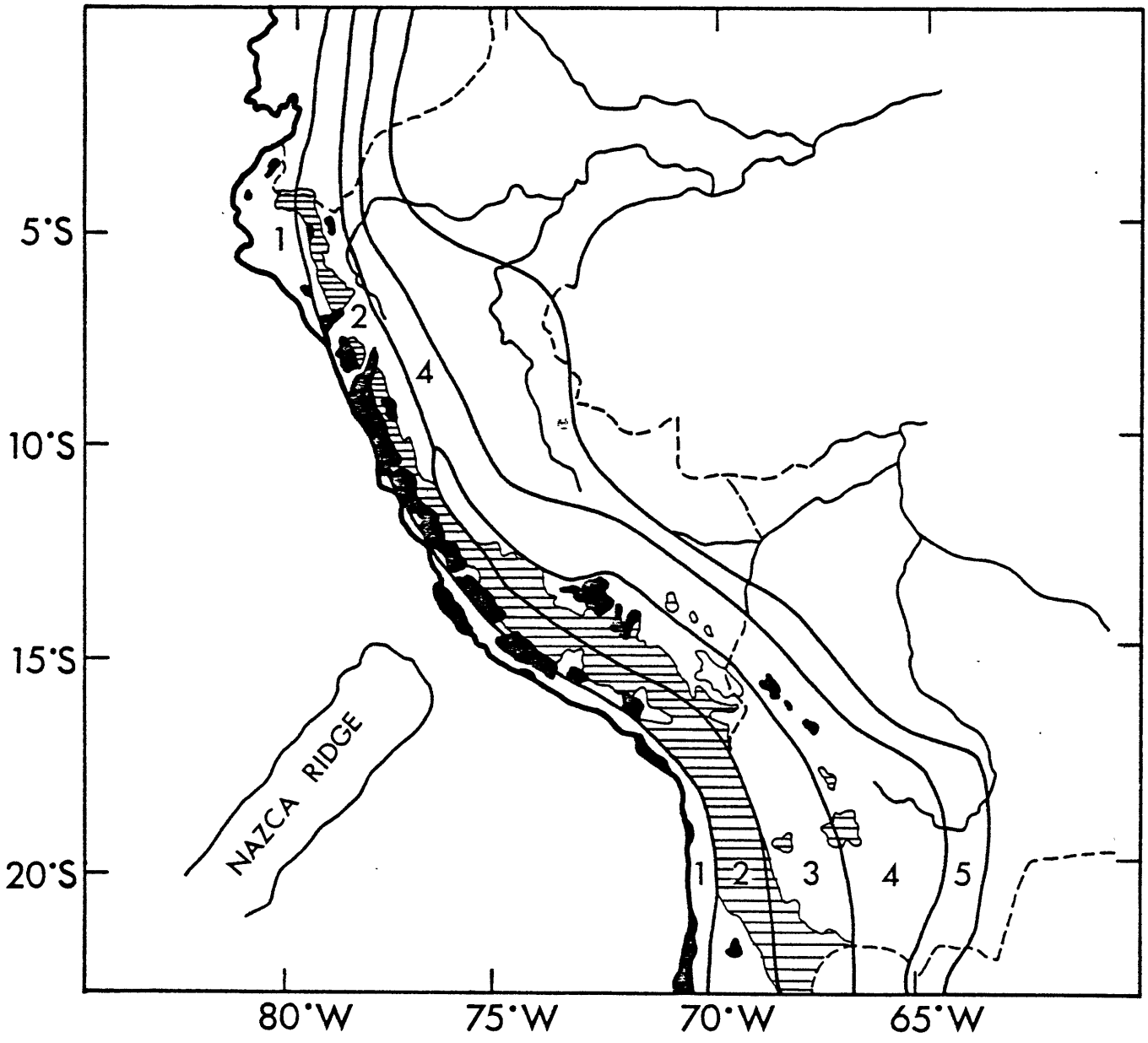

Figure 1

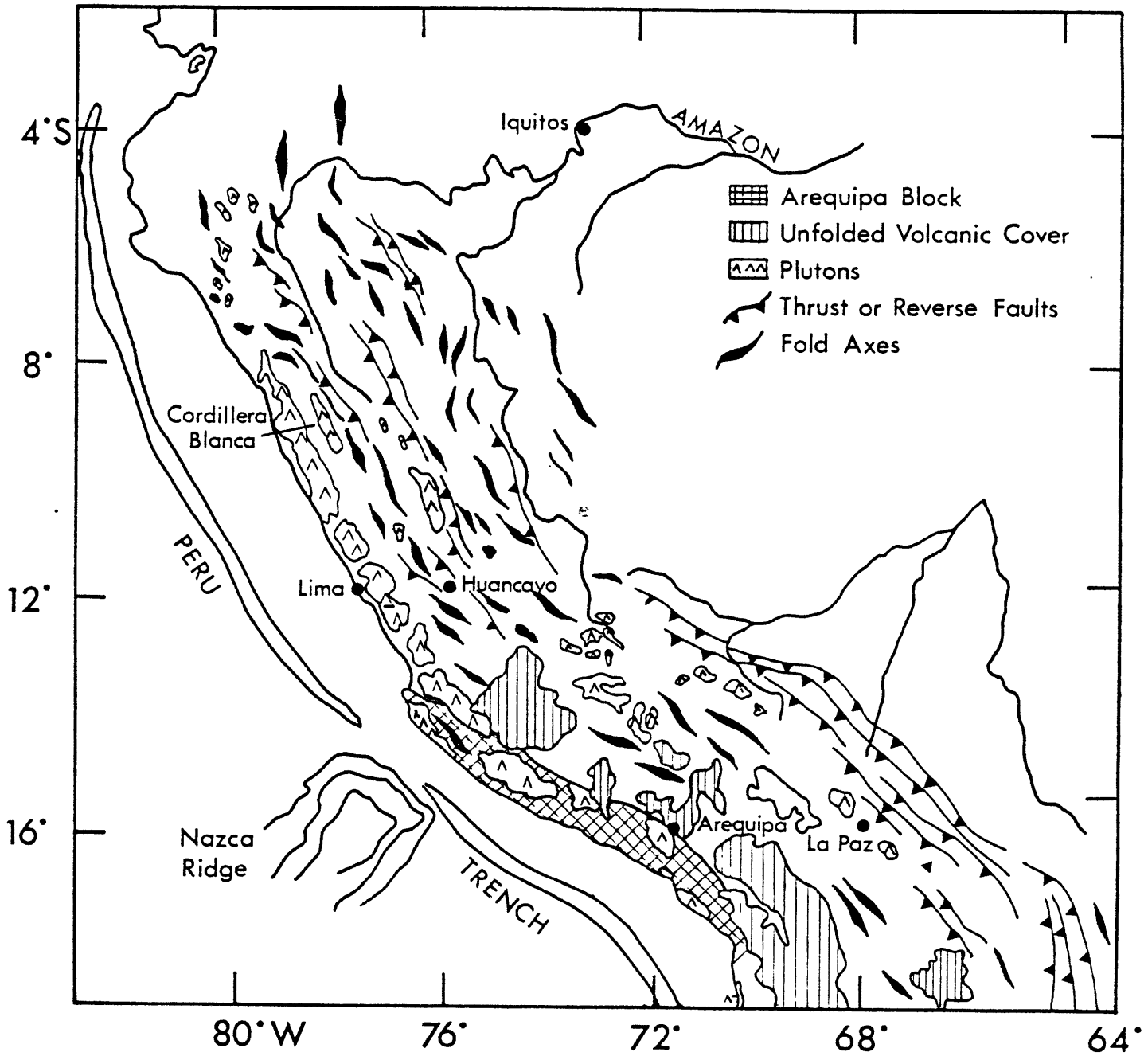
4°S
8°
12°
16°
80°W
76°
72°
68°
64°
Iquitos
AMAZON
Arequipa Block
Unfolded Volcanic Cover
Plutons
Thrust or Reverse Faults
Fold Axes
Cordillera Blanca
PERU
Lima
Huancayo
Arequipa
La Paz
Nazca Ridge
TRENCH

Figure 2

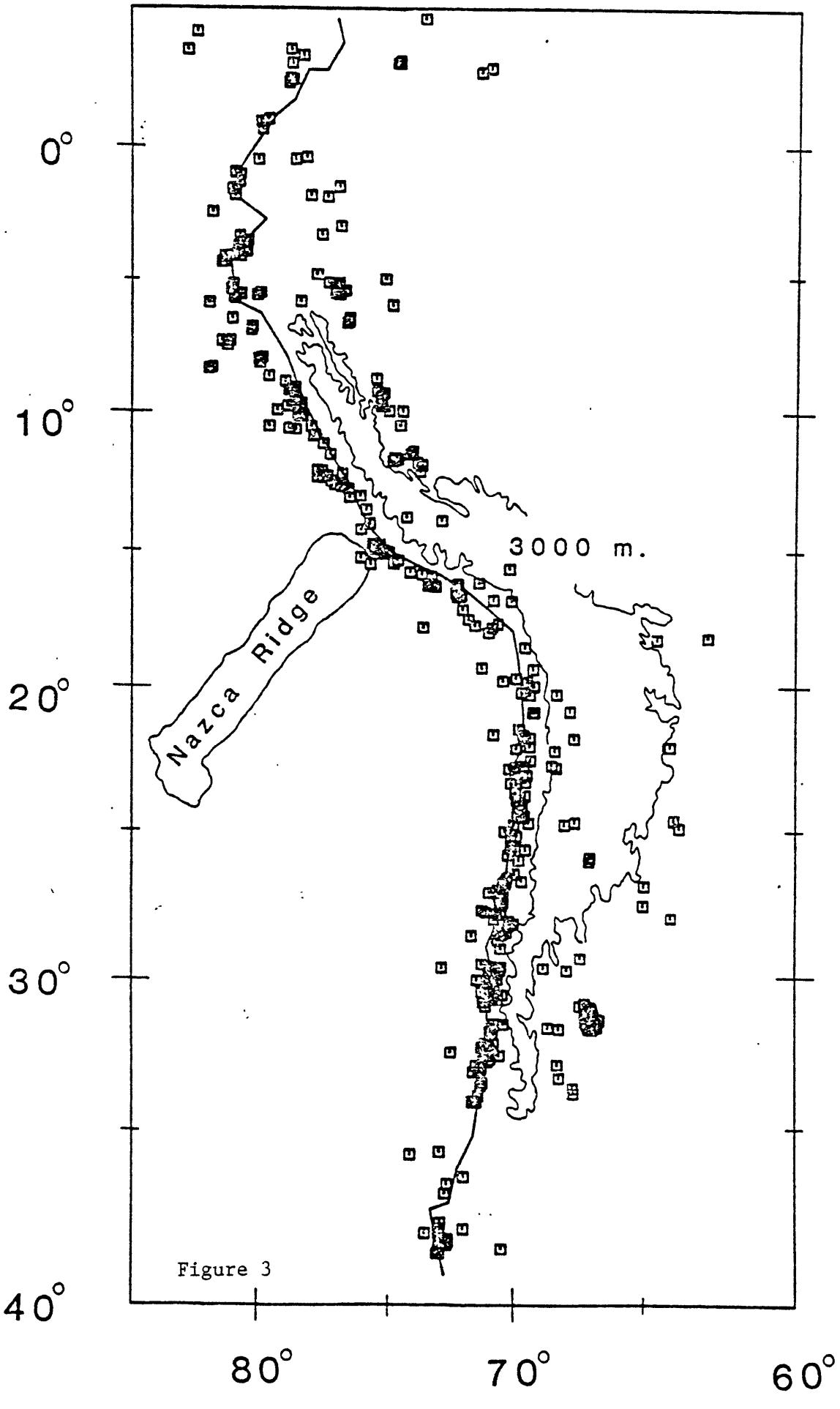

Figure 3

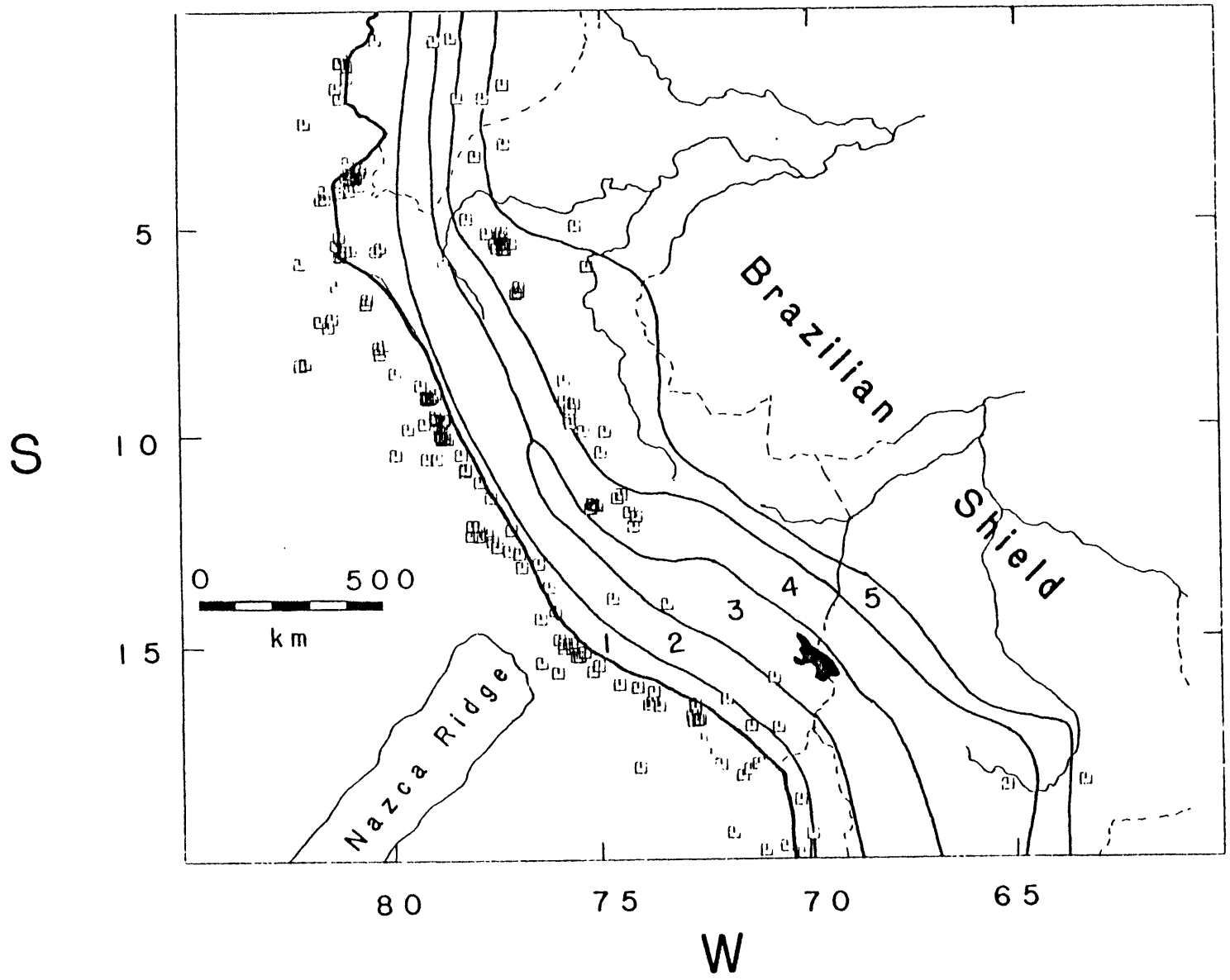
5
10
15
S
0
500
km
1
2
3
4
5
Nazca Ridge
Brazilian
Shield
80
75
70
65
W

Figure 4

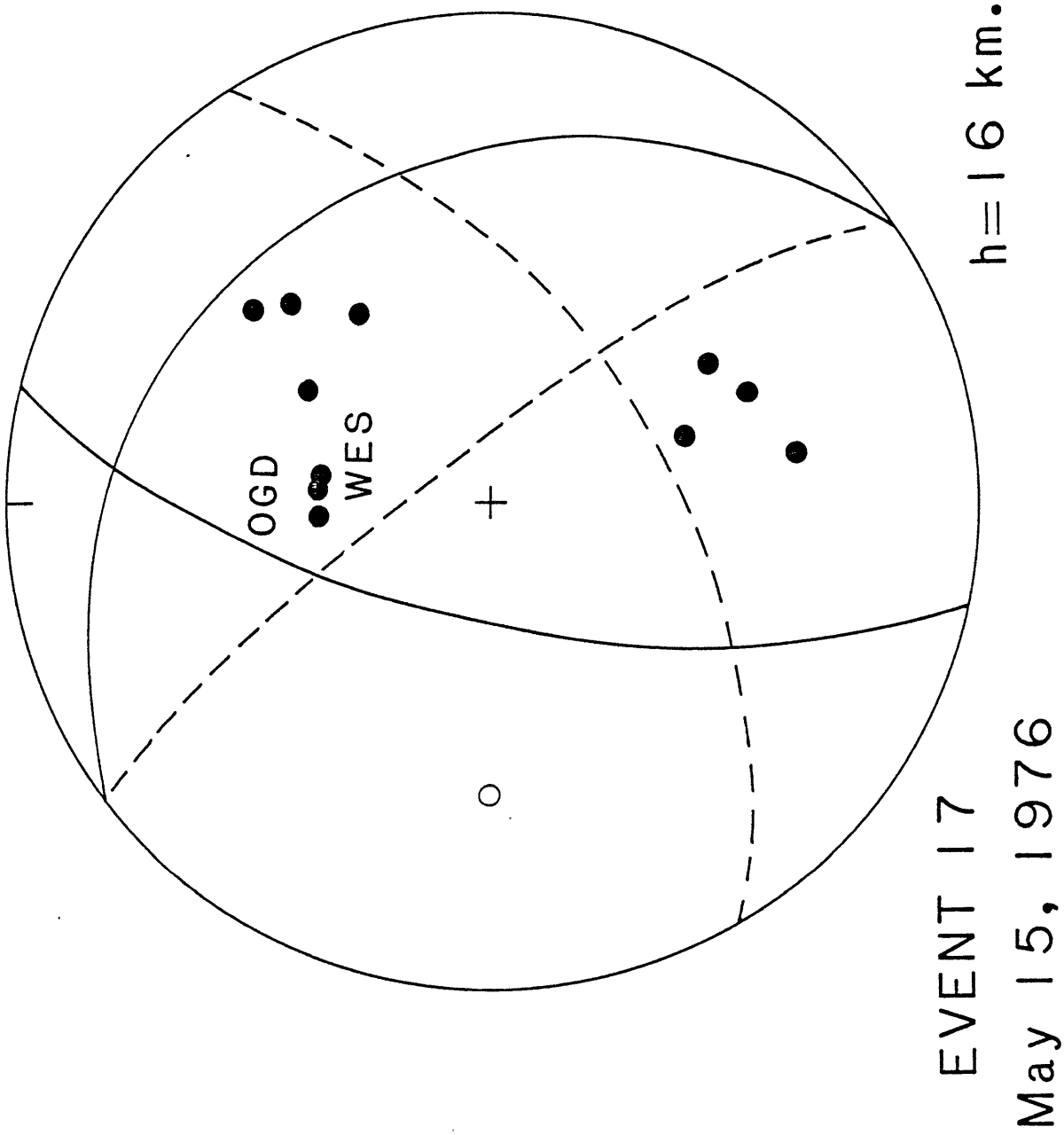

Figure 5

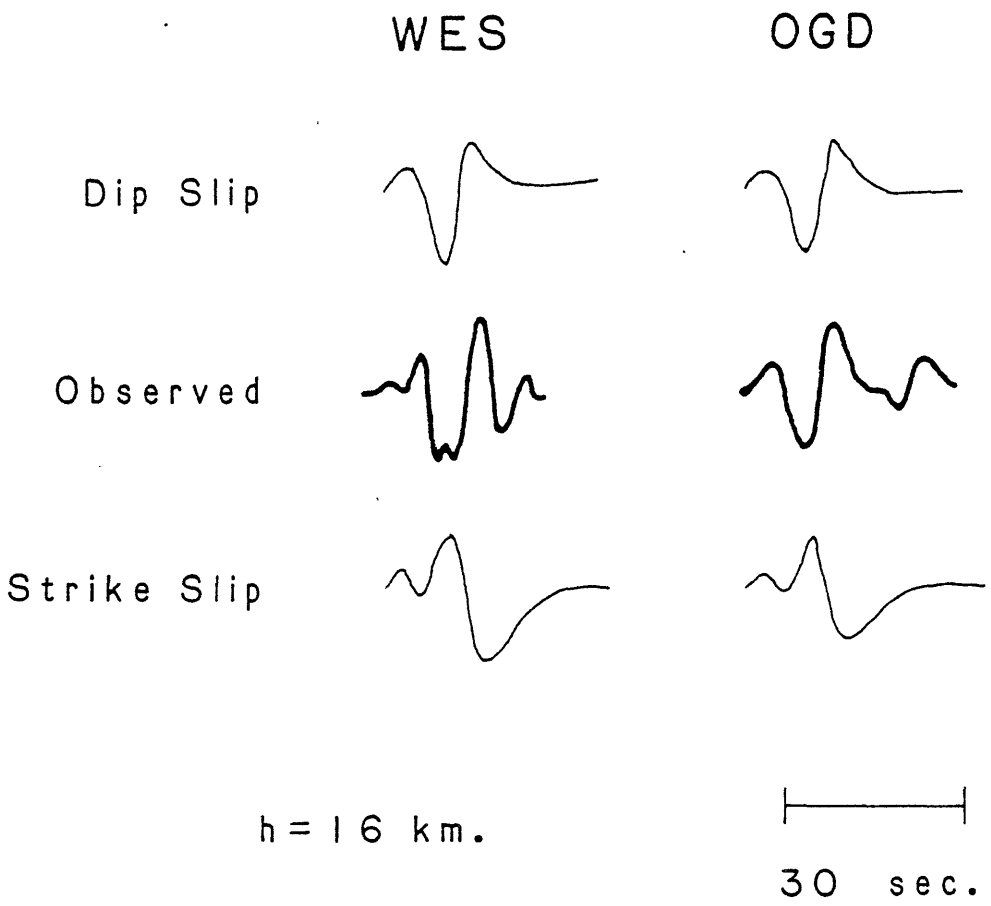

Figure 6

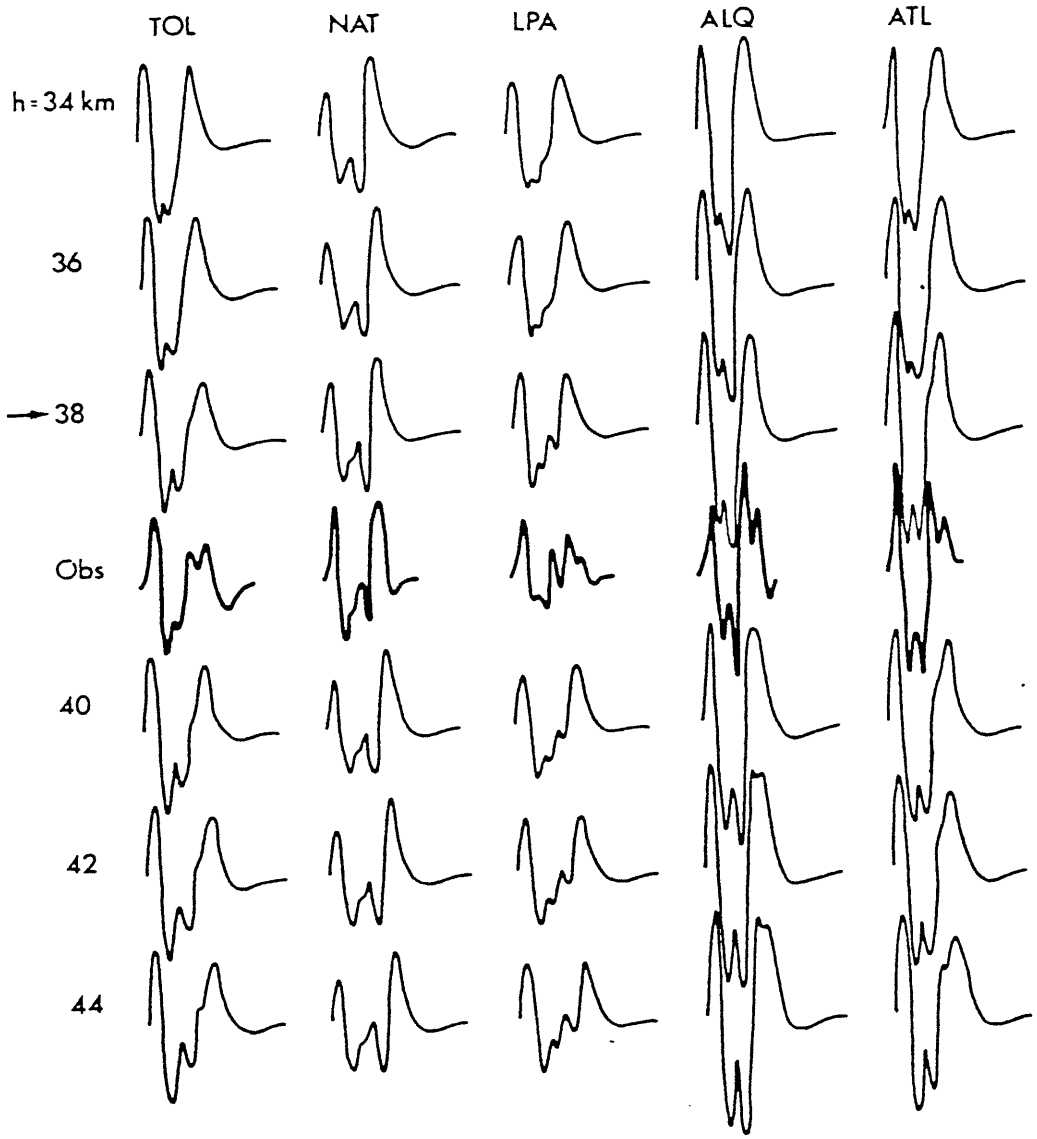

Figure 7

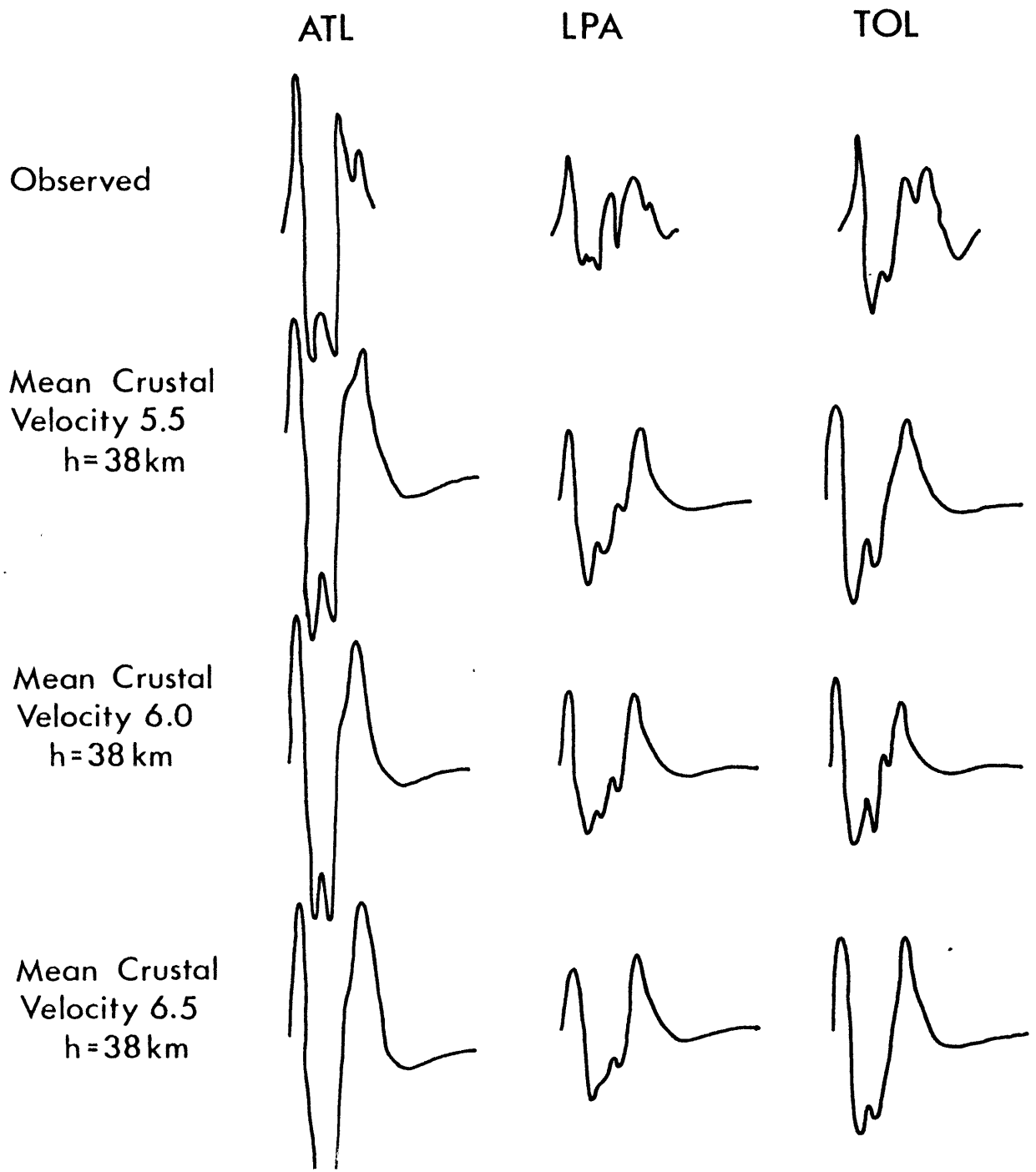
ATL
LPA
TOL
Observed
Mean Crustal
Velocity 5.5
h=38km
Mean Crustal
Velocity 6.0
h=38km
Mean Crustal
Velocity 6.5
h=38km

Figure 8

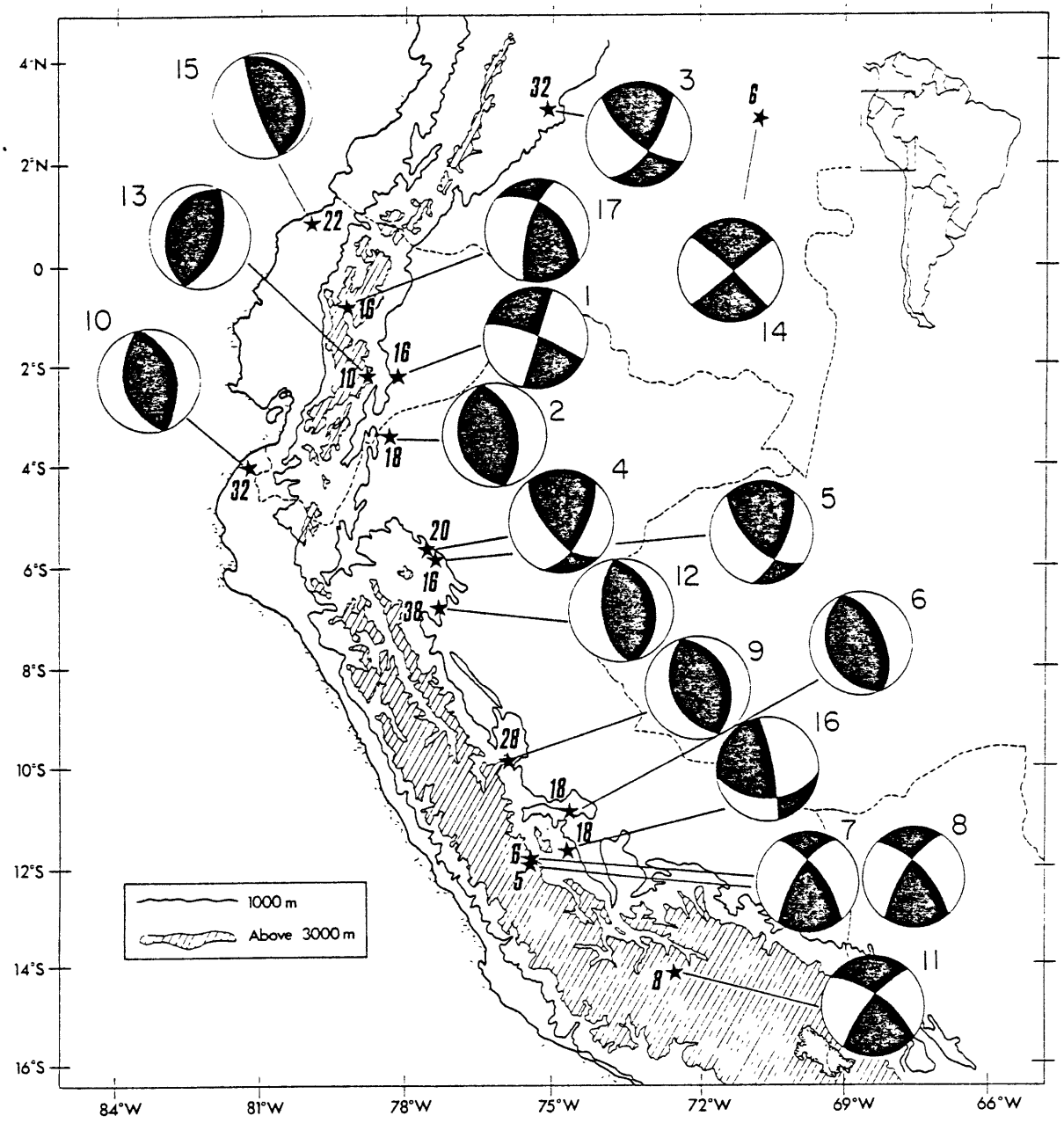
4°N
2°N
0
2°S
4°S
6°S
8°S
10°S
12°S
14°S
16°S
84°W
81°W
78°W
75°W
72°W
69°W
66°W
15
13
10
3
17
1
2
4
5
12
9
6
16
7
8
11
14
32
22
16
10
16
18
32
20
16
38
28
18
18
6
5
8
6
1000 m
Above 3000 m

Figure 9

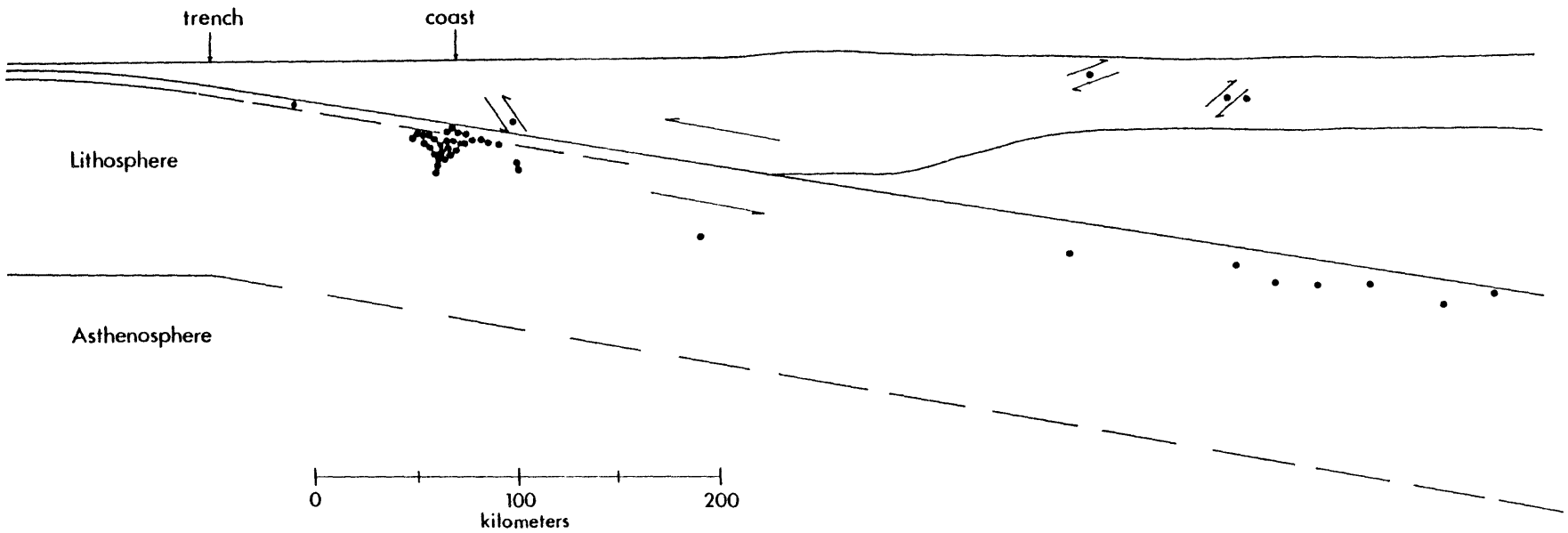
trench
coast
Lithosphere
Asthenosphere
0
100
200
kilometers

Figure 10

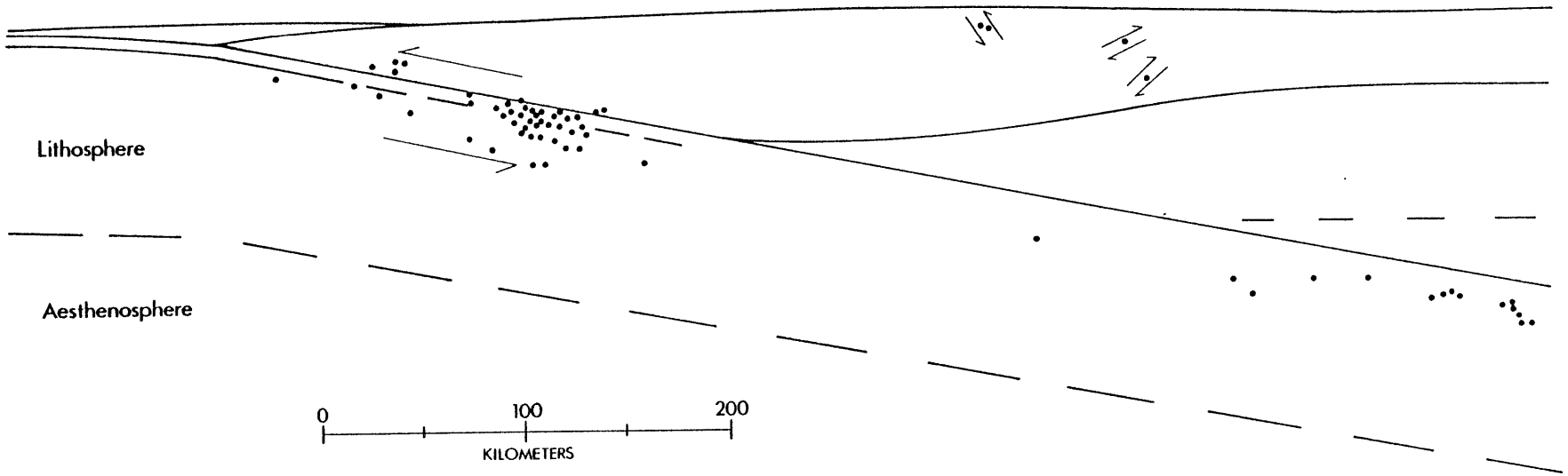

Figure 11

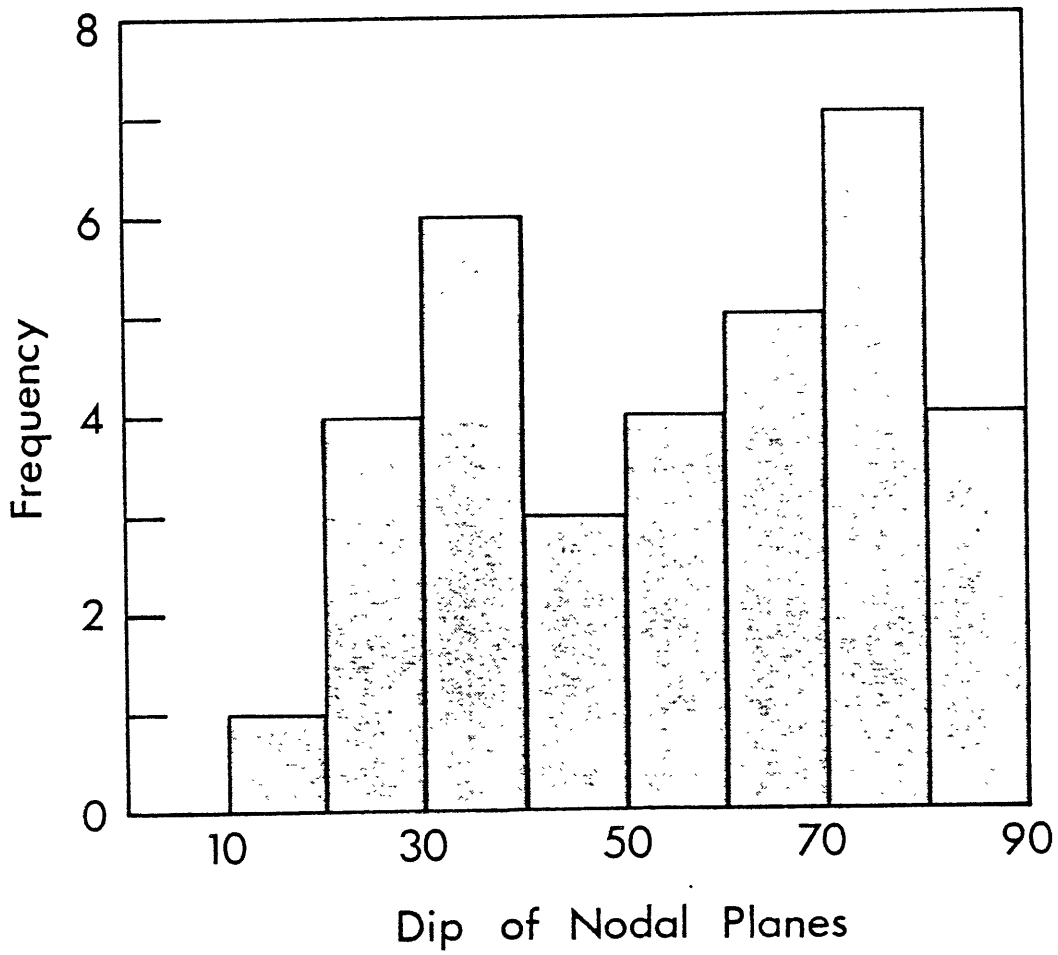

Figure 12

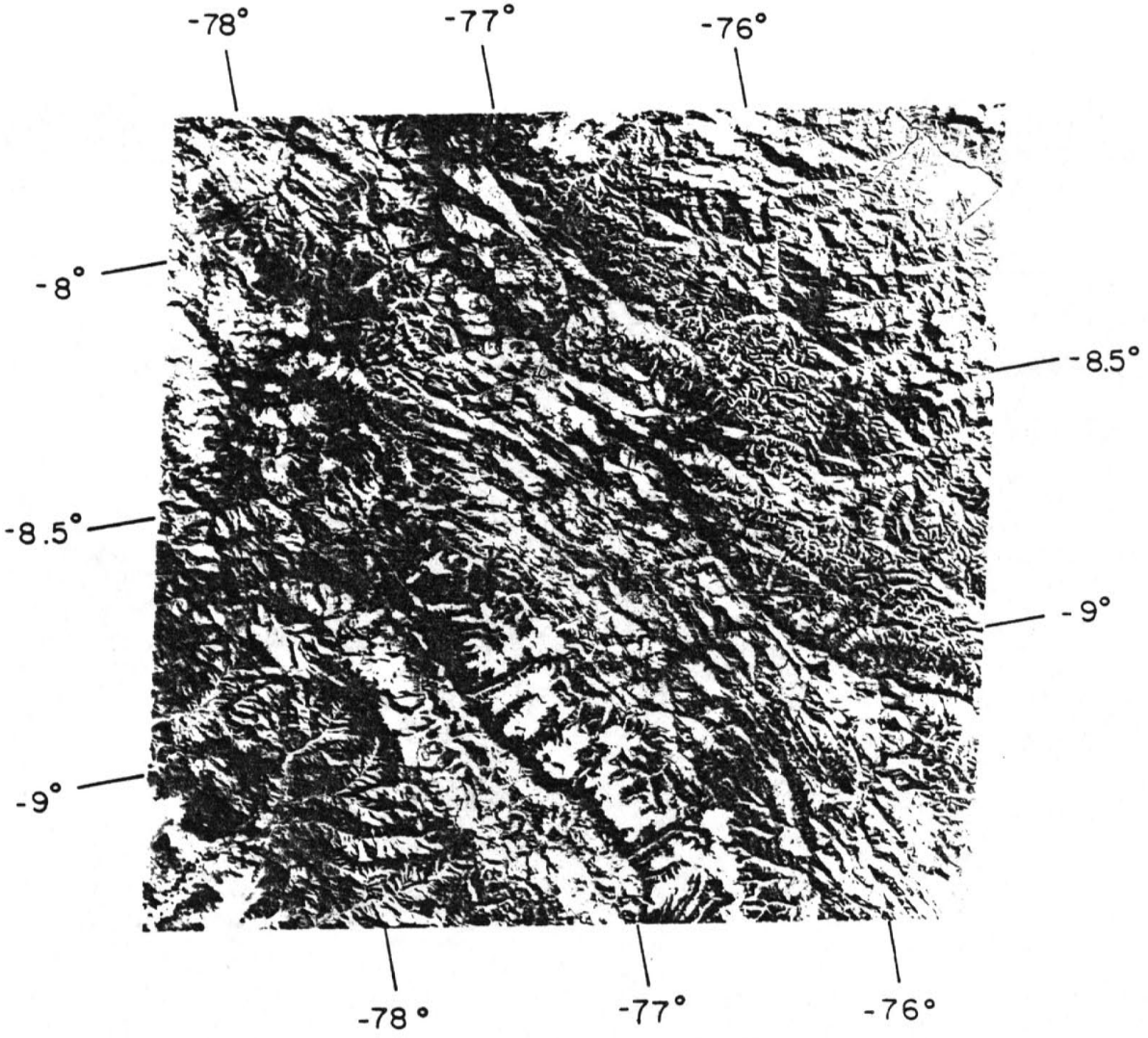

Figure 13

Figure 14

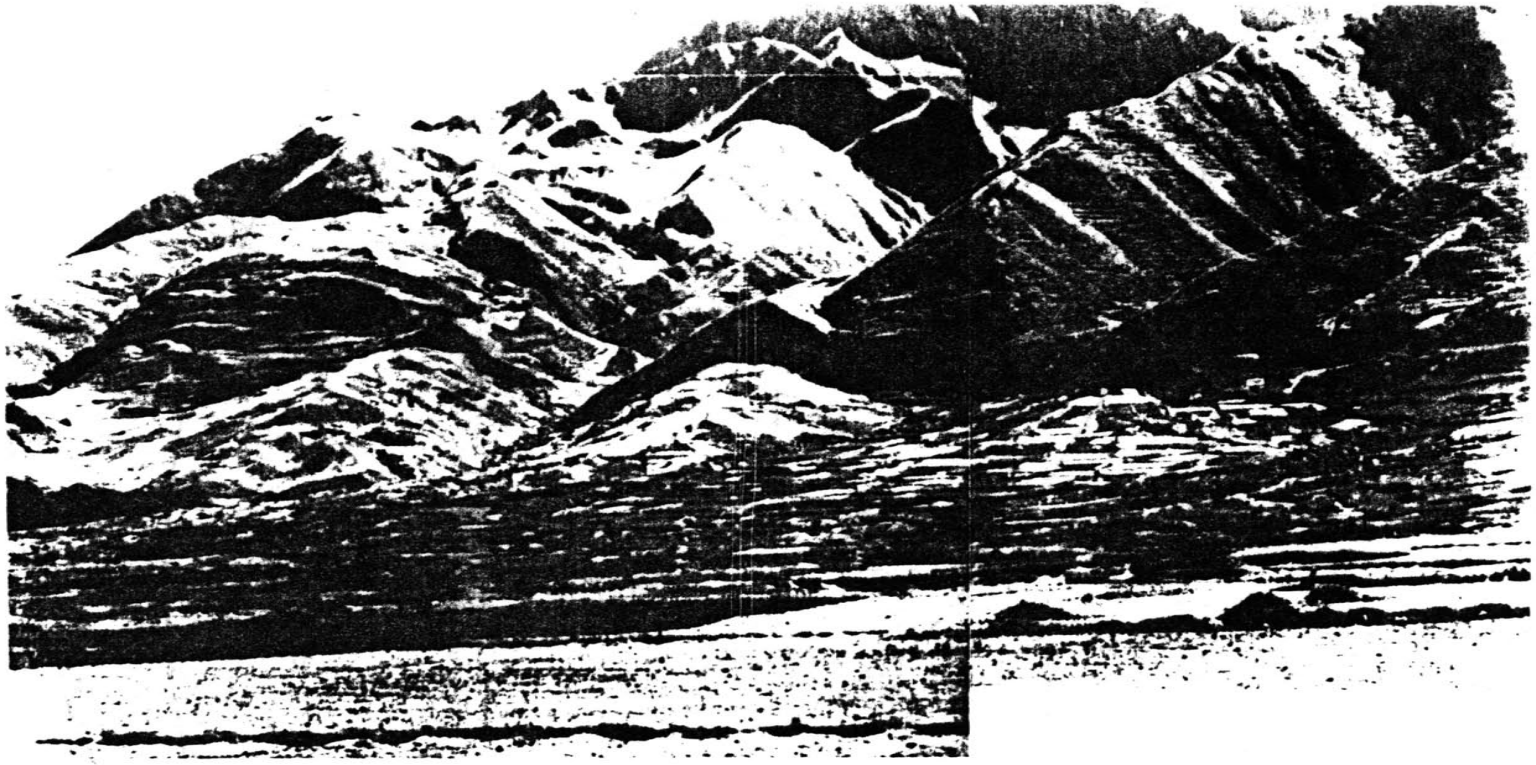

Figure 15

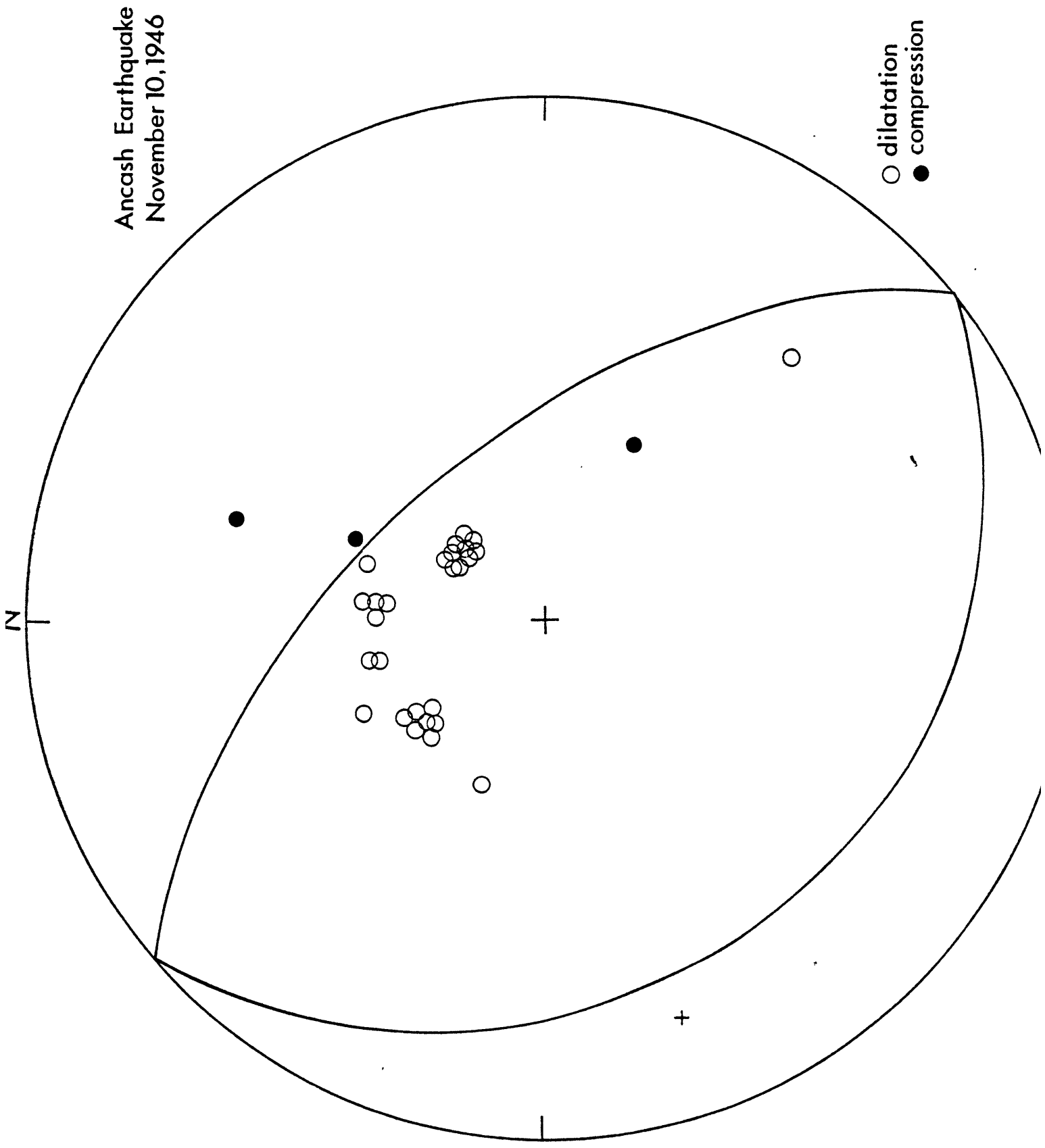
Ancash Earthquake
November 10, 1946
○ dilatation
● compression
N

Figure 16

Horizontal Stress (σ_{xx}) Near a Ridge

Due to Tectonic Compression

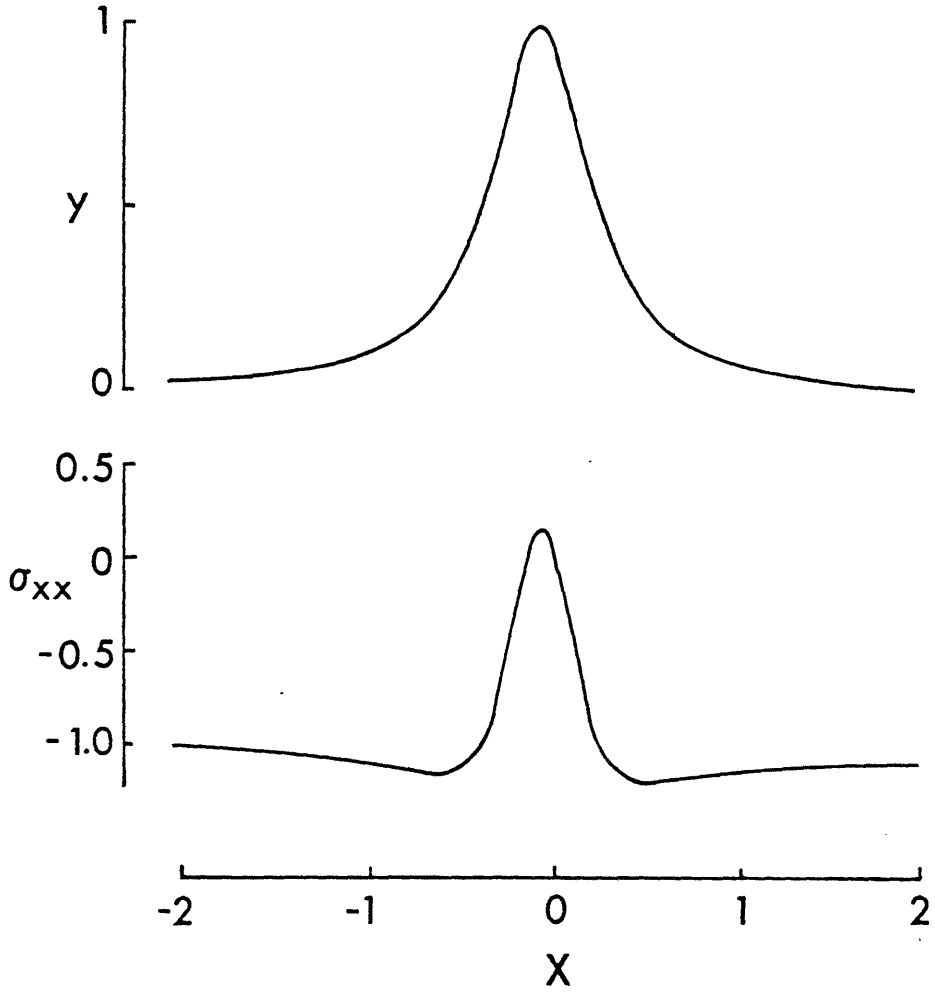

Figure 17

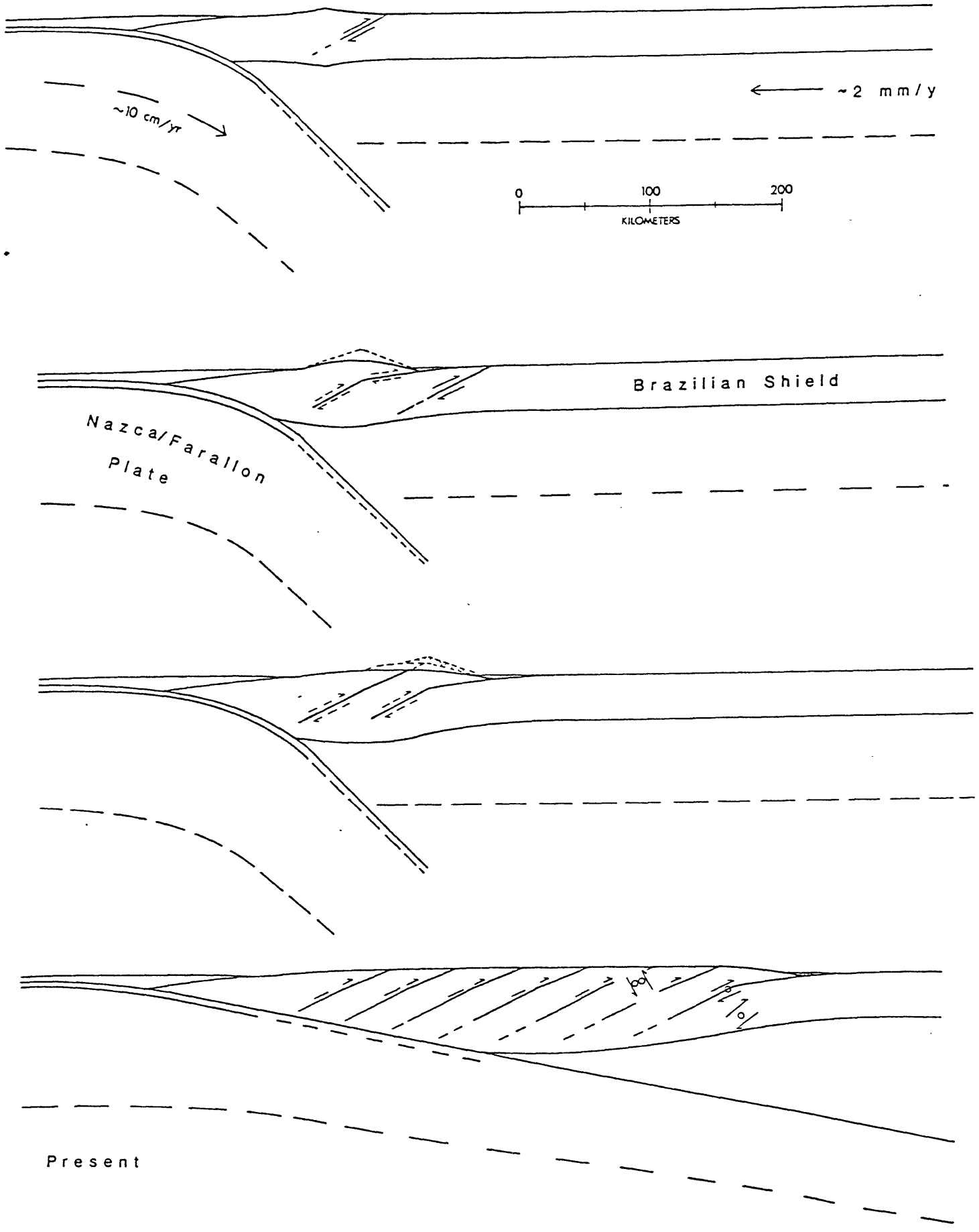
~10 cm/yr
~2 mm/y
0
100
200
KILOMETERS
Brazilian Shield
Nazca/Farallon
Plate
Present

Figure 18

Chapter 3

Introduction

The west coast of South America is the major active margin where an oceanic plate is being subducted beneath a continental plate. It represents a contemporary example of the tectonic regime that is often presumed to have existed along the western margin of North America before the subduction of oceanic material ceased during the late Cenozoic (e.g. Atwater, 1970; Hamilton, 1969). Thus, understanding the style of deformation and evolution of the Andes, an orogenic belt uncontaminated by a continental collision, may play a crucial role in trying to decipher the complex tectonic history of previously active margins that are now dormant, or where an "Andean" margin has been followed by a continental collision, as in the case of the Alpine-Himalayan belt.

A useful tool to glean the style of deformation and tectonic regime of an active mountain belt is the study of the seismicity ocurring in it. The spatial distribution of seismic activity indicates where deformation is taking place, while the type of faulting inferred from fault-plane solutions allows inferences of the orientation of the

stresses responsible for, at least, the brittle deformation. In the Andes, crustal seismic activity is low compared to that of the subduction zone, and the routine hypocentral locations published by the International Seismological Centre (ISC) and the United States Geological Survey (USGS) are not accurate due both to the poor geographic distribution of stations, and to the sparse coverage of the local stations; this is specially true for focal depth.

To examine the active deformation of the central Andes, we installed a temporary network of portable seismographs in the Altiplano and Eastern Cordillera of the central Andes, east of the city of Lima (Figure 1).

Methods of Analysis

Station Distribution

From May 13 to June 12, 1980, we operated a network of up to sixteen portable seismographs complementing the less dense permanent seismic network operated by the Instituto Geofisico del Peru (Figure 2 and Table 1). Our goal was to monitor the seismic activity in the High Plateaus and the Eastern Cordillera in the vicinity of the city of Huancayo (Figures 1 and 2). Originally, our objective was to monitor

the seismic activity in the High Plateaus, the Eastern Cordillera, and the western margin of the sub-Andes. Unfortunately, the poor conditions of the roads after the rainy season and the lack of topographic maps or navigated aerial photographs required to determine the geographic coordinates of the stations did not permit us to install stations in the sub-Andes, and coverage there and along the Pacific coast was provided by stations of the permanent network. The geographic coordinates and elevation above sea level of the portable stations were determined using topographical maps published by the Instituto Geografico Militar of Peru at a scale of 1:100,000 (Table 1). We estimate the uncertainty of the positions of the stations to be in the order of 250 meters.

Recording Procedure

We used Sprengnether MEQ-800 seismographs with Mark Products L4-C vertical seismometers. The amplifiers were generally set to 84 db, corresponding to a magnification of about 5×10^5 at 10 Hz. Earthquakes were recorded by a fine stylus on smoked paper at a speed of 60 mm/min. Records were changed every 48 hours and the drift of the internal clock of each instrument was checked at this same time interval, by directly recording time pulses transmitted by the WWV station in Colorado, USA. Clock drifts during these 48 hour periods were always less than 0.1 sec.

The arrival times of the phases of interest were digitized on a table-top digitizer. The accuracy of the readings depended on the level of background noise and the sharpness of the onsets. On the average we estimate an accuracy of about 0.1 seconds for P arrival times. S waves were also picked when they could be confidently identified, and we estimate the error in S wave arrival times to be in the order of 1 second.

Location Procedure

In this study, earthquakes were located using the computer program HYPOINVERSE developed at the USGS by Klein (1978). The problem of locating earthquakes is one of the oldest inverse problems in geophysics and thorough reviews of the problem have been given by various authors (e.g. Aki and Richards, 1980; Buland, 1976; Lee and Stewart, 1981). Here, we shall briefly describe the method of singular value decomposition used by the HYPOINVERSE program and point out some of the distinct advantages of this method to estimate the quality of hypocentral locations.

Through succesive iterations, we seek the solution in the least-squares sense of the system of equations:

$$R_{m} = A_{mxn} \cdot X_{n} \qquad (1)$$

by minimizing:

$$(R - A \cdot X)^2 \qquad (2)$$

where R is the vector of travel time residuals (i.e. observed arrival time minus the theoretical arrival time calculated for the hypocentral location and origin time of the revious step), A is a matrix containing the partial derivatives of the travel times with respect to variations in the earthquake location and origin time, and X is the vector of adjustments to the current hypocenter and origin time that we solve for. Begining with an initial trial solution, the hypocenter is determined by successively solving for the adjustment vector X and improving the hypocentral parameters obtained in the previous step until a convergence criterion is reached.

Equation 2 is solved in terms of the generalized inverse of A using the singular-value decomposition of A (Lanczos, 1961; Lawson and Hanson, 1974). In this method, the matrix A is decomposed into:

$$\mathbf{A} = \mathbf{U} \cdot \mathbf{S} \cdot \mathbf{V}^T \qquad (3)$$

where U and V represent the eigenvector matrices, and S is the diagonal matrix of the eigenvalues of the matrix A^TA. The generalized inverse of A can be defined as:

$$\mathbf{A}^{-1} = \mathbf{V} \cdot \mathbf{S}^{-1} \cdot \mathbf{U}^T \qquad (4)$$

and substituting in (2) the adjustment vector, X, is solved as:

$$\mathbf{X} = \mathbf{A}^{-1} \cdot \mathbf{R} \qquad (5)$$

For the problem of hypocentral determination the generalized inverse is equivalent to the least-squares solution since the system of equations is usually overdetermined. The advantage of the singular value decomposition is that the covariance, resolution, and data importance matrices are readily obtained.

The covariance matrix C is obtained from elements of the decomposition of the matrix **A** as:

$$\mathbf{C} = \sigma^2 \quad \mathbf{V} \cdot \mathbf{S}^{-2} \cdot \mathbf{V}^T \qquad (6)$$

where σ^2 is the variance of the arrival times. The covariance matrix, C, gives estimates of the errors in the hypocentral solution due to errors in the data but does not include errors introduced by using an erroneous velocity structure. The four diagonal elements of the covariance matrix represent the variance of the origin time, latitude, longitude, and depth of the final hypocentral solution, respectively.

The data resolution or information density matrix expressed by:

$$\mathbf{B} = \mathbf{U} \cdot \mathbf{U}^T \qquad (7)$$

is a parameter that is not computed by most standard location problems. It is a by-product of the singular-value decomposition scheme and it represents the weight of each of the observations to the final solution. The data importance is useful for examining the effect of the network geometry for individual events and to identify which arrival times contribute the most towards the hypocentral location. This is specially useful to study events falling outside of the network, where the resolution of the hypocentral parameters is low.

Another advantage of the singular-value decomposition scheme is that the eigenvalues of the matrix $\mathbf{A}^T\mathbf{A}$, corresponding to each one of the hypocentral parameters is explicitly obtained. If one or more of the eigenvalues in $\mathbf{S}$ becomes very small, the errors in the direction of their associated eigenvectors (parameters) will be large (Equation 6). In general, the largest eigenvalue corresponds to origin time and is of order 5. The eigenvalues corresponding to the spatial coordinates are of order 0.5; where the eigenvalue associated with focal depth is usually the smallest (Klein, 1978). The explicit decomposition of eigenvalues and their associated eigenvectors provides another element with which to judge the quality of a hypocentral location. The application of this technique in other parts of the world empirically shows that when any of

the eigenvalues of the matrix $\mathbf{A}^T\mathbf{A}$ becomes less than about 0.02, the hypocentral solution is unstable and very poorly constrained (Klein, 1978).

For the first iteration, P arrival times were assigned a weight of 1 and S arrival times a weight of 0.5. The smaller weights of the S arrival times compensates the larger uncertainty in arrival-time readings of S waves and their inherently greater importance to the solution. The algorithm assigns weights to the observed arrival times as a function of the residual from the previous iteration. This is useful for damping outliers, i.e. arrival times that are grossly in error, as in the case of misidentified phases.

Accuracy of the Locations

Effects of the Velocity Structure Used

The velocity structure in central Peru is poorly known. The refraction studies undertaken to determine the crustal structure of the central Andes have been carried out in southern Peru and northern Bolivia (e.g. Ocola et al, 1971; Ocola and Meyer, 1973; Tatel and Tuve, 1958). Thus, since the velocity models available are based on data from outside the study area, the sensitivity of the

hypocentral locations to the assumed velocity model was investigated by testing three alternative velocity models of the crustal structure of the Andes.

One velocity model used was determined by Ocola and Meyer (1973) from a refraction survey across the Andes in southern Peru. Their study spans the region from the trench to the Altiplano, and we have used their results for the eastern Altiplano and Cordillera Oriental. A second model is that of James (1971) who determined the thickness and velocity structure of the crust beneath the Andes studying the dispersion of Rayleigh and Love waves along various paths. Finally, a velocity structure based on the results of a deep crustal refraction experiment carried out in southern Colombia by Meissner et al (1977) serves as a comparison to crustal models proposed for southern Peru and northern Bolivia. The crustal models used have thicknesses of between 55 and 65 km and are listed in Table 2.

A ratio of V_p/V_s of 1.75 corresponding to a Poisson ratio of 0.25 was used in all cases and a station time correction (station delay) was applied to all arrival times at a given station to compensate for differences in elevation. Station elevation varied from a few tens of meters to 4600 meters above sea level (Table 1). The station corrections were applied assuming a reference datum of 3500 meters (the average elevation at the center of the array) and assuming a mean P-wave velocity of 5.0 km/sec for the top crustal

layer. Other studies have shown that varying the ratio of V_p/V_s by about 0.03 produces changes in the hypocentral locations usually not larger than 2 km (e.g. Prevot et al, 1980; Trehu, 1982).

A random selection of 29 earthquakes ocurring at various depths were located using these three seismic velocity structures (Table 3). The epicentral coordinates and focal depths of events located with the crustal model of Ocola and Meyer (1973) were substracted from the hypocentral coordinates obtained using the velocity structure proposed by James (1971) and Meissner et al (1977) and are shown independently in Figures 3 and 4 in histogram form. In general, epicentral locations do not seem to depend strongly on the choice of the velocity structure; changes in epicentral coordinates are usually less than four to six kilometers. Focal depths are more sensitive to changes in the velocity structure and may change by as much as 8 to 14 km depending upon the location of the event relative to the network, and the velocity model used. In both cases, however, those earthquakes that exhibited changes in epicentral coordinates larger than about 10 km are events that are poorly constrained because they lie outside or on the periphery of the network (Table 3).

The velocity model obtained by Ocola and Meyer (1973) generally produced the smallest root mean square (rms) val-

ues of travel time residuals (Table 3) and was adopted to locate all the events recorded.

Selection Criteria

During the four weeks of recording a total of 344 earthquakes were located (Figure 5). The located events span an area of about 400 by 400 km. Most shallow activity (pluses in Figure 5) occurred within the crust in the sub-Andes, east of the Andean Cordillera. The high Andes appear to be seismically relatively inactive with the exception of the region near the Huaytapallana fault in the Eastern Cordillera, (near 12°S, 75°N). This activity defines a clear linear northwest-southeast trend (Figure 5). Intermediate-depth events (triangles in Figure 5) were also located beneath the high Andes and the sub-Andes. Very few events, however, were recorded along the main thrust contact between the Nazca and the South American plate probably because this area is far from our network.

As can be observed in Figure 5, many of the events lie outside the network and the maximum azimuthal gap is sometimes quite large. Using synthetic data, Lilwall and Francis (1978) showed that this does not necesarily imply poor resolution of the hypocentral coordinates if the distance from the epicenter to the nearest station is not large. A useful rule of thumb for judging the accuracy of hypocentral depth determination is that the distance from

the event to the closest station should be less than or roughly equal to the focal depth. For most of the crustal earthquakes in the sub-Andes this is clearly not the case; focal depths for these crustal events appear to be less than 40 km and the distance to the closest station is often a few tens of kilometers. This lack of resolution in focal depth is evident when one examines the eigenvalues for these shallow events in the sub-Andes. For most of these events, the eigenvalue associated with depth is usually very small (less than 0.015), and the calculated error in focal depth is accordingly very large (see equation 7). Roecker (1981) concluded that the critical geometric factor controlling the location of the earthquake is the spread of ray take-off angles from the source to the stations. Clearly, refracted rays deflected at the same layer leave the source with the same ray take-off angle, and focal depth and origin time cannot be resolved.

Therefore, many of the events located have large errors in the epicentral coordinates (ERH) and the focal depth (ERZ). and it is necessary to establish screening criteria to separate well located earthquakes from poor and unreliable locations. We consider as reliable locations those events for which at least five arrivals, including at least one S phase were used, and the condition number of the matrix (the ratio of the largest to the smallest eigenvalue) was less than 200. This implies a cutoff value

for the smallest eigenvalues of about 0.02, which Klein (1978) empirically determined to be the minimum value required for a stable and well constrained solution. We also required that the values of calculated errors in the horizontal (ERH) and vertical (ERZ) directions be less than 10 km and the rms of the travel time residuals to be less than 0.5 sec. Admittedly, an rms value of 0.5 for the travel time residuals is large. However, large residuals may be a function of local lateral variations of the assumed velocity structure rather than indicative of poor locations. The screened events are shown projected onto cross section A-B (Figure 6) in Figure 7.

Seismicity of the High Andes

Seismicity in the Altiplano

It is clear that crustal seismicity in the Altiplano is relatively low (Figures 5, 6, and 7). Although the majority of our portable stations were deployed in the western part of the Altiplano, only about fifteen crustal earthquakes were located within the network; the overwhelming majority of the crustal earthquakes occureed in the eastern margin of the Cordillera and the sub-Andes (Figures 5 and 6). This pattern of

seismicity is consistent with studies of teleseismic events showing that most large, shallow events occur in the western part of the sub-Andes (e.g. Stauder, 1975; Suarez et al, 1983). Thus, insofar as both the microearthquakes reported here and the historic seismicity reflect the degree of active tectonics, the Altiplano appears to be more stable and at present is not subjected to orogenic deformation as intense as that affecting parts of the Eastern Cordillera and the whole of the western sub-Andes, unless the deformation is absorbed by creep or viscoelastic behavior.

Those few events registered in the Altiplano are all very small, and unfortunatley none of them yielded a well constrained fault-plane solution. Thus,we could not address one of our original objectives: whether or not normal faulting occurs in the Altiplano of the central Andes, as it does in the Cordillera Blanca of the high Andes in northern Peru (Dalmayrac, 1974; Yonekura et al, 1979) and in the Bolivian Altiplano (Lavenu, 1978, 1979; Mercier, 1981).

The Huaytapallana Fault

The Huaytapallana fault is located in the Eastern Cordillera of central Peru, a few kilometers east of the city of Huancayo (Figure 1). Two fault-plane solutions of two large earthquakes that occurred on this fault in July

24, 1969 and October 1, 1969 show reverse faulting (Stauder, 1975). This latter event caused great damage in the nearby villages killing 130 people (ISC Bulletin). The October 1, 1969 earthquake produced a steep fault scarp dipping east, with a vertical displacement reaching 1.6 meters (Deza, 1971; Philip and Megard, 1977) (see Figure 8). Philip and Megard interpret the fault as one of a group of reactivated parallel faults trending NNW-SSE. Two of these faults mark the contact between three different formations: from east to west the Precambrian gneiss of the Huaytapallana Range, an intermediate block of Triassic metamorphosed limestones, and a block of Late Paleozoic sandstones and limestones (Paredes, 1972) (Figure 9).

The existence of a large number of small microearthquakes shows that the Huaytapallana fault (or system of faults) is still active (Figures 6 and 9). Station HYT, installed at the southeastern end of the mapped surface rupture, registered an average of about 30 events per day with S-P time differences of less than 4 seconds. The epicenters of earthquakes located in the vicinity of the Huaytapallana area follow a trend in a NNW-SSE direction, parallel to the the mapped surface faults and to the strike of the east-dipping nodal plane of the fault-plane solutions of the two largest Huaytapallana earthquakes (Stauder, 1975, Suarez et al, 1983) (Figure 9). It is not

clear, however, whether the seismicity is due to activity along a single fault or a series of faults.

Both the fault-plane solution of one of the largest events and a composite fault-plane solution for four events show reverse faulting with some left-lateral strike-slip motion ocurring on a fault plane dipping east with a strike of about 30° east of north (Figures 11 and 13). This agrees with the sense of motion observed at the fault (Philip and Megard, 1977) and with the fault plane-solutions of the two large 1969 earthquakes.

In the basins just west of the Huaytapallana fault, Dollfus and Megard (1968) reported folding of Quaternary glacial terraces. The strike of these folds, in a direction N30°W, and the orientation of the P axes of the fault-plane solutions of earthquakes in the Huaytapalllana fault (Figure 11) suggest this region is experiencing horizontal crustal shortening oriented roughly east-west, in the direction of relative Nazca-South American plate motion.

Based on a study of the fault scarp, Philip and Megard (1977) suggest that the overall length of the fault is approximately 3.5 km. The length of the fault that ruptured during the October 1, 1969 earthquake can be estimated by considering the average displacement u on the fault to be 1.6 m, the rigidity μ equal to 3.3×10^{11}, a fault width of between 10 to 15 km, and a seismic moment of 1.0×10^{26} dyne cm (Suarez et al, 1983). From the formula

$M_O=u_\mu S$ (Aki, 1966), where S is the area of the fault, the October 1 earthquake requires a fault about 12 to 20 km long. Thus, it is likely that the 1969 earthquakes ruptured a fault that extends north of the surface break, to where the microseismicity occurs today. The epicenters of most of the earthquakes recorded in this area lie about 10 km east of the projected location of the fault (Figure 9).

A cross section across the fault shows that the earthquakes deepen towards the east (Figure 10), consistent with an east-dipping fault plane (Figure 11). The deepest events occur at a depth of about 18 km. The locations are not accurate enough to determine, however, whether the earthquakes take place on a single fault plane or a on a series of imbricate faults.

Although focal depths and epicentral locations are poorly constrained, epicenters of a group of crustal earthquakes are aligned in the same general direction of the Huaytapallana fault east of the station PAM, to the southeast of Huaytapallana (see Figure 5). Only one of these events passed our filtering criteria and appears to be well constrained. The fault-plane solution for this event (Figure 12) is not well constrained and could be interpreted as a pure strike-slip or a pure dip-slip event, or a combination of both. The first motions, however, suggest that the P axes lie in a general east-west direction, as for the events in the Huaytapallana. Another large historical

event occurred in this part of the Eastern Cordillera. On November 1, 1947 an earthquake of magnitude 7.3 occured about 50 kilometers northwest of the Huaytapallana fault.

The Huaytapallana fault is one of only two reverse faults in the high Andes known to have broken by an earthquake that has been instrumentally recorded. The other is associated with both the 1944 and the 1979 San Juan earthquakes in central Argentina. It is interesting that both faults occur where an aseismic ridge is being subducted: the Nazca Ridge in Peru and the Juan Fernandez Ridge in central Argentina, and that normal faulting and crustal extension occurs in much of the rest of the high Andes. Suarez et al (1983) associate this apparently greater horizontal compressive stress with the added resistance of these high and buoyant ridges to subduction of the Nazca plate.

Seismicity of the sub-Andes

Description of the Seismicity

The sub-Andes of central Peru are seismically more active than the high Andes and appear to be the physiographic province in the central Andes currently undergoing the most intense brittle deformation. The vast

majority of earthquakes in the overiding continental plate are concentrated in the western margin of the sub-Andean region, over an area roughly 100 km wide. These events lie east of the main Andean Cordillera and occur beneath areas of low topographic elevation (Figures 5 and 6). Most of these events occurred at large distances from the eastern margin of the network, and therefore the focal depths of these events are very poorly resolved. Station POC operated by the Instituto Geofisico del Peru is the only station located in the sub-Andes, but due to its low gain it could not be used to locate most of the microearthquakes that occurred in the area.

Despite the errors in focal depths, there are enough well located events to show that the seismicity in the sub-Andes affects most of the crust at least to depths of about 40 to 50 kilometers, in agreement with the depths of two nearby larger events (Suarez et al, 1983). Although most of the microearthquakes seem to occur at midcrustal depths between 15 and 25 km, one event clearly takes place at a depth of about 50 km. This earthquake occurred beneath the network and was located by 15 stations; the horizontal distance to the nearest station was about 30 km. Although the rms travel-time residuals are relatively large (about 0.4 sec), the estimated focal depth changes by less than 5 km for the different velocity models used (Table 3), and the values of ERZ are always less than five kilometers.

Below a depth of about 50 km no earthquakes occur within the South American plate. An aseismic zone extends to a depth of about 90 km where intermediate depth earthquakes associated with the subducted slab occur (Figure 7).

Fault Plane Solutions and Tectonic Interpretation

A composite fault-plane solution from six events located just east of the network at depths of between 15 and 26 km shows thrust faulting with a component of strike-slip motion (Figure 14). This solution is very similar to that of a larger event that occurred about 25 km east of this group of events at a depth of 20 km (Suarez et al, 1983) (Figures 13 and 14). A fault-plane solution obtained for a single event in the in the sub-Andes suggests nearly pure reverse faulting (Figure 15). Both of these fault mechanisms have P axes oriented northwest-southeast, in the same general direction as the subduction of the Nazca plate beneath South America, and similar to those of the larger events (Suarez et al, 1983) in the sub-Andes.

The existence of earthquakes in the sub-Andes at middle and lower crustal depths of between 20 and 50 km is unusual. Chen and Molnar (1981) and Meissner and Strelhau (1982) compiled catalogs of earthquakes ocurring in intracontinental areas of the world and show that, in general, brittle behavior of the crust is confined to roughly the

top 15 km of the upper crust. This is inferred to be due to the sharp decrease in strength of the typical crustal minerals at that depth, under normal geothermal gradients (e.g. Brace and Kohlstedt, 1980; Caristan, 1980). To explain both the concentration of intense deformation along the western margin of the sub-Andes and the unusually deep brittle deformation up to 40 or 50 km, Suarez et al (1983) suggested that the seismicity results from an underthrusting of the cold Brazilian shield beneath the eastern margin of the Cordillera Oriental. Crustal shortening thickens the crust and uplifts the topography of the eastern Cordillera causing the Andean mountain range to grow eastward, with progressively younger deformation to the east (e.g. Megard, 1978; Dalmayrac et al, 1980).

Intermediate Depth Microearthquakes

Shape of the Subducion Zone Beneath the Central Andes

Based on the study of a carefully selected catalog of teleseismically located events, Barazangi and Isacks (1976, 1979) inferred that the seismic zone beneath Peru dips at about 10°. As James (1978) pointed out, most of the events used by Barazangi and Isacks to infer this dip are shallow events along the coast or from a cluster of

intermediate-depth earthquakes in northern Peru (section B in Figure 16).

Using earthquakes recorded by a network of nine stations in southern Peru, Hasegawa and Sacks (1981) inferred the seismic zone beneath the northern part of their network dips at about 30° down to a depth of 100 km and then flattens. Because of the locations of their stations, Hasegawa and Sacks (1981) could not confidently locate events more than 150 km from the coast to determine how far the seismic zone remains horizontal.

During our field investigation we recorded about twenty well located intermediate-depth earthquakes ranging in depth from 85 to 110. They too seem to define a flat seismic zone about 25 km thick beneath the Andes (Figure 7). Therefore our data supports Hasegawa and Sacks's contention and suggest the seismic zone remains flat at a depth of about 100 km for at least a distance of 450 km from the trench (Figure 7) and does not seem to dip at a constant slope of 15° as inferred by Barazangi and Isacks (1976, 1979)

Very few events were located on the main thrust contact between the Nazca and South American plates and we were unable to document the dip of the initial portion of the subduction zone.

Fault Plane Solutions and the Continuity of the Slab

The fault-plane solutions determined for four of these intermediate-depth microearthquakes show normal faulting with almost horizontal T axes and parallel to the direction of relative plate motion (Figures 18 and 19). The orientation of the T axes in the direction of of the dip of the seismic zone at intermediate depths in other subduction zones of the world has usually been interpreted as a result of the gravitational body force acting on the downgoing slab (Isacks and Molnar, 1969). If the intermediate part of the slab lies flat, however, and it is decoupled from its deepest segment as suggested by the absence of earthquakes at depths of between 200 and 550 km in Peru, it becomes rather difficult to explain the nature of these normal faults. Hasegawa and Sacks (1981) suggest that the normal faults could be explained by a continous slab descending to a depth of 600 km with an aseismic portion between 200 and 550 km. Their results and our microearthquake study suggest the slab remains horizontal to a distance of about 650 km from the trench, where it bends again and continues to greater depth with a relatively steep angle. This interpretation is supported by the presence of a cluster of intermediate-depth events ocurring at depths of about 150 km beneath eastern Peru (see section B in Figure 16). In this scenario, these earthquakes would represent the kneecap of a second bend in the slab (Figure

20). One could speculate that a large number of earthquakes occur here because of the stresses produced by the forces bending the slab, in a situation analogous to that of a plate bent at a trench.

It is unclear what causes these contortions of the downgoing slab: a sudden unbending of the plate to underplate the Andes over a distance of about 300 km, and a second sharp change in dip thereafter. A possible culprit for this behavior may be the buoyant nature of the Nazca ridge that resists subduction due to its lighter composition. Based on reconstructions of past plate motions, Pilger and Handshumacher (1981) suggest the Nazca and Tuamotu Ridges represent mirror images of hot-spot traces formed at the Pacific-Farallon plate boundary, the former resting now on the Nazca plate, the latter on the Pacific plate. Being a mirror image of the Tuamotu Islands, the subducted eastern continuation of the Nazca Ridge bends to the northeast and lies now beneath Peru (Pilger, 1981) (Figure 21). The buoyancy added to the slab by the ridge would induce the very shallow dip of the subduction zone in this area. South of the Nazca Ridge, in southern Peru and northern Chile, the subducted slab does not possess this positive buoyancy and the subduction process reverts to a steeper and more normal dip of about 30°. The steep-dipping slab lying to the east of the flat seismic zone (Figure 20) may be interpreted as a remnant of a normal episode of plate

subduction prior to the arrival of the easternmost extension of the Nazca Ridge to the trench.

Summary

During the summer of 1980 we operated a network of portable seismographs to monitor the seismicity in the Central Andes of Peru east of the city of Lima. Although most of our stations were located in the High Plateau only about 15 earthquakes were located in the crust beneath the network. The majority of the microearthquakes in the crust occurred along the eastern margin of the Cordillera Oriental in the sub-Andes. The western part of the sub-Andes appears to be the physiographic province subjected to the most intense brittle deformation. Focal depths for these crustal earthquakes are as deep as 50 km. The Huaytapallana fault in the Cordillera Oriental also shows relatively high seismicity along a northeast-southwest trend that agrees with the fault scarp and the east-dipping nodal plane of two large earthquakes that occurred on this fault on July 24 and October 1, 1969. The fault-plane solutions of events in the sub-Andes and near the Huaytapallana fault show P axes oriented east-west, in the general direction of relative plate motion between the Nazca and the South American plate. Microearthquakes of

intermediate depth recorded during the experiment show a flat seismic zone about 25 km thick at a depth of 100 km. This agrees with the contention of Hasegawa and Sacks (1981) who suggest that beneath Peru the slab first dips at an angle of 30° to a depth of 100 km and then flattens. The fault-plane solutions of intermediate-depth microearthquakes have horizontal T axis oriented in an east-west direction

TABLE 1

STATION COORDINATES

NAME	LAT	LONG	DELAY (sec)	LOCATION	ELEV (m)
ACO	-11.981	-75.095	0.08	ACOPALCA	3900
SAC	-11.778	-75.191	0.16	SACSACANCHA	4250
MAR	-11.604	-75.653	0.11	MARCAJASHA	4050
UNC	-11.235	-75.374	-0.36	UNCUSH	1925
COS	-12.140	-75.562	0.23	COSMOS	4600
CUL	-12.203	-75.211	0.06	CULHUAS	3800
LAI	-12.308	-75.359	0.07	LAIVE	3850
PAC	-11.778	-75.727	0.03	PACHACAYO II	3700
HYT	-11.960	-75.039	0.23	HUAYTAPALLANA	4600
PAM	-12.435	-74.870	0.04	PAMPAS	3750
PAG	-12.003	-74.917	0.01	PAGUA	3600
ATO	-12.341	-75.087	0.08	ATOMPAMPA	3900
MOL	-11.726	-75.409	0.02	MOLINOS	3650
PAR	-11.666	-75.085	0.12	PARCO II	3000
COC	-11.890	-75.305	-0.01	CONCEPCION	3500
COM	-11.699	-75.082	-0.12	COMAS	3000
YAU	-11.714	-75.469	-0.02	YAULI	3450
PA1	-11.782	-75.721	-0.03	PACHACAYO I	3700
PR1	-11.672	-75.083	-0.12	PARCO I	3000
VIS	-12.592	-74.961	0.12	VISCAPATA	4100
CHA	-12.011	-75.374	0.00	CHAMBARA	3350
GUA	-13.993	-75.789	-0.64	GUADALUPE	678
CAL	-12.627	-75.978	-0.42	CALACOCHA	1655
QUI	-12.943	-76.437	-0.68	QUILMANA	510
SJU	-15.356	-75.189	-0.77	SAN JUAN	75
NNA	-11.998	-76.843	-0.67	NANA	555
LM2	-12.068	-77.033	-0.67	LIMA2	127
HUA	-12.038	-75.323	-0.05	HUANCAYO	3313
VES	-12.213	-76.937	-0.77	V.EL SALVADOR	110
ANC	-11.775	-77.150	-0.78	ANCON	56
AYA	-13.080	-74.250	-0.17	AYACUCHO	2800
POC	-11.250	-74.600	-0.63	PTO OCOPA	750

TABLE 2

VELOCITY MODELS

Ocola and Meyer (1975)

Vp (km/sec)	Depth to layer (km)
5.0	0.0
5.6	10.0
6.0	22.0
7.9	65.0
8.0	100.0

Meissner et al (1977)

Vp (km/sec)	Depth to layer (km)
5.9	0.0
6.2	10.0
6.7	30.0
8.1	50.0

James (1970)

Vp (km/sec)	Depth to layer (km)
5.0	0.0
6.0	8.0
6.6	25.0
7.9	60.0
8.0	100.0

TABLE 3

COMPARISON OF HYPOCENTRAL LOCATIONS USING DIFFERENT VELOCITY MODELS°

DATE	TIME	LAT	LON	H	RMS	ERX	ERZ	DIST	NUMBER PHASES
800513	16:35:22.5	11.05	74.67	106.4	0.35	5.20	4.00	23.1	14
800513	16:35:23.3	11.02	74.67	107.6	0.31	5.50	4.50	26.4	
800513	16:35:23.0	10.93	74.64	112.4	0.28	4.30	2.80	35.8	
800515	7:57: 3.8	11.68	74.77	23.4	0.06	6.50	5.10	47.40	8
800515	7:57: 5.1	11.69	74.79	14.3	0.07	3.90	11.10	44.90	
800515	7:57: 5.4	11.68	74.77	12.4	0.06	4.60	2.10	46.80	
800519	13:23:49.4	12.22	76.22	37.9	0.23	5.10	14.00	52.30	10
800519	13:23:50.6	12.21	76.23	24.4	0.27	49.60	51.50	53.40	
800519	13:23:51.4	12.21	76.21	22.4	0.24	5.30	21.30	52.60	
800520	1: 3:36.6	10.98	74.86	24.4	0.05	9.50	93.60	80.80	12
800520	1: 3:37.8	10.97	74.86	24.1	0.13	14.20	31.50	81.50	
800520	1: 3:37.8	10.96	74.85	24.9	0.12	3.10	2.20	83.50	
800523	1:39:27.2	11.97	74.90	9.4	0.13	1.50	0.60	3.90	9
800523	1:39:27.7	11.97	74.91	6.2	0.12	1.40	0.70	3.80	
800523	1:39:28.1	11.97	74.88	2.8	0.11	2.80	5.10	5.90	
800523	9:32:30.1	11.53	75.31	27.1	0.04	3.10	5.60	26.90	5
800523	9:32:30.1	11.52	75.31	30.3	0.04	3.80	5.80	27.30	
800523	9:32:30.1	11.52	75.31	32.7	0.04	4.60	5.40	27.80	
800523	13:34:31.2	11.87	77.33	54.8	0.42	6.00	2.90	22.0	8
800523	13:34:31.3	11.87	77.39	56.6	0.48	7.60	4.40	27.6	
800523	13:34:31.2	11.85	77.45	57.9	0.52	8.70	6.70	33.4	
800529	3:45:38.7	11.88	75.06	12.9	0.01	1.50	3.50	9.30	6
800529	3:45:39.1	11.88	75.06	9.8	0.05	1.50	4.70	9.50	
800529	3:45:39.8	11.88	75.06	6.1	0.06	1.20	5.10	9.60	
800530	4:57:16.3	11.20	75.02	40.8	0.08	3.60	4.50	52.40	7
800530	4:57:20.2	11.35	75.08	29.2	0.05	13.40	5.10	35.80	
800530	4:57:20.2	11.33	75.07	29.3	0.05	14.10	3.10	38.10	

800530	10:41:57.5	12.70	76.48	46.3	0.47	2.80	6.60	27.0	14
800530	10:41:57.7	12.77	76.53	53.1	0.37	2.10	1.20	21.9	
800530	10:41:59.6	12.73	76.49	38.9	0.31	1.40	1.20	24.6	
800530	10:45:16.2	11.13	73.88	11.9	0.20	21.60	57.60	143.90	13
800530	10:45:19.9	11.18	73.99	8.1	0.20	22.20	4.70	131.40	
800530	10:45:20.1	11.17	73.95	16.4	0.19	17.90	5.80	136.10	
800531	1:57:21.1	11.91	75.89	104.3	0.12	5.10	5.70	55.90	9
800531	1:57:22.7	11.91	75.89	98.4	0.12	6.40	10.60	55.80	
800531	1:57:22.7	11.94	76.02	92.0	0.09	3.80	7.10	71.20	
800531	3: 3: 6.8	12.11	75.60	110.3	0.13	6.40	15.20	43.90	11
800531	3: 3: 8.4	12.10	75.59	105.7	0.10	4.30	6.90	42.60	
800531	3: 3: 8.9	12.10	75.60	108.0	0.11	5.10	8.40	44.10	
800602	16: 3:18.8	11.11	74.79	50.7	0.38	3.30	6.10	25.8	12
800602	16: 3:22.8	11.22	74.86	17.4	0.38	2.40	2.00	28.5	
800602	16: 3:21.7	11.12	74.81	33.7	0.45	13.30	19.80	27.3	
800602	20:58:44.4	12.26	75.35	9.8	0.10	2.00	1.60	5.30	7
800602	20:58:44.6	12.29	75.33	9.3	0.09	2.00	3.30	3.60	
800602	20:58:44.0	12.34	75.32	14.1	0.07	1.20	2.30	5.70	
800603	3:44:59.4	11.05	74.72	21.3	0.14	7.70	22.90	74.30	12
800603	3:44:59.7	11.03	74.68	17.9	0.13	2.60	3.50	78.90	
800603	3:44:59.6	10.99	74.65	16.6	0.17	2.40	46.80	83.50	
800603	11:14:55.4	11.87	76.23	108.9	0.09	2.40	7.80	68.40	9
800603	11:14:57.6	11.88	76.22	97.2	0.11	1.90	4.30	68.90	
800603	11:14:58.5	11.87	76.23	96.6	0.07	2.10	6.40	68.50	
800603	16:31:13.1	11.24	74.59	88.8	0.14	2.20	2.80	71.30	23
800603	16:31:13.4	11.18	74.52	88.2	0.15	2.60	3.80	81.70	
800603	16:31:13.6	11.12	74.45	84.7	0.19	3.00	5.00	91.90	
800604	3: 8: 5.8	11.78	75.10	13.5	0.08	1.40	3.40	10.00	6
800604	3: 8: 6.3	11.78	75.10	10.2	0.11	1.50	4.40	10.40	
800604	3: 8: 7.0	11.78	75.10	6.2	0.12	1.10	3.60	10.00	
800604	4: 7:28.1	11.12	75.13	54.5	0.42	2.80	4.30	29.5	15
800604	4: 7:28.6	11.06	75.11	53.6	0.34	2.50	4.00	34.2	
800604	4: 7:29.4	11.05	75.10	45.3	0.40	3.30	2.10	36.8	
800604	6:22: 7.3	11.73	74.76	25.6	0.10	2.50	3.60	36.50	9
800604	6:22: 7.9	11.73	74.75	23.2	0.10	2.20	4.50	36.80	
800604	6:22: 7.9	11.72	74.71	20.5	0.12	2.50	5.40	40.90	
800604	12:37:30.2	11.86	75.05	15.7	0.10	0.50	0.90	11.5	12
800604	12:37:31.0	11.86	75.06	8.7	0.15	0.60	2.30	11.5	
800604	12:37:31.7	11.86	75.06	4.4	0.12	0.50	2.30	11.5	

800605	20:42:25.7	13.13	76.42	48.4	0.45	3.30	1.20	20.80	15
800605	20:42:25.0	13.33	76.45	41.8	0.48	4.70	1.70	42.90	
800605	20:42:24.9	13.39	76.64	35.6	0.50	5.00	1.80	54.30	
800606	3:26: 0.7	12.93	76.31	91.0	0.25	4.40	5.90	13.5	9
800606	3:26: 3.0	12.94	76.26	77.4	0.28	3.50	4.10	18.6	
800606	3:26: 3.9	12.93	76.31	78.2	0.23	3.00	3.30	13.8	
800606	6: 3:36.6	12.19	76.17	79.3	0.19	1.70	9.60	76.50	10
800606	6: 3:37.0	12.18	76.19	91.8	0.17	2.10	8.80	73.90	
800606	6: 3:37.3	12.16	76.21	99.5	0.16	2.50	9.40	71.60	
800609	0: 5: 8.5	12.12	75.23	98.8	0.18	2.20	3.40	9.60	15
800609	0: 5: 9.6	12.13	75.23	98.0	0.19	2.60	4.30	8.60	
800609	0: 5: 9.7	12.14	75.23	102.4	0.20	2.90	4.50	6.60	
800610	7:42:18.9	11.87	75.59	97.6	0.14	1.80	6.10	17.9	12
800610	7:42:20.6	11.87	75.59	92.3	0.14	1.80	6.20	17.9	
800610	7:42:21.8	11.87	75.59	87.2	0.14	1.80	6.10	18.0	
800610	23:17:34.0	11.82	75.16	12.7	0.02	0.60	2.40	18.5	5
800610	23:17:34.4	11.82	75.16	7.3	0.02	0.50	0.50	18.6	
800610	23:17:35.2	11.82	75.16	1.1	0.05	0.50	25.60	18.6	
800611	14:25:41.0	12.75	75.10	116.0	0.33	37.90	44.20	45.30	10
800611	14:25:44.9	12.65	75.12	95.5	0.37	6.10	7.20	34.80	
800611	14:25:45.0	12.72	75.11	96.2	0.30	6.10	6.70	42.30	

°Latitudes and longitudes in degrees, south and west, respectively; H is the focal depth in km; rms root mean square travel time residual; ERX and ERZ are the projections of the error ellipse onto the horizontal and vertical planes, respectively; DIST is the distance of the epicenter to the closest station. The three epicenters and origin times for each microearthquake correspond to locations using the velocity models of Ocola and Meyer (1973), James (1971), and Meissner et al (1977).

TABLE 4

HYPOCENTRAL PARAMETERS OF SCREENED EVENTS°

DATE	TIME	LAT	LON	H	RMS	ERX	ERZ	DIST	NUMBER PHASES
800513	5:31:14.6	10.94	74.67	18.9	0.01	3.20	2.70	35.1	5
800513	13:49:53.9	11.56	73.80	20.9	0.24	2.50	3.90	148.4	12
800513	16:35:22.5	11.05	74.67	106.4	0.35	5.20	4.00	23.1	14
800514	3:46:49.6	12.12	74.71	95.4	0.09	4.50	8.60	39.1	5
800514	8:53:52.1	11.76	75.05	13.5	0.07	1.10	1.20	15.8	8
800514	9: 0:30.0	11.77	75.05	12.6	0.09	1.40	1.60	15.4	10
800515	3:52:32.7	12.36	74.75	17.0	0.11	2.40	1.50	15.3	7
800515	7:57: 5.3	11.72	74.85	23.6	0.08	2.40	1.60	38.0	8
800515	22:26:49.6	13.79	73.59	34.5	0.43	9.90	3.40	204.4	10
800516	4: 1:53.8	11.45	77.51	30.5	0.29	3.60	1.70	95.1	8
800517	3: 6:16.7	11.83	75.07	11.3	0.16	1.00	3.50	14.1	6
800517	11:12:50.4	11.24	75.56	111.4	0.16	2.30	3.80	20.4	11
800518	7: 3: 7.1	12.51	75.23	101.8	0.07	2.40	5.70	30.2	6
800518	23: 2:49.2	11.82	75.08	17.1	0.19	1.00	2.40	13.6	8
800519	6:21: 4.8	11.78	75.08	12.3	0.08	0.90	1.40	12.0	8
800519	8:48:15.6	11.91	75.03	13.6	0.02	0.90	2.70	16.0	6
800519	19:38:53.8	11.24	75.44	19.7	0.01	4.30	0.90	47.0	5
800520	1: 3:37.6	10.97	74.86	24.2	0.17	2.70	1.80	80.8	12
800520	2:48:48.1	11.91	74.74	18.3	0.08	9.80	7.50	21.9	5
800520	22:18:44.7	11.91	75.05	12.8	0.26	1.10	2.90	9.3	7
800521	4:25:47.0	11.25	77.71	15.9	0.14	2.80	2.30	234.1	6
800521	6: 8:22.8	13.79	74.72	108.2	0.16	4.40	5.30	93.3	11
800522	17:35:12.1	11.55	75.19	23.4	0.19	8.10	3.90	18.4	5
800522	21:13:14.1	11.26	74.64	92.4	0.12	3.10	2.40	66.6	8
800522	23:33:21.4	12.88	75.00	95.6	0.43	5.30	2.50	32.8	14
800523	1:39:27.1	11.97	74.90	9.5	0.12	0.80	0.30	4.3	9
800523	9:32:30.2	11.53	75.31	27.1	0.05	1.40	2.40	26.9	5
800523	13:34:31.2	11.87	77.33	54.8	0.42	6.00	2.90	22.0	8
800524	7:36:39.5	11.97	74.90	15.3	0.21	2.30	2.20	4.0	6
800524	8:39:20.8	11.42	74.69	32.1	0.06	1.90	2.50	51.0	6
800525	10:35: 7.4	11.75	75.20	92.6	0.06	2.90	8.10	15.9	5
800525	23:20:31.0	11.82	75.07	18.3	0.07	0.80	1.90	14.4	5
800526	10:25:59.0	12.23	77.04	52.6	0.07	1.40	0.60	10.9	7
800527	1:16:18.4	11.10	74.95	35.2	0.05	6.70	4.60	48.7	6
800528	12: 4:47.7	11.33	75.31	103.9	0.12	1.70	4.20	12.2	8
800528	12:28:31.9	11.90	75.92	105.0	0.49	3.00	5.30	25.6	15
800528	18:31:13.2	11.88	74.48	31.0	0.07	1.60	3.40	49.7	8
800528	21: 5:34.9	11.84	75.07	9.3	0.02	0.50	0.60	15.1	5
800529	0: 3: 9.5	11.06	74.96	38.5	0.13	5.20	3.40	49.4	11

800529	3:45:38.7	11.88	75.06	13.0	0.02	0.60	1.40	9.3	6
800529	9:29:58.8	12.50	75.13	85.9	0.17	2.50	2.50	18.5	12
800529	18:16:49.6	12.56	75.36	90.8	0.22	3.30	2.40	38.6	9
800529	18:29:44.9	12.34	75.09	10.7	0.03	2.20	2.20	0.8	5
800529	19: 6:16.8	11.42	74.71	25.9	0.11	1.90	3.20	49.5	12
800530	4:57:18.4	11.32	75.07	38.0	0.05	2.60	2.10	39.5	7
800530	7:25:51.7	11.27	75.47	19.2	0.13	1.10	0.80	11.3	12
800530	10:41:57.5	12.70	76.48	46.3	0.47	2.80	6.60	27.0	14
800530	13: 0:24.0	11.73	74.69	27.1	0.05	2.80	1.90	39.6	8
800530	13:57:28.7	11.90	75.05	82.2	0.18	1.80	1.00	6.5	13
800530	14:15:14.0	11.84	75.06	9.7	0.02	1.00	0.70	13.9	5
800531	3: 3: 8.9	12.13	75.56	93.2	0.18	3.10	4.20	38.6	11
800531	21:56:31.3	11.03	74.89	38.3	0.04	1.60	3.20	57.0	6
800531	22:46:24.7	11.93	75.00	13.2	0.30	1.00	1.60	5.3	12
800601	4:45:22.3	11.02	74.99	34.7	0.15	1.00	2.30	48.3	18
800601	15:53: 8.1	12.29	74.66	80.7	0.13	3.00	1.30	27.3	8
800601	17:32:41.3	11.20	75.28	21.2	0.24	2.40	1.00	11.5	11
800602	6:52: 0.9	12.29	75.35	14.2	0.06	0.60	0.90	2.5	8
800602	11:12:48.0	12.12	75.09	87.9	0.14	2.20	1.20	15.9	10
800602	20:58:42.2	12.37	75.35	22.1	0.11	2.00	1.30	7.0	7
800602	21:14:59.6	11.87	74.96	17.3	0.12	3.50	1.40	13.3	5
800603	8: 8:41.6	11.08	74.74	20.6	0.15	1.40	1.90	71.0	15
800603	10:10:27.8	11.13	74.78	20.9	0.13	2.50	1.10	65.4	11
800603	10:43:29.8	11.31	75.22	28.9	0.27	1.20	1.80	18.8	19
800603	11:14:55.4	11.87	76.23	108.7	0.09	1.20	3.80	68.5	9
800604	0:55:56.4	11.19	74.86	21.6	0.11	5.10	1.10	56.3	7
800604	2: 9:35.8	11.23	74.86	21.5	0.05	7.50	1.00	53.9	6
800604	3: 8: 5.8	11.78	75.10	13.6	0.08	0.70	1.60	10.0	6
800604	4: 7:28.1	11.12	75.13	54.5	0.42	2.80	4.30	29.5	15
800604	6:22: 7.9	11.74	74.79	26.2	0.09	1.20	1.50	32.7	9
800604	12:37:30.2	11.86	75.05	15.7	0.10	0.50	0.90	11.5	12
800604	23:19:57.9	10.98	74.28	10.1	0.41	5.60	3.10	45.9	14
800605	4:48: 4.6	11.14	74.75	19.8	0.13	2.90	1.40	68.5	6
800605	5: 0:21.7	11.29	75.04	23.6	0.07	1.20	2.90	42.0	5
800605	7: 9:27.9	10.67	74.88	19.5	0.48	5.80	3.60	82.9	16
800605	10:13:33.7	11.21	74.85	33.1	0.22	1.40	2.80	27.7	16
800605	15:42:59.4	10.97	74.60	18.9	0.16	2.50	2.80	89.8	8
800605	23:11: 0.8	11.09	74.74	20.9	0.14	1.90	2.50	70.6	8
800606	0:39:17.6	11.21	74.60	82.3	0.13	1.20	2.30	73.5	10
800606	1:10: 3.6	11.66	74.62	21.5	0.06	1.00	0.50	50.3	11
800606	3:26: 0.7	12.93	76.31	91.0	0.25	4.40	5.90	13.5	9
800606	5:37: 8.2	12.45	76.66	50.3	0.18	1.40	3.50	53.7	10
800606	14: 8: 5.8	12.31	74.26	18.1	0.24	3.30	1.60	89.3	7
800607	5: 7:34.4	11.93	75.00	14.1	0.33	1.10	1.70	5.0	16
800607	5:50:21.7	11.93	74.95	15.6	0.01	0.70	1.00	9.8	7
800607	6:29:52.7	12.39	74.37	18.7	0.20	3.50	2.80	78.3	6
800607	13:46:28.5	11.22	74.72	19.9	0.12	1.40	0.70	63.6	10
800608	2:54:42.5	11.35	75.14	16.8	0.16	1.40	3.00	28.4	9
800608	6:32:42.4	10.89	75.11	43.2	0.08	1.10	1.50	47.5	10
800608	9:52:31.4	11.42	74.84	72.2	0.11	6.10	5.80	38.0	7
800608	10:51:10.0	11.04	74.80	20.3	0.13	1.20	0.90	66.3	10
800608	13: 9:45.2	11.83	75.06	9.8	0.02	0.70	4.90	14.1	5
800608	15:23:32.8	11.83	75.03	9.9	0.08	3.80	4.20	14.8	6

800608	15:48:24.5	11.36	74.81	32.3	0.07	1.10	2.20	46.0	7
800608	16:40:31.3	11.22	74.92	18.9	0.37	5.60	1.80	52.1	14
800608	20:17: 2.6	11.26	74.66	20.4	0.12	1.10	0.90	64.6	9
800609	0: 5: 9.2	12.11	75.25	92.3	0.15	1.20	2.20	11.1	15
800609	6: 8:14.9	11.81	75.15	20.4	0.13	0.50	1.30	5.6	11
800609	7:10:39.6	11.83	75.15	15.0	0.08	0.40	1.00	6.7	10
800609	9:35:28.2	14.22	76.45	36.4	0.43	2.80	0.90	75.6	15
800609	18:58:23.9	11.37	74.82	31.5	0.13	1.00	2.30	44.1	10
800610	1:37:43.0	12.08	75.22	87.3	0.10	1.00	2.50	13.3	13
800610	1:41: 0.0	11.38	74.93	84.2	0.10	3.00	3.60	35.4	7
800610	7:42:18.9	11.87	75.59	97.6	0.14	1.80	6.10	17.9	12
800610	7:55:26.9	11.10	74.85	28.7	0.12	2.00	7.60	67.8	6
800610	8: 1:58.8	11.42	75.67	19.7	0.15	1.90	1.00	20.6	8
800610	8:47:38.6	11.43	75.31	96.3	0.10	2.00	3.90	34.6	10
800610	9: 4: 0.9	11.34	75.12	21.9	0.10	1.70	0.60	36.4	6
800610	11:17:26.2	11.83	75.04	13.1	0.10	0.80	2.10	14.4	7
800610	23:17:34.0	11.82	75.16	12.7	0.02	0.60	2.40	18.5	5
800611	5: 5:11.9	11.84	75.05	11.0	0.02	0.60	1.60	13.5	5
800611	6:53:26.3	11.81	75.09	14.0	0.20	1.20	3.40	15.6	8
800611	8:55: 6.9	11.74	74.48	19.9	0.01	1.80	1.20	56.1	6
800611	11:38:23.1	11.39	75.18	23.2	0.23	1.90	2.60	32.4	7
800612	10:36:22.1	11.91	74.94	7.0	0.05	0.50	2.00	11.0	6

°See note on Table 3 for abbreviations.

Figure Captions

Figure 1. Main physiographic units of the central Andes of Peru (after Megard, 1978). Dotted area is the coastal batholith and hatchured area indicates location of Andean volcanic rocks.

Figure 2. Location of the seismographic stations used in the study. Open symbols show the portable stations; filled symbols are the stations of the permanent Peruvian Network.

Figure 3. Histograms showing distances between calculated epicenters and focal depths for 29 events using the velocity structures proposed by Ocola and Meyer (1973) and James (1971) for the central Andes.

Figure 4. Histograms showing distances between calculated epicenters and focal depths for 29 events using the velocity structures proposed by Ocola and Meyer (1973) for southern Peru and by Meissner et al (1977) for southern Colombia.

Figure 5. Epicenters of all 344 earthquakes recorded during field experiment. Crosses indicate calculated depths

shallower than 50 km and the triangles events deeper than 50 km. Closed symbols show locations of stations used to locate the earthquakes. Dashed lines show the 1000 and 3000 meter topographic contours of the central Andes.

Figure 6. Epicenters of screened catalog of well located microearthquakes. Symbols as in Figure 5.

Figure 7. Hypocenters of screened microearthquakes shown in Figure 6 projected on the cross section A-B. Vertical lines show the projected positions of the stations.

Figure 8. Fault scarp of the Huaytapallana fault produced by the October 1, 1969 earthquake (after Philip and Megard, 1977).

Figure 9. Epicenters of shallow events in the vicinity of the Huaytapallana fault plotted on a gelogical sketch-map of the Eastern Cordillera (after Philip and Megard, 1977). Closed circles show epicenters and filled symbols the seismic stations. Stars are the epicentral locations of the July 24 and October 1, 1969 earthquakes given by the ISC. Their uncertainties are at least 10 km and perhaps 20 km.

Figure 10. Hypocenters of the events shown in Figure 9 projected onto cross section A-B (Figure 9). Arrows indi-

cate position of the stations and dashed line is the assumed dip of the Huaytapallana fault from the fault-plane solution of the 1969 events (Stauder, 1975).

Figure 11. a) Composite fault-plane solution of four earthquakes b) Solution for single event located near the Huaytapallana fault, and c) Fault-plane solution for the July 24, 1969 earthquake (Suarez et al, 1983). Lower-hemisphere equal-area projection. Open symbols indicate dilatation and closed symbols compression.

Figure 12. Two alternative fault-plane solutions for an earthquake occuring in the high Andes at a depth of 17 km, southeast of the Huaytapallana fault. Symbols as in Figure 11.

Figure 13. Map of the central Andes summarizing lower hemispheric projections of fault-plane solutions of shallow crustal events obtained in this study. Dark areas represent quadrants of compressional first motion. Also shown are the fault-plane solutions of two large events (stars) studied by Suarez et al (1982) in this area.

Figure 14. Comparison of the composite fault-plane solution for six events in the sub-Andes and the fault-plane

solution of the May 15, 1976 earthquake (Suarez et al, 1982) that was located about 20 km east of the events used in the composite solution. Symbols as in Figure 11.

Figure 15. Fault-plane solution of an earthquake located in the western sub-Andes. Symbols as in Figure 11.

Figure 16. Seismicity map of Peru showing the events selected by Barazangi and Isacks (1979).

Figure 17. Vertical cross sections of earthquakes relocated by Hase g awa and Sacks (1981) inside rectangles shown in the inserted map. Solid line is the assumed shape of the seismic zone inferred from the seismicity below a depth of 50 km.

Figure 18. Fault-plane solutions for four intermediate-depth events recorded in this study. Note T axes are nearly horizontal and oriented roughly east-west in all cases.

Figure 19. Map of central Peru summarizing lower hemisphere projections of the fault plane-solutions of intermediate-depth earthquakes obtained in this study. Shown as stars are the locations and fault-plane solutions of the

intermediate-depth events studied by Stauder (1975). Dark areas indicate quadrants of compressional first motions.

Figure 20. Cross section showing the inferred geometry of the subducted slab beneath Peru. To the earthquakes located in this study (shown as circles) we have added the intermediate-depth events selected by Barazangi and Isacks (1976) in Peru (shown as squares). T axes of intermediate-depth events in this area are shown as arrows.

Figure 21. Position of the Nazca and Juan Fernandez Ridges on the Nazca plate relative to South America as a function of time (after Pilger, 1981).

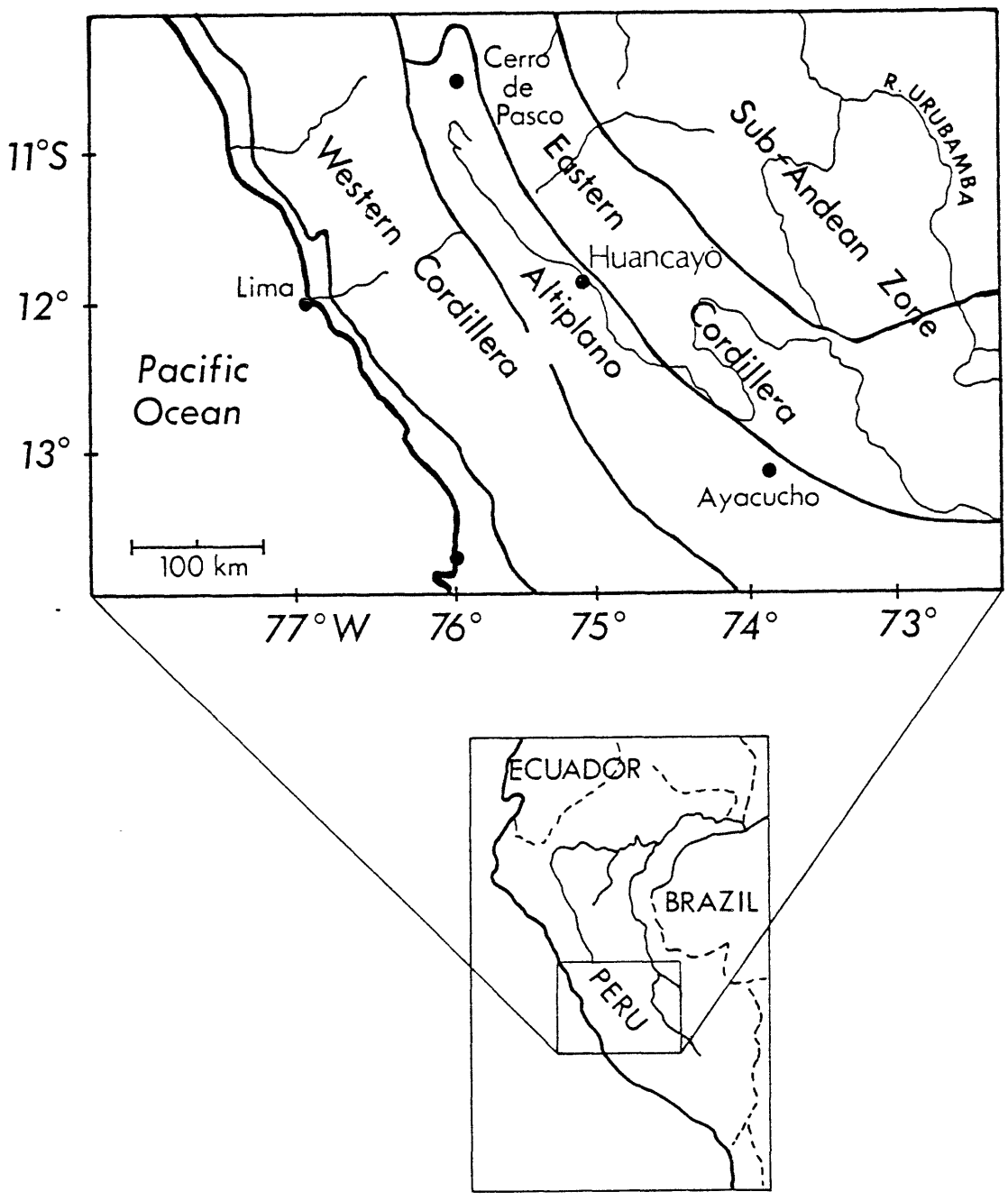
11°S
12°
13°
77°W
76°
75°
74°
73°
Cerro de Pasco
Western Cordillera
Eastern Altiplano
Sub-Andean Zone
R. URUBAMBA
Huancayo
Lima
Cordillera
Pacific Ocean
Ayacucho
100 km
ECUADOR
BRAZIL
PERU

Figure 1

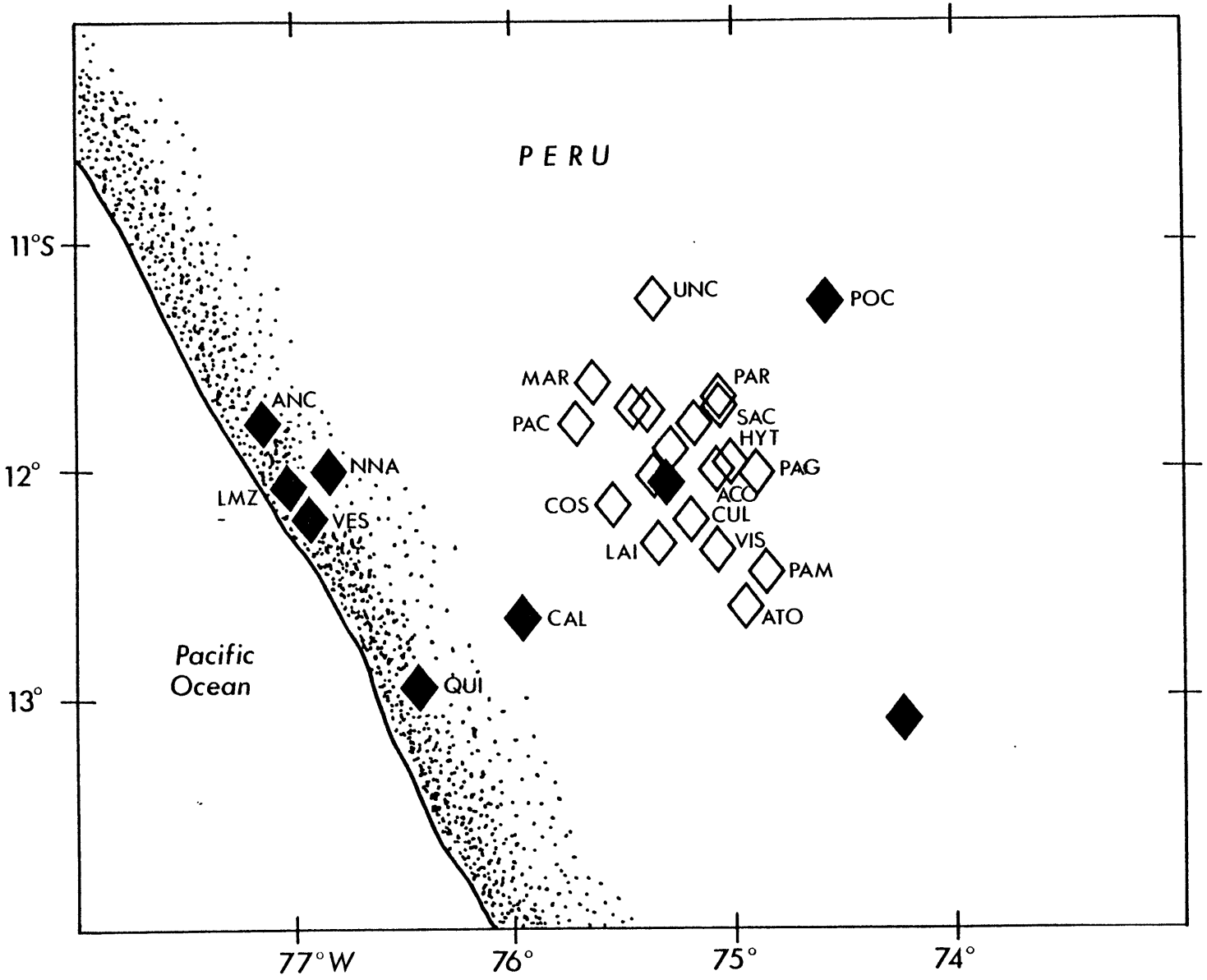
PERU
11°S
12°
13°
77°W
76°
75°
74°
UNC
POC
MAR
PAR
PAC
SAC
HYT
PAG
ACO
COS
CUL
LAI
VIS
PAM
ATO
CAL
ANC
NNA
LMZ
VES
QUI
Pacific
Ocean

Figure 2

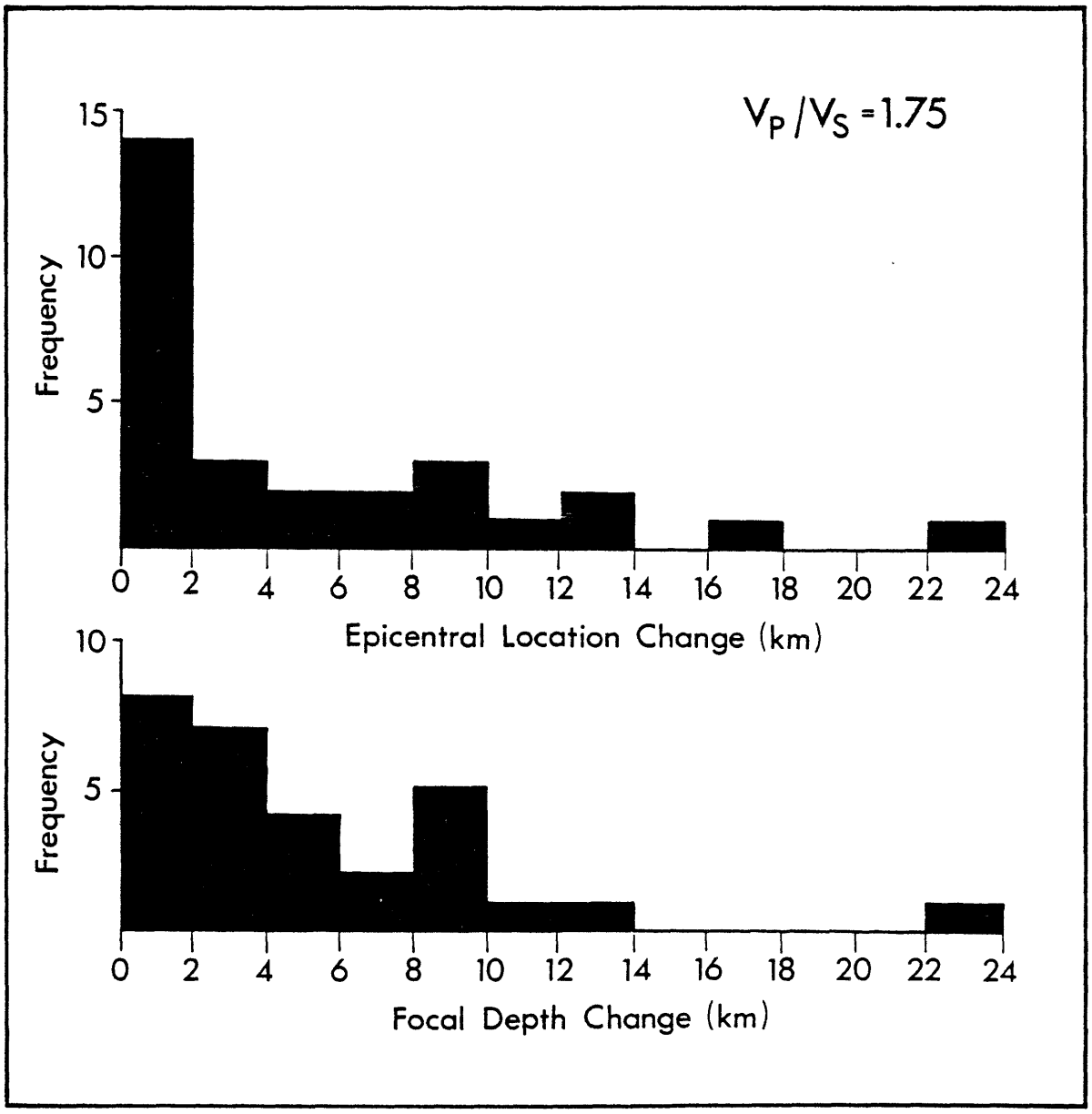
$V_P / V_S = 1.75$
15
10
5
Frequency
0 2 4 6 8 10 12 14 16 18 20 22 24
Epicentral Location Change (km)
10
5
Frequency
0 2 4 6 8 10 12 14 16 18 20 22 24
Focal Depth Change (km)

Figure 3

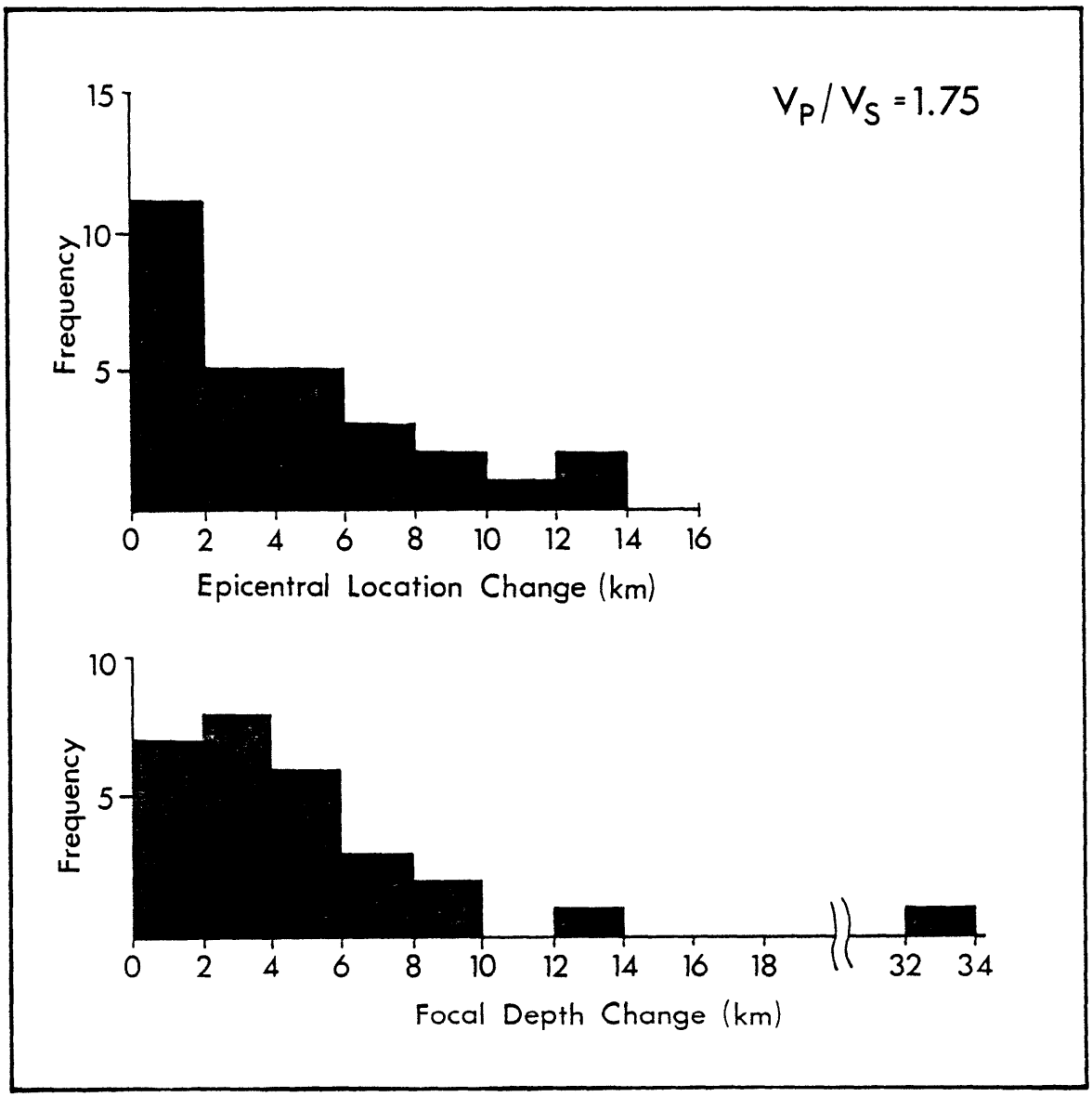
$V_P / V_S = 1.75$
15
10
5
Frequency
0 2 4 6 8 10 12 14 16
Epicentral Location Change (km)
10
5
Frequency
0 2 4 6 8 10 12 14 16 18 32 34
Focal Depth Change (km)

Figure 4

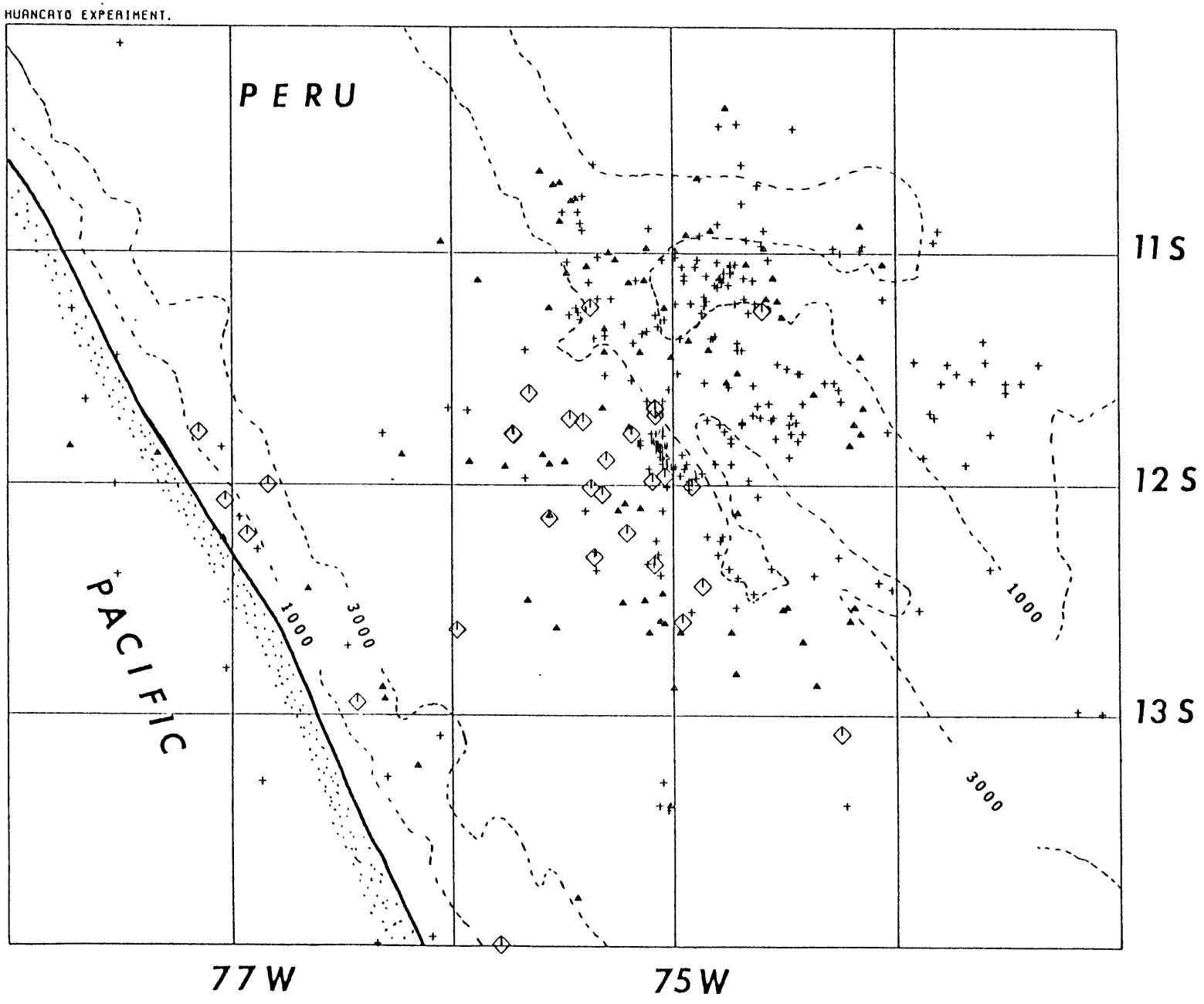
HUANCAYO EXPERIMENT.
PERU
PACIFIC
1000
3000
1000
3000
11 S
12 S
13 S
77 W
75 W

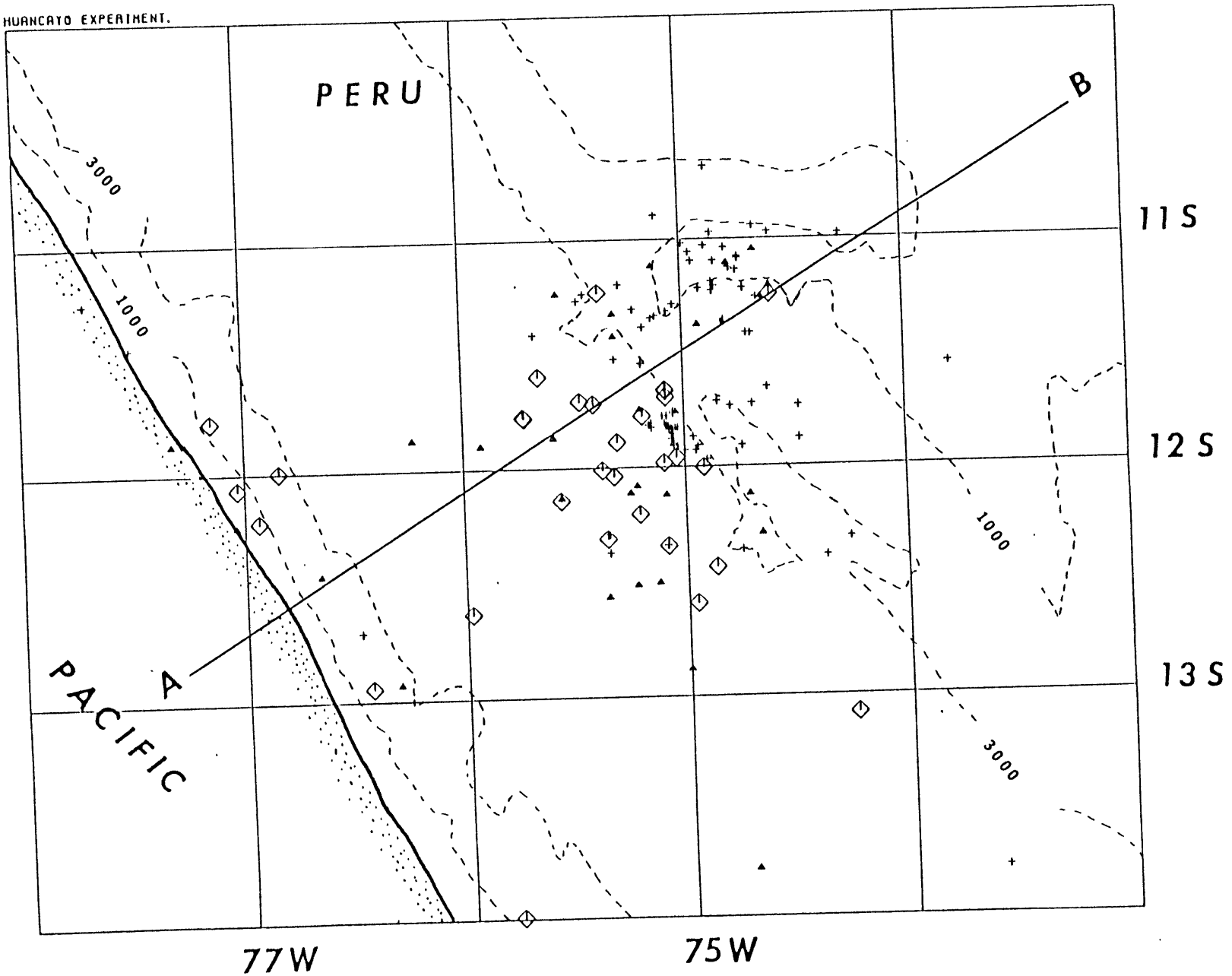
HUANCAYO EXPERIMENT.
PERU
B
A
PACIFIC
3000
1000
1000
3000
11 S
12 S
13 S
77W
75W

Figure 6

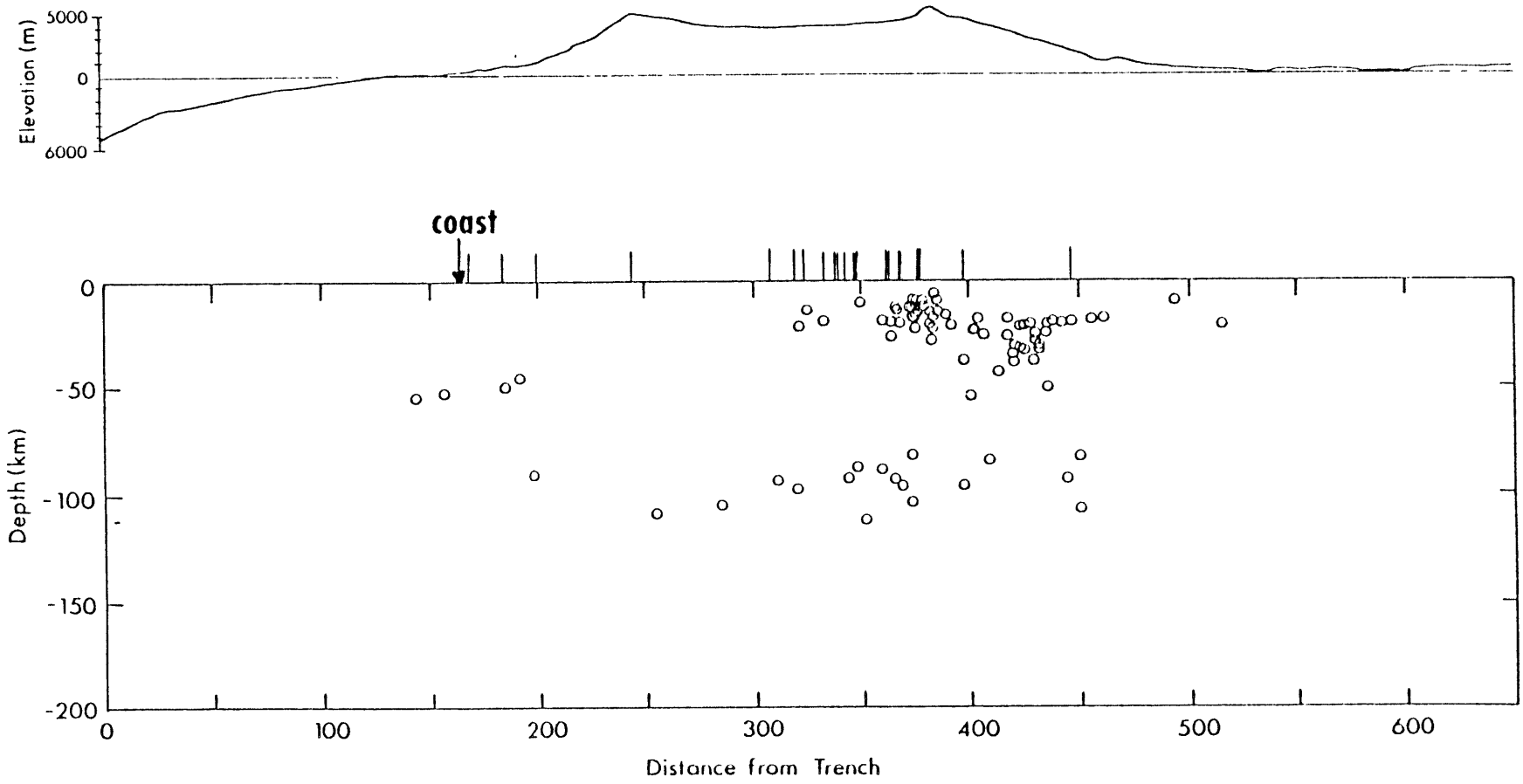
5000
0
6000
Elevation (m)
coast
0
-50
-100
-150
-200
Depth (km)
0
100
200
300
400
500
600
Distance from Trench

Figure 7

Figure 8

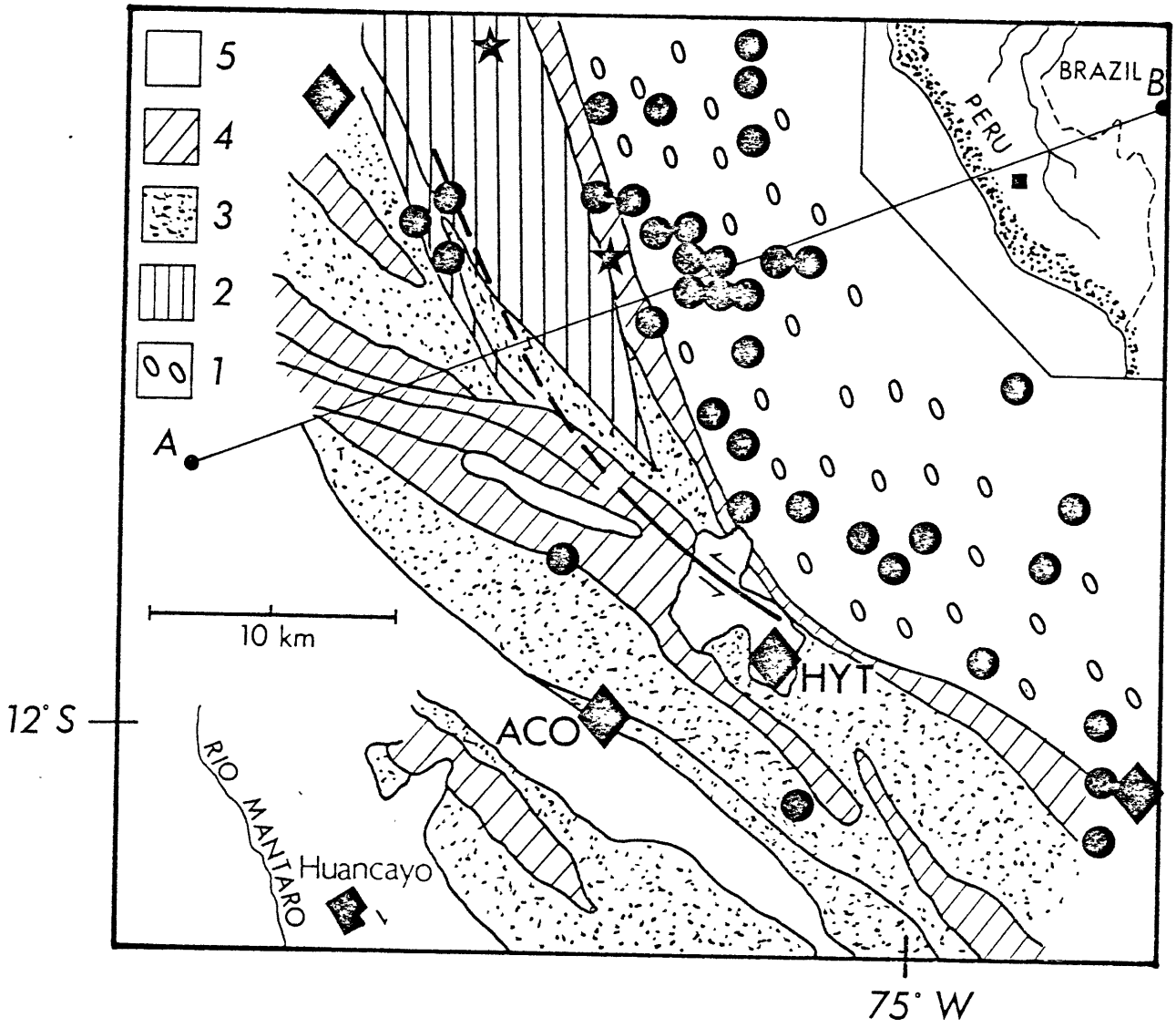
5
4
3
2
1
A
B
BRAZIL
PERU
10 km
HYT
ACO
RIO MANTARO
Huancayo
12° S
75° W

Figure 9

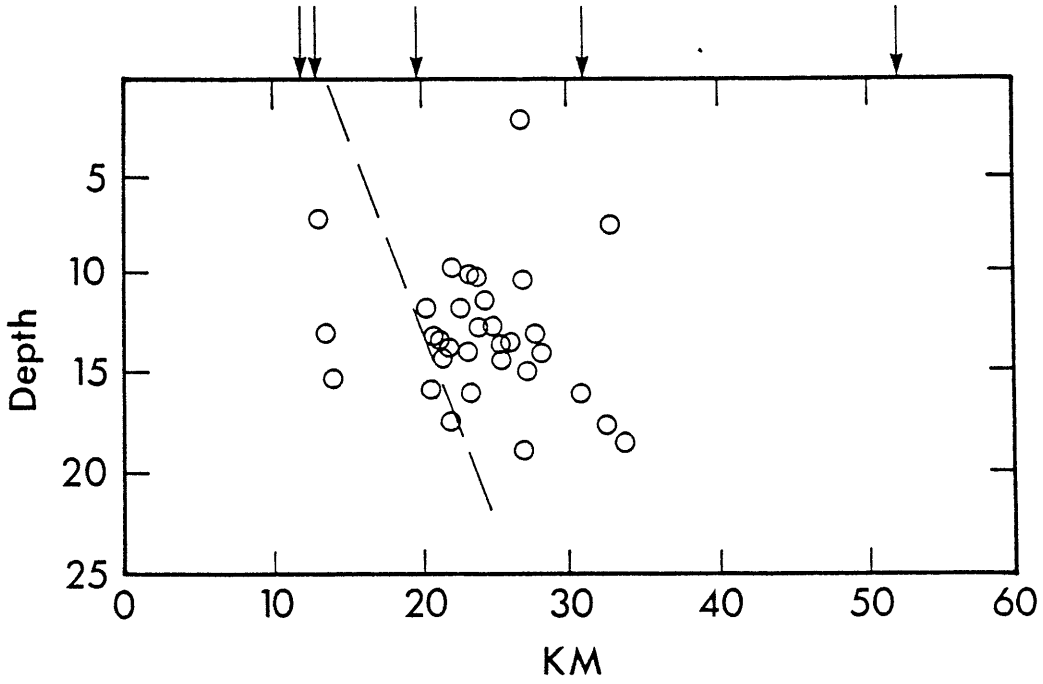

Figure 10

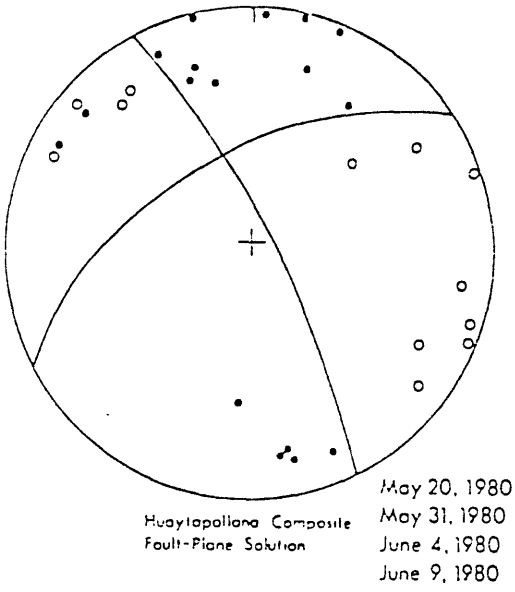

(a)

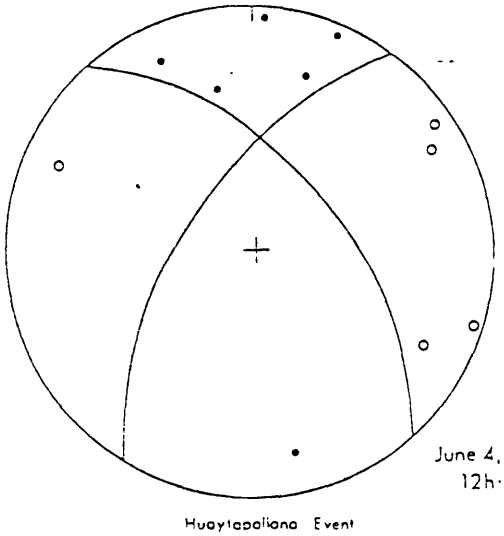

(b)

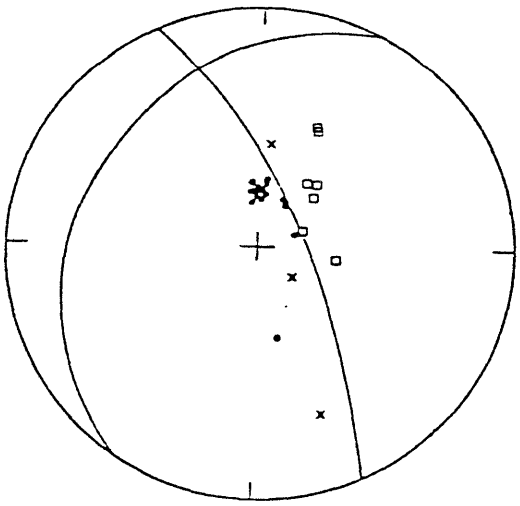

(c)

Figure 11

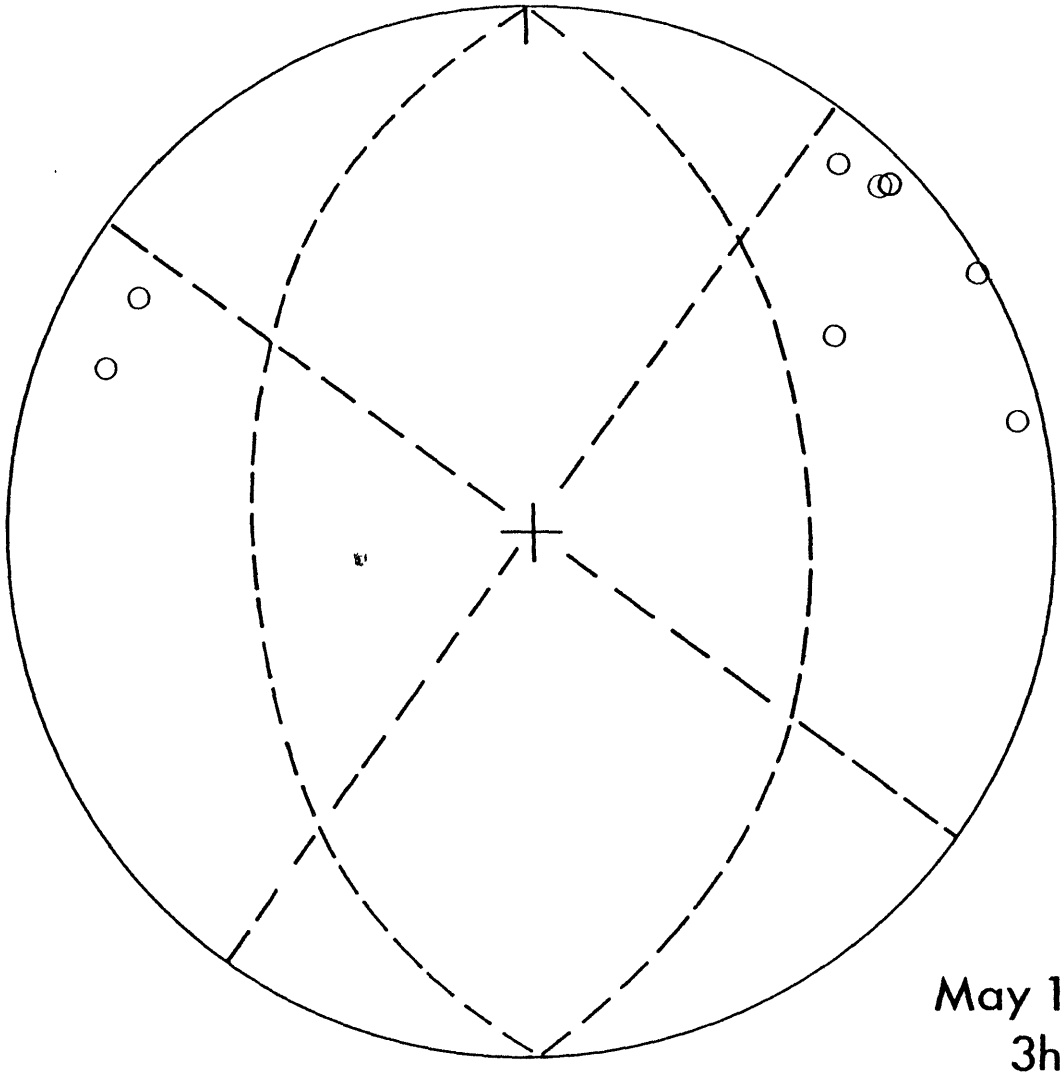

May 15, 1980
3h:52'

Event in the
High Andes
Near Station
PAM

Figure 12

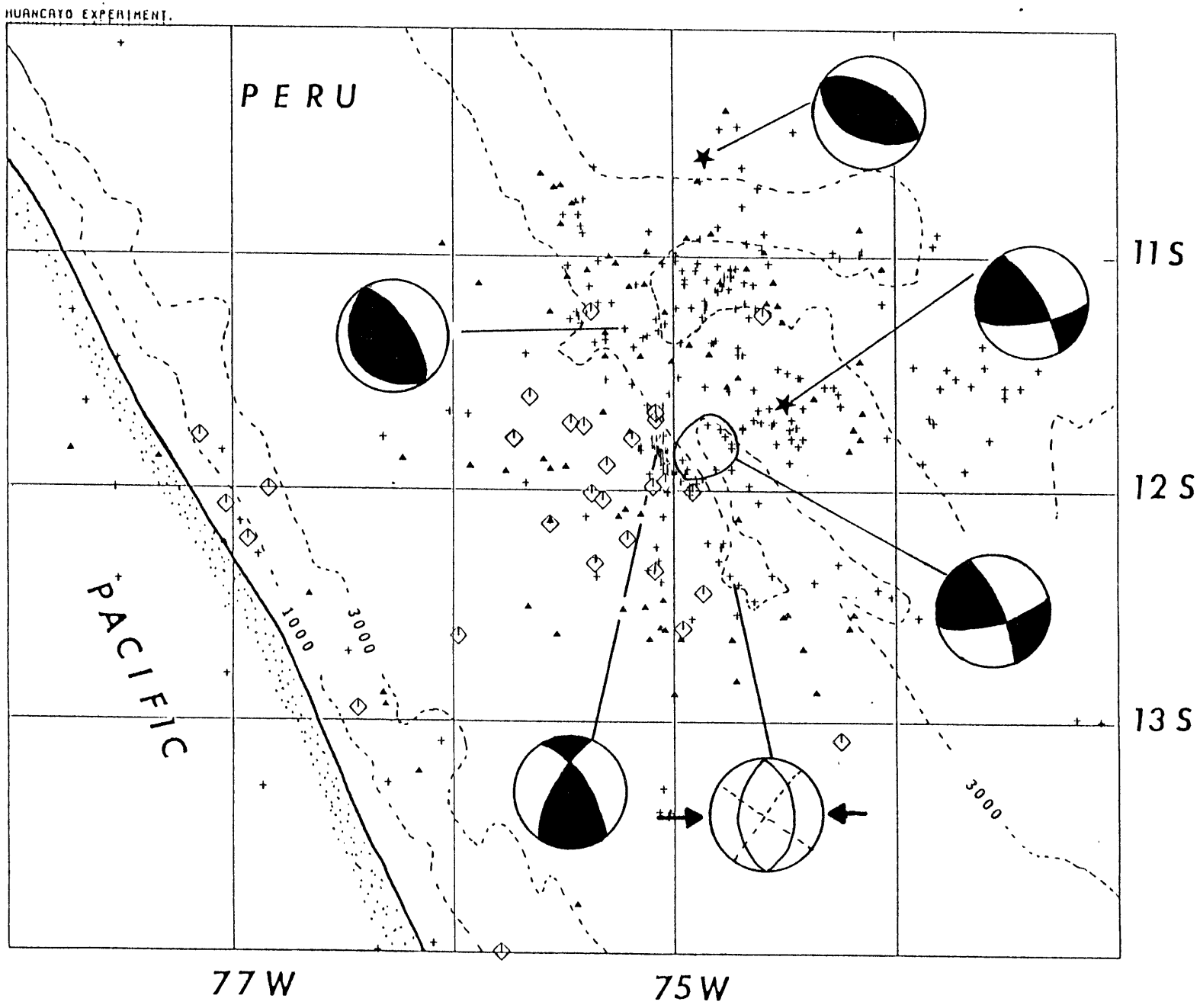
HUANCAYO EXPERIMENT.
PERU
PACIFIC
1000
3000
3000
11 S
12 S
13 S
77 W
75 W

Figure 13

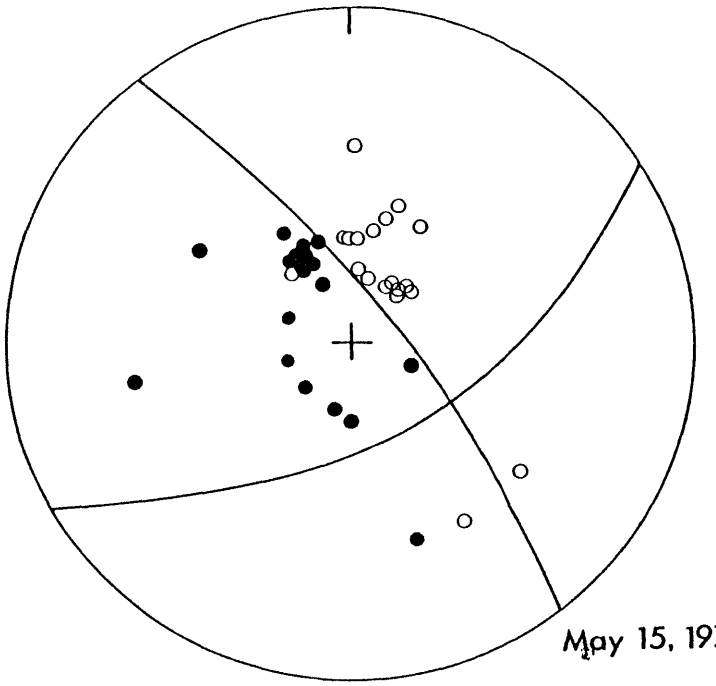

Teleseismic Event
in the Sub-Andes

May 15, 1980 7h:57′
May 20, 1980 2h:48′
May 24, 1980 7h:36′
May 25, 1980 23h:20′
June 4, 1980 6h:22′
June 7, 1980 5h:07′

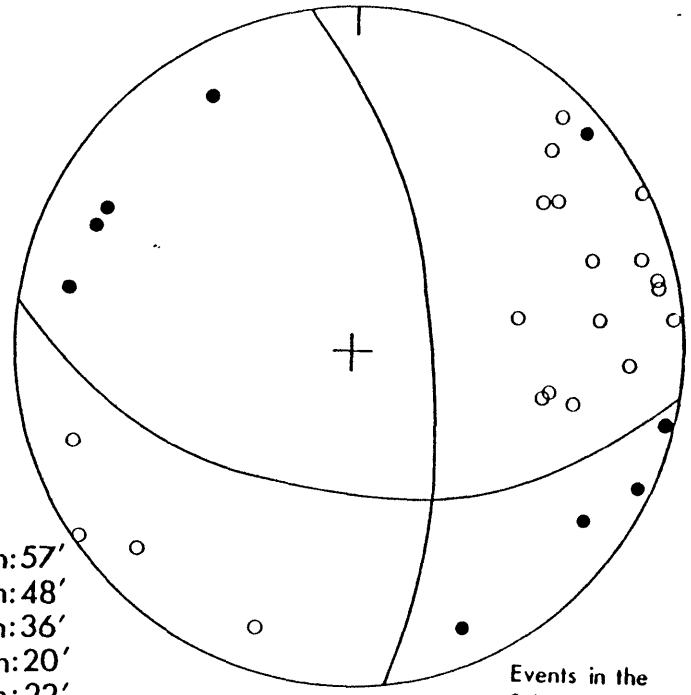

Events in the
Sub-Andes

Figure 14

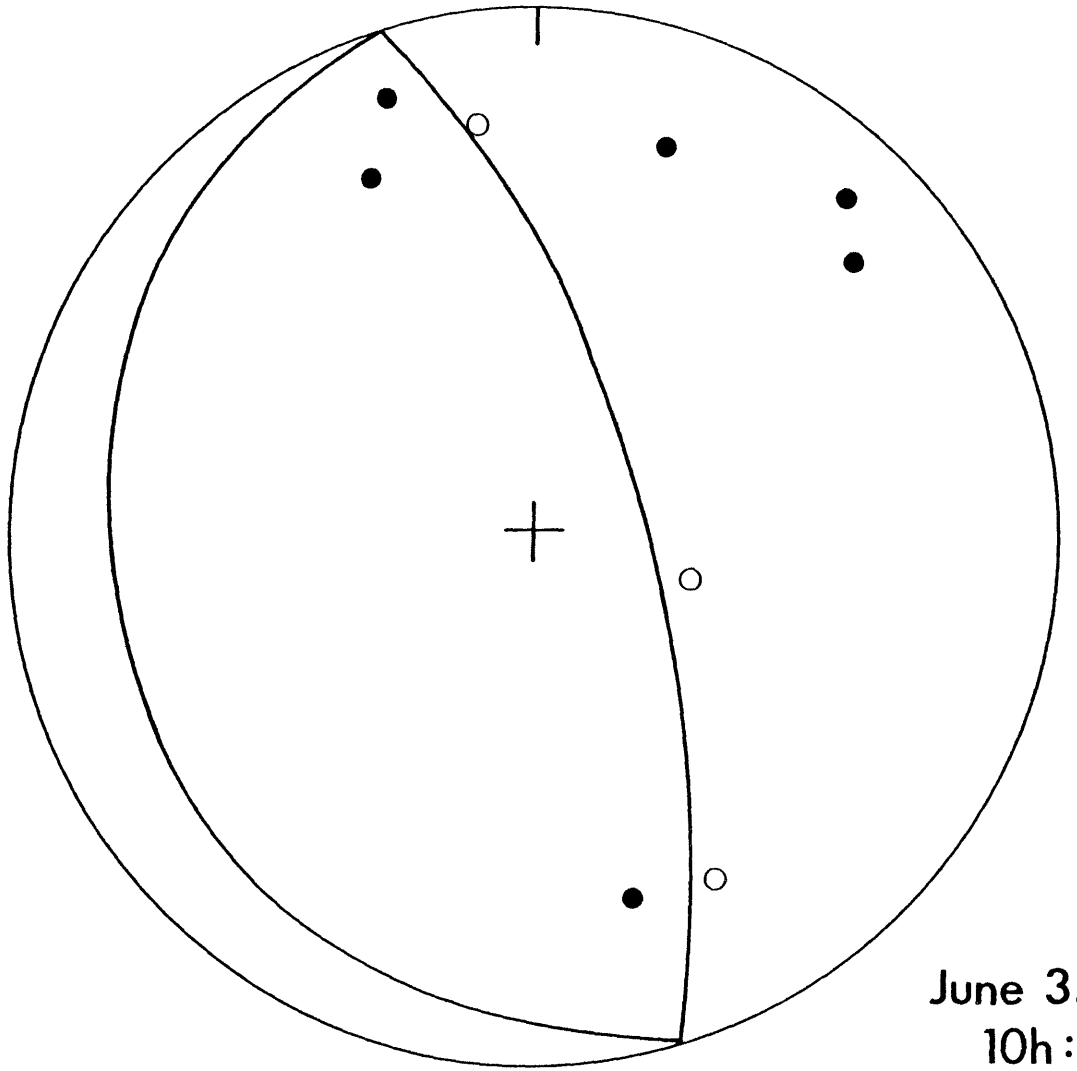

Figure 15

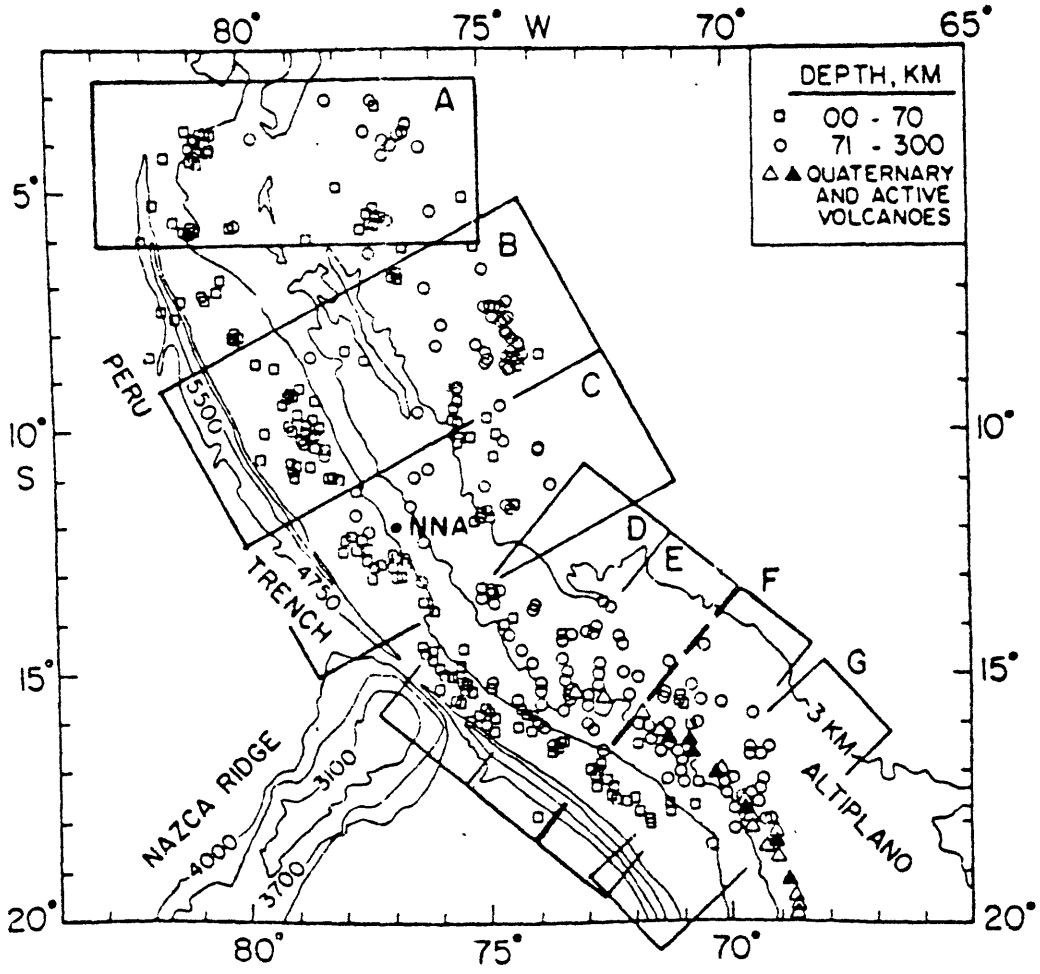
80°
75° W
70°
65°
DEPTH, KM
00 - 70
71 - 300
QUATERNARY AND ACTIVE VOLCANOES
A
B
C
D
E
F
G
5°
10° S
15°
20°
PERU
5500
TRENCH
4750
NNA
NAZCA RIDGE
4000
3700
3100
3 KM
ALTIPLANO

Figure 16

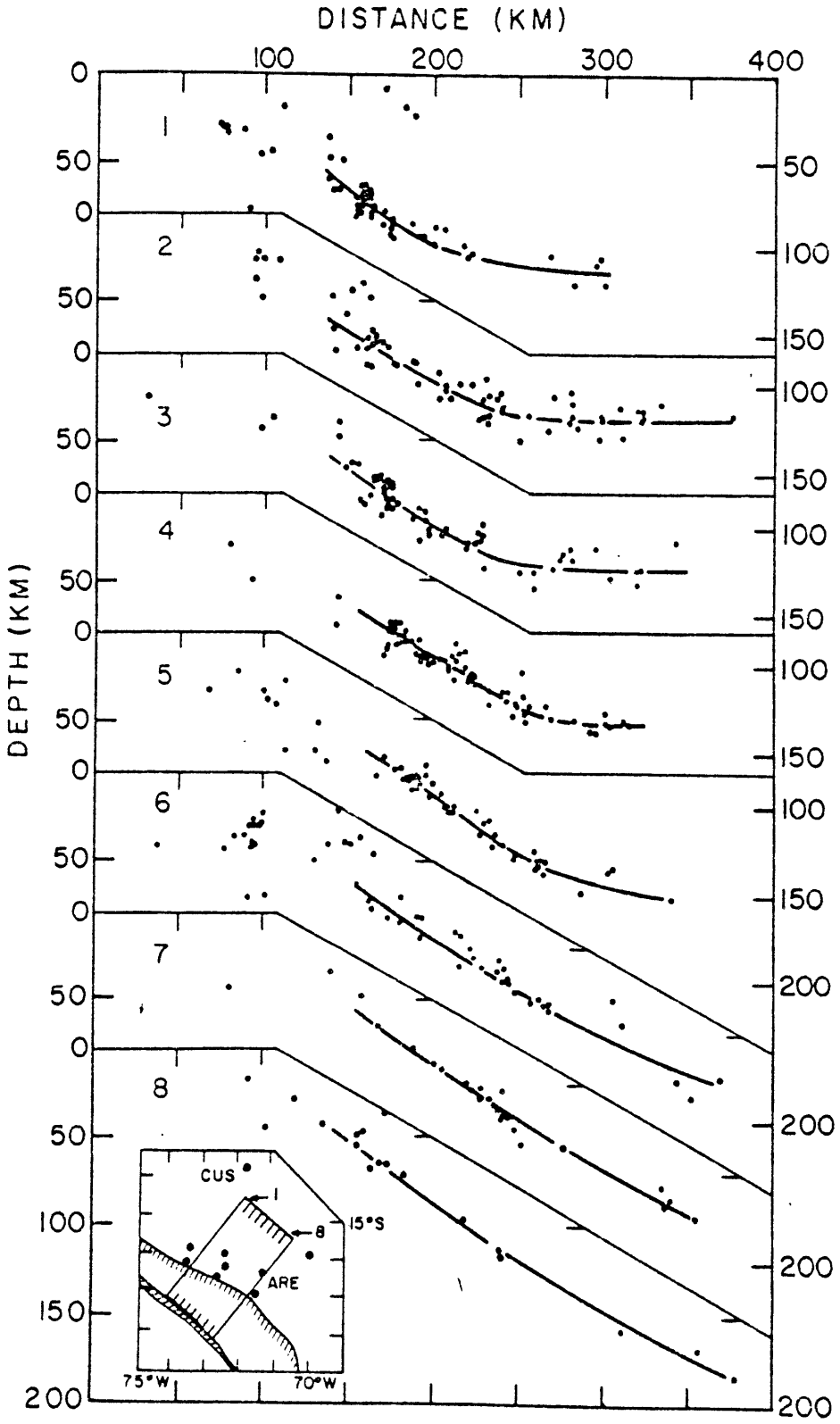
DISTANCE (KM)
100
200
300
400
DEPTH (KM)
0
50
100
150
200
1
2
3
4
5
6
7
8
CUS
ARE
15°S
75°W
70°W

Figure 17

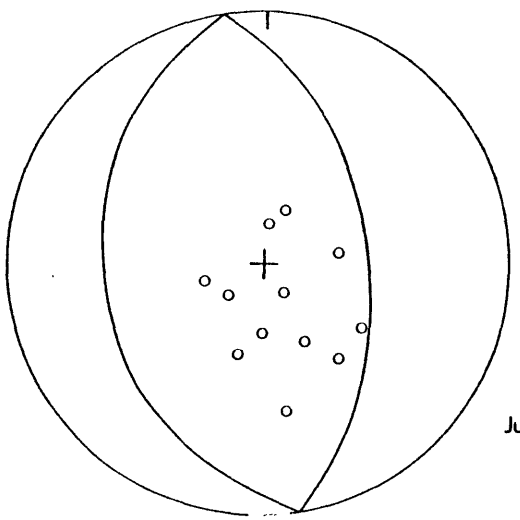

June 10, 1980
12h:06'

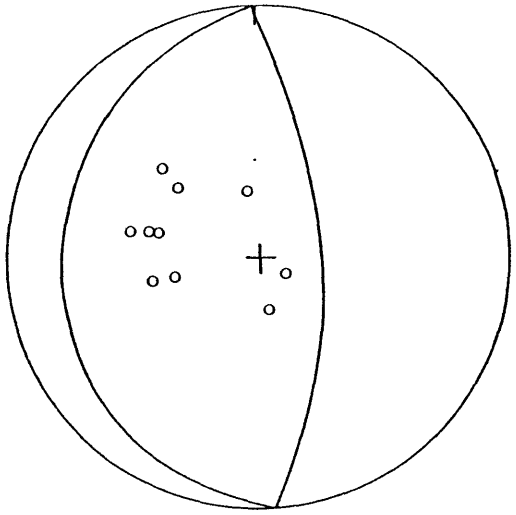

June 10, 198
7h:42

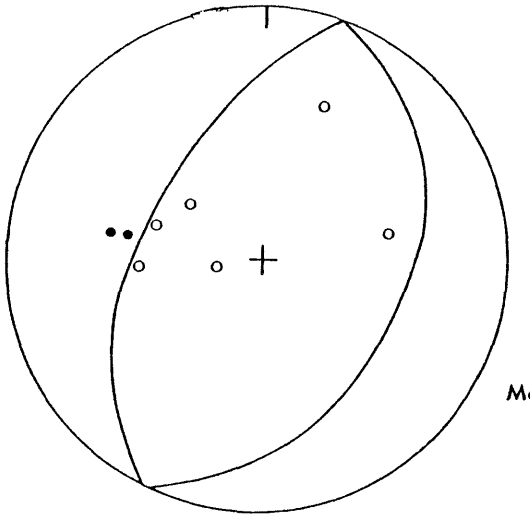

May 22, 1980
2h:28'

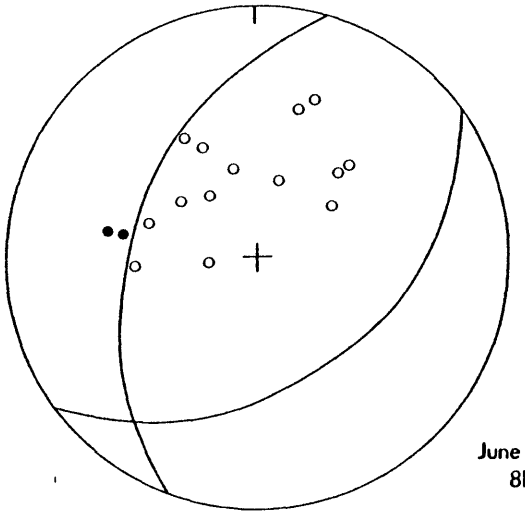

June 10, 1980
8h:47'

Figure 18

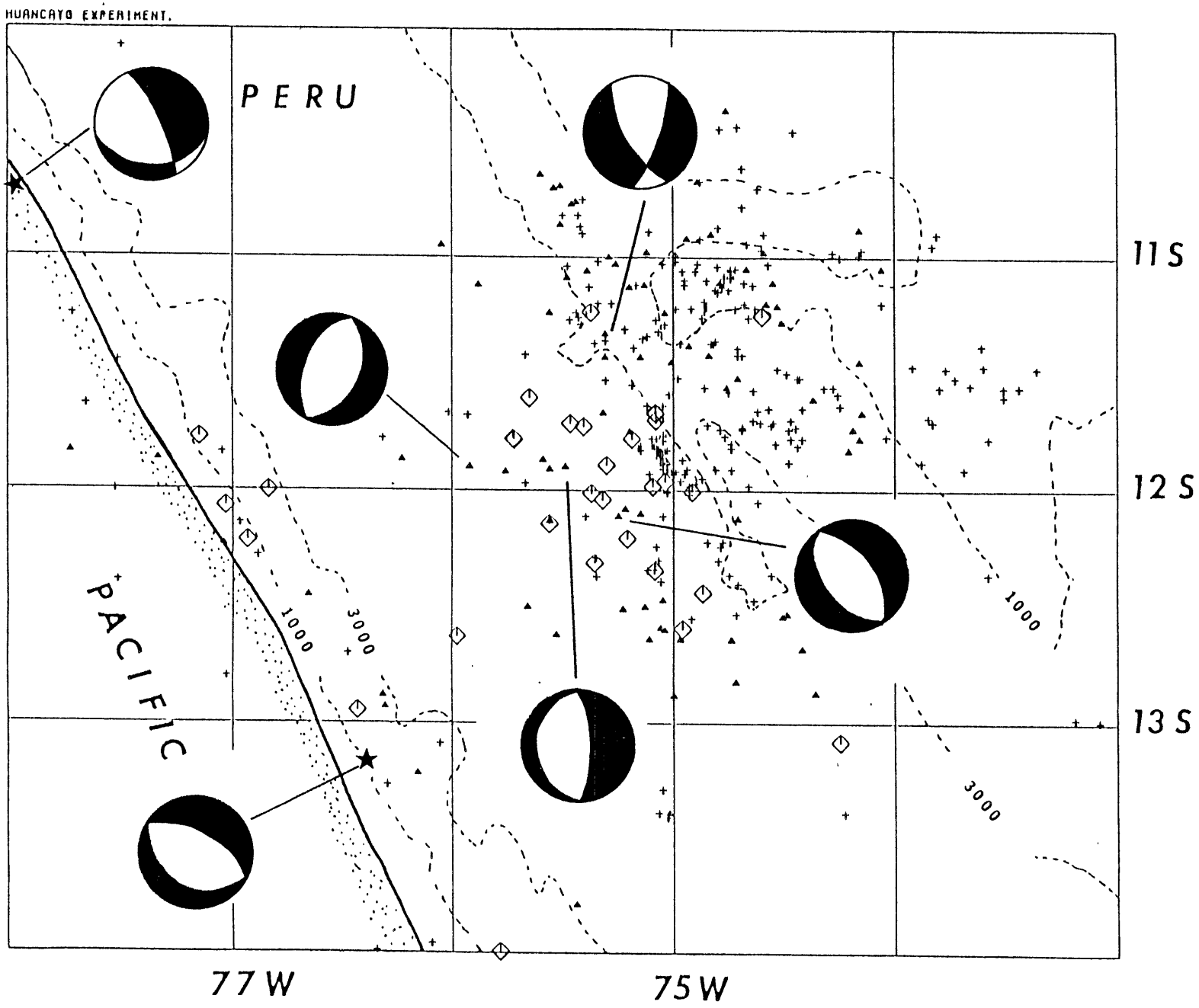
HUANCAYO EXPERIMENT.
PERU
PACIFIC
1000
3000
1000
3000
11 S
12 S
13 S
77 W
75 W

Figure 19

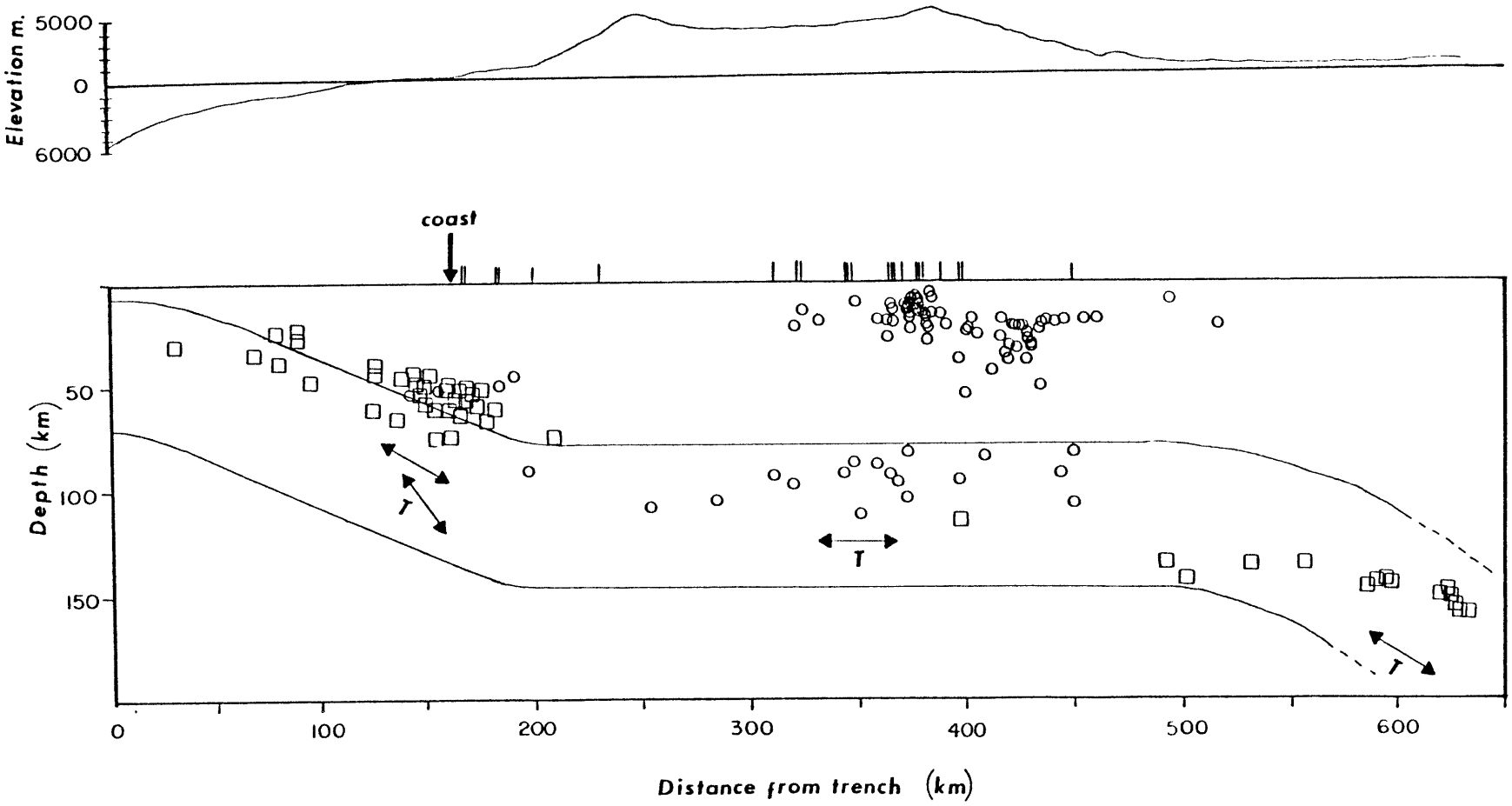
Elevation m.
5000
0
6000
coast
Depth (km)
50
100
150
T
T
T
0
100
200
300
400
500
600
Distance from trench (km)

Figure 20

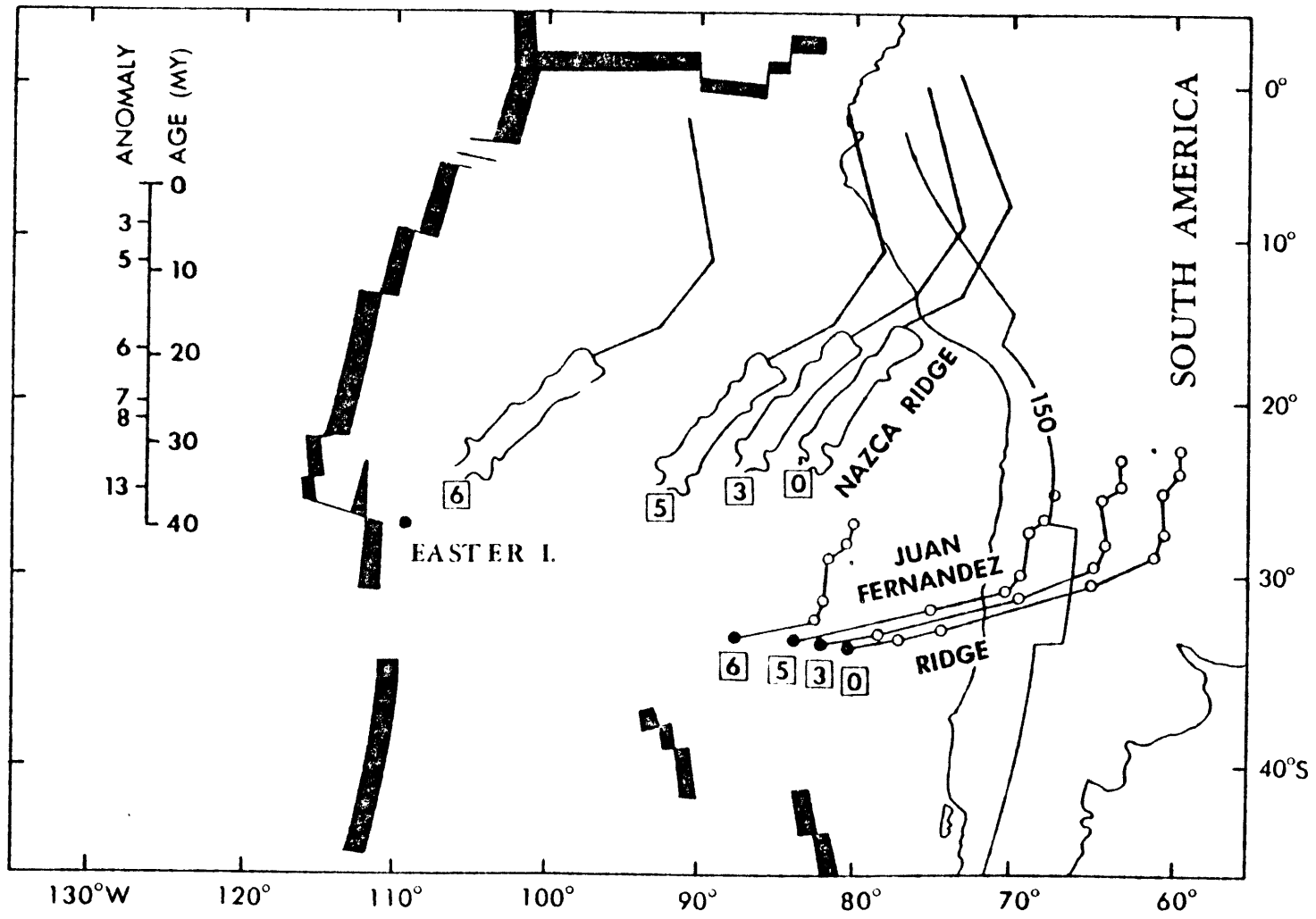
ANOMALY
AGE (MY)
0
3
5
10
6
20
7
8
30
13
40
EASTER I.
NAZCA RIDGE
JUAN FERNANDEZ RIDGE
150
SOUTH AMERICA
6
5
3
0
0°
10°
20°
30°
40°S
130°W
120°
110°
100°
90°
80°
70°
60°

Figure 21

Chapter 4

Introduction

Long period surface waves have been used frequently to determine the source mechanism and focal depth of earthquakes. Early studies, where the observations were compared to theoretical results on a trial-and-error basis (eg. Tsai and Aki, 1966; Weidner and Aki, 1973) have been replaced by efficient inversion methods in the framework of the moment tensor inversion formulation (Gilbert, 1970; Mendiguren, 1977; McCowan, 1976). Inversion of the moment tensor components from Rayleigh waves has been applied succesfully to a number of earthquakes in different parts of the world (eg. Kanamori and Given, 1982; Patton, 1978; Romanowicz 1981; Trehu et al 1981). If the complex spectrum is available, the inversion is linear and yields a unique solution. If only the amplitude spectra is available, the method requires the solution of a system of non-linear equations using an iterative least-squares scheme. Furthermore, independent information on the source mechanism is required, usually from body wave data, to constrain the direction of slip on the nodal plane, which the amplitude data alone cannot discriminate.

To form the complex spectrum, however, the observed phase must be corrected for the propagation effects of phase velocity. For periods between 20 and 100 seconds, the period range most frequently used, phase velocities depend largely on the crustal structure along the path and, therefore, vary greatly for different paths. To perform the linear inversion, phase velocities must be known with an accuracy of about 0.5% (Aki and Patton, 1978). Worldwide regional values of phase velocities are not known yet well enough to predict accurate phase velocities for any given wave path on the surface of the earth. This lack of accurate regional phase velocities has severely limited the application of the moment tensor inversion on a routine basis for cataloguing or scientific purposes.

The objective of this paper is to present a new method to perform the moment tensor inversion using only the amplitude spectrum. The method is an extension of the scheme suggested for the linear inversion by Romanowicz (1982a). While not completely eliminating the non-linearity of the inversion, the proposed method offers some distinct advantages over that proposed originally by Mendiguren (1977). It is substantially faster than the traditional approach (eg. Mendiguren, 1977; Kafka and Weidner, 1979) and, as shown by Romanowicz (1982a), it eliminates some of the errors and biases in the data.

Examples of earthquakes in the North Atlantic, Central Asia, and North America show that encouraging results are obtained using Rayleigh-wave amplitude data as a means of source parameter and focal depth retrieval. It is important to be able to retrieve this information for many events in the magnitude range 5 to 5.5 that are not large enough to produce adequate body waves at sufficiently numerous teleseismic stations, whereas they yield fundamental mode Rayleigh waves that are well above the noise level.

The Method

The observed spectrum, $u(\omega,\theta,r)$, of vertical-component Rayleigh waves on a flat layered medium due to a point source and observed at a distance r, and azimuth θ, is related to the source spectrum $A(\omega)e^{i\phi(\omega)}$ by:

$$u(\omega,\theta,r) = S(\omega)\cdot I(\omega)\cdot e^{-i\omega r/C(\omega)}e^{-\eta r}\cdot A(\omega)e^{i\phi(\omega)} \qquad (1)$$

where $I(\omega)$ is the instrument response, and $C(\omega)$ and η are, respectively, the average phase velocity and attenuation coefficient along the propagation path as a function of frequency ω. The complex function $S(\omega)$ contains the geometrical spreading factor and other constants.

Once corrected for propagation effects and instrument response, the observed complex source spectrum can be expressed as a linear combination of the moment tensor components M_{ij} (Mendiguren, 1977) as:

$$A(\omega)e^{i\varphi(\omega,\theta)} = \alpha + i\beta \qquad (2)$$

where,

$$\begin{aligned} \alpha &= M_{zz}(G_2-G_1) - (M_{yy}-M_{xx})G_1\cos 2\theta + 2M_{xy}G_1\sin 2\theta \\ \beta &= M_{xz}G_3\cos\theta + M_{yz}G_3\sin\theta \end{aligned} \qquad (3)$$

The variables G_i are the excitation functions for a given earth model and have a non-linear dependence on frequency and depth. Equation (3) implies that $\Sigma M_{ii}=0$, i.e. the earthquake is assumed to be a point source with no net volume change (Mendiguren, 1977; Patton, 1978).

In the scheme originally proposed by Mendiguren (1977), the observed amplitude spectrum, $A=(\alpha^2+\beta^2)^{1/2}$, is used to invert for the moment tensor elements in α and β. This non-linear system of N equations, where N is the number of stations used times the numbers of frequencies sampled, is solved at different trial depths h_i. The residuals in the least-square sense of these successive inversions are then plotted as a function of depth; true focal depth is interpreted as that where the minimum in the residual curve occurs.

An alternative approach to invert for the moment tensor components can be obtained following the two-step procedure suggested by Romanowicz (1982a) for the linear moment tensor inversion. We recognize that equations (3) are of the form:

$$\begin{aligned} \alpha(\omega_k,\theta) &= A_k + B_k\cos 2\theta + C_k\sin 2\theta \\ \beta(\omega_k,\theta) &= D_k\cos\theta + E_k\sin\theta \end{aligned} \qquad (4)$$

where the quantities $A_k, B_k, \ldots E_k$ are uniquely determined at each frequency ω_k by the uniqueness of the Fourier expansion in the variable θ (Romanowicz, 1982a) Note that equations (4) are linear and completely decoupled from depth-dependent terms, and are only a function of frequency and azimuth. The relations between the parameters $A_k, B_k, \ldots E_k$ and the moment tensor elements are then as follows:

$$\begin{aligned} A_k &= M_{zz}(G_2(\omega_k,h)-G_1(\omega_k,h) \\ B_k &= -(M_{yy}-M_{xx})G_1(\omega_k,h) \\ C_k &= 2M_{xy}G_1(\omega_k,h) \\ D_k &= M_{xz}G_3(\omega_k,h) \\ E_k &= M_{yz}G_3(\omega_k,h) \end{aligned} \qquad (5)$$

Expressing the observed amplitude spectrum **A** as:

$$\mathbf{A}^2(\omega_k) = (A_k+B_k\cos 2\theta+C_k\sin 2\theta)^2 + (D_k\cos\theta+E_k\sin\theta)^2 \qquad (6)$$

it is possible to proceed in two steps to determine the moment tensor elements. First, the non-linear system of equations (6) is solved at each frequency ω_k to determine the quantities $A_k, B_k, \ldots E_k$. Once these parameters are obtained for each of the frequencies selected in the inversion ($\omega_k = \omega_1, \omega_2, \ldots \omega_n$), the system of equations (5) can be solved for the moment tensor components M_{ij} at each desired trial depth h_i. The focal depth is interpreted as that where the minimum residual occurs.

For example, to solve for the component M_{zz}, the system of equations,

$$A_k = M_{zz}(G_2(\omega_k, h_i) - G_1(\omega_k, h_i)) \qquad (7)$$

is solved for different values of depth, h_i. The residuals in the least square sense are then plotted as a function of depth to determine the minimum. Thus, the sensitivity of each of the moment tensor elements due to changes in depth can be monitored separately.

As was pointed out by Mendiguren (1977), there is an inherent limitation in using only the amplitude spectra of Rayleigh waves to determine the source mechanism. Using amplitude spectra alone, it is not possible to determine the sense of direction of slip on the fault plane. Thus, it is not possible to differentiate, for example, between a pure thrust and a pure normal fault. Furthermore, since the radiation pattern of Rayleigh waves has a two-fold

symmetry, the solution can be rotated by 180° and still satisfy the data. Additional information, usually in the form of a few first motion data or geological information is required to constrain the fault-plane solution.

Advantages of the method

While the non-linear character of the method is not totally eliminated, the advantage over the classical approach is threefold. First, similarly to the case of complex spectra (Romanowicz, 1982a), this procedure eliminates biases arising from innacurate propagation corrections whose dependence on azimuth is orthogonal to the sub-space spanned by the functions $1, \sin\theta, \cos\theta, \ldots \cos 4\theta$. This can be seen when the expression for A^2 (equation 5) is expanded into a linear combination of trigonometric functions. Since the variations with azimuth of the errors in amplitude are more erratic than those of the phase, errors are reduced less significantly for the amplitude than for the phase, where the highest order trigonometric function not eliminated is in 2θ

Secondly, we can monitor the variance as a function of depth for each of the five moment tensor components independently. This is very useful to constrain focal depth since some of the moment tensor components are more sensi-

tive to variations in depth than others (eg. Patton, 1980; Romanowicz, 1981).

Finally, from a purely computational point of view, this approach simplifies considerably the inversion process. The advantage is that instead of performing a non-linear inversion at each trial depth, an average of 10 to 12 inversions if we want a large and closely sampled depth interval, the non-linear scheme is used in the first step only once at each of the frequencies selected (usually, six to eight frequencies distributed over a broad frequency range suffice). Furthermore, the number of equations in the non-linear procedure is substantially reduced. In the traditional approach, the number of equations to solve at each trial depth is equal to the number of frequencies sampled times the number of stations. In the proposed method, however, the number of non-linear equations to solve at each frequency reduces to only the number of stations used. From our experience, the inversion was 20 to 30 times faster using the two-step method. The second step of the inversion is a simple linear procedure that only increases computational time marginally when the number of trial depths is increased. This enables us to closely scan a larger depth range without being penalized by long computation times.

Examples of the Application of the Method

In this section several examples of the application of this moment tensor inversion method are presented. The results of the moment tensor inversion are compared with solutions obtained from body wave modelling data, when the latter are available. The epicentral data of the events studied are given in Table 1.

The 1982 New Brunswick Earthquake

On January 9, 1982, a moderate-size earthquake (m_b=5.7) occurred in the central part of the province of New Brunswick, Canada. The geographic location of this event provides an excellent opportunity to invert for the source parameters from the amplitude spectra of Rayleigh waves using high-quality digital seismograms (Figure 1). A large fraction of the Seismic Research Observatiories (SRO), Modified Seismic Research Observatories (ASRO), and digital WWSSN stations are located in North America, Europe, and South America. Complemented by stations from the WWSSN and Canadian networks, digitized manually on a table-top digitizer, they provide excellent station coverage in azimuth.

The moment tensor inversion was performed using nine periods in the range of between 68 and 26 seconds. The residuals of the inversion as a function of depth are shown in

Figure 2. A clear minimum centered at a depth of about 8 km indicates that the focal depth is in the order of between 4 and 10 km. At a focal depth of 8 km, the solution is an almost pure dip-slip mechanism oriented in a north-south direction (Figure 3). This solution agrees closely with the results obtained by Nabelek et al (1982) from the simultaneous inversion of short and long period body waves (Figure 3). For this solution, the value of the moment tensor elements M_{xz} and M_{yz} is negligible compared to the other three independent components (Table 2). In light of this fact, we can apply the constraints $M_{xz}=M_{yz}=0$ in the inversion. These constraints are equivalent to constraining the fault mechanism to be a pure double couple and, either, a pure strike-slip on a vertical fault plane, or a pure dip-slip on a fault plane dipping at 45° (Kanamori and Given, 1982). Performing the inversion under these constraints yields a sharper residual- versus-depth curve. The resulting fault plane solution at a depth of 8 km shows a pure dip-slip mechanism with nodal planes oriented north-south.

As mentioned before, one of the advantages of the method proposed here is the possibility of monitoring independently the variation of the residuals in the inversion for each of the moment tensor elements. Figure 4 shows the residuals for the moment tensor elements that form the real part of the spectrum. As discussed by Patton (1978), the moment

tensor components that form the imaginary part of the spectrum are not very sensitive to changes in depth.

The residual-versus-depth curves of the individual moment tensor elements show that M_{zz} is the most sensitive to focal depth variations. It exhibits a sharp minimum at 8 km that rises suddenly for depths larger than 10 km. The other two components are less sensitive to depth. $M_{yy}-M_{xx}$ shows a broad minimum centered at 10 km and M_{xy} is virtually constant as a function of depth.

The sharp reduction in residuals constraining the depth to be between 5 and 10 km, and the excellent agreement of the focal depth and source mechanism gleaned from the inversion with those obtained by Nabelek et al (1982) using body wave data are the result of two important factors. Firstly, most of the paths from source to station are short and lie generally within a single tectonic province. Secondly, the results reflect the quality and high signal-to-noise ratios of the digital seismographic stations used. Clearly, the possibility of applying moment tensor inversions on a routine basis will become feasible when world-wide coverage of digital stations improves.

An Aftershock of the 1974 Gibbs Transform Fault Earthquake

This earthquake is an aftershock that occurred in the Gibbs transform fault in the North Atlantic, a few days after the large 1974 earthquake studied in detail by

Kanamori and Stewart (1978). The body wave magnitude reported by the International Seismological Center for this event is 4.9.

This event is a good example of an earthquake for which a fault plane solution could not be obtained because it did not produce large enough body waves to be observed at enough WWSSN stations at teleseismic distances. However, very clear Rayleigh waves were recorded at a number of stations around the epicenter offering adequate azimuthal coverage to perform a moment tensor inversion from them (Figures 5 and 6). The results of the moment tensor inversion applied using a period range of between 55 and 26 sec shows excellent agreement to the solution obtained by Kanamori and Stewart (1978) for the main shock (Figure 7). The inversion converged to the same solution regardless of the orientation of the nodal planes in the starting solution. Only when the initial guess on the value of the scalar moment was wrong by about a factor of 5 did the solution fail to converge to the fault plane solution shown in Figure 7. The residual versus depth curve shows that the earthquake occurred at a depth of between 5 to 15 km beneath the sea floor (Figure 8). Although the curve does not show a sharp minimum, it resolves the depth considerably better than using the method suggested by Mendiguren (1977). (Figure 8).

Although we do not constrain the solution to be a double-couple source, the solution obtained at a depth of 9 km is almost a pure double-couple; the value of the B axis is about one and one-half orders of magnitude smaller than that of the P and T axes.

An earthquake in the Tien Shan

This earthquake occurred in the Tien Shan mountains in central Asia on June 24, 1972. The focal depth of this event was studied by Romanowicz (1982b) using long-period body wave modelling following a fault-plane solution by Roecker et al (1980). Romanowicz (1982b) obtained a focal depth of approximately 15 km based on the comparison of theoretical and observed body waves. The depth reported by ISC was 47 km.

The moment tensor inversion of Rayleigh wave amplitude data yields a focal depth of 15 km (Figure 10) in agreement with the result obtained using body-wave modelling. The resulting fault plane solution shows a dip-slip mechanism with some strike-slip motion. It agrees in general with the result of Roecker et al (1980) although it violates a few first motion data (Figure 9). As in the previous examples, the solution is independent of the initial guess used in the inversion and shows better depth resolution than the traditional approach (Figure 10).

Summary

A new approach to invert for the moment tensor components using only the amplitude spectra of vertical component Rayleigh waves is discussed. The method consists of two steps: First, the amplitude spectra are decoupled from their depth dependent terms and fit with a smooth function of azimuth at each frequency selected for the inversion. This has the effect of eliminating some biases and errors in the data. In the second part, each of the five independent moment tensor components is monitored separately at various trial depths. True focal depth is then determined as the minimum in the variance versus depth curve. Encouraging results are obtained applying the method to earthquakes in Central Asia, North America, and the Mid-Atlantic Ridge. The method is shown to be a useful tool to determine the source parameters of a number of local or intraplate earthquakes for which a poorly constrained solution is obtained from body wave data alone, and when the absence of accurate regional phase velocities precludes the use of a linear moment tensor inversion.

TABLE 1

HYPOCENTRAL DATA OF EARTHQUAKES STUDIED°

EVENT LOCATION	DATE	LAT	LON	DEPTH (ISC)	ESTIMATED DEPTH	mb
Gibbs Transform Fault	11/16/74	52.64N	32.15W	26	9	4.9
Tien Shan Mountains	06/24/72	36.30N	69.69E	47	15	5.9
New Brunswick Earthquake	01/09/82	46.98N	66.66W	7	8	5.7

°All data from the ISC catalog except for the New Brunswick event which is from the USGS Preliminary Epicentral Determinations.

Table 2

RESULTS OF MOMENT TENSOR INVERSION

New Brunswick Event Depth=8 km

M_{zz}	$= -1.04 \times 10^{24}$	dynes/cm
$M_{yy}-M_{xx}$	$= -1.24 \times 10^{24}$	"
M_{xy}	$= -1.19 \times 10^{23}$	"
M_{xz}	$= 2.80 \times 10^{18}$	"
M_{yz}	$= -2.64 \times 10^{18}$	"

Gibbs Transform Fault Event Depth=9 km

M_{zz}	$= 1.57 \times 10^{22}$	dynes/cm
$M_{yy}-M_{xx}$	$= 7.52 \times 10^{22}$	"
M_{xy}	$= -1.60 \times 10^{23}$	"
M_{xz}	$= -1.69 \times 10^{18}$	"
M_{yz}	$= -7.09 \times 10^{18}$	"

Tien Shan Earthquake Depth=15 km

M_{zz}	$= 8.99 \times 10^{24}$	dynes/cm
$M_{yy}-M_{xx}$	$= -7.37 \times 10^{24}$	"
M_{xy}	$= 3.46 \times 10^{24}$	"
M_{xz}	$= -3.24 \times 10^{24}$	"
M_{yz}	$= -1.81 \times 10^{24}$	"

Figure Captions

Figure 1. Location of the January 9, 1982 New Brunswick event. Squares indicate the seismographic stations used in the inversion.

Figure 2. Residual versus depth curve for the moment tensor inversion of the New Brunswick earthquake. Open circles for the unconstrained inversion, closed circles for the constrained inversion ($M_{xz}=M_{yz}=0$). Residuals are normalized to the maximum value in each case.

Figure 3. a)Closed circles are compressional first motions of P waves plotted on a lower-hemispheric projection. Solid line is the fault plane solution obtained from the unconstrained moment tensor inversion, dashed line is the solution of the constrained inversion, and dotted line is the solution determined by Nabelek et al (1982) inverting body wave data. b) Rayleigh-wave amplitude radiation pattern at a period of 50 seconds.

Figure 4. Normalized residuals versus depth for the three moment tensor elements in the real part of the spectrum.

Figure 5. Location of the earthquake in the Gibbs transform fault and the stations used in the moment tensor inversion.

Figure 6. Examples of Rayleigh waves recorded at vaious WWSSN stations from an earthquake in the Gibbs transform fault (m_b = 4.9).

Figure 7. a) Source mechanism of the aftershock in the Gibbs transform fault obtained from the moment tensor inversion (dashed line). Solid line is the fault plane solution determined by Kanamori and Stewart (1976) for the main shock. b) Rayleigh-wave amplitude radiation pattern at a period of 40 seconds.

Figure 8. Normalized residuals versus depth for the Gibbs transform fault event. Closed circles using the method proposed in this paper, squares using the traditional method.

Figure 9. a) Fault plane solution of the earthquakes in the Tien Shan. Closed circles are compressional first motions and open circles dilatational first motions. Solid line is the fault plane solution (Roecker et al, 1980), dashed line is the solution of the moment tensor inversion. b) Amplitude radiation pattern of Rayleigh waves for a period of 70 seconds.

Figure 10. Normalized residuals versus depth for the Tien Shan earthquake. Closed circles using the method presented in this paper, squares using the traditional approach.

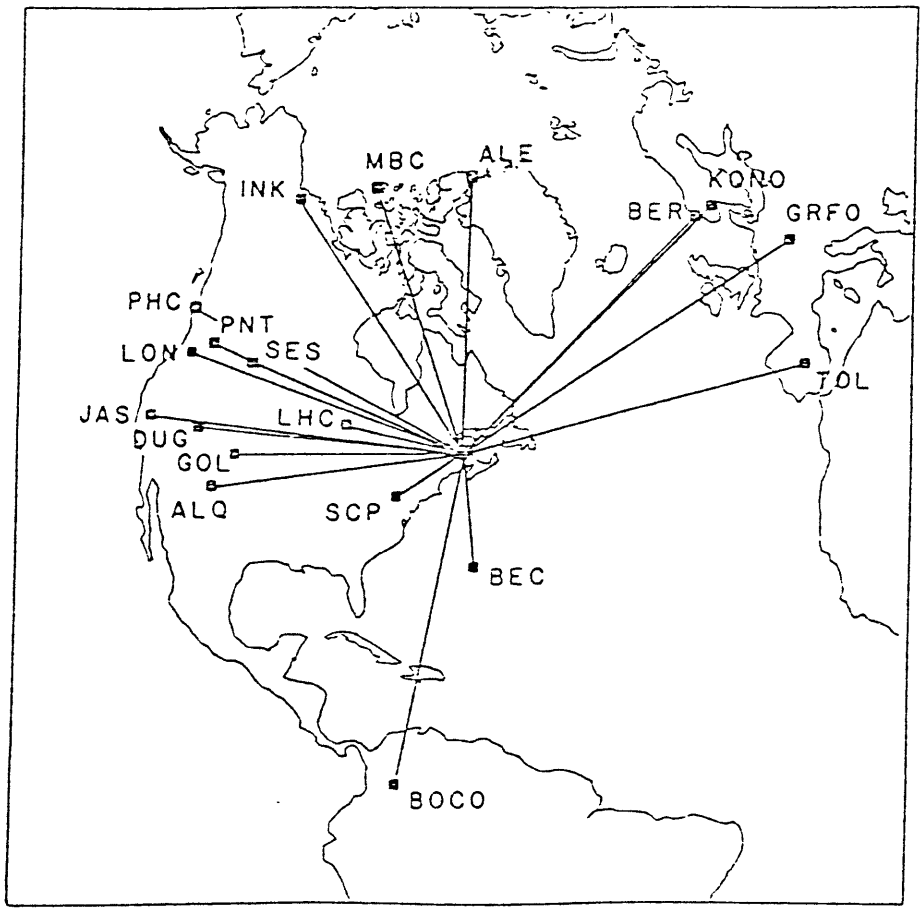
MBC
ALE
INK
KORO
BER
GRFO
PHC
PNT
LON
SES
TOL
JAS
LHC
DUG
GOL
ALQ
SCP
BEC
BOCO

Figure 1

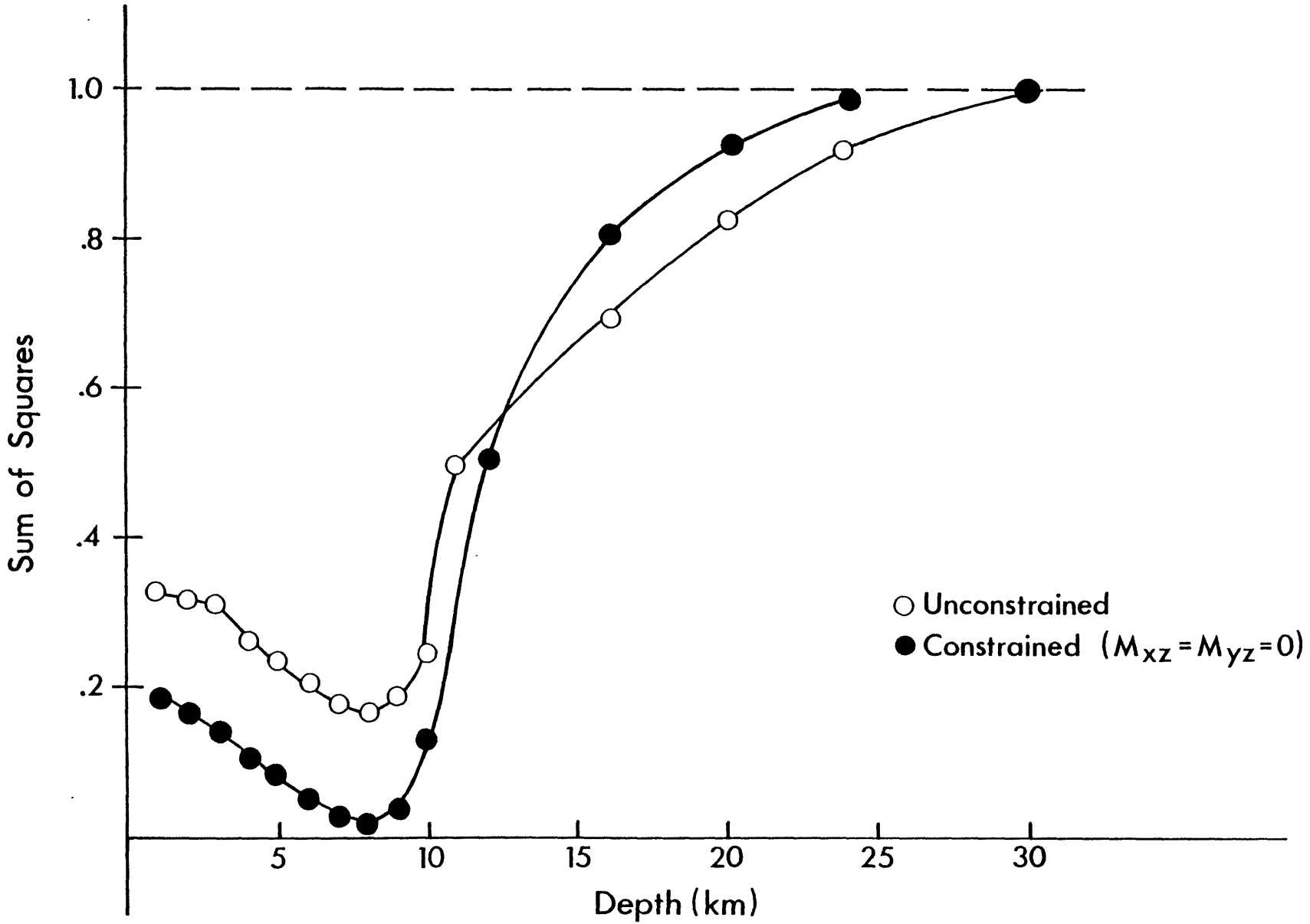
1.0
.8
.6
.4
.2
Sum of Squares
5
10
15
20
25
30
Depth (km)
Unconstrained
Constrained ($M_{xz} = M_{yz} = 0$)

Figure 2

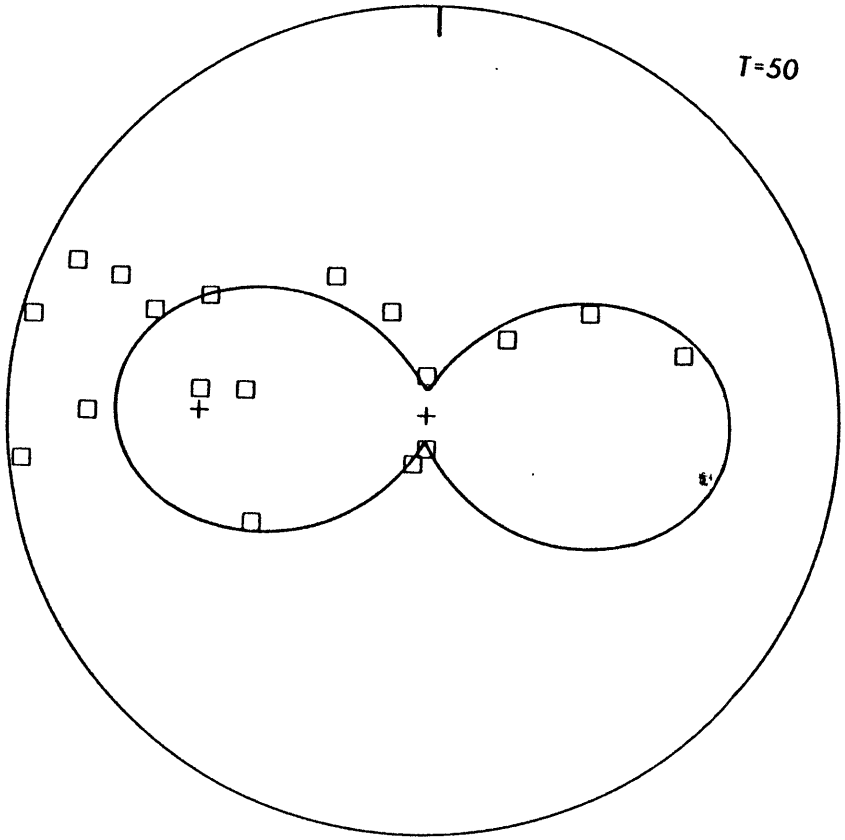

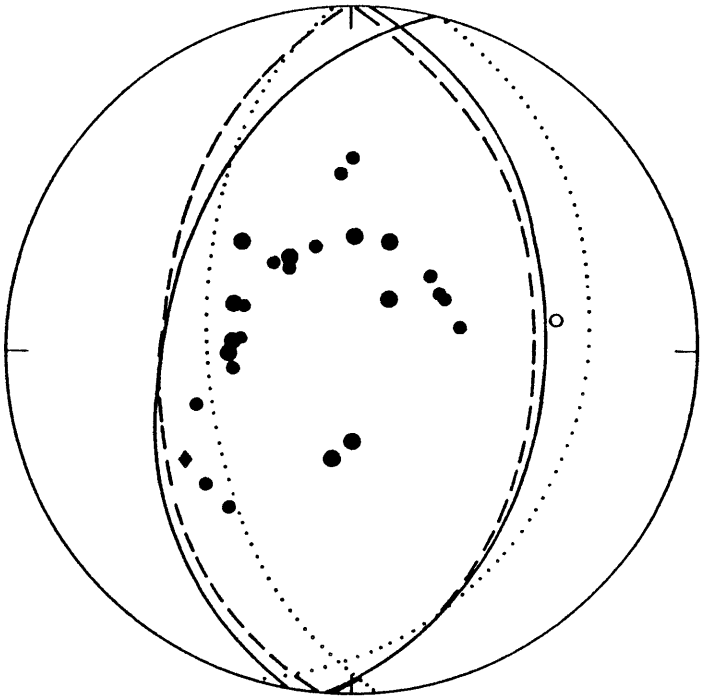

——— UNCONSTRAINED MOMENT TENSOR INVERSION

– – – – – CONSTRAINED MOMENT TENSOR INVERSION ($M_{XY}=M_{YZ}=0$)

····· BODY WAVE INVERSION (NABELECK ET AL, 1982)

Figure 3

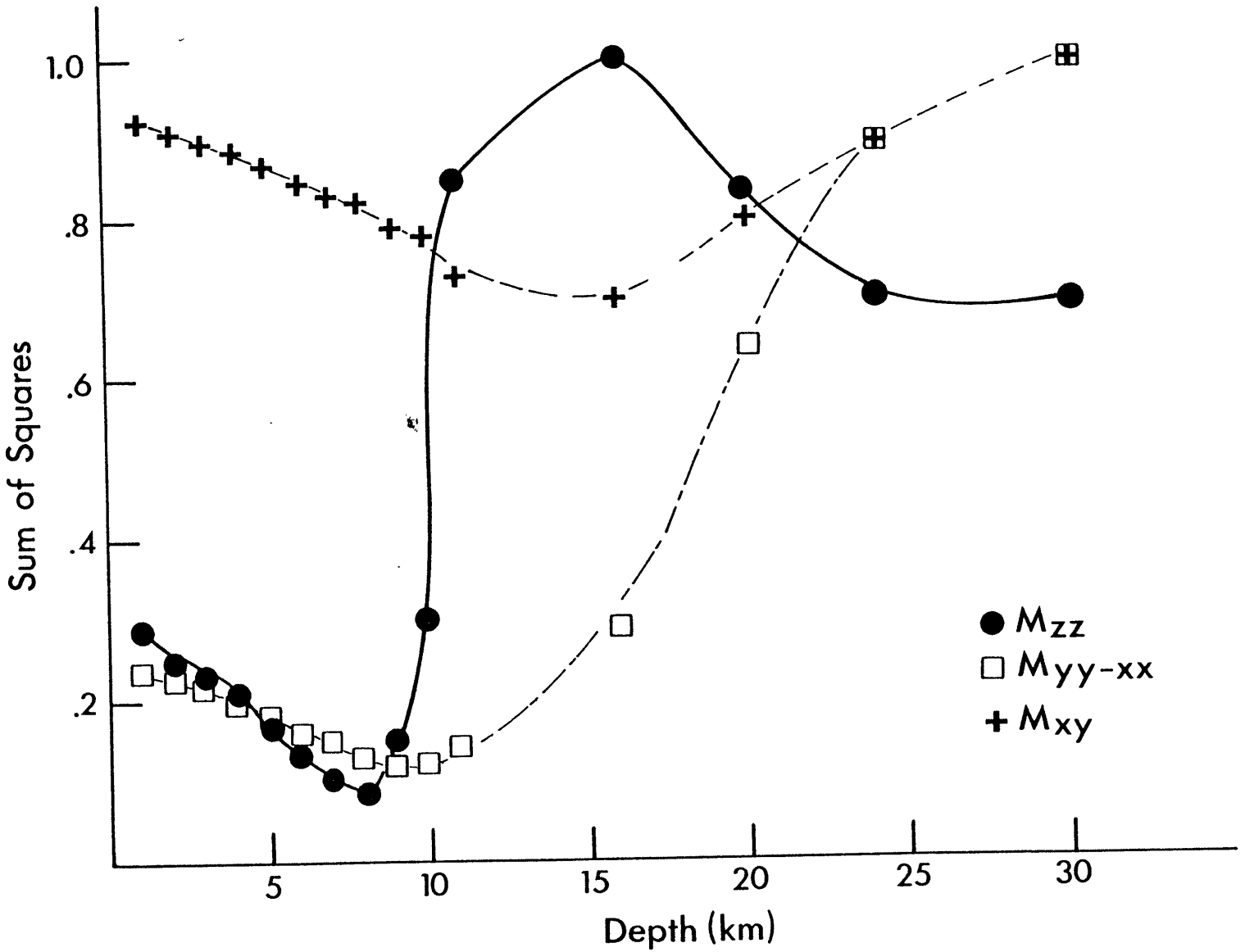

Figure 4

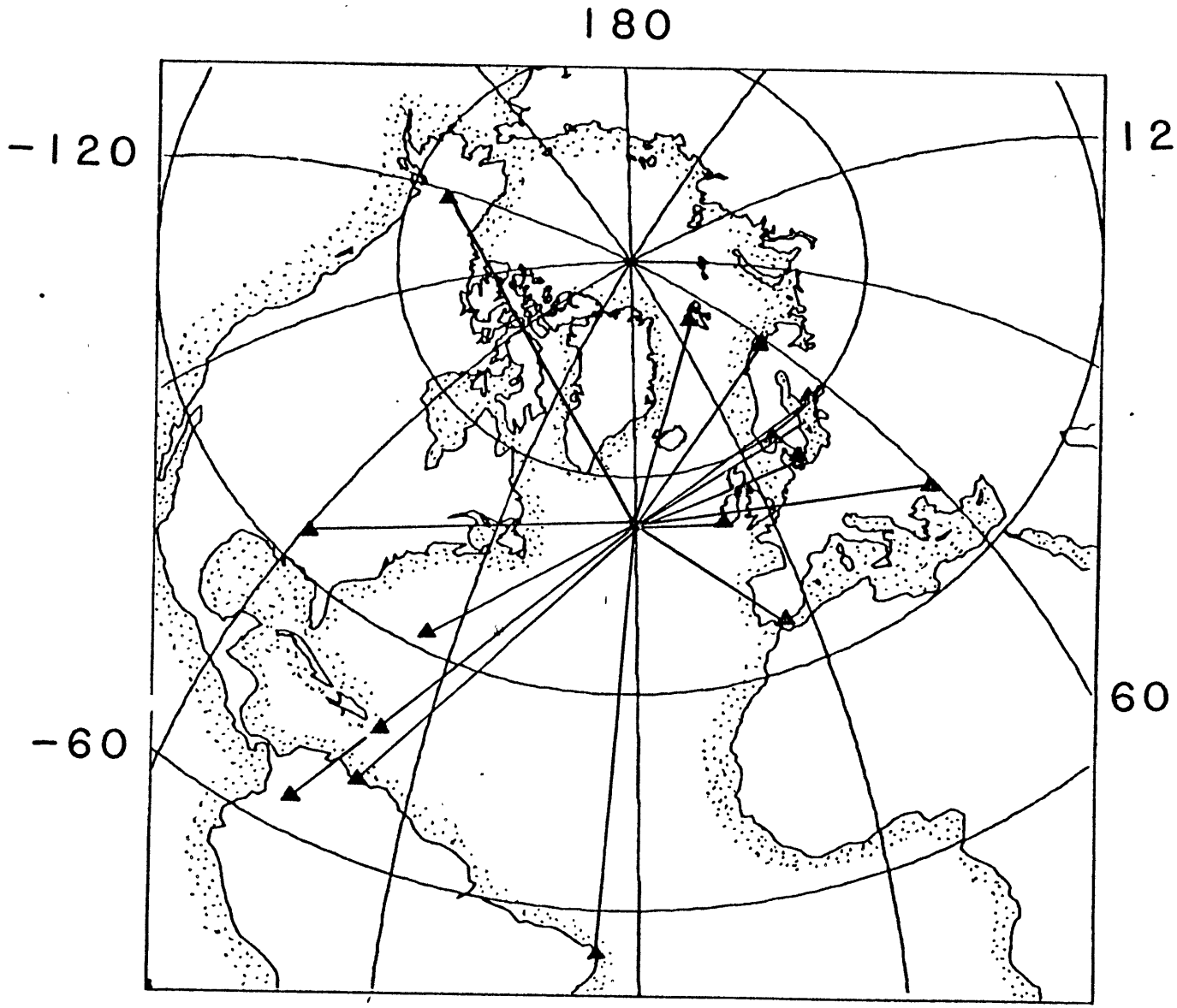

Earthquake in the Gibbs Transform Fault

Nov 16,1974 Mb 4.9

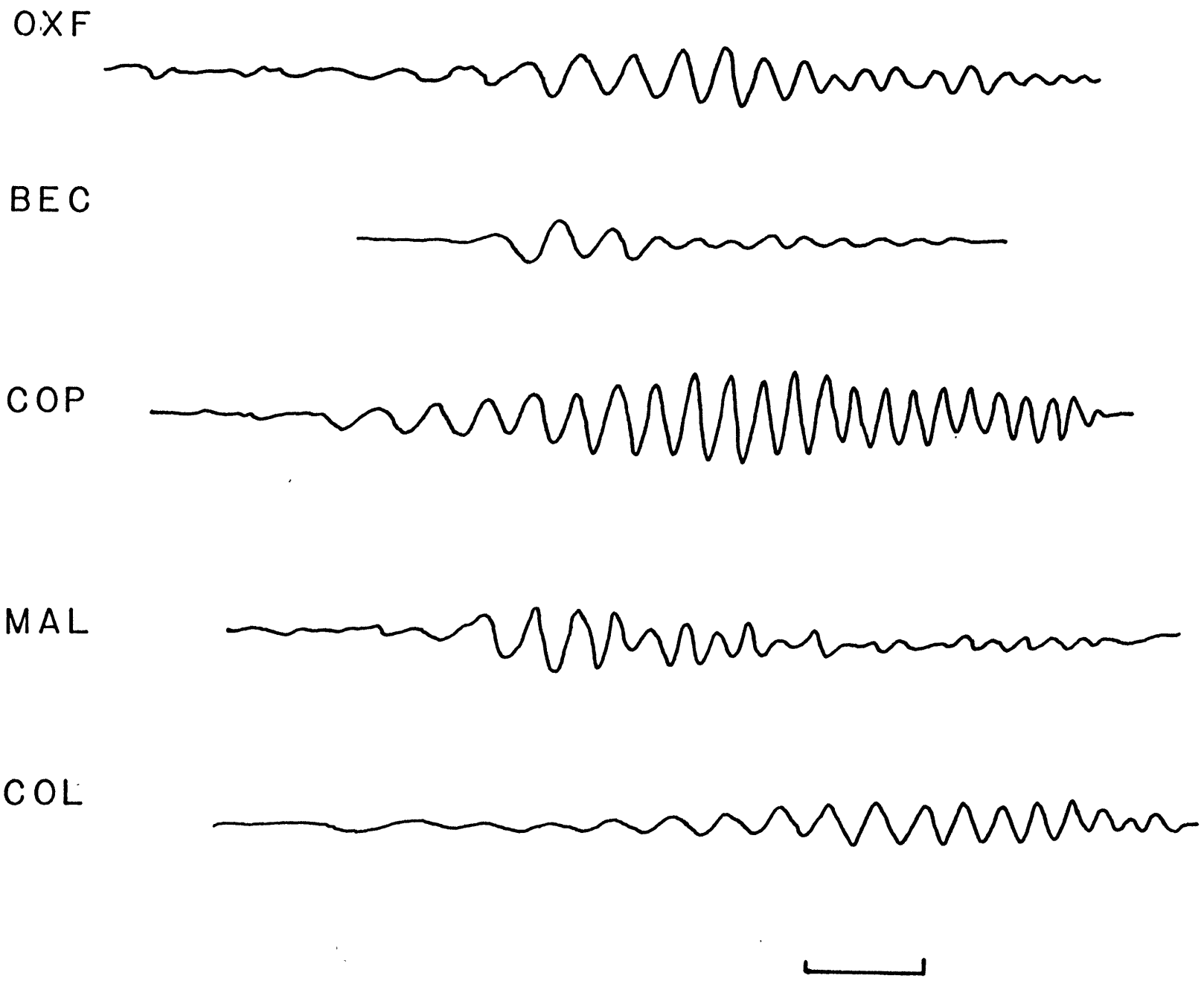

Figure 6

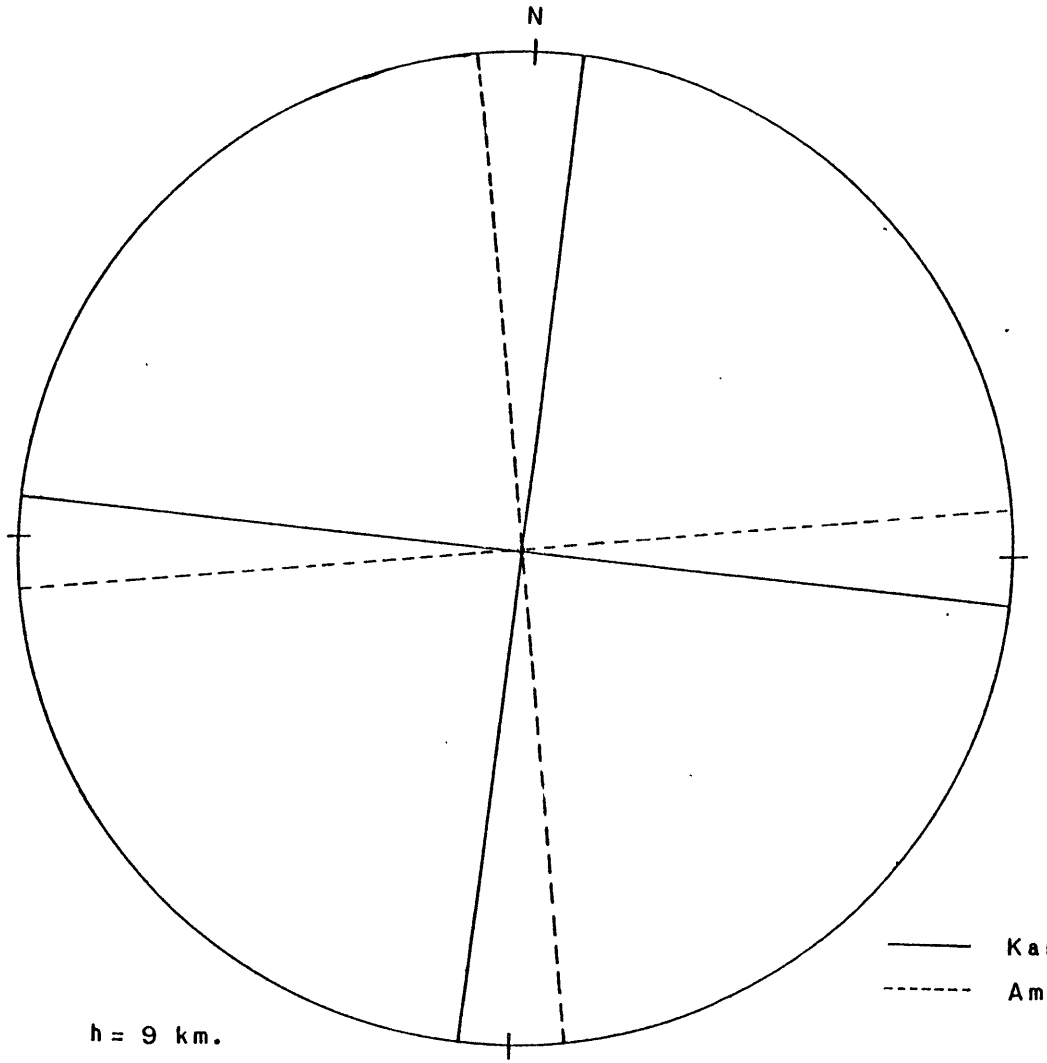

(a)

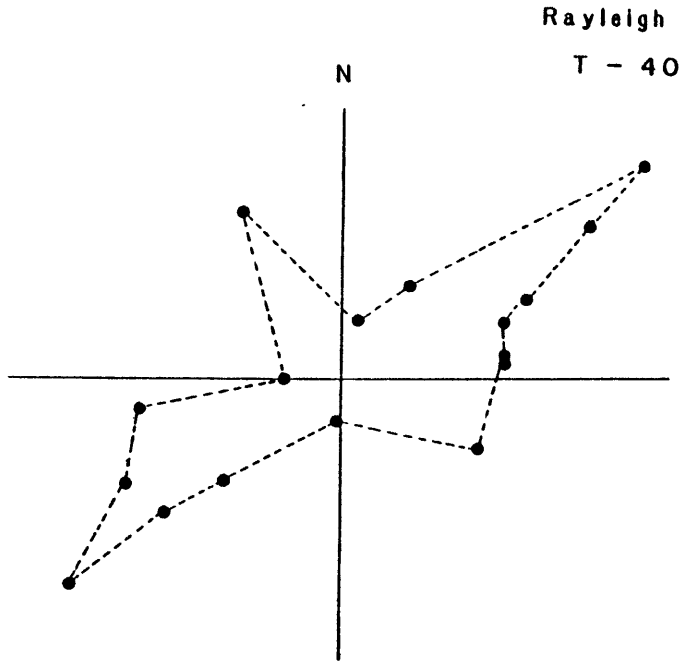

(b)

Kanamori and Stewart (1976)

Amplitude Inversion

Figure 7

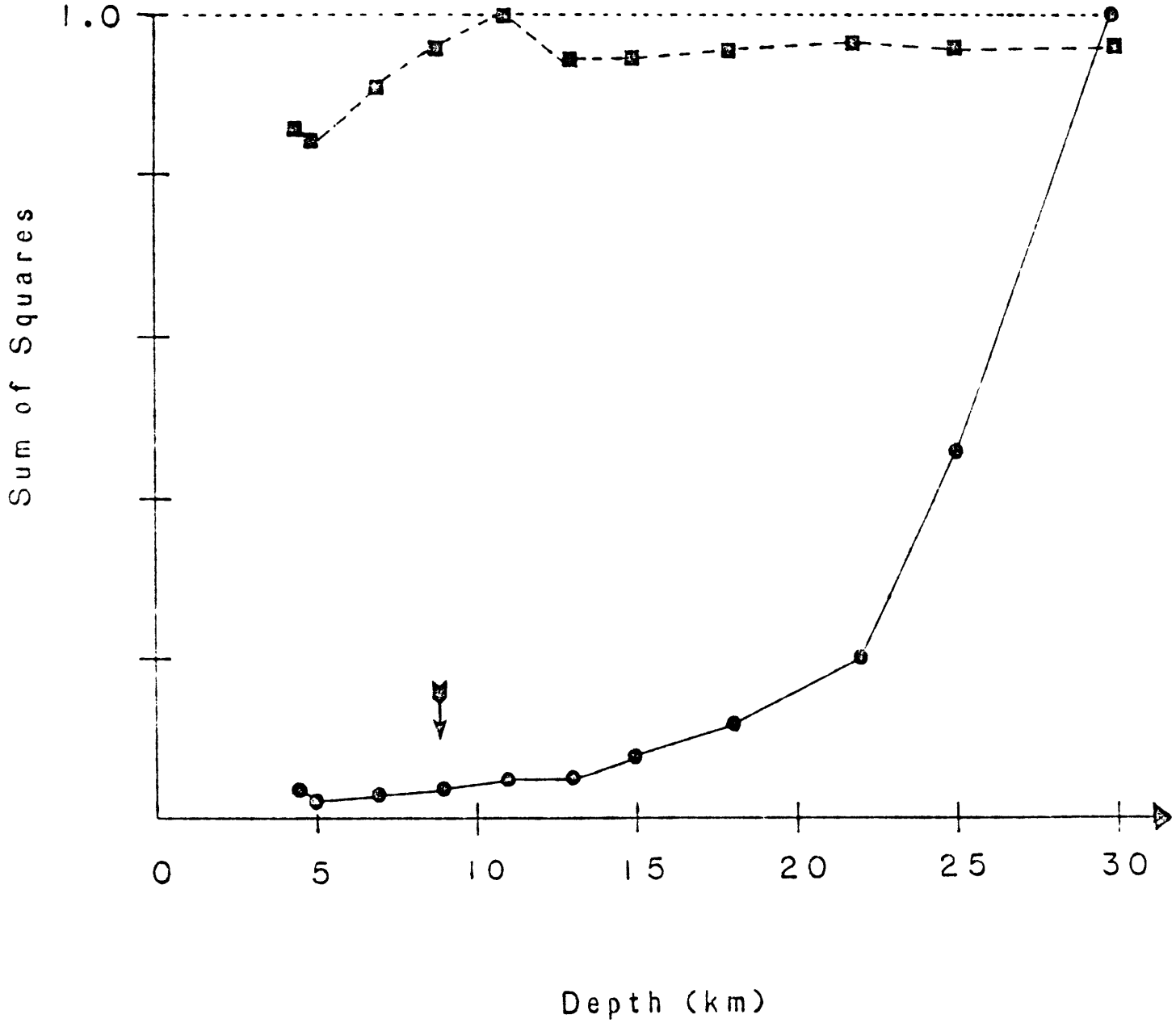
Earthquake in the Gibbs Transform Fault
1.0
Sum of Squares
0
5
10
15
20
25
30
Depth (km)

Figure 8

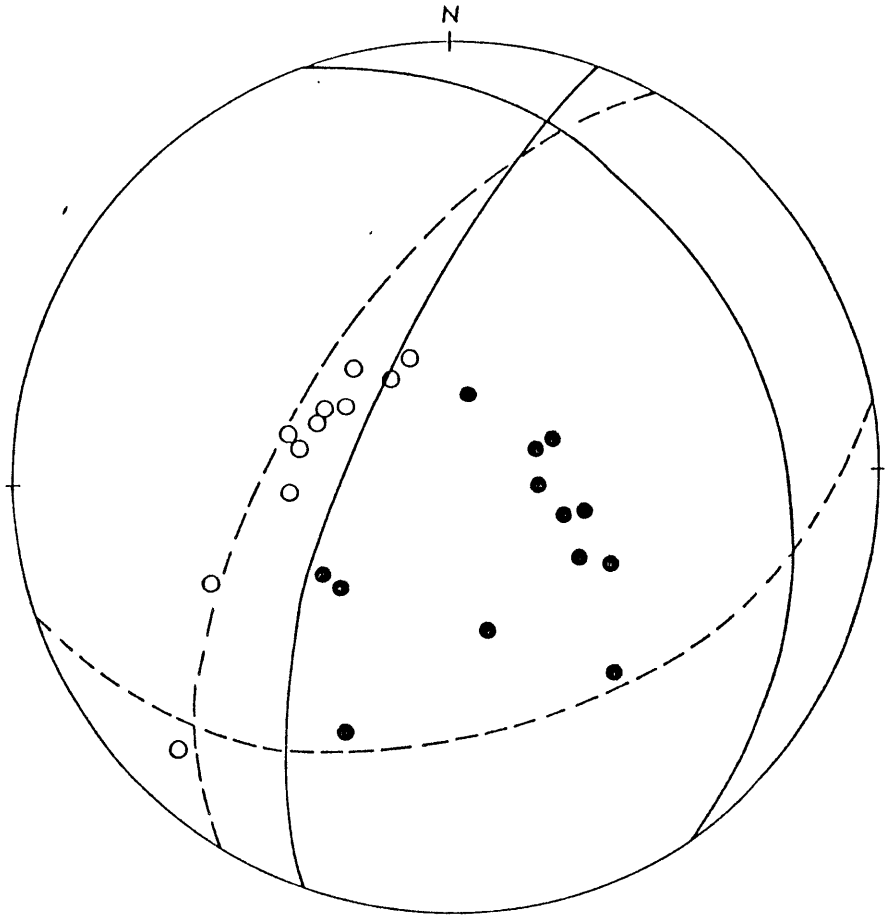

(a)

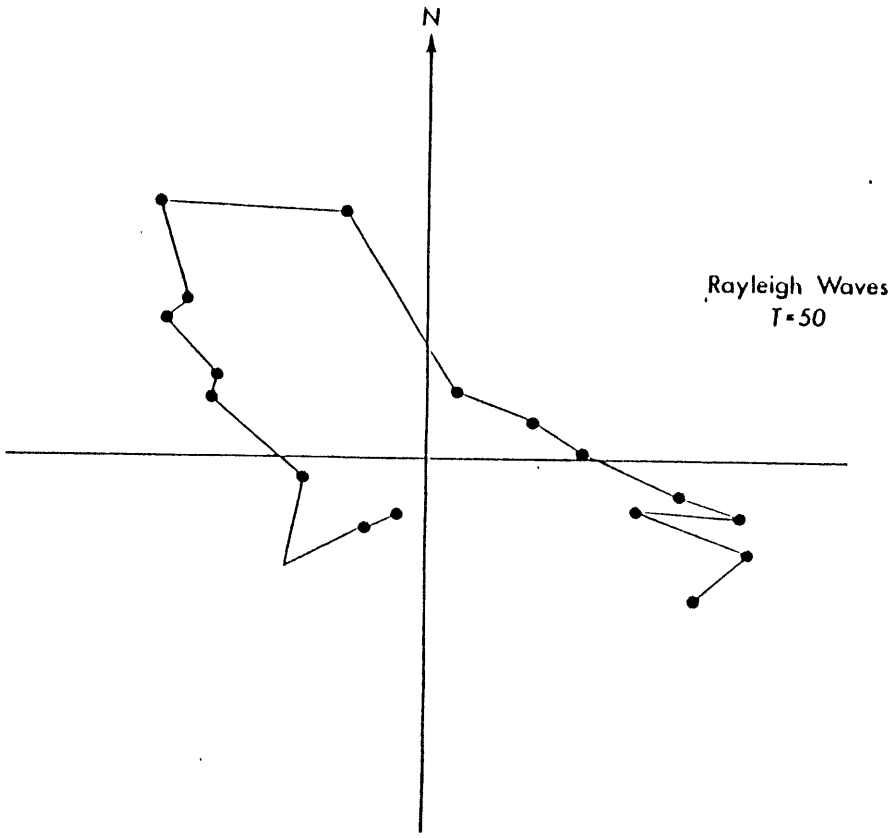

(b)

Figure 9

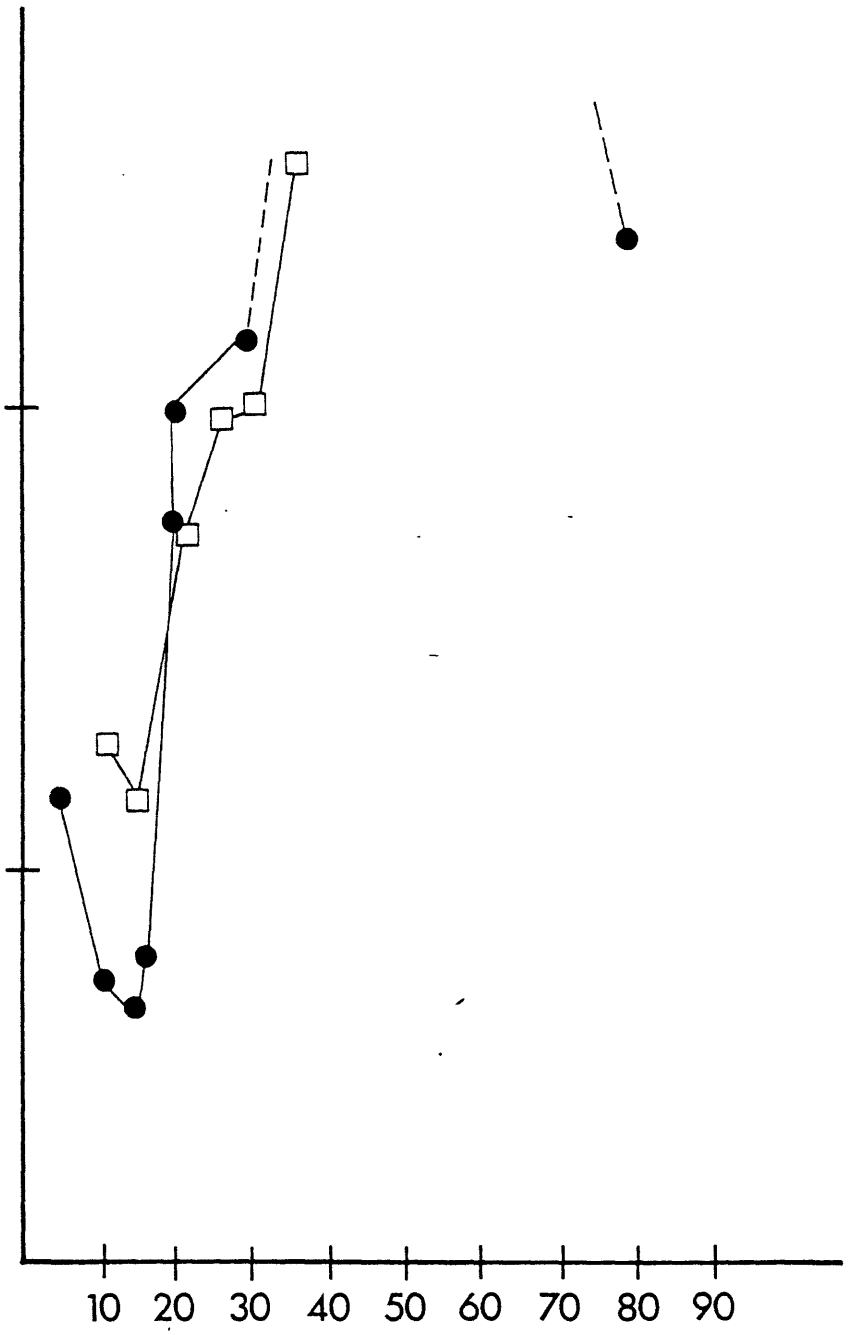

Figure 10

Chapter 5

Introduction

Linear moment tensor inversion in the period range of 90 to 20 sec has been succesfully applied to retrieve the source parameters and focal depths of earthquakes in Central Asia (Patton, 1978, 1980; Romanowicz, 1981), the north Atlantic (Trehu et al, 1981), and the Java trench (Fitch et al, 1981). Our objective in this paper is to implement this technique for earthquakes in the Central Andes. One of our original intentions in this study was to use the linear moment-tensor inversion method to retrieve the focal depth and source mechanism of a number of relatively small events (between 4.8 and 5.5 m_b) that occur in the northern Altiplano, where normal faulting has been observed on Quaternary sediments (e.g. Lavenu, 1979). This proved to be difficult, however, because none of these events were not recorded at a large enough number of stations around the world due to the long epicentral distances.

For earthquakes in this area the azimuthal coverage of WWSSN stations is good but the paths from the source to the station are considerably longer than those used in the studies mentioned before. We have studied seven earthquakes

occurring within the crust of the central Andes, for which the focal depth and fault-plane solution have been constrained comparing the observed body-wave signals with theoretical waveforms (Chapter 2). This will permit us to judge the accuracy of the results of the moment tensor inversion.

A reference-point method, as described by Patton (1980), is implemented using a cluster of events to obtain accurate phase velocities to stations around the world. We explore the possibility of applying the inversion routinely, by investigating how far one can select events away from this reference point and still be able to invert succesfully for the moment tensor and focal depth, using the same phase velocity measurements. Here, we will judge the goodness of fit of the moment tensor and depth estimates by their agreement with the results of the body-wave analysis.

Method

The linear inversion of the moment tensor from the complex spectra of vertical-component Rayleigh waves has been discussed extensively in the literature (McCowan, 1976; Mendiguren, 1977; Aki and Patton, 1978, Patton, 1978). In this paper we use a modification of the linear moment tensor inversion method proposed by Romanowicz

(1982a), which significantly improves the resolution of the focal depth and the source mechanism. The algorithm is essentially the same as the one used to invert the moment tensor using only the amplitude spectra of Rayleigh waves that was presented in Chapter 4.

As shown in Chapter 4, we proceed with the inversion in two steps. First, the real and imaginary part of the spectra corrected for inelastic attenuation and the dispersion of surface waves, are considered a continous function in azimuth and expressed only as a function of azimuth, &th., and five constants A_k, B_k, C_k, D_k, E_k, at frequency ω_k (Equations 1 through 5 in Chapter 4). In the case of the linear moment tensor inversion, however, since we recover both the phase and amplitude spectra, the real and imaginary parts of the spectrum can be separated. Therefore, the constants $A_k, B_k, \ldots E_k$ are determined at every frequency sampled by simply solving the two systems of linear equations shown in Equation 4.4. Once these constants are determined, Equations 4.5 are used to solve for the moment tensor components at various trial depths. The least square residuals obtained for these different trial depths in Equations 4.5 are plotted as a function of depth and the minimum in this curve is interpreted as the best estimate of focal depth. The P, B, and T axes of the fault plane solution correspond to the eigenvectors of the diagonalized moment tensor (Mendiguren, 1977). As dis-

cussed by Mendiguren (1977) the success of this method hinges on our ability to define a clear and significant minimum in the residuals-versus-depth curve.

Romanowicz (1982b) has shown convincingly that this method is more robust than inverting directly for the moment tensor elements from Equation 4.3. Using this two-step procedure, it is possible to eliminate most of the errors and biases in the data that are not 1 periodic in azimuth from the source. These errors and biases introduced by using inexact propagation corrections, as well as by errors in the location and origin time of the event, are not coupled with the source parameters and depth in the inversion, and tend to flatten the residual curve.

Data Analysis

Earthquakes Studied

We have selected seven crustal earthquakes with body-wave magnitudes of between 5.7 and 6.1 that occurred in the Andes within the South American plate (Figure 1). The fault-plane solution and focal depth of the earthquakes used in the study have been constrained using body-wave modelling in Chapter 2. This will help provide an independent test on the accuracy of the focal depth and source

mechanism obtained using the linear moment tensor inversion. The seven events selected are those which showed good quality long-period data on vertical component seismograms on WWSSN stations distributed around the epicenter (Figure 2). The epicentral data of these events is shown in Table 1.

Signal Analysis

The main Rayleigh wave train was identified in the seismogram and digitized on a table-top digitizer over a time window corresponding to a group velocity of between 4.2 and 2.2 km/sec, at evenly spaced intervals of about one second. The digitized time series were plotted and compared with the original seismograms to detect any errors in the digitization procedure. The time series were then detrended and fourier transformed, and the instrument response removed using the instrumental constants supplied by a particular station (Hagiwara, 1958). To eliminate background noise present at the station and signal-generated noise such as body-wave interference, multipathing, and scattering, the time series were filtered using a time-variable filter (Landisman et al, 1969). This is a two-step procedure that requires, first, the determination of group velocity. Group velocities were obtained using a moving-window analysis that yields the energy contained in a windowed portion of the seismogram on a

velocity-versus-period plot. The group velocity of the fundamental-mode Rayleigh wave is identified by contouring the region where the maximum energy arrives. Figure 3 shows energy plots and contoured group velocities for various seismograms. The second step consists of applying a band-pass time-variable filter to the time series that passes only wave packets arriving at the group velocity of the fundamental-mode Rayleigh waves. This filtering allows us to eliminate noise of the same frequency band as the seismic signal of interest, without distorting the original time series (Figure 4). The time-variable filter has the effect of smoothing both the amplitude and phase spectra, without introducing phase delays or distortions (Figure 5) (Weidner, 1972).

The Earth Model

The application of the moment tensor inversion requires the prescription of an earth model in the source region, to estimate the excitation functions. We have used the crustal velocity structure suggested by Ocola and Meyer (1973) for the Eastern Cordillera over a Gutenberg earth model. The thickness of the crust has never been directly measured in the sub-Andes. Based on phase-velocity measurement of surface waves, James (1971) suggests a crustal thickness of 70 km for the Altiplano. Since most of the earthquakes selected occur in the sub-Andes and the crust

probably thins to the east, we have used a mean crustal thickness of 50 km to calculate the excitation functions (Saito, 1967).

Initialization of the Propagation Corrections

The Reference Point Method

As discussed above, to apply the linear moment tensor inversion we need to know the propagation corrections very accurately. Aki and Patton (1978) showed that phase velocities must be known to within 0.5% to succesfully invert for the moment tensor and focal depth. Romanowicz (1982b) suggests that using the modified scheme described above, the accuracy with which we should know the phase velocity is relaxed, and shows that an event with well-constrained focal mechanism and depth can be succesfully used to obtain an initial estimate of phase velocities.

To initially establish the propagation corrections from a cluster of events in Central Asia, Patton (1978) used the double-event parameter search developed by Weidner and Aki (1973). This method, however, requires two events with different fault-plane solutions located close to one another, and is cumbersome and time-consuming. Here, we initialize the propagation corrections as follows: First, we use the

non-linear moment tensor scheme described in Chapter 4 to obtain the source mechanism and focal depth of event 1. This event was selected because it is very well recorded in most of the stations of interest around the epicenter. Furthermore, this event produced a surface rupture (Philip and Megard, 1975; Chapters 2 and 3) which will help in judging the results of the non-linear inversion method. If the results of the non-linear inversion are compatible with the body-wave study and the geological information, we can safely assume that the surface wave data is of sufficient quality to obtain a first estimate of the propagation parameters. Then, following the reference-point technique developed by Patton (1978, 1980), we refine the estimation of phase velocity and attenuation by inverting for the depth and moment tensor of other events that occur closeby. Once the source parameters of these new events are obtained, these earthquakes are added to the reference point and the propagation correction is updated and improved using the maximum-likelihood estimator developed by Pisarenko (1970).

We can visualize this method by considering that the earth acts as a linear operator, $re^{i\theta}$, to the propagation of surface waves. The input signal to this system is the source spectrum and the seismogram represents the output. The amplitude and phase response of the system, namely the effect of attenuation and phase velocity along the path,

can be obtained by taking the spectral ratio of the output spectrum to that of the input. Earthquakes located in a tight cluster and registered at the same seismographic station represent independent inputs to a common "earth operator" or transfer function (Figure 6). Assuming that the noise at both the source and the station obeys Gaussian distributions independent from each other, the method developed by Pisarenko (1970) yields the maximum likelihood estimation of the transfer function $\hat{r}e^{i\hat{\theta}}$, given n independent observations. Here, we treat, earthquakes 1,2, and 3, occurring in a tight cluster in central Peru as the events forming the reference point.

Results of the Amplitude Inversion

The moment-tensor inversion of the amplitude spectrum of event 1 was performed sampling a set of eight periods between 80 and 30 sec. The results of the non-linear moment-tensor inversion for event 1 show good agreement with the results of the body-wave modelling (Figure 7). The normalized residuals shown in Figure 7 show a minimum centered at about 8 km, in good agreement with a focal depth of 5 km obtained in Chapter 2 from body wave modelling. The residuals increase rapidly away from the minimum and after a depth of around 50 km, they decrease slowly forming a broad minimum in a shape that is characteristic of shallow events (Patton, 1978; Romanowicz, 1980). The strike of

the resulting source mechanism agrees to within 15° with the results of the body wave data. However, the orientation of the east-dipping fault plane is not well constrained and violates a few of the first motion data. The resulting source mechanism agrees with the general orientation and direction of slip determined from the body-waves.

These results confirm that the Rayleigh-wave data collected for this event may be used to make an initial estimate of the propagation parameters. To estimate the phase velocities we use a single-event technique (e.g. Aki and Richards, 1980) taking the spectral ratios between the observed spectra and the theoretical source spectra. In this case, the theoretical source spectra was calculated using the fault parameters determined from the body-wave study.

Adding new events to the reference point

Event 2 This earthquake occurred a couple of months before event 1. The fault-plane solutions of these two events are virtually identical and body wave modelling suggests they occur at practically the same depth. Not surprisingly, the Rayleigh wave trains of these two earthquakes are very similar. Using the phase velocities calculated from event 1 and a set of periods spanning the range between 70 and 26

seconds, we applied the linear inversion method to obtain the moment tensor and focal depth. The results show a sharp minimum centered at a depth of 8 km and the resulting source mechanism agrees with the first motion data to within 20° in strike. (Figure 8).

To refine the phase velocities measured from the reference point, the theoretical source spectrum for the mechanism obtained in the inversion of event 2 is combined with that of event 1.

Event 3 This earthquake is located about 50 kilometers east of events 1 and 2 (Figure 1). The phase velocities obtained from the stacking of events 1 and 2 were used to correct the observed spectra of event 3 for propagation. The inversion was then applied using a period range of between 80 and 30 seconds. Figure 9 shows the residual versus depth curve and the resulting source mechanisms compared to first motion data. The minimum occurs at a depth of 15 km which is somewhat shallower than the depth of 18 km obtained in Chapter 2. This difference in focal depth, however, certainly falls within the errors of both methods. The resulting source mechanism shows thrust faulting with a component of right-lateral strike-slip motion also in agreement with the body wave data.

As in the case of event 2, the theoretical spectra for the resulting source mechanism are calculated and stacked

with those of events 1 and 2 to improve the estimates of phase velocity using the method proposed by Pisarenko (1970).

In our experience, Pisarenko's formulation works well down to periods of about 30 sec. As discussed by Patton (1978), the method does not work as well at shorter periods, probably because the statistical model used in deriving Pisarenko's formulas assume an additive Gaussian noise distribution. For short periods (less than about 30 or 40 sec) the prevalent noise in the signal is due to scattering and interference which are signal generated and cannot be modeled by a superposed ambient Gaussian noise. In these cases, we use a simple phase averaging scheme to obtain a mean phase delay. The phase velocities resulting by stacking the data of events 1,2, and 3 are shown in Appendix 2 grouped by the geographic location of the station.

Inversion of Events Away from the Reference Point

Events 4 and 5

These two earthquakes occur within 300 km of the reference point. For event 4 the residual-versus-depth curve shows a clear minimum centered at a depth of 6 km, and the

resulting source mechanism indicates pure-strike slip motion consistent with the fault-plane solution (Figure 10). The residual curve for event 5 shows a broad minimum from about 20 to 40 km centered at a depth of 32 km (Figure 11). The depth resolution for this deeper event is not as good as for the shallower earthquakes. However, the source mechanism obtained from the moment tensor inversion shows a pure dip-slip mechanism that agrees to within 5° in strike with the one obtained from the first motion data (Figure 11). This is probably due to the excellent azimuthal coverage available for this earthquake. The radiation pattern of event 5 clearly shows a two-lobed pattern with nodes to the north and south (Figure 12).

Event 6

This earthquake is located about 700 km northwest of the reference point. It is the deepest crustal earthquake obtained in Chapter 2. The inversion shows a residual-versus-depth curve with a broad minimum from 30 to 50 km. (Figure 13), and as in the case of event 5 the depth resolution lies probably within ± 8 km. The mid-point of that broad minimum, however, is centered around a focal depth of 40 km that agrees with the focal depth determined on the basis of body-wave modelling. The source mechanism at a depth of 40 km (Figure 13) shows a thrust mechanism with a component of strike-slip motion that violates some

of the first motion data. The type of faulting mechanism and the general orientation of the P axes, however, are consistent with the fault-plane solution.

Event 7

Event 7 occurred in central Ecuador on October 6, 1976 and is located about 1400 km nortwest of the reference point. The moment tensor inversion was performed using a period range of between 66 and 30 sec. In this case, the residual curve does not show a clear and well defined minimum. The depth inferred from the residual reduction is about 12 km and roughly agrees with the focal depth of 16 km inferred from the body-wave modelling study (Figure 14). The residual reduction, however, is marginal and probably indicates that we are reaching the limit of applicability of the phase velocities obtained from the reference point. The source mechanism obtained is still compatible with the first motion data inasmuch the type of thrusting mechanism and crude orientation of the fault plane solution is retrieved. The dip of the nodal planes, however, differs by about 40° from those determined using first motion data.

Figure 15 shows a comparison between the phase velocity from the reference point to station WES, in the eastern United States, and the phase velocity computed using the source parameters of event 7 determined from the body-wave modelling study. The differences between these two curves

are as large as 2% even for the long periods, and this innacurate propagation correction is reflected in a poor residual reduction.

In summary, the maximum distance away from the vicinity of a well established reference point from which the same phase velocities can be used appears to be not more than about 800 km in the Andes. For events at distances less than about 800 km, the moment-tensor inversion yields source mechanisms for which the nodal planes agree with those obtained using body-wave modelling to within 20°, and focal depths to ± 8 km As shown by Romanowicz (1981) the minimum in residual-versus-depth curves become less sharp as one moves away from a well established reference point and the phase velocity corrections become more and more imprecise.

A prevalent feature in our results as well as those of Romanowicz (1981) is the lack of resolution of the moment tensor inversion method to constrain small strike-slip components in dip-slip mechanisms. This is probably due to the fact that the small lobes in the radiation pattern associated with them are either buried or exagerated by the noise.

Phase Velocity Measurements

The phase velocities determined in this study show relatively small variations for stations located in the same geographical area (Appendix 2). This is in contrast with the results of Patton (1978), who shows that large variations in phase velocity exist even for stations located in the same general area. Figure 16 compares the phase velocities determined from Patton's reference point and those obtained in this study for stations located in the Iberian Peninsula and the British Isles. Patton's phase velocities show variations of up to 0.1 km/sec among them. Even though the paths from the reference point developed in this study are longer, differences among the measurements for different stations in this area are comparable. This is clearly due to the fact that the paths from South American events travel through the Brazilian Shield and the North Atlantic region which are much more homogeneous than the Eurasian continent.

Most of the wave-paths to stations outside South America and the Caribbean region have a substantial fraction of the total path length in oceanic terranes. This may explain our success in retrieving the source mechanism and focal depth of earthquakes in South America by using the moment tensor inversion, even though the average path length is about 35% longer than those from Central Asian earthquakes (Patton,

1978; Romanowicz, 1981). In fact, in the period range of 40 to 100 seconds phase velocities measured from the reference point to any station outside South America vary less than 3.0% among them (Figure 17).

These small changes in phase velocity for various paths clearly reflect the well known lateral homogeneity of the oceanic crust and upper mantle (Forsyth, 1975). More interestingly, however, they also show that the cratonic South American shield should also be very homogeneous since the paths to eastern North America, Europe, and Africa have long portions of the paths over different parts of the shield (Figure 2). This lateral homogeneity of the Brazilian shield is clearly shown by the only two pure-path phase velocity measurements in the South American craton. Up to a period of 60 sec, the phase velocities to station NAT in northeastern Brazil, and to station TRN in Trinidad are virtually identical (Figure 18). We were not able to determine the phase velocity for periods longer than 70 sec in the Brazilian shield. The phase velocity measurements obtained for the Brazilian shield are very similar to those of the Canadian (Brune and Dorman, 1963) and the Indian shield (Patton, 1978), except at periods less than about 40 sec long, for which the velocity across the Brazilian Shield is lower than that of the Indian and the Canadian shields (Figure 19). The smaller phase velocity at shorter periods in the Brazilian shield could be interpreted as a

result of a slightly thicker crust in the Brazilian shield than in the Indian and Canadian shields. To our knowledge, the measurements presented here are the only pure-path published phase velocities in the Brazilian shield.

Due to the sparse coverage of WWSSN stations in the Andes and to the contorted shape of the South American coastline we were not able to obtain pure-path phase velocities with trajectories wholly within the Andes. The mixed path to station LPA in Argentina (RFP-LPA in Figure 20) crosses the Andes of central Peru, the Altiplano, and a portion of the Argentinian lowlands. The phase velocity measured along this path, however, is very similar to the phase velocity determined by James (1971) for the eastern part of the Altiplano from the path LPB-CUS (Figure 21).

Summary

In order to test the feasibility of applying routinely the method of moment-tensor inversion in a particular area of the world, we developed accurate phase velocity measurements stacking data from a tight cluster of events in central Peru using the maximum-likelihood estimator developed by Pisarenko (1970). These phase velocities were then used to invert for the moment tensor and focal depth of other earthquakes in the central Andes, as far as about 1400 km

away from the reference point. The results in South America show that if the distances between the reference point and the earthquake of interest is less than about 800 km, the moment-tensor inversion yields results that agree to within 20° with the nodal planes determined using first motion data and long-period body-wave modelling. The estimated focal depths appear to be within ± 8 km to those obtained from body-wave studies, and the uncertainty increases with increasing depth. The one event studied that was located at a distance of about 1400 km from the reference event shows a marginal residual reduction for inversions at different trial depths, and the dip of the nodal planes of the resulting mechanism differs by over 30° with those determined from the first motion data.

TABLE I

LIST OF EARTHQUAKES STUDIED

Event	Date	Latitude	Longitude	Origin Time	Depth	Magnitude
1	Oct. 1, 1969	-11.75	-75.15	5^h 5' 50.0"	6	5.8
2	Jul.24, 1969	-11.84	-75.10	2^h 59' 20.9"	5	5.9
3	May 15, 1976	-11.62	-74.45	21^h 55' 55.0"	18	5.9
4	Oct.15, 1971	-14.20	-73.45	10^h 33' 46.3"	8	5.7
5	Feb.14, 1970	-9.84	-75.55	11^h 17' 16.4"	28	5.8
6	Mar.20, 1972	-6.79	-76.76	7^h 33' 48.7"	38	6.1
7	Oct. 6, 1976	-0.76	-78.75	9^h 12' 39.0"	16	5.7

Figure Captions

Figure 1. Map showing surface wave paths from the epicenter to the WWSSN stations (closed circles) used in the study.

Figure 2. Location of the earthquakes studied. The number beside the epicentral locations (stars) indicates the depth estimated from a body-wave modelling study. Dark areas indicate compressional first motions on these lower hemispheric projections of the fault-plane solutions obtained from the body-wave analysis.

Figure 3. Examples of energy arrival on a period versus velocity plot. Letters and numbers indicate the energy of a particular period, Z being the maximum and decreasing 2 db for every letter. Lines show contours of maximum-energy arrivals that indicate the group velocity of the fundamental Rayleigh-wave mode.

Figure 4. Examples of raw and filtered seismograms.

Figure 5. Comparison between the phase and amplitude spectra of a raw (solid line) and filtered (dashed line) seismogram.

Figure 6. a) Schematic representation ofa linear operator with n independent samples. b) Lowes' (1970) graphic representation of Pisarenko's estimator.

Figure 7. a) Fault plane solution of event 1. Closed circles indicate compressional first motion and open circles dilatational on a lower-hemispheric projection. Crosses represent nodal readings. Dashed line is the solution determined from a body-wave modelling study (Chapter 2), and the solid line is the solution obtained using the moment-tensor inversion. b) Residual-versus-depth curve resulting from the moment-tensor inversion at different trial depths. Arrow points to estimate of focal depth from the body-wave modelling study

Figure 8. Results for event number 2. Symbols as in Figure 7.

Figure 9. Results for event number 3. Symbols as in Figure 7.

Figure 10. Results for event number 4. Symbols as in Figure 7.

Figure 11. Results for event number 5. Symbols as in Figure 7.

Figure 12. Radiation pattern of the amplitude spectrum of event number 5 at a period of 76 sec.

Figure 13. Results for event number 6. Symbols as in Figure 7.

Figure 14. Results for event number 7. Symbols as in Figure 7.

Figure 15. Comparison of phase velocities to station WES, in the eastern United States. Open circles represent phase velocity measured from the reference point. Closed circles are the phase velocity measured from event 7 using the one-station method. The theoretical source spectrum for event 7 was calculated using the focal depth and fault-plane solution determined comparing observed and synthetic long-period body waves (Chapter 2).

Figure 16. Comparison of phase velocities measured to stations in the Iberian peninsula and British Isles from a) Patton's reference point (1980) and b) this study. Note similarity in paths from South America and large scatter for Eurasian paths.

Figure 17. Typical phase velocities measured from central Peru to stations in various geographical areas.

Figure 18. Phase velocity measurements on pure-paths accross the Brazilian shield to station NAT in Brazil, and TRN in Trinidad.

Figure 19. Phase velocity measured for the Brazilian shield compared to those of the Indian (Patton, 1978) and Canadian Shield (Brune and Dorman, 1963).

Figure 20. Surface wave paths across the central Andes. Line indicates the 3000 meter elevation contour.

Figure 21. Phase velocity measured from central Peru to station LPA in Argentina compared with phase velocities for other Andean paths (James, 1970) and a pure-path measurement in Tibet (Romanowicz, 1982b).

Figure 1

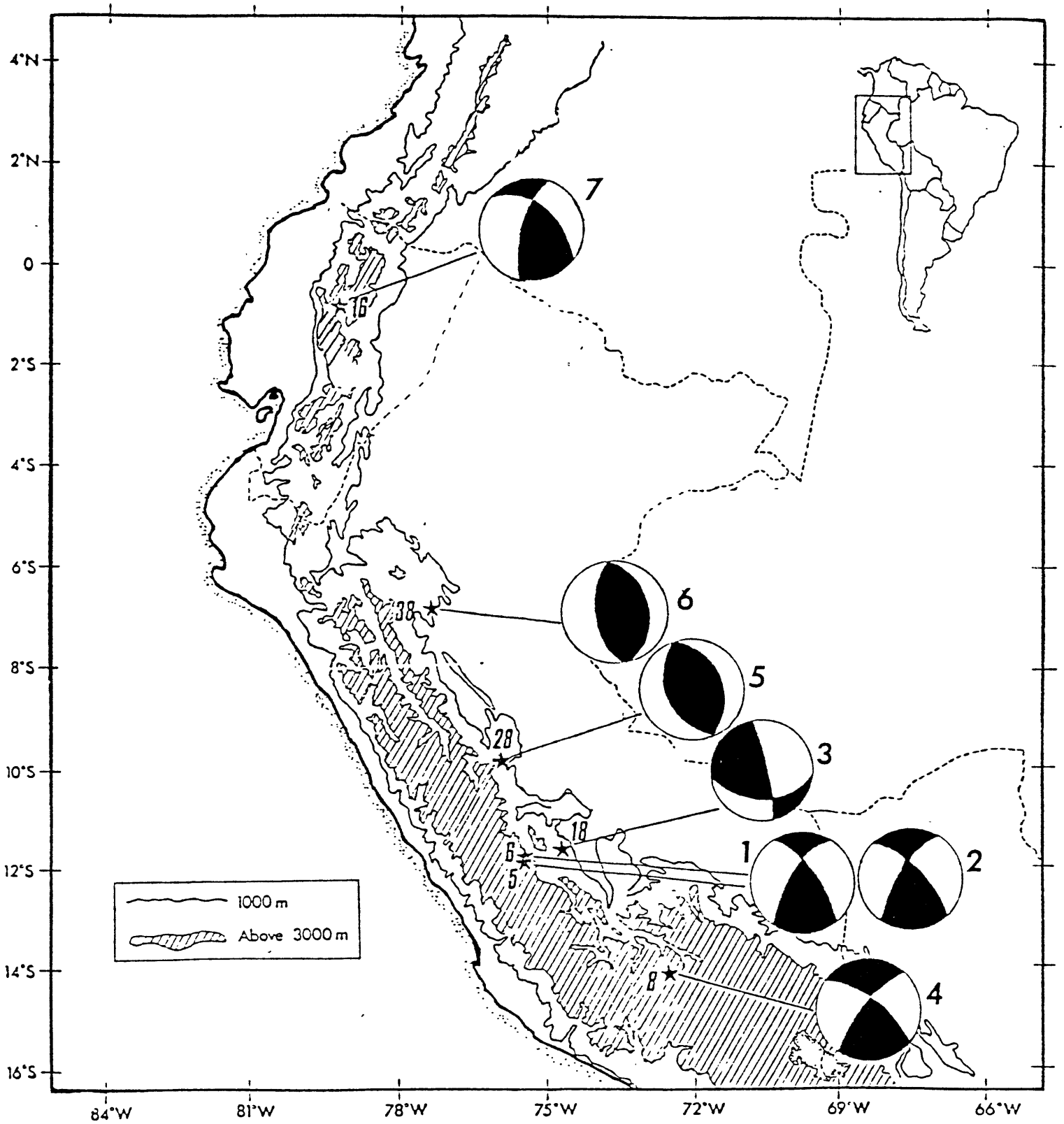
4°N
2°N
0
2°S
4°S
6°S
8°S
10°S
12°S
14°S
16°S
84°W
81°W
78°W
75°W
72°W
69°W
66°W
7
16
6
38
5
28
3
18
6
5
1
2
8
4
1000 m
Above 3000 m

Figure 2

Group Velocity km/sec
2.6
2.8
3.0
3.2
3.4
3.6
3.8
4.0
4.2
Period sec.
10.0
11.3
12.7
14.3
16.1
18.2
20.5
23.1
26.1
29.4
33.1
37.4
42.1
47.5
53.5
60.3
68.0
76.7
86.4
97.5
109.9
123.8
139.6
157.4
177.4
200.0
Period sec.
10.0
11.3
12.7
14.3
16.1
18.2
20.5
23.1
26.1
29.4
33.1
37.4
42.1
47.5
53.5
60.3
68.0
76.7
86.4
97.5
109.9
123.8
139.6
157.4
177.4

Figure 3

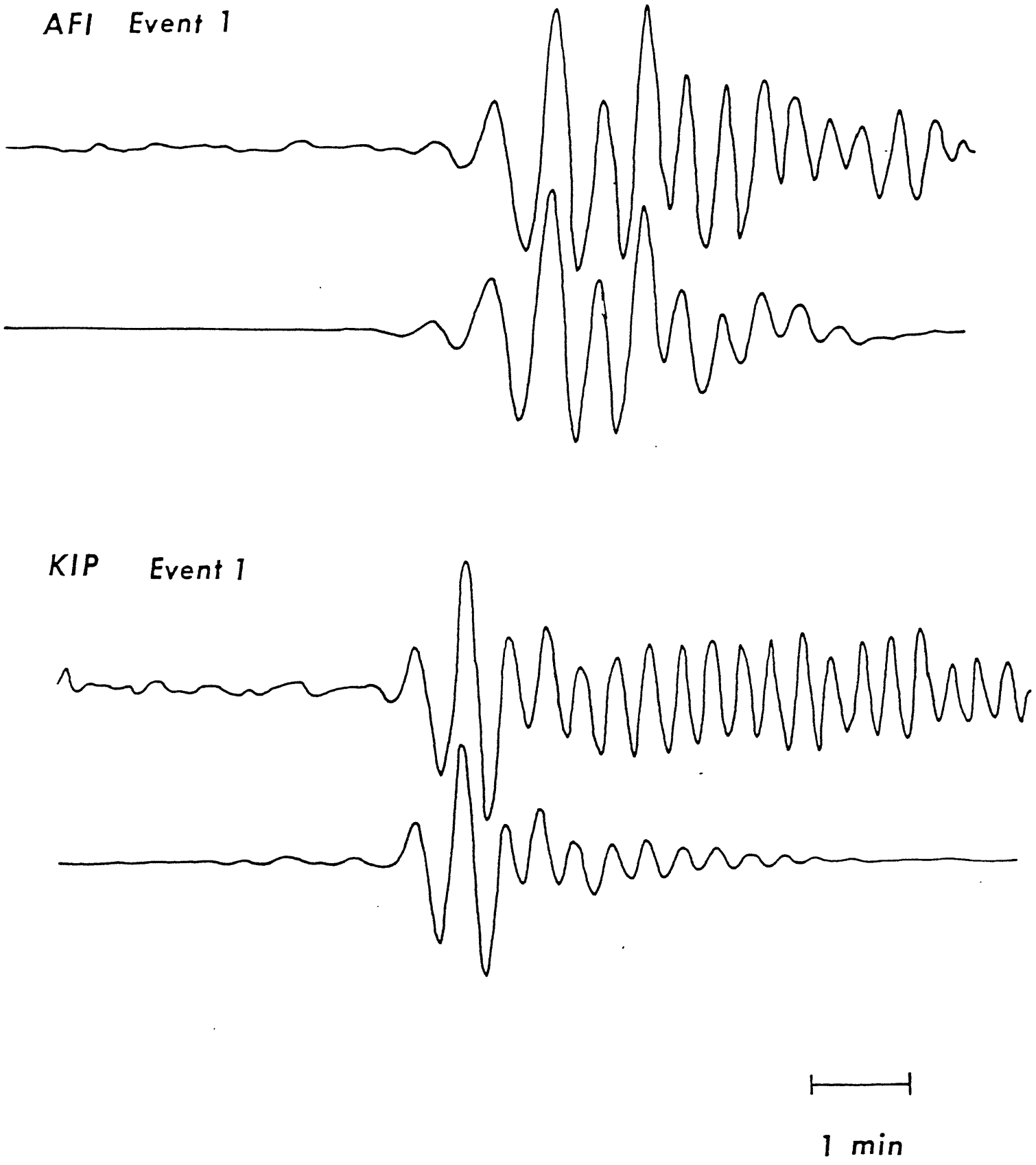

Figure 4

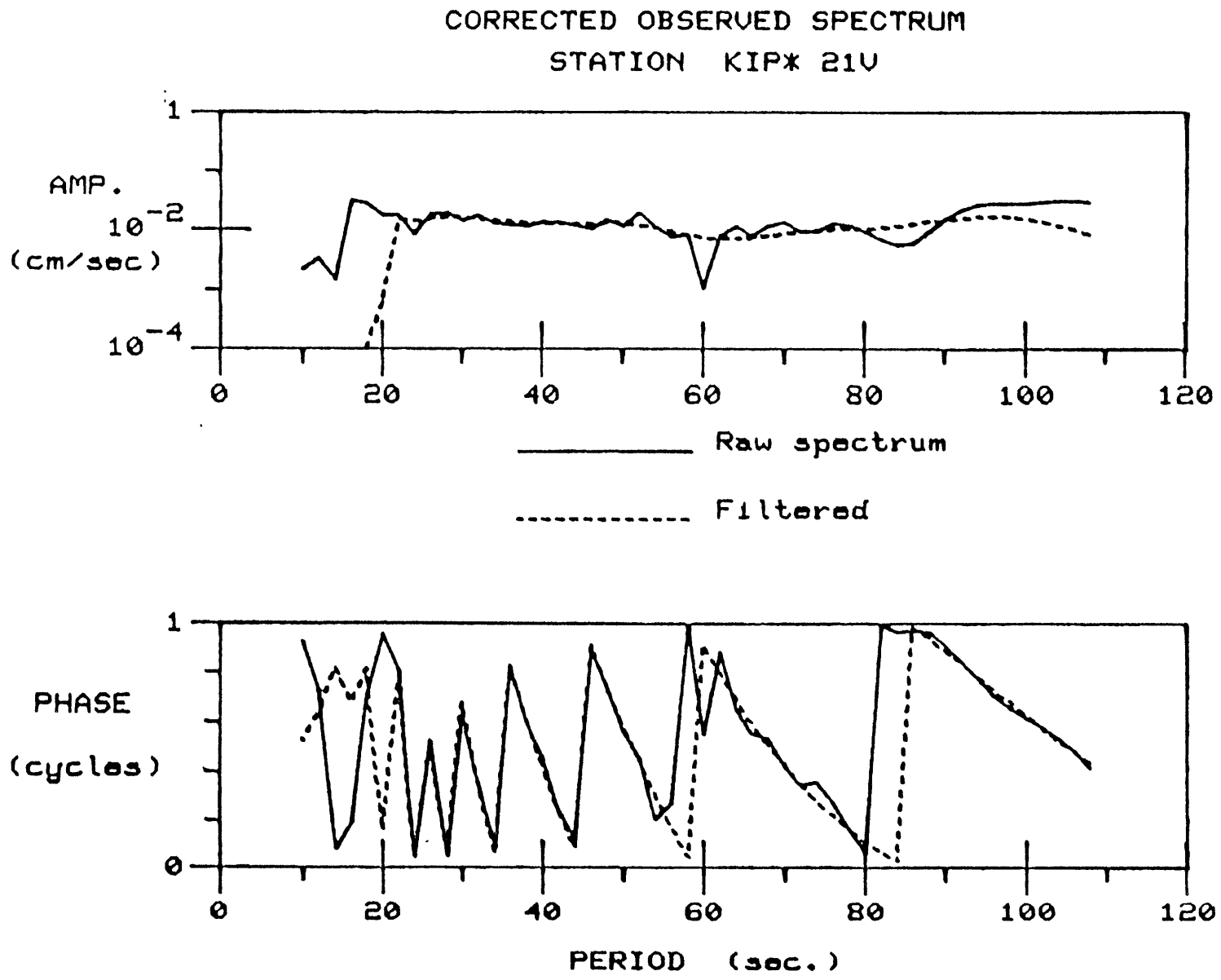
CORRECTED OBSERVED SPECTRUM
STATION KIP* 21V
AMP.
(cm/sec)
1
10^-2
10^-4
0
20
40
60
80
100
120
Raw spectrum
Filtered
PHASE
(cycles)
1
0
PERIOD (sec.)

Figure 5

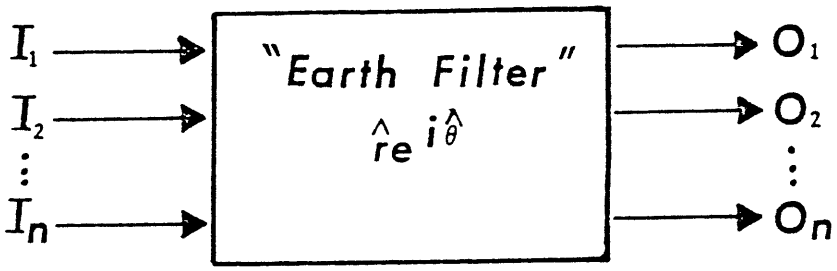

(a)

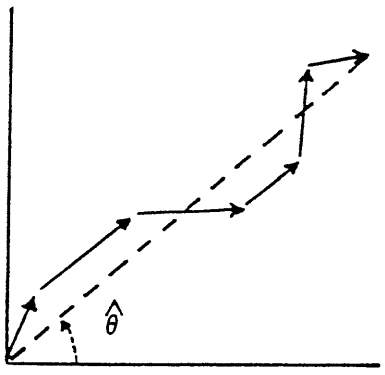

(b)

Figure 6

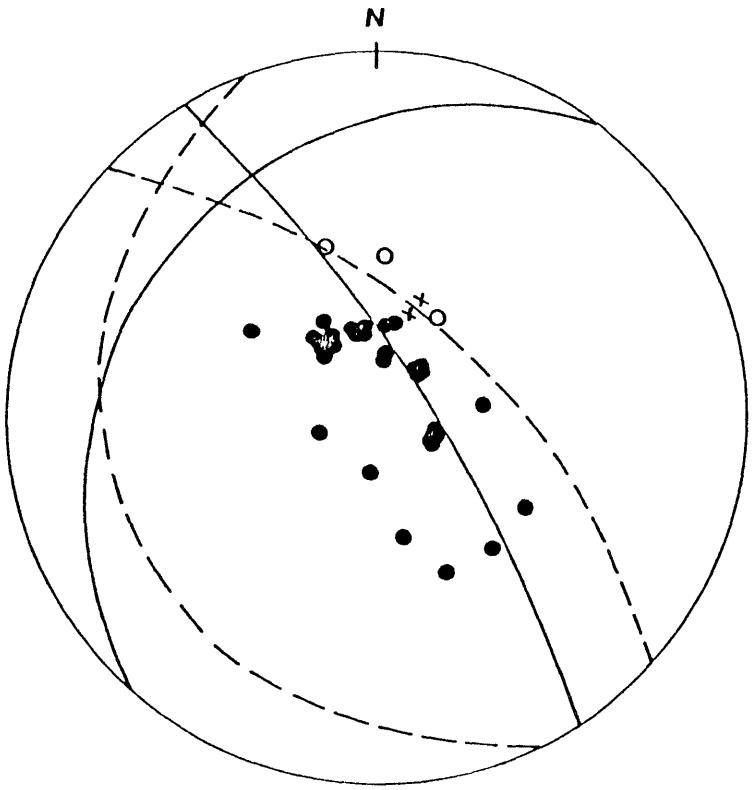
N
Oct 1, 1969

(a)

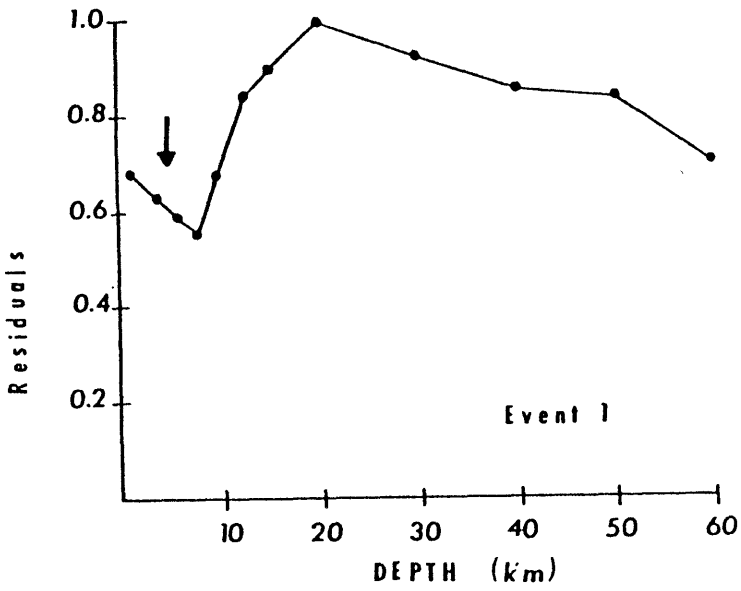
1.0
0.8
0.6
0.4
0.2
Residuals
Event 1
10
20
30
40
50
60
DEPTH (km)

(b)

Figure 7

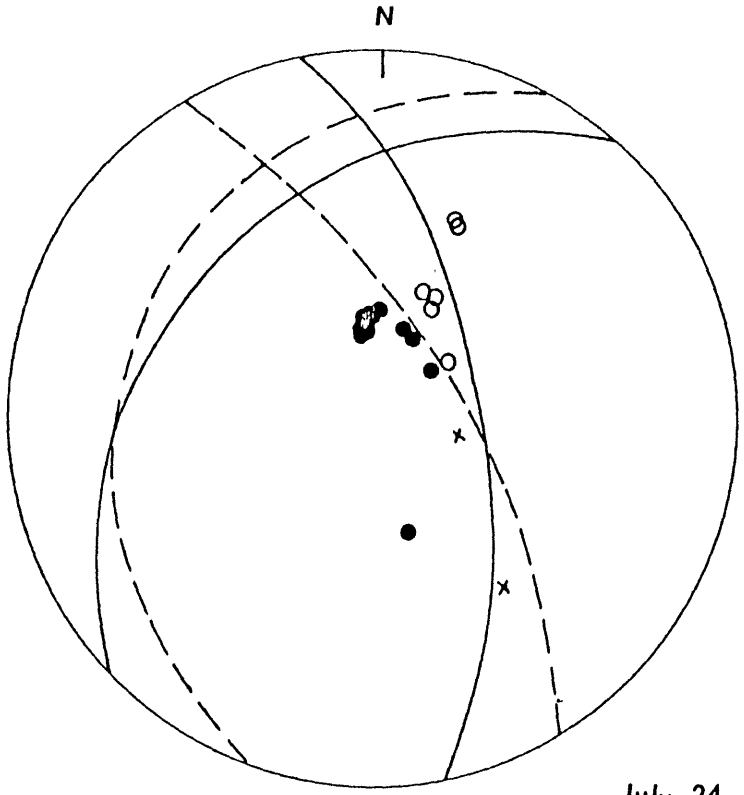
N
July 24, 1969

(a)

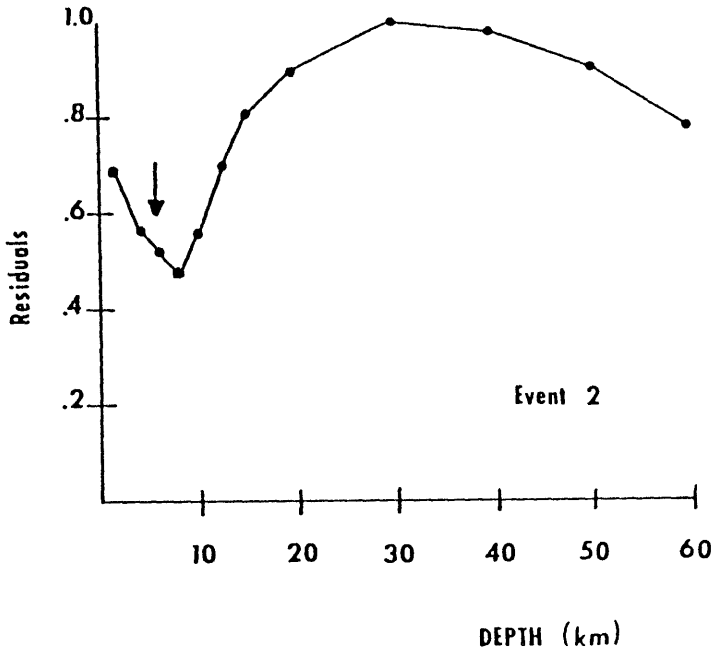
1.0
.8
.6
.4
.2
Residuals
Event 2
10
20
30
40
50
60
DEPTH (km)

(b)

Figure 8

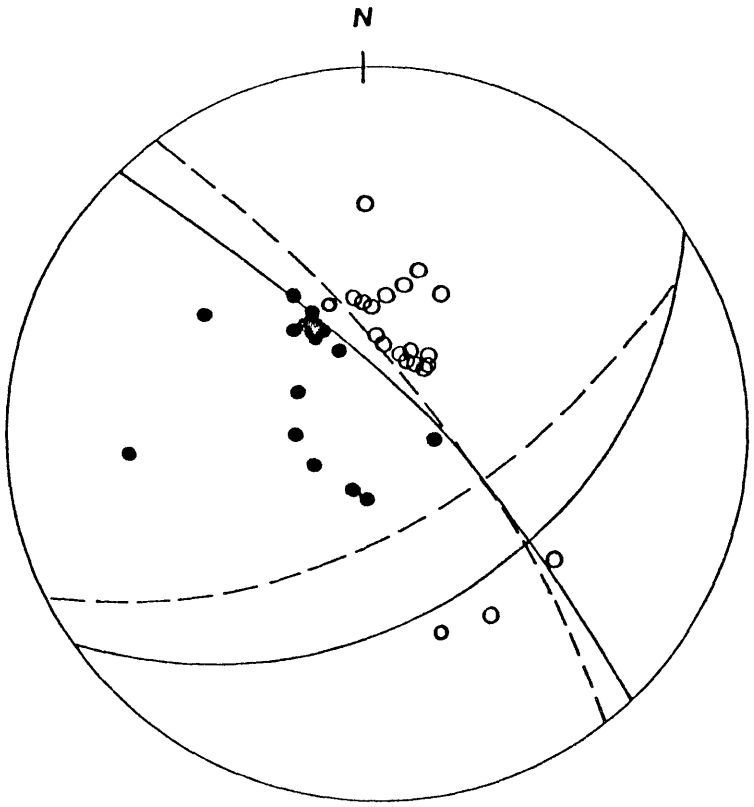

May 15, 1976

(a)

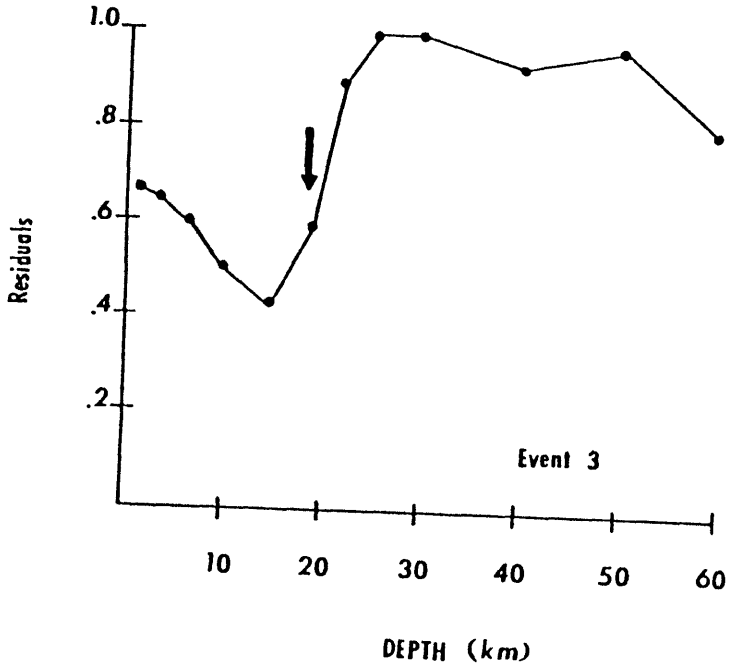

(b)

Figure 9

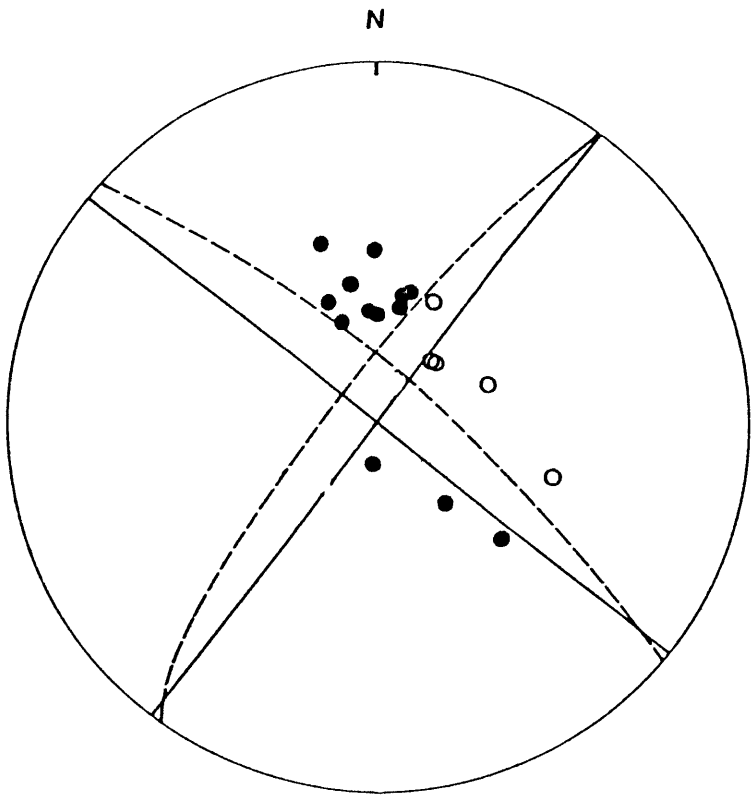
N
Oct 15, 1971

(a)

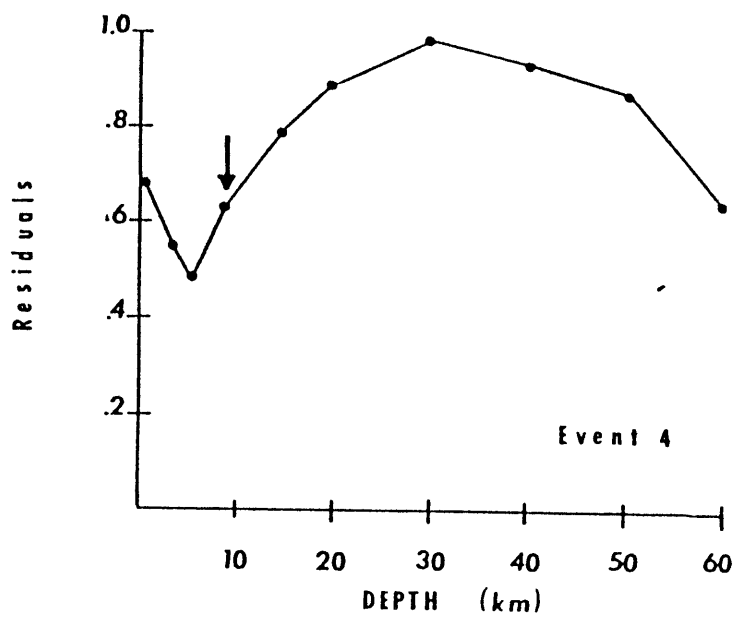
Residuals
1.0
.8
.6
.4
.2
Event 4
10
20
30
40
50
60
DEPTH (km)

(b)

Figure 10

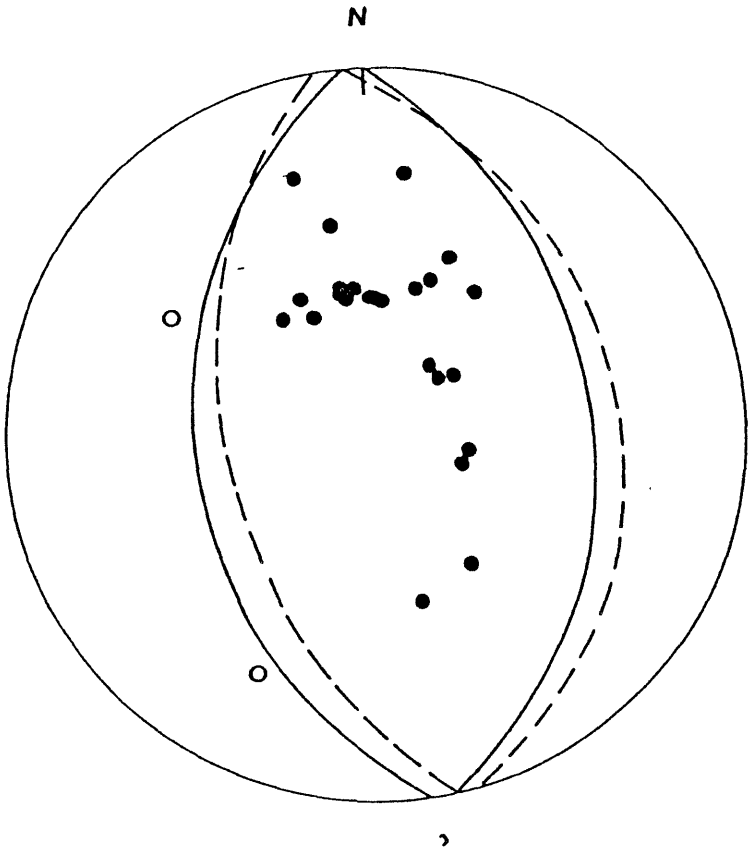
N
Feb 14, 1970

(a)

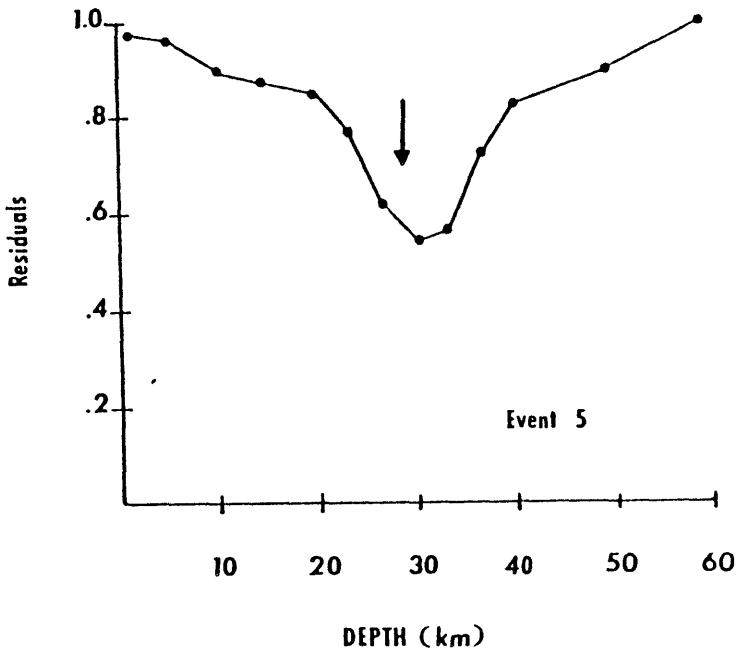
1.0
.8
.6
.4
.2
Residuals
Event 5
10
20
30
40
50
60
DEPTH (km)

(b)

Figure 11

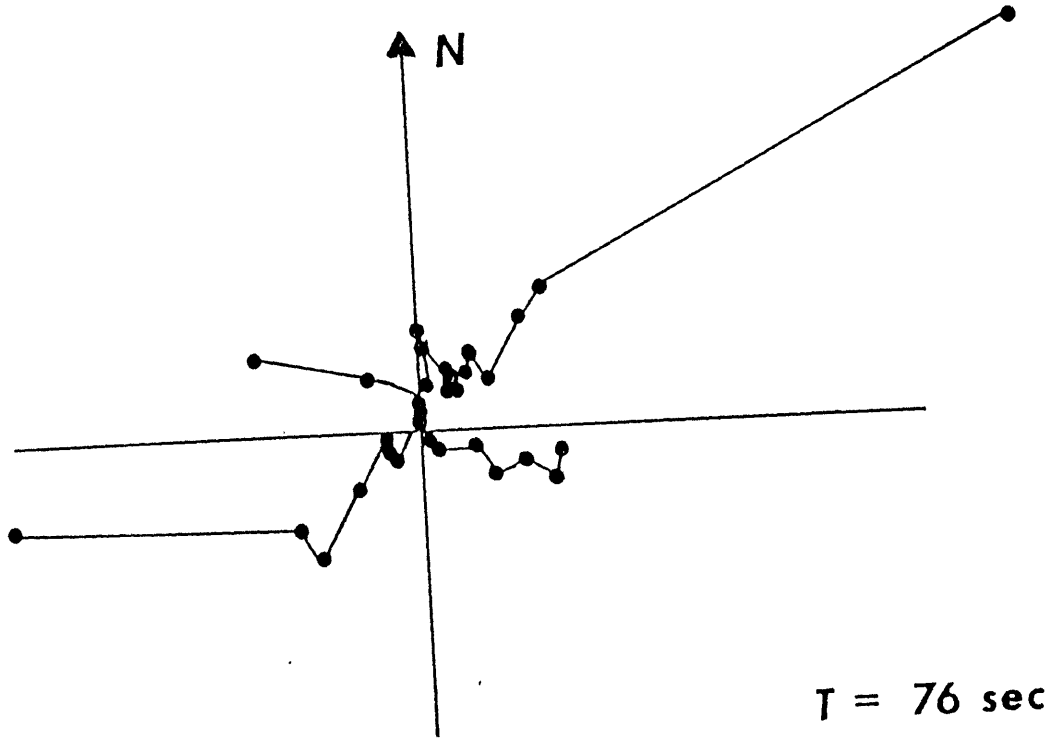

Figure 12

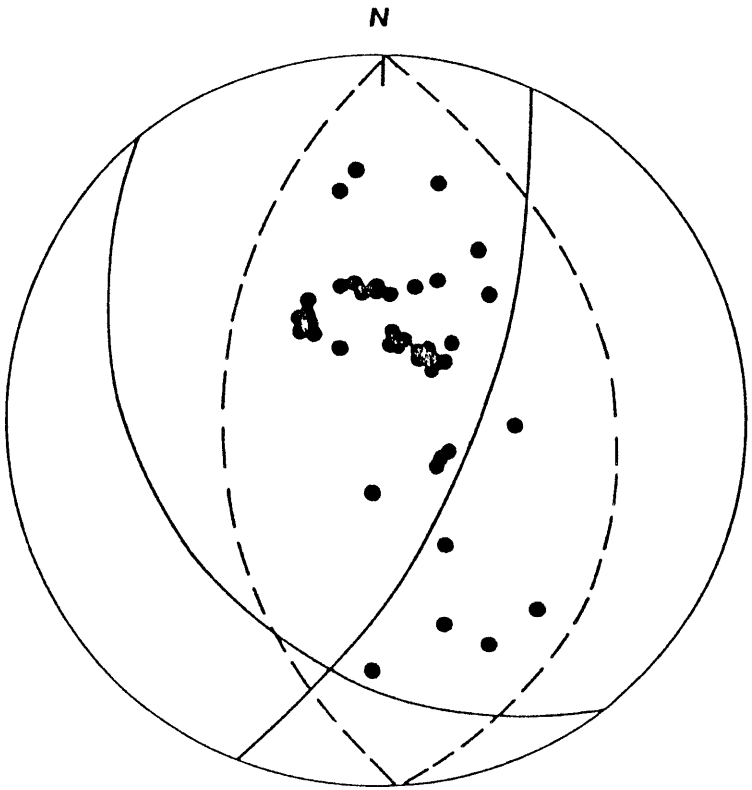

March 20, 1972

(a)

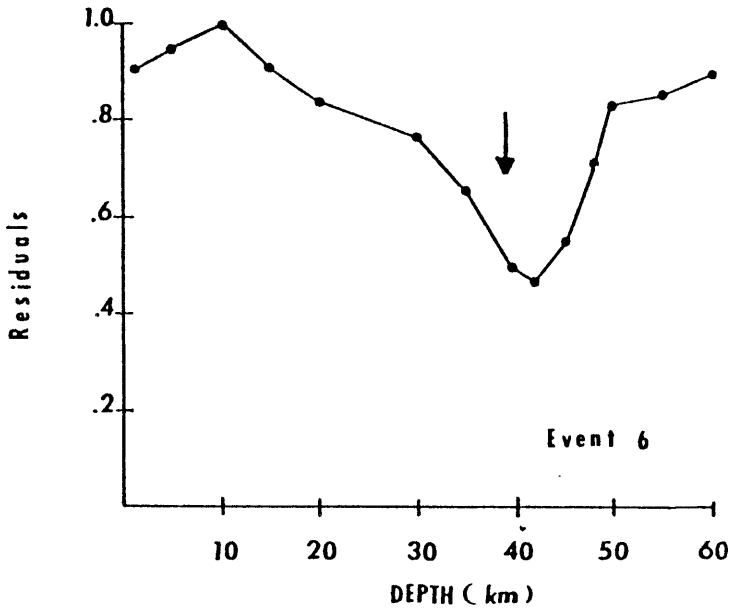

(b)

Figure 13

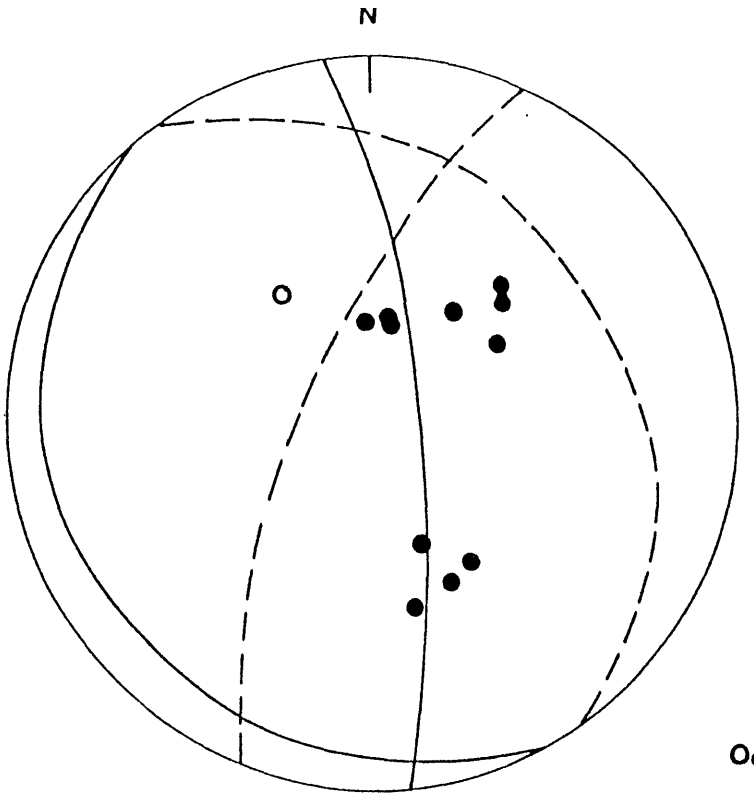
N
O
Oct 6, 1976

(a)

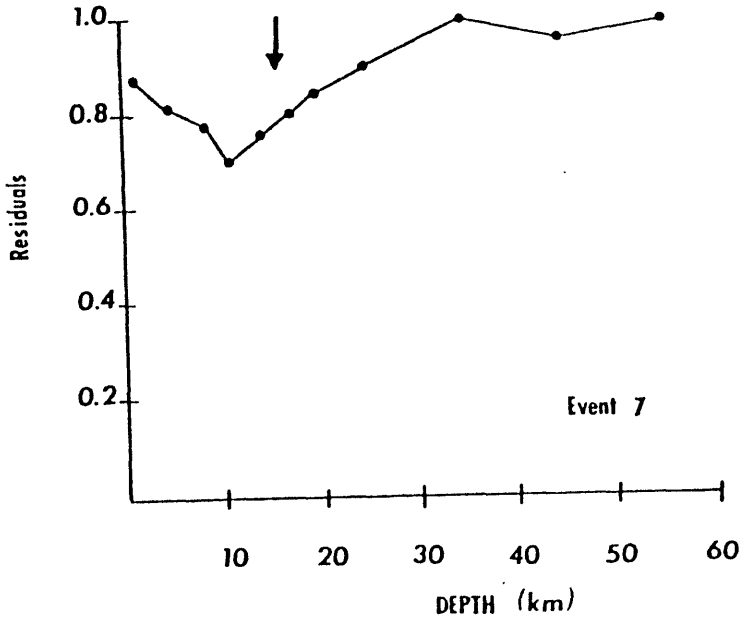
1.0
0.8
0.6
0.4
0.2
Residuals
Event 7
10
20
30
40
50
60
DEPTH (km)

(b)

Figure 14

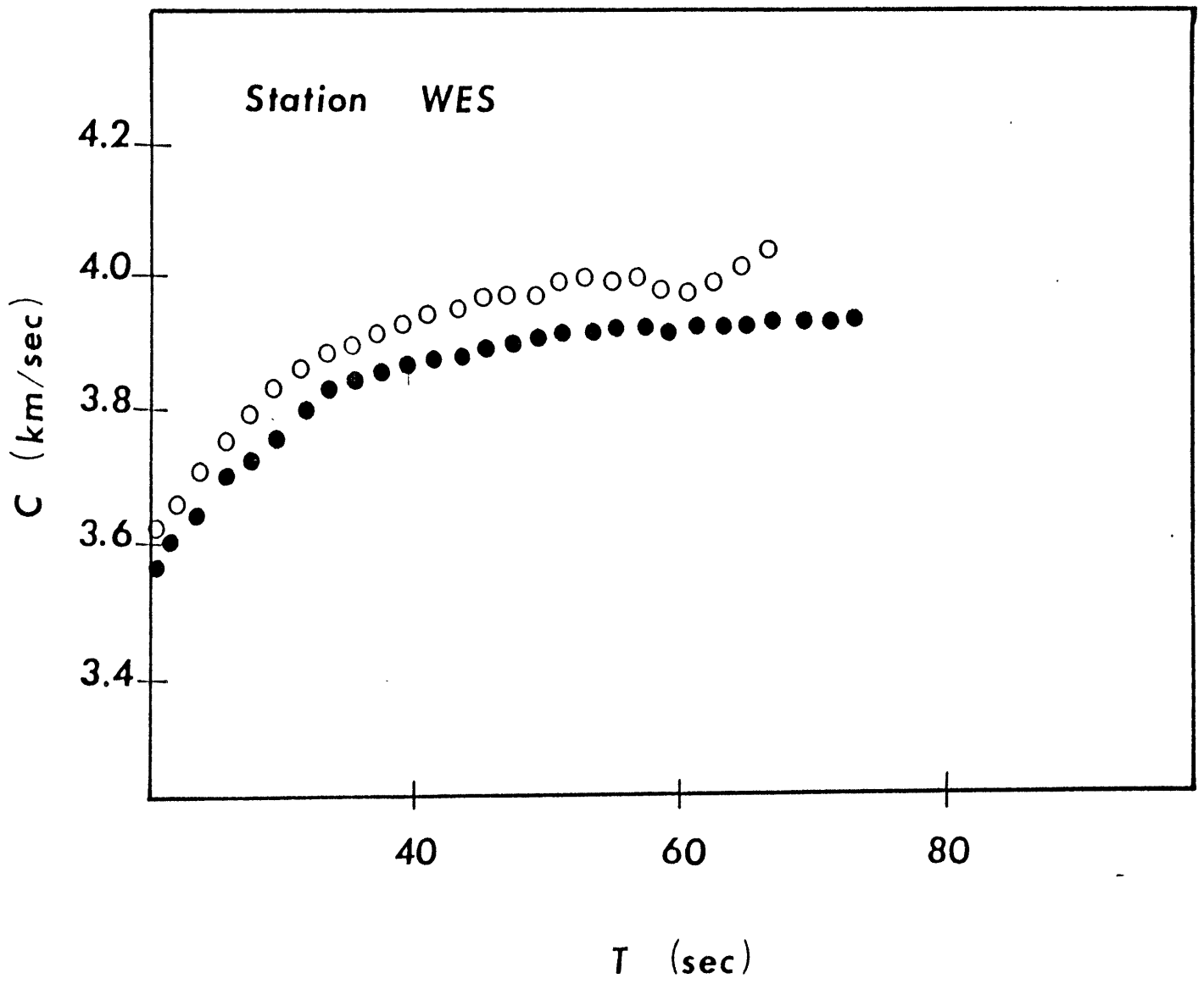

Figure 15

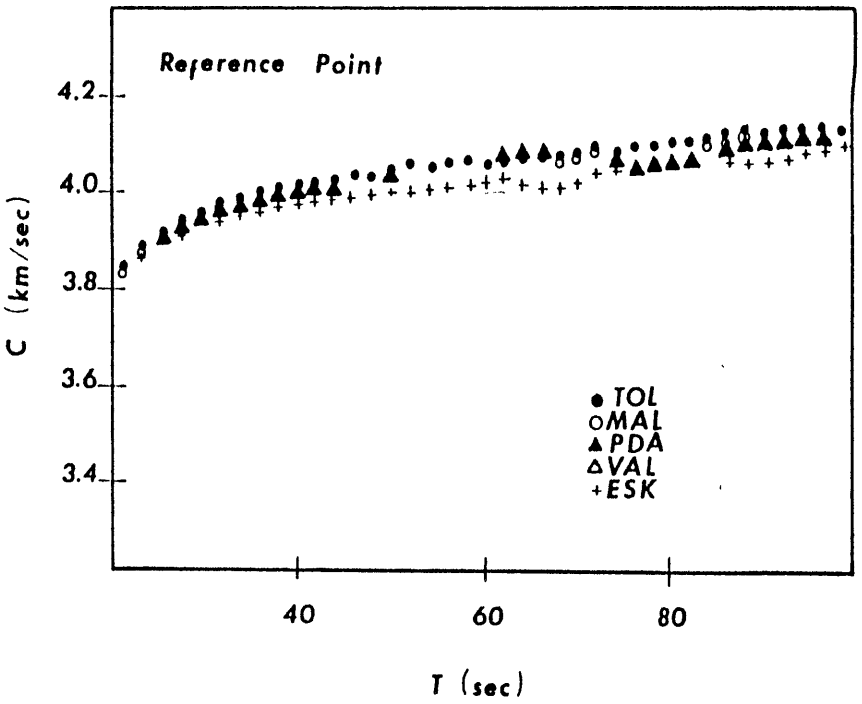
Reference Point
4.2
4.0
3.8
3.6
3.4
C (km/sec)
40
60
80
T (sec)
TOL
MAL
PDA
VAL
ESK

(a)

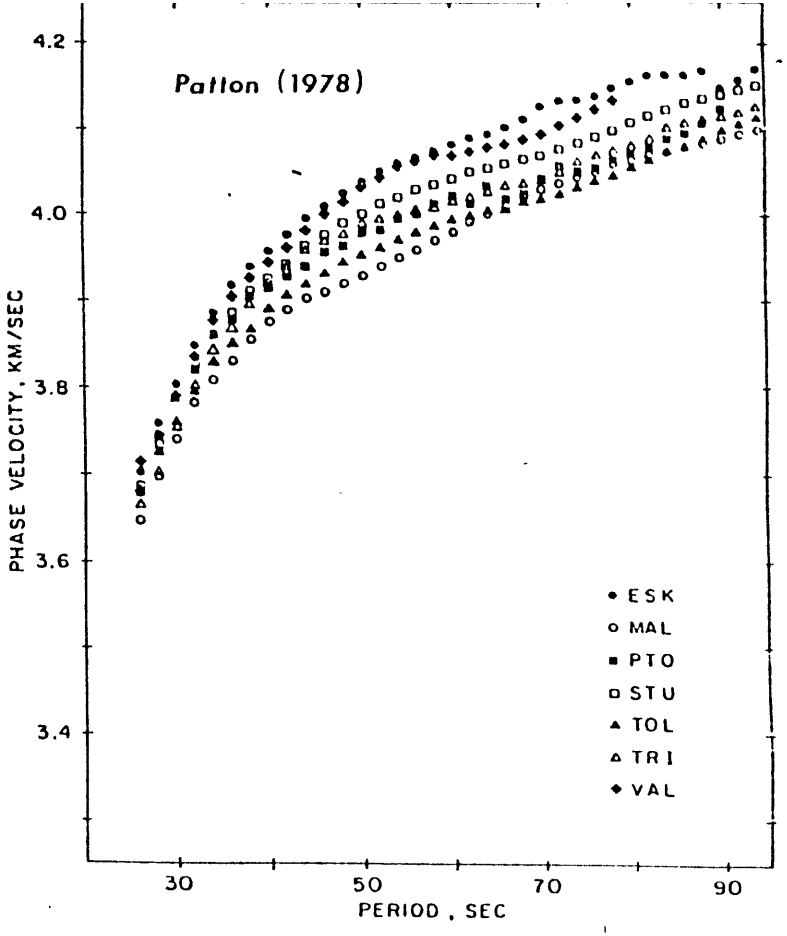
Patton (1978)
4.2
4.0
3.8
3.6
3.4
PHASE VELOCITY, KM/SEC
30
50
70
90
PERIOD, SEC
ESK
MAL
PTO
STU
TOL
TRI
VAL

(b)

Figure 16

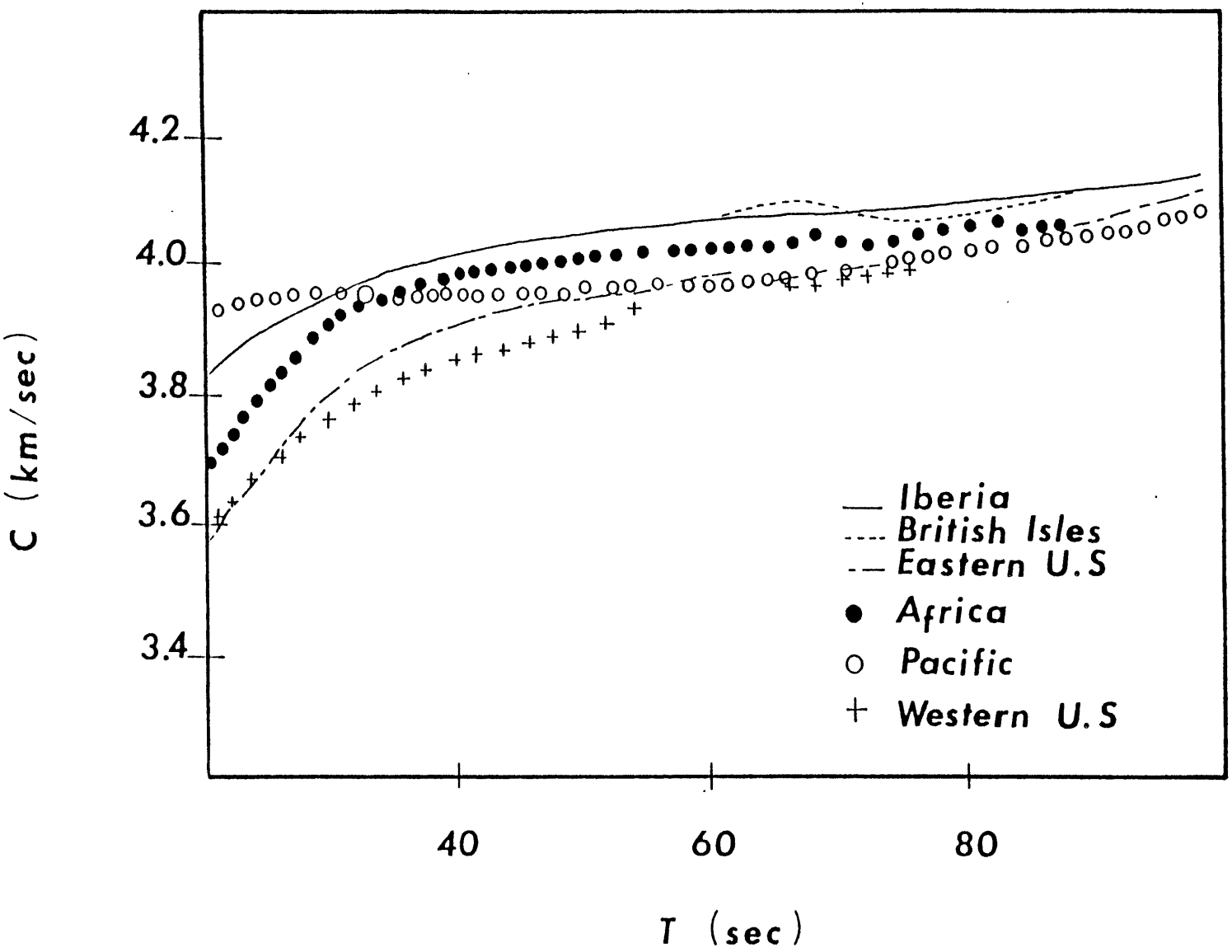
4.2
4.0
3.8
3.6
3.4
C (km/sec)
40
60
80
T (sec)
Iberia
British Isles
Eastern U.S
Africa
Pacific
Western U.S

Figure 17

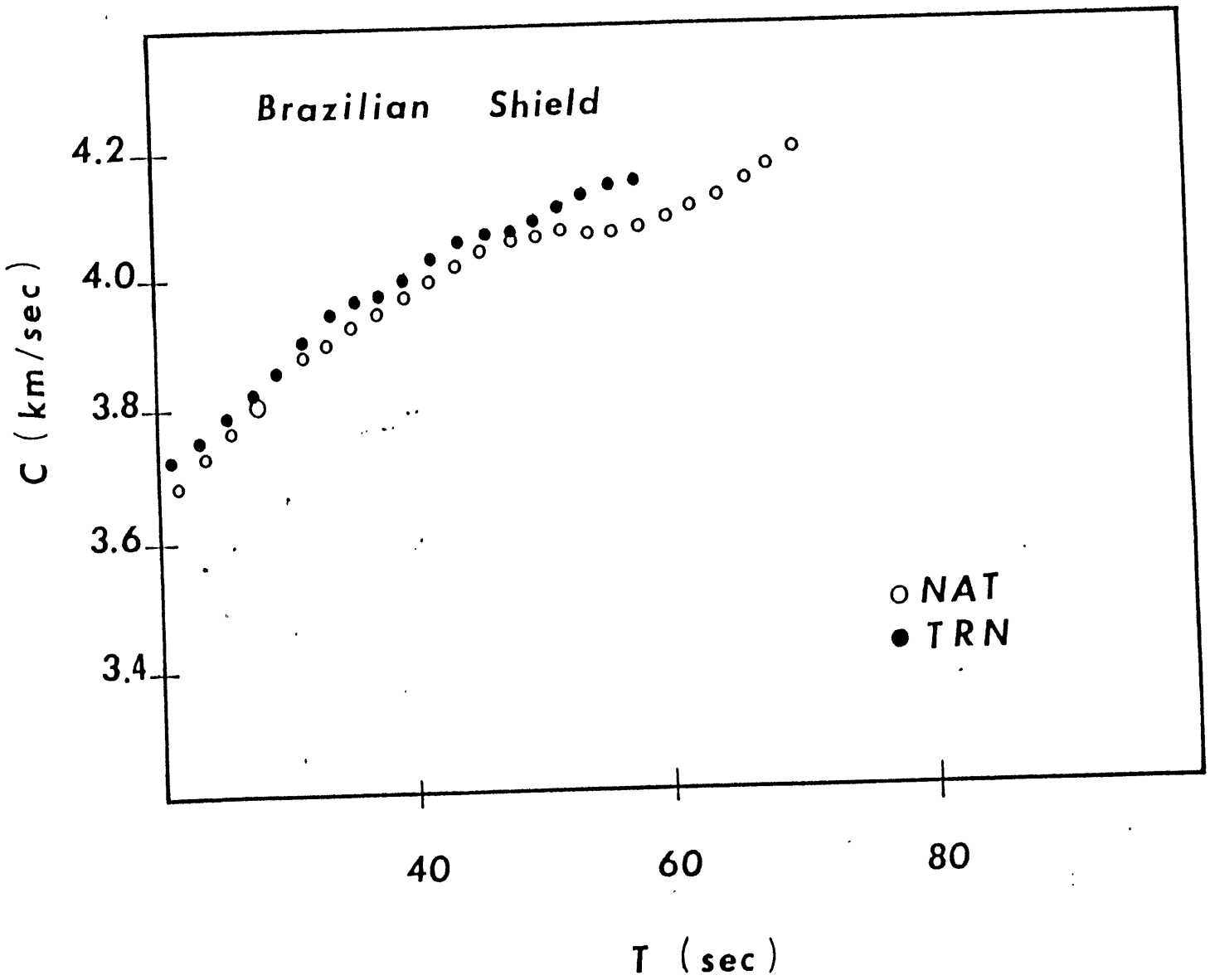

Figure 18

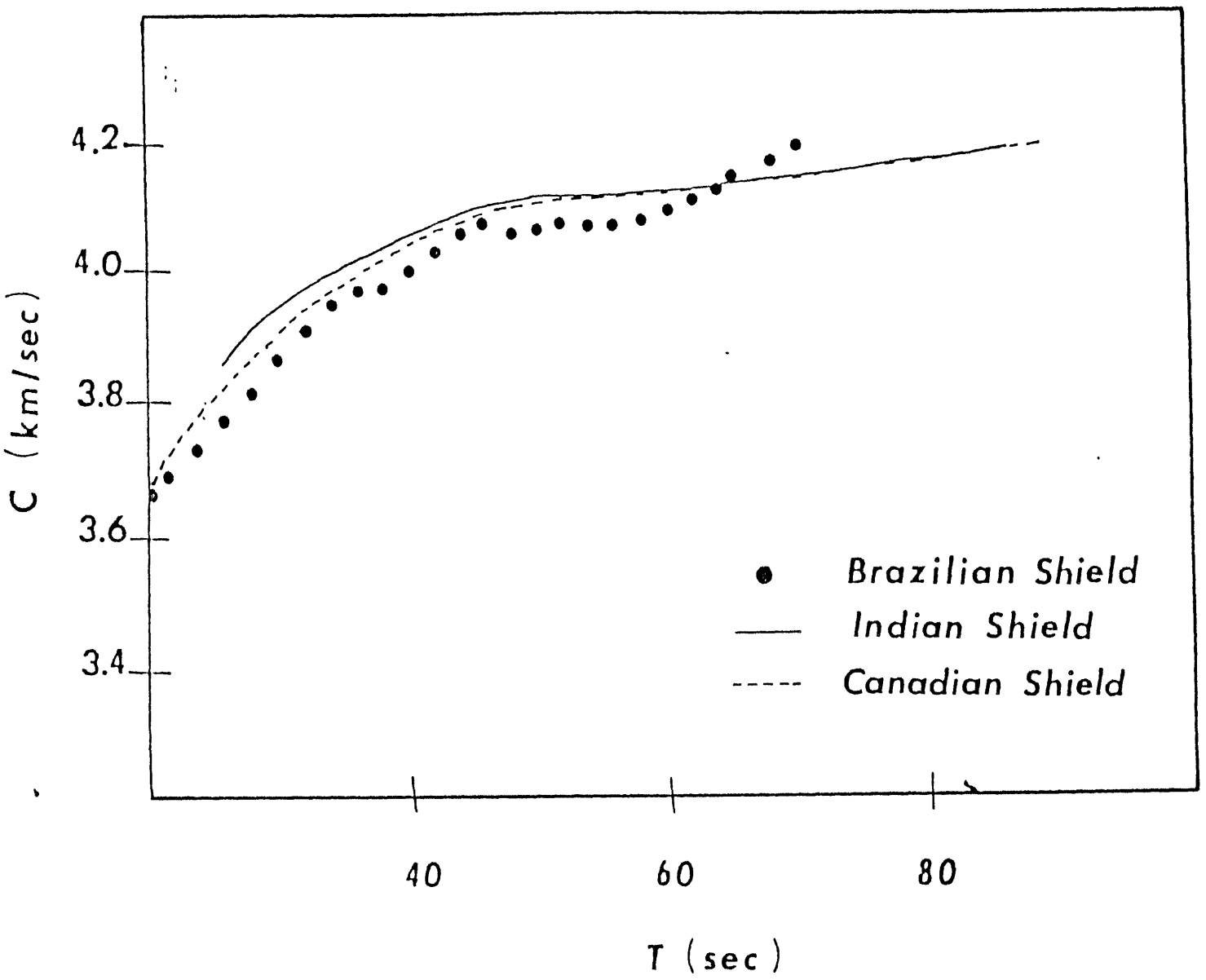
4.2
4.0
3.8
3.6
3.4
C (km/sec)
Brazilian Shield
Indian Shield
Canadian Shield
40
60
80
T (sec)

Figure 19

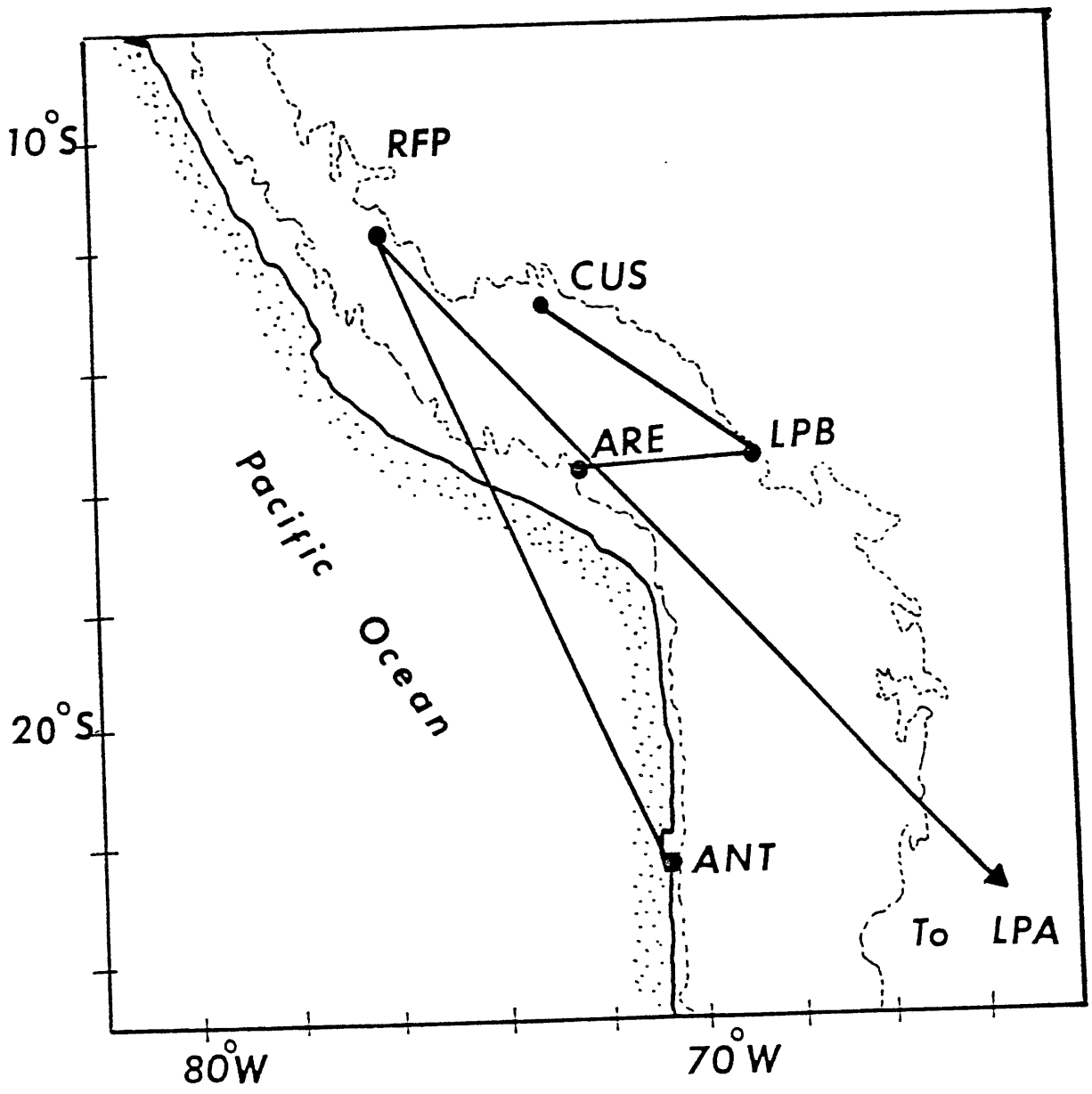

Figure 20

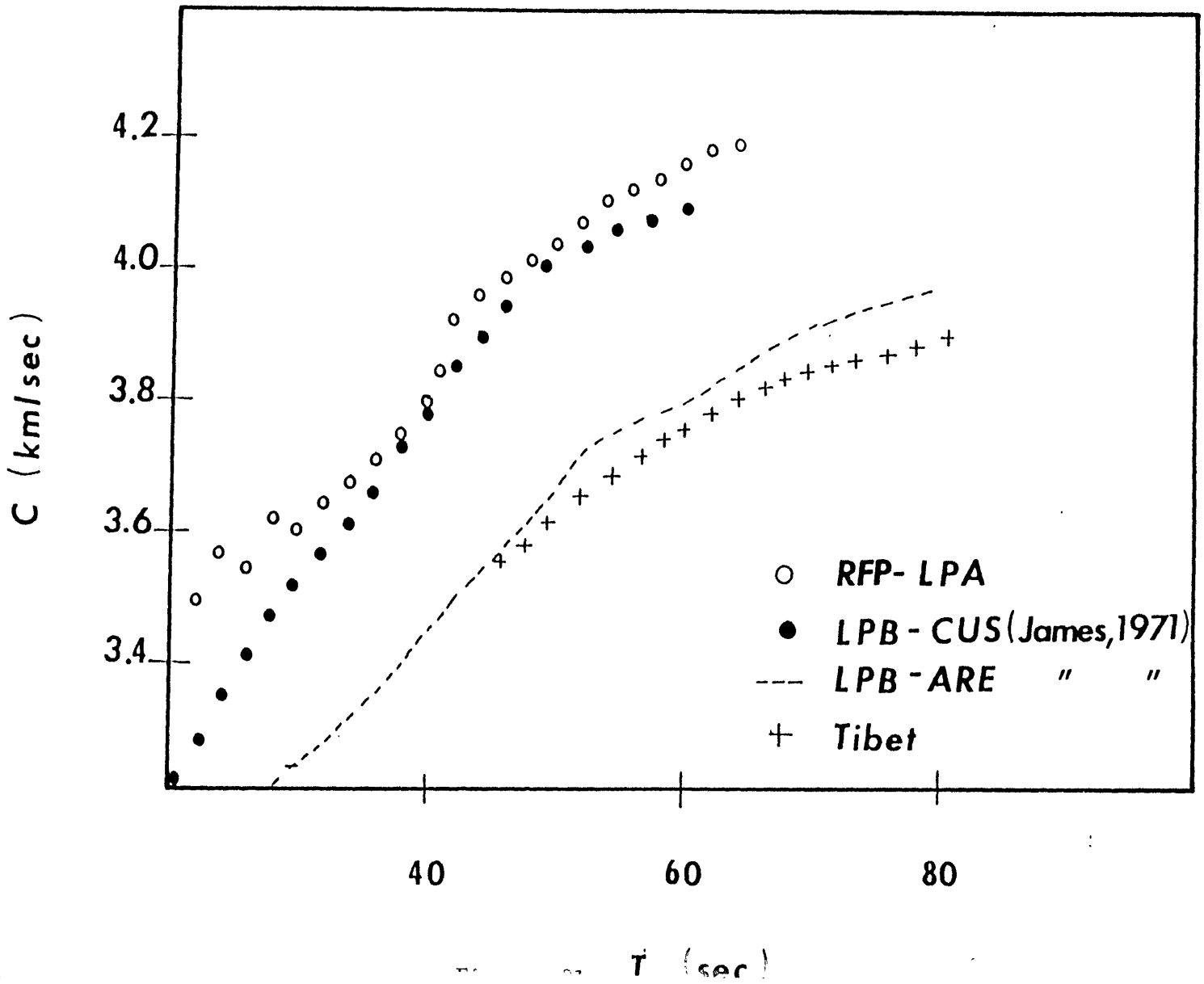
4.2
4.0
3.8
3.6
3.4
C (km/sec)
40
60
80
T (sec)
RFP- LPA
LPB - CUS (James, 1971)
LPB - ARE " "
Tibet

References

Aki, K., Generation and propagation of G waves from the Niigata earthquake of June 16, 1964, 2, Estimation of earthquake moment, released energy, and stress-strain drop from G wave spectrum, Bull. Earthquake Res. Inst. Tokyo, 44, 73-88, 1966.

Aki, K., and H. Patton, Determination of seismic moment tensor using surface waves, Tectonophys., 49, 213-222, 1978.

Aki, K., and P.G. Richards, Quantitative Seismology, Vol. 2, W.H. Freeman, San Francisco, 932pp., 1980.

Atwater, T., Implications of plate tectonics for the Cenozoic tectonic evolution of western North America, Geol. Soc. Amer. Bull, 81, 3513-3536, 1970.

Audebaud, E., R. Capdevilla, B. Dalmayrac, J. Debelmas, G. Laubacher, C. Lefevre, R. Marocco, C. Martinez, M. Mattauer, F. Megard, J. Paredes, and P. Tomasi, Les traits geologiques essentiels des Andes Centrales (Perou-Bolivie), Revue de Geographie Physique et de Geologie Dynamique (2), 15, 73-114, 1973.

Bally, A.W., P.L. Gordy, and G.A. Stewart, Structure, seismic data and orogenic evolution of the southern Canadian Rocky Mountains, Bull. Can. Petr. Geol., 14, 337-381, 1966.

Barazangi, M., and B.L. Isacks, Spatial distribution of earthquakes and subduction of the Nazca plate beneath South America, Geology, 4, 686-692, 1976.

Barazangi, M., and B.L. Isacks, Subduction of the Nazca plate beneath Peru: evidence from spatial distribution of earthquakes, Geophys. J.R. astr. Soc., 57, 537-555, 1979.

Brace, W.F., and D.L. Kohlstedt, Limits on lithospheric stress imposed by laboratory experiments, J. Geophys. Res., 85, 6248-6252, 1980.

Brewer, J.A., S.B. Smithson, J.E. Oliver, S. Kaufman, and L.D. Brown, The Laramide orogeny: Evidence from COCORP deep crustal seismic profiles in the Wind River mountains, Wyoming, Tectonophys., 62, 165-189, 1980.

Brune, J.N., Seismic moment, seismicity, and rate of slip along major fault zones, J. Geophys. Res., 73, 777-784, 1968.

Brune, J.N., and J. Dorman, Surface waves and earth structure of the Canadian shield, Bull. Seism. Soc. Amer., 53, 167-210, 1963.

Buland, R., The mechanics of locating earthquakes, Bull. Seism. Soc. Am., 66, 173-187, 1976.

Burchfiel, B.C., and G.A. Davis, Structural framework and evolution of the southern part of the Cordilleran orogen, western United States, Am. J. Sci., 272, 97-118, 1972.

Burchfiel, B.C., and G.A. Davis, Nature and controls of Cordilleran orogenesis, western United States: Extension of an earlier synthesis, Am. J. Sci., 275-A, 363-396, 1975.

Bussell, M.A., W.S. Pitcher, and P.A. Wilson, Ring complexes of the Peruvian coastal batholith: a long standing subvolcanic regime, Can. J. Earth Sci., 13, 1020-1030, 1976.

Chanove, G., M. Mattauer, and F. Megard, Precisions sur la tectonique tangentielle des terrains secondaries du massif de Pirin (NW du Lac Titicaca, Perou), C.R. Acad. Sci. Paris, 268, ser D, 1698-1701, 1969.

Chen, W.P., and P. Molnar, Depth distribution of earthquake foci and its possible implications for the rheological structure of the crust and upper mantle, (abs.), EOS, 62, 397, 1981.

Chen, W.P., and P. Molnar, Seismic moments of major earthquakes and the average rate of slip in central Asia, J. Geophys. Res., 82, 2945-2969, 1977.

Chinn, P.S., B.L. Isacks, and M. Barazangi, High-frequency seismic wave propagation in western South America along the continental margin, in the Nazca plate and across the Altiplano, Geophys. J. Roy. astr. Soc., 60, 204-244, 1980.

Cobbing, E.J., and W.S. Pitcher, The coastal batholith of central Peru, Q.J. geol. Soc. Lond., 128, 421-460, 1972.

Cobbing, E.J., W.S. Pitcher, and W.P. Taylor, Segments and super-units in the coastal batholith of Peru, J. Geol., 85, 625-631, 1977.

Coney, P.J., Structural evolution of the Cordillera Huayhuash, Andes of Peru, Geol. Soc. Am. Bull., 82, 1863-1884, 1971.

Dalmayrac, B., Un example de tectonique vivante: les failles sub-actuelles du pied de la Cordillera Blanche (Perou), Cah. ORSTOM, Ser. Geol., 6, 19-27, 1974.

Dalmayrac, B., Geologie de la Cordillere orientale de la region de Huanuco: sa place dans une transversale des Andes du Perou central (9°S a 30°S), Travaux et Documents de l'ORSTOM, 161 pp., Office de la Recherche Scientifique et Technique Outre-Mer, Paris, France, 1978.

Dalmayrac, B., and P. Molnar, Parallel thrust and normal faulting in Peru and constraints on the state of stress, Earth. Plan. Sci. Lett., 55, 473-481, 1981.

Dalmayrac, B., J.R. Lancelot, and A. Leyerloup, Two-billion-year granulites in the late Precambrian metamorphic basement along the southern Peruvian coast, Science, 198, 49-51, 1977.

Dalmayrac, B., G. Laubacher, and R. Marocco, Geologie des Andes Peruviennes, Caracteres generaux de l'evolution geologique des Andes peruviennes, Travaux et Documents de l'ORSTOM, Editions de l'Office de la Recherche Scientifique et Technique Outre-Mer, Paris, France, 1980.

Davies, G.F., and J.N. Brune, Regional and global fault rates from seismicity, Nat. Phys. Sci., 229, 101-107, 1971.

Dewey, J.F., and Bird, J.M., Mountain belts and the new global tectonics, J. Geophys. Res., 75, 2625-2647, 1970.

Deza, E., The Pariahuanca earthquakes, Huancayo, Peru: July-October 1969, in Recent Crustal Movement, R. Soc. N. Z. Bull., 9, 77-83, 1971.

Dollfus, O., and F. Megard, Les formations Quaternaires du basin de Huanayo et leur neotectonique (Andes centrales peruviennes), Rev. Geograph. Phys. Geol. Dynamique (2), X, 5, 429-440, 1968.

Fitch, T.J., R.G. North, and M.W. Shields, Focal depths and moment tensor representations of shallow earthquakes associated with the great Sumba earthquake, J. Geophys. Res., 86, 9357-9374, 1981.

Forsyth, D.W., The early structural evolution and anisotropy of the oceanic upper mantle, Geophys. J. R. astron. Soc., 43, 103-162, 1975.

Gansser, A., Facts and theories on the Andes, Q.J. geol. Soc. Lon., 129, 93-131, 1973.

Gee, D.G., Nappe displacement in the Scandinavian Caledonides, Tectonphys., 47, 393-419, 1978.

Gilbert, F., Excitation of the normal modes of the earth by earthquake sources, Geophys. J. R. astr. Soc., 22, 223-226, 1970.

Hagiwara, T., A note on the theory of the electromagnetic seismograph, Bull. Earthquake Res. Inst. Tokyo Univ., 36, 139-164, 1958.

Ham, C.K., and L.J. Herrera, Jr., Role of subandean fault system in tectonics of eastern Peru and Ecuador, in Childs, O.E., and Beebe, R.N., eds., Backbone of the Americas, Am. Assoc. Petr. Geol. Mem., 2, 47-61, 1963.

Hamilton, W., The volcanic central Andes - a modern model for the Cretaceous batholiths and tectonics of western North America, Oregon Dept. Geology and Mineral Industries, Bull., 65, 175-184, 1969.

Hanks, T.C., and H. Kanamori, A moment magnitude scale, J. Geophys. Res., 84, 2348-2350, 1979.

Harrington, H.J., Paleogeographic development of South America, Bull. Am. Assoc. Petr. Geol. Bull., 46, 1173-1814, 1962.

Hasegawa, A., and I.S. Sacks, Subduction of the Nazca plate beneath Peru as determined from seismic observations, J. Geophys. Res., 4971-4980, 1981.

Helwig, J., Plate tectonic model for the evolution of the Central Andes: Discussion, Geol. Soc. Am. Bull., 84, 1493-1496, 1973.

Hodgson, J.H., and P.C. Bremmer, Direction of faulting in the Ancash, Peru, earthquake of November 10, 1946, from teleseismic evidence, Seism. Soc. Am. Bull., 43, 121-125, 1953.

Isacks, B., and P. Molnar, Mantle earthquake mechanism and the sinking of the lithosphere, Nature, 223, 1121-1124, 1969.

Jackson, J., and T. Fitch, Basement faulting and the focal depth of the larger earthquakes in the Zagros Mountains (Iran), 64, 561-586, 1981.

James, D., Subduction of the Nazca plate beneath Central Peru, Geology, 7, 174-178, 1978.

James, D.E., Andean crustal and upper mantle structure, J. Geophys. Res., 76, 3246-3271, 1971.

James, D.E., I.S. Sacks, E. Lazo, and O. Aparicio, On locating local earthquakes using small networks, Seis. Soc. Am. Bull., 59, 1201-1212, 1969.

Jordan, T.E., B.L. Isacks, R.W. Allmendinger, J.A. Brewer, V.A. Ramos, and C.J. Ando, Andean tectonics related to geometry of subducted Nazca plate, submitted to Geol. Soc. Am. Bull., 1982.

Kafka, A.L., and D.J. Weidner, The focal mechanisms and depths of small earthquakes as determined from Rayleigh wave radiation patterns, Bull. Seismol. Soc. Am., 69, 1379-1390, 1979.

Kanamori, H., and J.W. Given, Use of long-period surface waves for past determination of earthquake source parameters, Phys. Earth Planet. Inter., 27, 8-31, 1981.

Kanamori, H., and G.S. Stewart, Mode of strain release along the Gibbs fracture zone, Mid-Atlantic ridge, Phys. Earth Planet. Int., 11, 312-332, 1976.

Kanamori, H., and G.S. Stewart, Seismological aspects of the Guatemala earthquake of February 4, 1976, J. Geophys. Res., 83, 3427-3434, 1978.

Kelleher, J., and W. McCann, Buoyant zones, great earthquakes and unstable boundaries of subduction, J. Geophys. Res., 81, 4885-4896, 1976.

Klein, F.W., Hypocenter location program HYPOINVERSE, Open-file report 78-694, United States Geological Survey, Menlo Park, 113pp., 1978.

Kostrov, V.V., Seismic moment and energy of earthquakes, and seismic flow of rock, Izv. Acad. Sci. USSR, Phys. Solid Earth, 1, 23-44, 1974.

Lanczos, C., Linear Differential Operators, Van-Nostrand Co. Ltd., London, 564pp., 1961.

Landisman, M., Z. Dzeiwonski, and Y. Sato, Recent Improvements in the analysis of surface wave observations, Geophys. J. R. astron. Soc., 17, 369-403, 1969.

Langston, C.A., A single station fault plane solution, Geophys. Res. Lett., 6, 41-44, 1979.

Langston, C.A., and D. Helmberger, A procedure for modeling shallow dislocation sources, Geophys. J. Roy. Astron. Soc., 42, 117-130, 1975.

Laubacher, G., Geologie de la Cordillera Oriental et de l'Altiplano au Nord et Nord-ouest du Lac Titicaca, Geologie des Andes Peruviennes, Trauvaux et Documents de l'ORSTOM, 95 pp., Office de la Recherche Scientifique et Technique Outre-Mer, Paris, France, 1978.

Lawson, C.L., and R.J. Hanson, Solving Least Squares Problems, Prentice Hall, Englewood Cliffs, 340pp., 1974.

Lavenu, A. Neotectonique des sediments plio-quaternaires du nord de l'Altiplano bolivien (Region de La Paz-Ayo-Ayo-Umala), Cah. O.R.S.T.O.M., ser. Geol., X, No. 1, 115-126, 1978.

Lavenu, A., and O. Ballivian, Estudios neotectonicos de las cuencas de las regiones de Cochabamba, Sucre, Tarija - Cordillera Oriental boliviana, Rev. Acad. Nac. Cien. Bolivia, 2, No. 3, 107-129, 1979.

Lee, W.H.K., and S.W. Stewart, Principles and Applications of Microearthquake Networks, Advances in Geophysics, Supplement 2, Academic Press, New York, 1981.

Lepry, L.A., and G.H. Davis, Influence of 'soft' basement on ramp thrusting in the Yauli dome foreland region, Cordillera Occidental, Peru, submitted to Geol. Soc. Am. Bull., 1982.

Lilwall, R.C., and T.J.G. Francis, Hypocentral resolution of small ocean bottom seismic networks, Geophys. J. R. astr. Soc., 54, 721-728, 1978.

Lohman, H.H., Outline of the tectonic history of Bolivian Andes, Am. Assoc. Petr. Geol. Bull., 54, 735-757, 1970.

McCowan, D.W., Moment tensor representation of surface wave sources, Geophys. J. R. astron. Soc., 44, 595-599, 1976.

McKenzie, D., Active tectonics of the Mediterranean region, Geophys. J.R. astr. Soc., 30, 109-185, 1972.

McTigue, D.F., and C.C. Mei, Gravity-induced stresses near topography of small slope, J. Geophys. Res., 86, 9268-9278, 1981.

Megard, F., Etude geologique des Andes du Perou central, Office de la Recherche Scientifique et Tecnique Outre-Mer, Mem. 86, 310 pp., 1978.

Megard, F., and H. Philip, Plio-Quaternary Tectono-Magmatic zonation and plate tectonics in the central Andes, Earth Plan. Sci. Lett., 33, 231-239, 1976.

Meissner, R., and J. Strehlau, Limits of stresses in continental crusts and their relation to depth-frequency distribution of shallow earthquakes, Tectonics, 1, 73-89, 1982.

Mendiguren, J.A., and F.M. Richter, On the origin of compressional intraplate stresses in South America, Phys. Earth Plan. Int., 16, 318-326, 1978.

Mercier, J.L., Extensional-compressional tectonics associated with the Aegean Arc: comparison with the Andean Cordillera of south Peru-north Bolivia, Phil. Trans. R. Soc. Lond., 300, 337-355, 1981.

Molnar, P., Earthquake recurrence intervals and plate tectonics, Bull. Seis. Soc. Am., 69, 115-133, 1979.

Molnar, P., and P. Tapponnier, Cenozoic tectonics of Asia: effects of a continental collision, Science, 189, 419-426, 1975.

Molnar, P., and P. Tapponnier, Active tectonics of Tibet, J. Geophys. Res., 83, 5361-5375, 1978.

Molnar, P., W.P. Chen, T.J. Fitch, P. Tapponnier, W.E.K. Warsi, and F.T. Wu, Structure and tectonics of the Himalaya; A brief summary of relevant geophysical observation, in Himalaya: Sciences de la Terre, pp. 269-294, Centre National de la Recherche Scientifique, Paris, 1977.

Nabelek, J., G. Suarez, and M.N. Toksoz, the 1982 New Brunswick Earthquake: Inversion of Focal Depth and Source Mechanism from Body and Surface Waves, in preparation, 1982.

Newell, N.D., Geology of the Lake Titicaca region, Peru and Bolivia, Geol. Soc. Am. Mem., 36, 111 pp., 1949.

Noble, D.C., and E.J. McKee, Spatial distribution of earthquakes and subduction of the Nazca plate beneath south: Comment, Geology, 5, 576-578, 1977.

Ocola, L.C., and R.P. Meyer, Crustal structure from the Pacific basin to the Brazilian shield between 12° and 30° south latitude, Bull. Seism. Soc. Amer., 84, 3387-3403, 1973.

Ocola, L.C., R.P. Meyer, and L.T. Aldrich, Gross crustal structure under Peru-Bolivia Altiplano, Earthquake Notes, 42, 33-48, 1971.

Paredes, J., Etude geologique de la feuille de Jauja au 1:100,000 (Andes du Perou Central), These 3eme Cycle, Univ. Sci. Tech. Languedoc, Montpellier, 79pp., 1972.

Patton, H., Source and Propagation effects of Rayleigh waves from Central Asian Earthquakes, Ph.D. thesis, 342pp., Mass. Inst. of Technol., Cambridge, 1978.

Patton, H., Reference point equalization method for determining the source and path effects of surface waves, J. Geophys. Res., 85, 821-848, 1980.

Pennington, W.D., Subduction of the Eastern Panama Basin and seismotectonics of Northwestern South America, 86, 10753-10770, 1981.

Philip, H., and F. Megard, Structural analysis of the superficial deformation of the 1969 Pariahuanca earthquakes (central Peru), Tectonophys., 38, 259-278, 1977.

Pilger, R.H., Plate reconstructions of aseismic ridges, and low angle subduction beneath the Andes, Geol. Soc. Am. Bull., 92, 448-456, 1981.

Pilger, R.H. and D.W. Handschumacher, The fixed-hotspot hypothesis and origin of the Easter-Sala y Gomez-Nazca trace, Geol. Soc. Amer. Bull., 92, 437-446, 1981.

Pisarenko, V.F., Statistical estimates of amplitude and phase corrections, Geophys. J. R. astron. Soc., 20, 89-98, 1970.

Pitcher, W., On the rate of emplacement of batholiths, Q.J. Geol. Soc. Lond., 581-591, 1975.

Plafker, G., Alaskan earthquake of 1964 and Chilean earthquake of 1960: implications for arc tectonics, J. Geophys. Res., 77, 901-925, 1972.

Prevot, R., D. Hatzfeld, S.W. Roecker and P. Molnar, Shallow Earthquakes and Active Tectonics in Eastern Afghanistan, J. Geophys. Res., 85, 1347-1357, 1980.

Price, R.A.,. and E.W. Mountjoy, Geologic structure of the Canadian Rocky Mountains between Bow and Athabaska Rivers - a progress report, Geol. Assoc. Canada Spec. Paper, 6, 7-25, 1970.

Rial, J.A., The Caracas, Venezuela, earthquake of July 1967: A multiple-source event, J. Geophys. Res, 83, 5405-5414, 1978.

Richter, C.F., Elementary Seismology, W.H. Freeman, San Francisco, 768 pp., 1958.

Rodriguez, A., and A. Chalco, Cuenca Huallaga, Resena geologica y posibilidades petroliferas, Bol. Soc. Geol. Peru, 49, 187-212, 1975.

Roecker, S.W., Seismicity and Tectonics of the Pamir-hindu Kush region of Central Asia, Ph.D. thesis, M.I.T., 297 pp., 1981.

Roecker, S.W., O.V. Soboleva, I.L. Nersesov, A.A. Lukk, D. Hatzfeld, J.L. Chatelain, and P. Molnar, Seismicity and fault plane solutions of intermediate depth earthquakes in the Pamir-Hindu Kush region, J. Geophys. Res., 85, 1358-1364, 1980.

Romanowicz, B., Depth resolution of Earthquakes in Central Asia by Moment Tensor Inversion of Long-Period Rayleigh Waves: Effects of Phase Velocity Variations across Eurasia, J. Geophys. Res., 86, 5963-5984, 1981.

Romanowicz, B., Moment Tensor Inversion of Long-Period Rayleigh Waves: A New Approach, J. Geophys. Res., 87, 5395-5407, 1982a.

Romanowicz, B., Constraints on the structure of the Tibet plateau from pure path phase velocities of Love and Rayleigh waves, J. Geophys. Res., 87, 6865-6883, 1982b.

Saito, M., Excitation of free oscillations and surface waves by a point source in a vertically heterogeneous earth, J. Geophys. Res., 72, 3689-3699, 1967.

Sales, J.K., Cordilleran foreland deformation, Am. Assoc. Petroleum Geol. Bull., 52, 2016-2044, 1968.

Sclater, J.G., V. Vacquier, and J.H. Rohrhirsch, Terrestrial heat flow measurements on Lake Titicaca, Peru, Earth Planet. Sci. Lett., 8, 45-54, 1970.

Shackleton, R.M., A.C. Ries, M.P. Coward, and P.R. Cobbold, Structure, metamorphism, and geochronology of the Arequippa Massif of coastal Peru, 136, 2, 195-214, 1979.

Silgado, E., The Ancash, Peru, earthquake of November 10, 1946, Bull. Seism. Soc. Am., 41, 83-100, 1951.

Smithson, S.B., J.A. Brewer, S. Kaufman, J.E. Oliver, and C.A. Hurich, Structure of the Laramide Wind River uplift, Wyoming, from COCORP deep reflection data and from gravity data, J. Geophys. Res., 84, 5955-5972, 1979.

Stauder, W., Mechanism and spatial distribution of Chilean earthquakes with relation to subduction of the oceanic plate, J. Geophys. Res., 78, 5033-5061, 1973.

Stauder, W., Subduction of the Nazca plate under Peru as evidenced by focal mechanisms and by seismicity, J. Geophys. Res., 80, 1053-1064, 1975.

Stearns, D.W., Faulting and forced folding in the Rocky Mountain foreland, in Matthews, V., III, ed., Laramide Folding Associated with Basement Block Faulting in the Western United States, Geol. Soc. Am. Memoir, 151, 1-37, 1978.

Stewart, J.S.W., J.F. Evernden, and N.J. Snelling, Age determinations from Andean Peru: a reconnaissance survey, Geol. Soc. Am. Bull., 85, 1107-1116, 1974.

Suarez, G., P. Molnar and B.C. Burchfiel, Seismicity, Fault Plane Solutions, Depth of Faulting, and Active Tectonics of the Central Andes, J. Geophys. Res., in press, 1983.

Tatel, H.E., and M.A. Tuve, Seismic studies in the Andes, Amer. Geophys. Union Trans., 39, 580-582, 1958.

Tapponnier, P., and P. Molnar, Active faulting and tectonics in China, J. Geophys. Res., 82, 1977.

Touzett, G., Evaluacion geologica del yacimiento petrolifero Agua Caliente, Bol. Soc. Geol. Peru, 48, 9-24, 1975.

Trehu, A.M., Seismicity and Structure of the Orozco Transform Fault from Ocean Bottom Seismic Observations, Ph.D. Thesis, Mass. Inst. of Technol./Woods Hole Oceanographic Inst., 370pp., 1982.

Trehu, A.M., J.L. Nabelek, and S.C. Solomon, Source characterization of two Reykjanes Ridge earthquakes: surface waves and moment tensors; P waveforms and nonorthogonal nodal planes, J. Geophys. Res., 86, 1701-1724, 1981.

Tsai, Y.-B., and K. Aki, Precise focal depth determination from amplitude spectra of surface waves, J. Geophys. Res., 75, 5729-5743, 1970.

Vicente, J.C., F. Sequeiros, M.A. Valdivia, and J. Zavala, El sobre-escurrimiento de Cincha-Lluta: Elemento del accidente mayor andino al NW de Arequipa, Bol. Soc. Geol. Peru, 61, 67-100, 1979.

Vogt, P.R., A. Lowrie, D.R. Bracey, and R.N. Hey, Subduction of aseismic oceanic ridges: effects on shape, seismicity and other characteristics of consuming plate boundaries, Geol. Soc. Am. Spec. Paper, 172, 59 pp., 1976.

Wagner, D., Statistical decision theory applied to the focal mechanism of Peruvian earthquakes, Ph.D. dissertation, 176 pp., St. Louis Univ., St. Louis, Mo., 1972.

Weidner, D.L., Rayleigh waves from mid-ocean ridge earthquakes: source and path effects, Ph.D. thesis, M.I.T., 253 pp., 1972.

Weidner, D.L., and K. Aki, Focal depth and mechanism of mid-ocean ridge earthquakes, J. Geophys. Res., 86, 1818-1831, 1973.

Wesnousky, S.G., C.H. Scholz, and K. Shimazaki, Deformation of an island arc: Rates of moment-release and crustal shortening in intraplate Japan determined from seismicity and Quaternary fault data, J. Geophys. Res., in press, 1982.

Wilson, J.J., Cretaceous stratigraphy of the central Andes of Peru, Amer. Assoc. Petr. Geol. Bull., 47, 1-34, 1963.

Wilson, J.J., L. Reyes, and J. Garayar, Geologia de los Cuadrangulos de Mollebamba, Tayabamba, Huaylas, Pomabamba, Carhuaz y Huari, Servicio de Geologia y Mineria, Bol. 16, Lima, Peru, 95 pp., 1967.

Yamashina, K., K. Shimazaki, T. Kato, Aseismic belt along the frontal arc and plate subduction in Japan, J. Phys. Earth, 26, 447-458, 1978.

Yonekura, N., T. Matsuda, M. Nogami, and S. Kaizuka, An active fault along the western part of the Cordillera Blanca, Peru, J. Geography Tokyo, 88, 1-19, 1979.

Zeil, W., The Andes a geological review, 260 pp., Gebruder Borntraeger, Berlin-Stuttgart, Germany, 1979.

Appendix 1

Fault plane solutions and synthetic waveforms for the earthquakes listed in Tables 1 and 2. First motion data are plotted on equal area lower hemispheric projections where the solid circles indicate compressional first motions and open circles dilatational first motions. Observed long period P waves and synthetic waveforms for the fault plane solutions shown are also presented for a few stations. Not all the stations used in the analysis are shown since many of them, specially those in North America and Europe, are clustered at similar azimuth and epicentral distance from the source and have very similar waveforms. Synthetic waveforms computed at various focal dephts are also shown versus the observed long period P waves at a few stations spanning a range of azimuths and epicentral distances. Arrow indicates preferred focal depth. ⊥ indicates amplitude was reduced in half for plotting purposes.

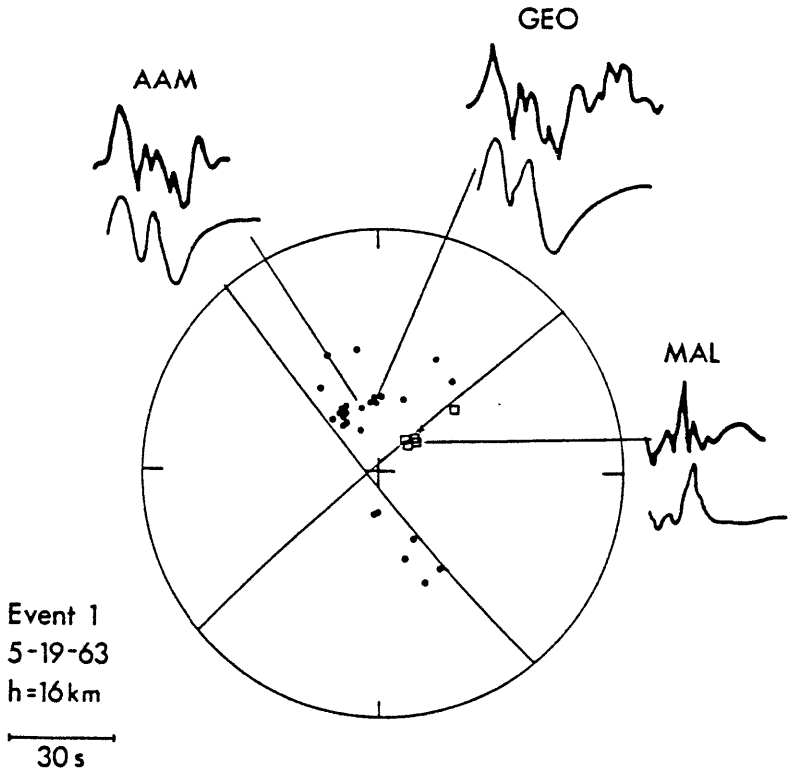
GEO
AAM
MAL
Event 1
5-19-63
h=16km
30s

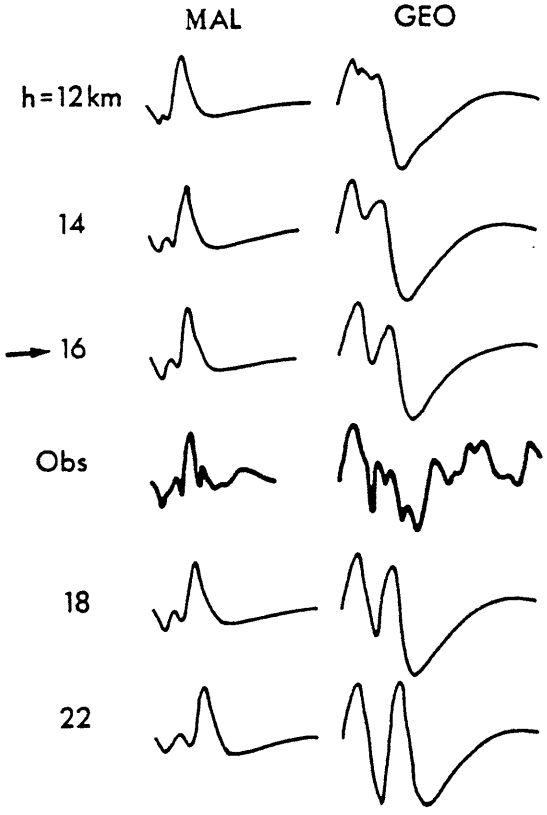
MAL
GEO
h=12km
14
16
Obs
18
22

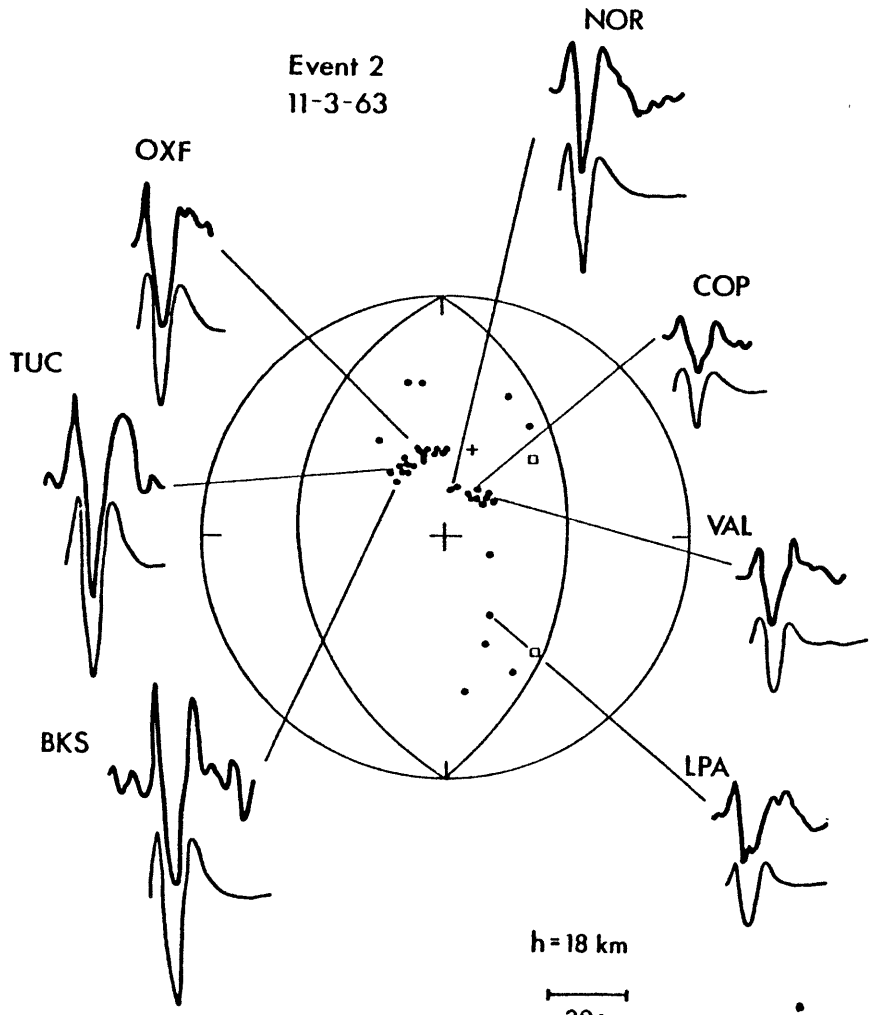
Event 2
11-3-63
NOR
OXF
COP
TUC
VAL
BKS
LPA
h = 18 km
30s

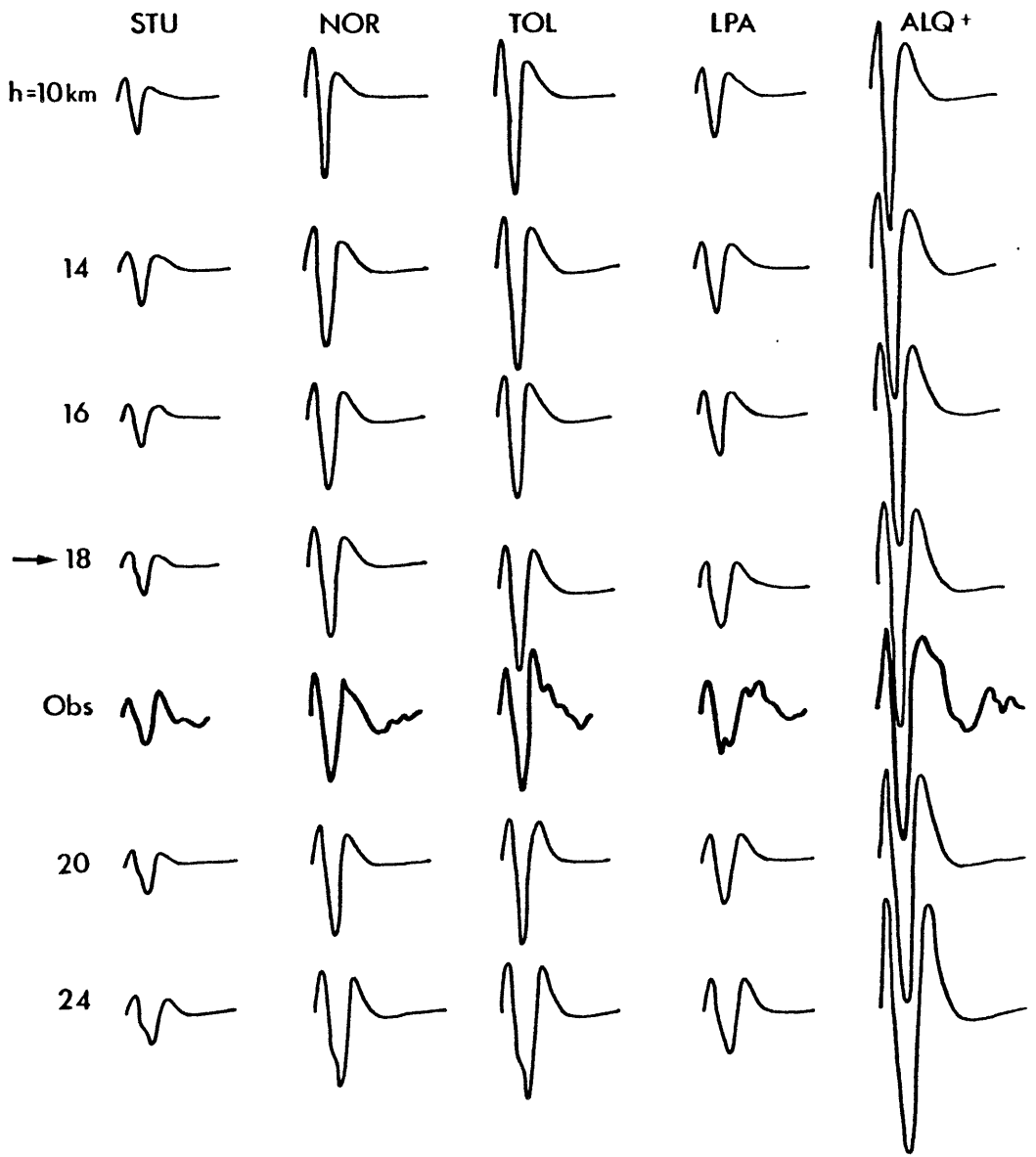
STU
NOR
TOL
LPA
ALQ +
h=10km
14
16
18
Obs
20
24

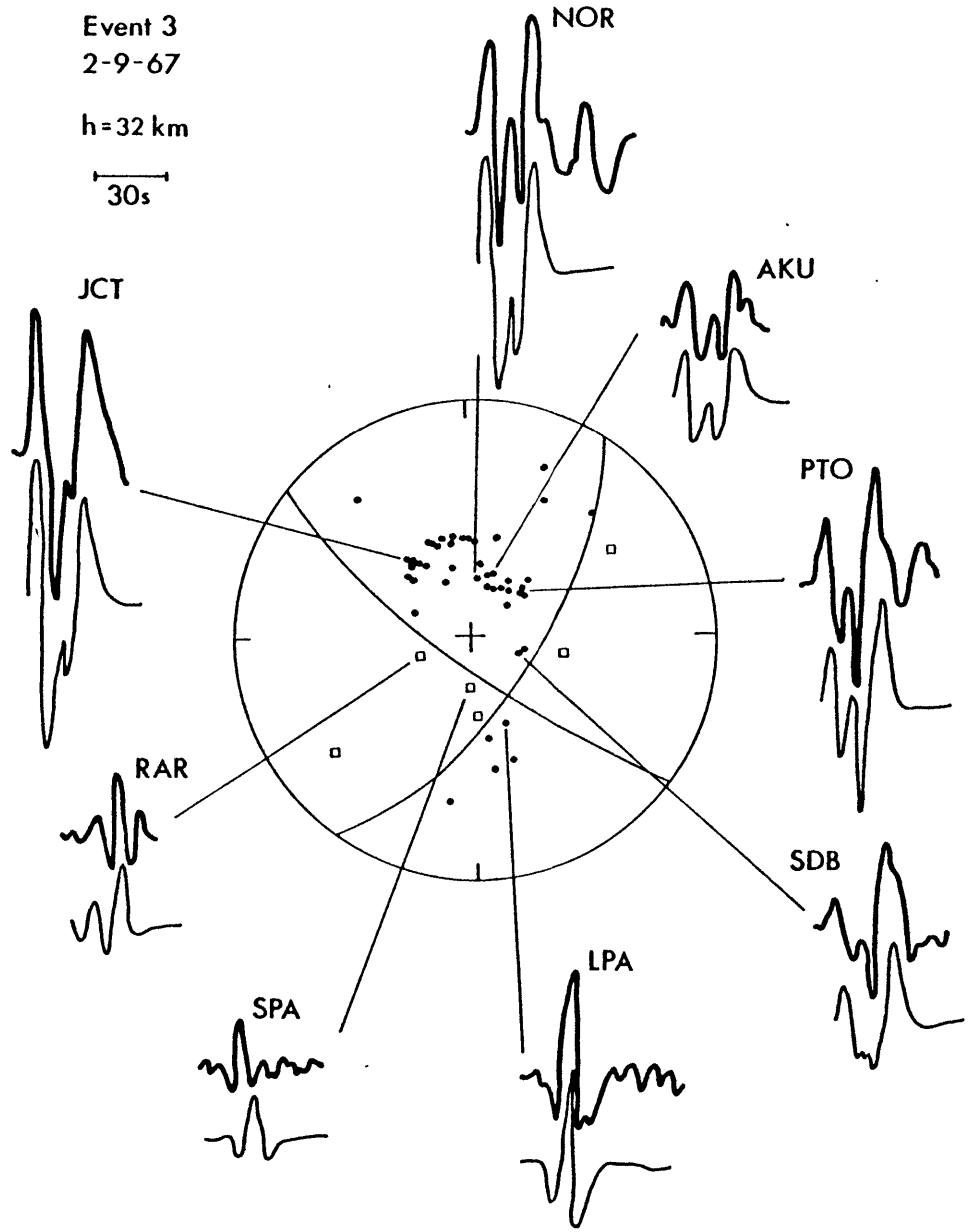
Event 3
2-9-67
h=32 km
30s
NOR
AKU
JCT
PTO
RAR
SDB
LPA
SPA

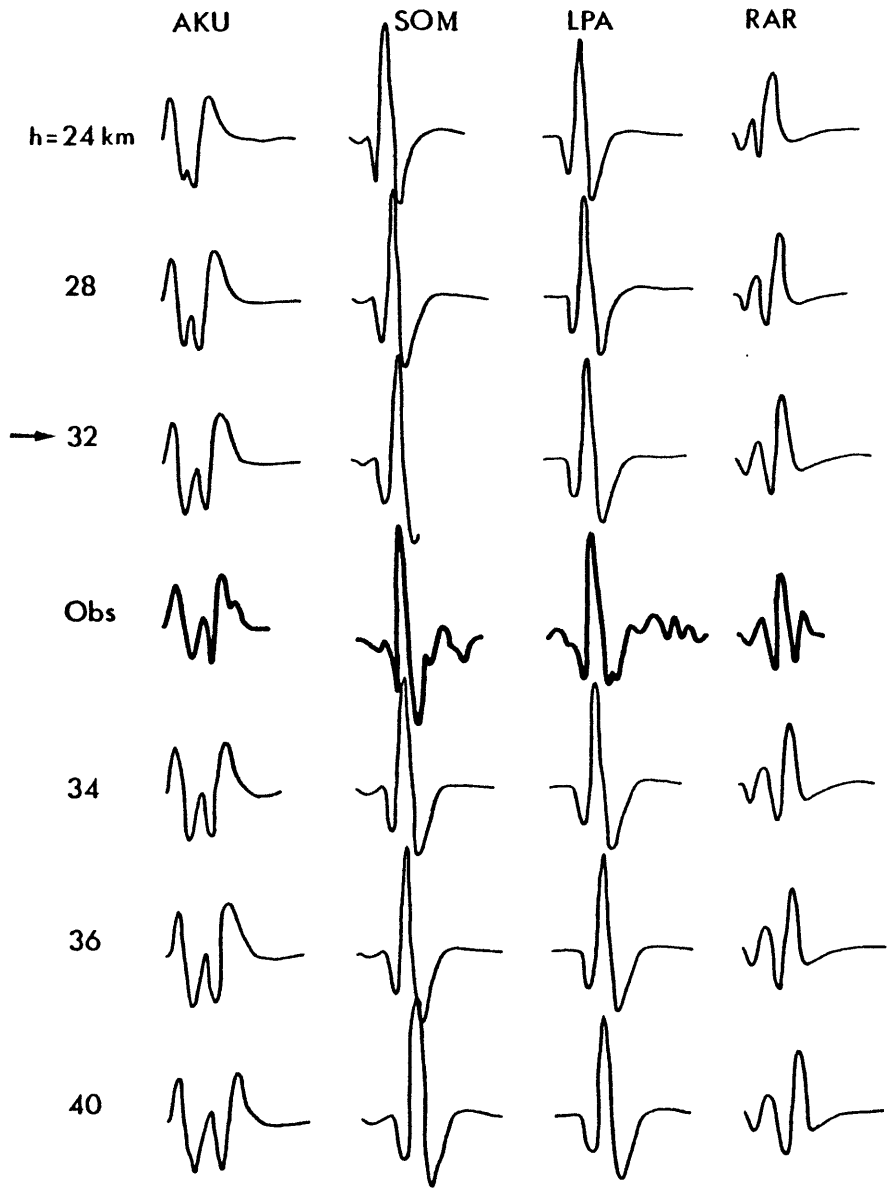
AKU
SOM
LPA
RAR
h=24 km
28
32
Obs
34
36
40

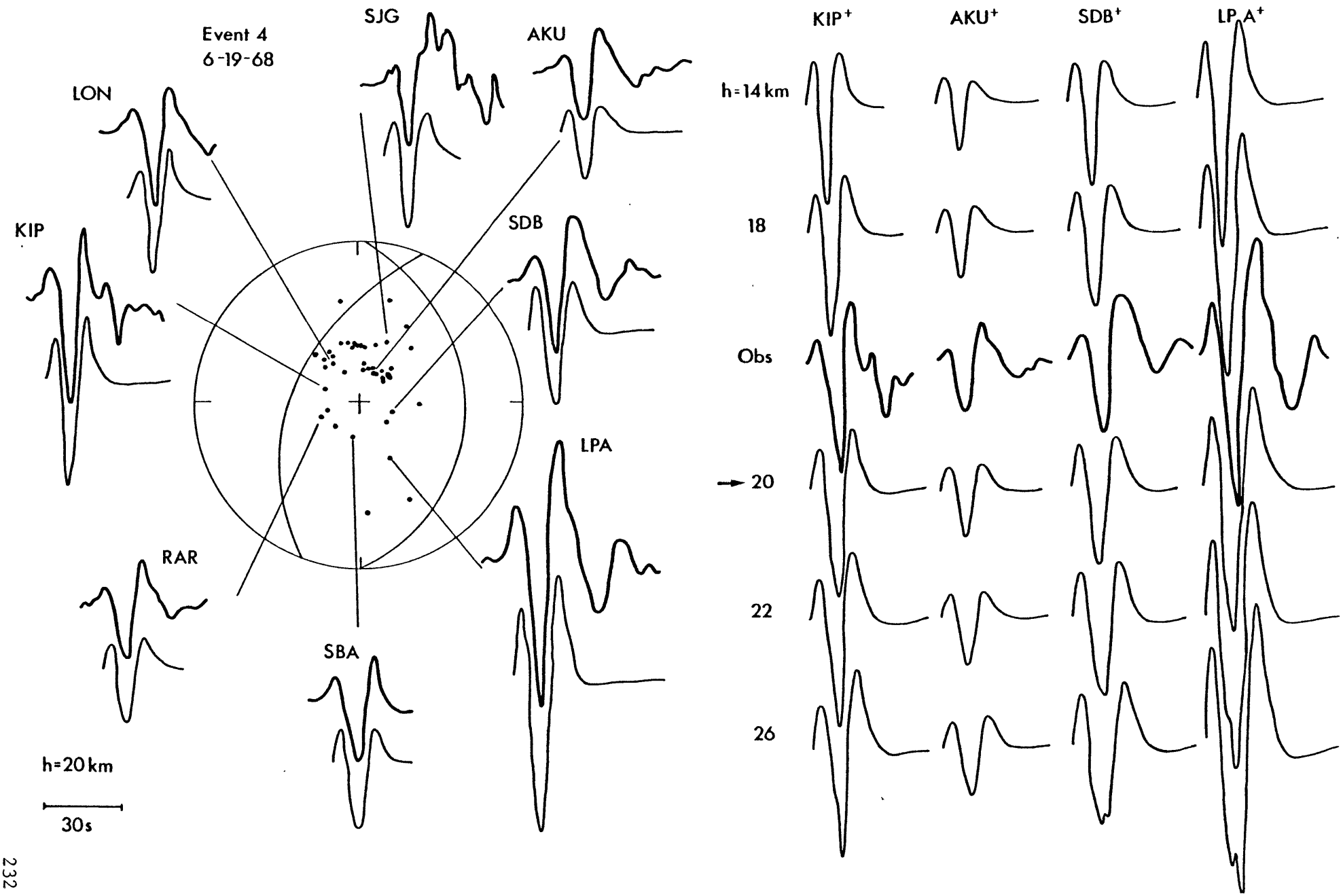
Event 4
6-19-68
SJG
AKU
LON
KIP
SDB
LPA
RAR
SBA
h=20 km
30s
KIP+
AKU+
SDB+
LP A+
h=14 km
18
Obs
20
22
26

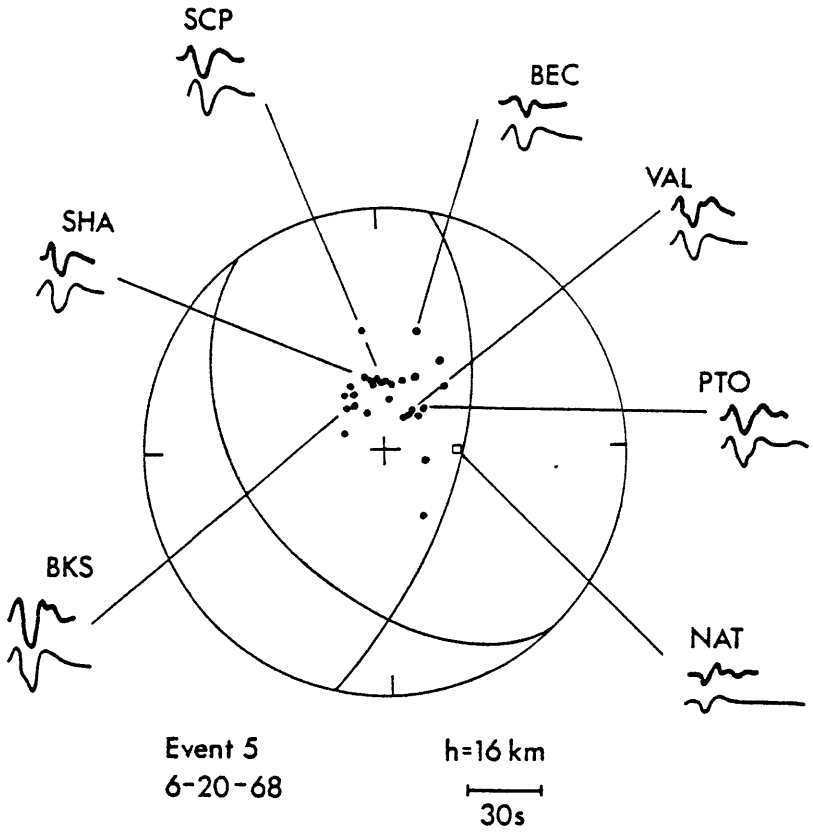
SCP
BEC
VAL
SHA
PTO
BKS
NAT
Event 5
6-20-68
h=16 km
30s

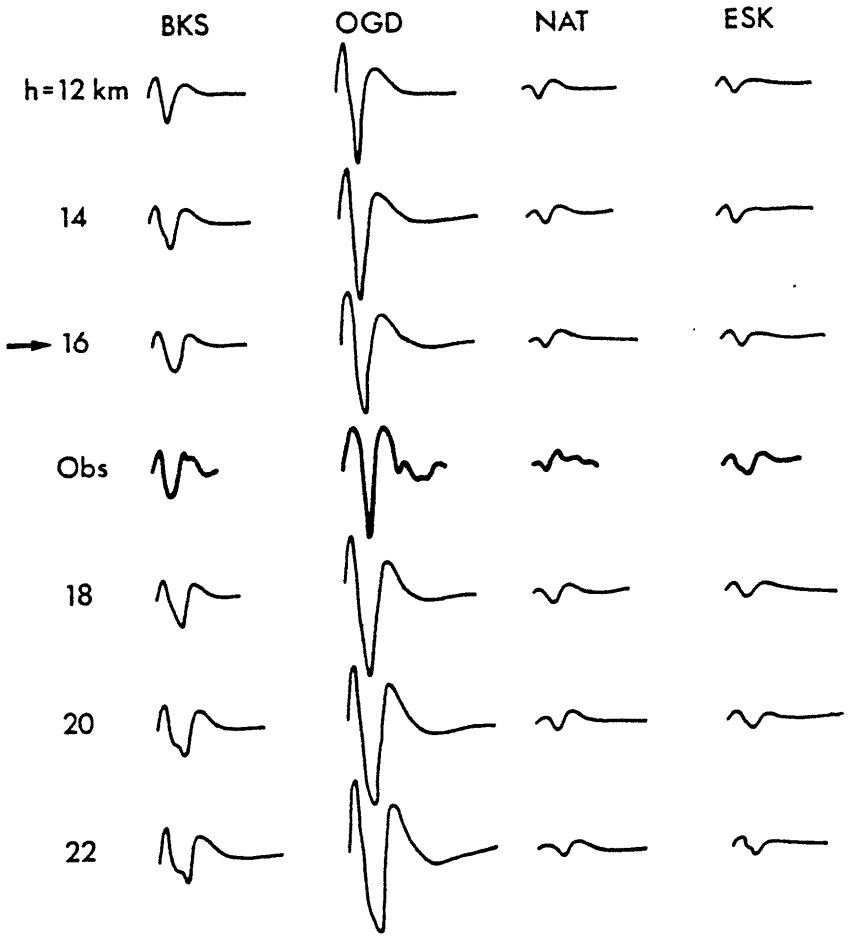
BKS
OGD
NAT
ESK
h=12 km
14
16
Obs
18
20
22

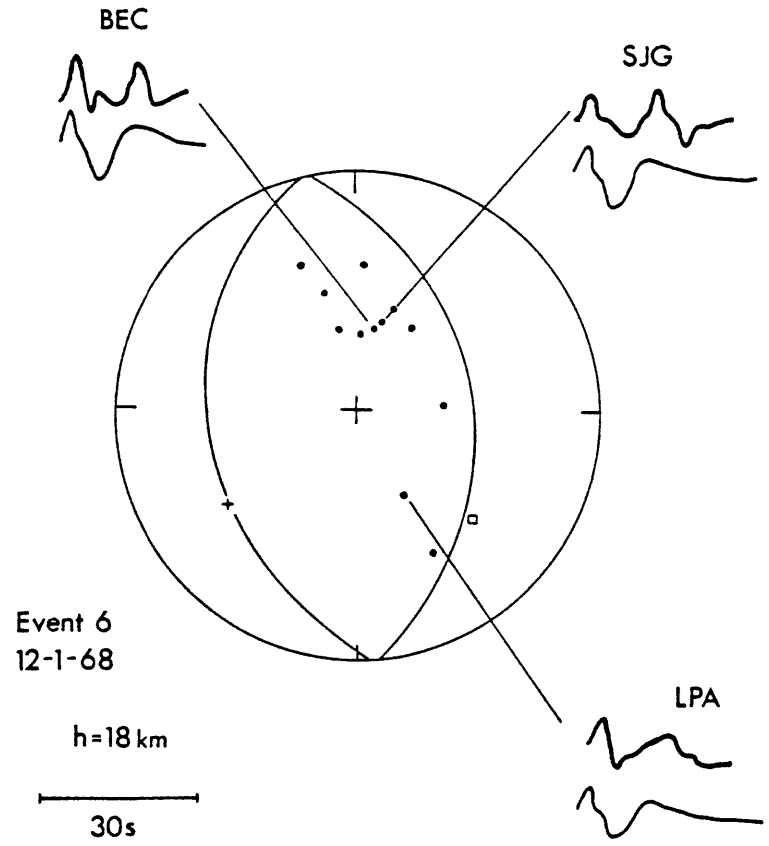
BEC
SJG
LPA
Event 6
12-1-68
h=18 km
30s

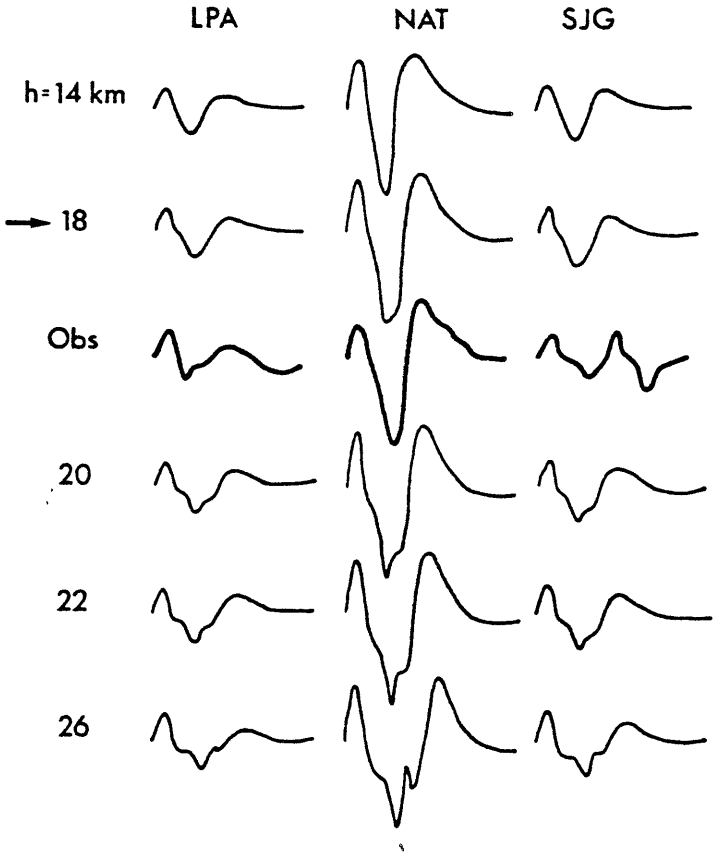
LPA
NAT
SJG
h=14 km
18
Obs
20
22
26

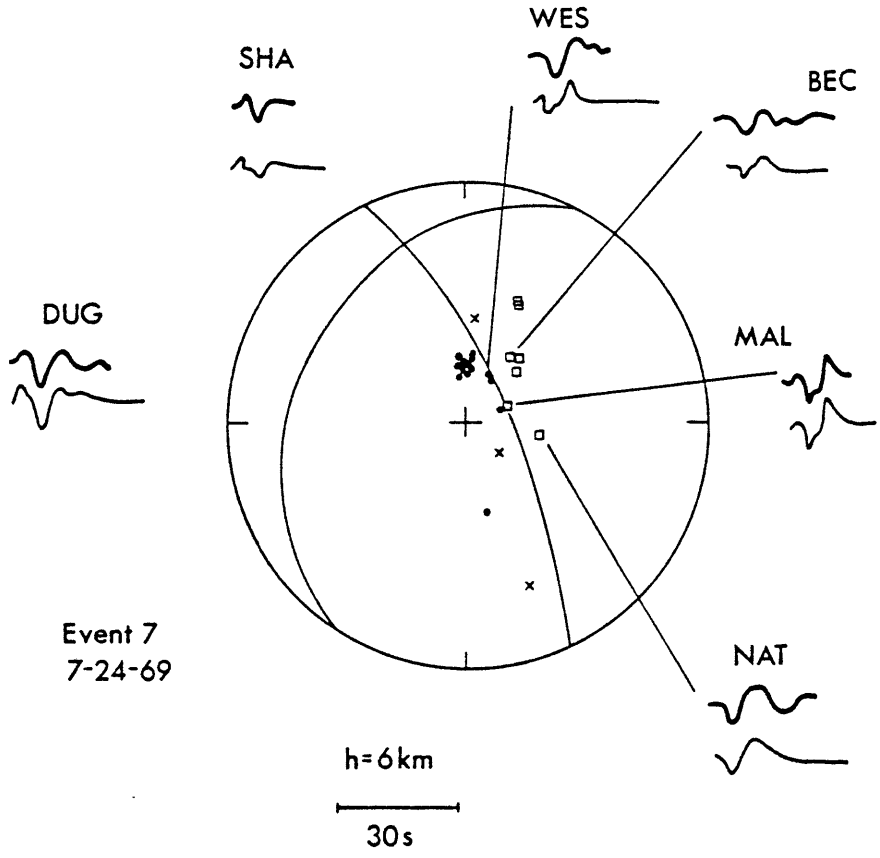
WES
SHA
BEC
DUG
MAL
NAT
Event 7
7-24-69
h=6km
30s

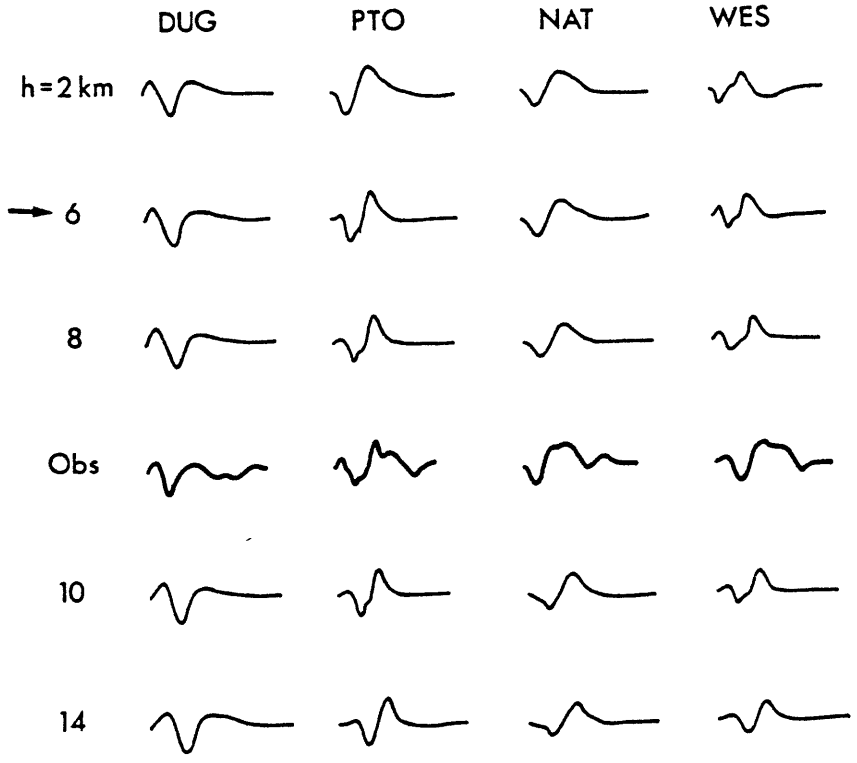
DUG
PTO
NAT
WES
h=2km
6
8
Obs
10
14

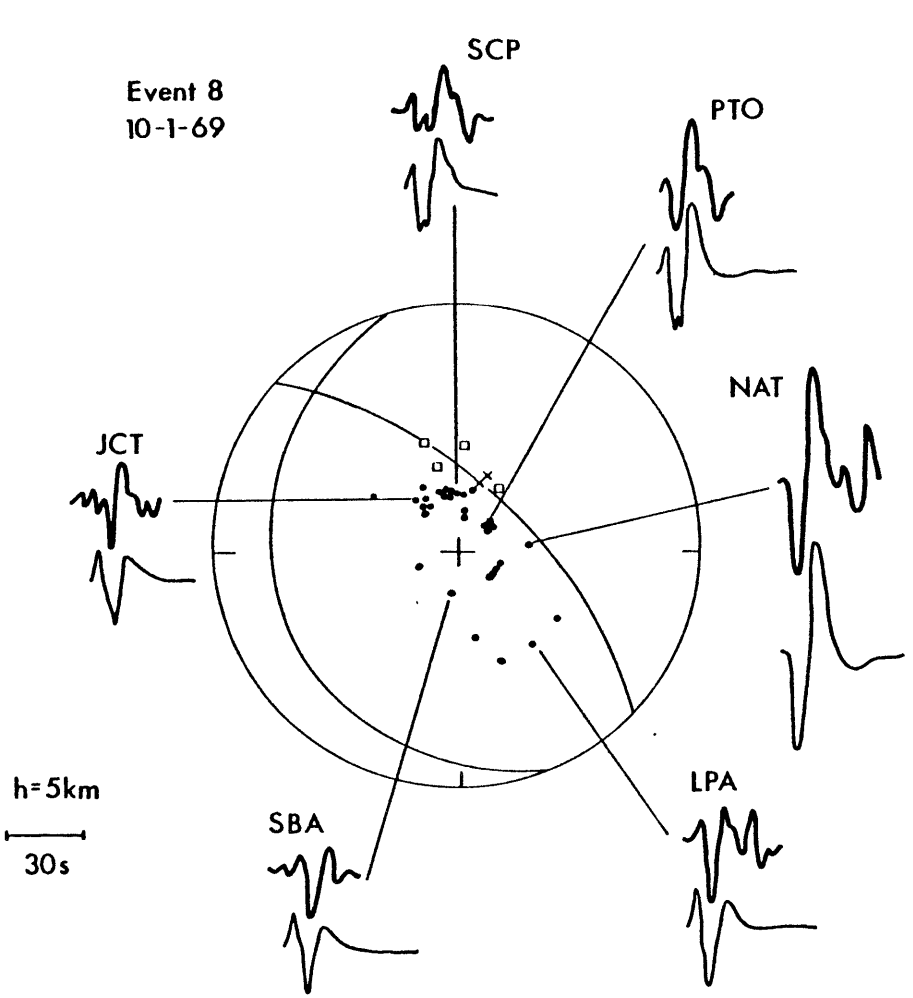
Event 8
10-1-69
SCP
PTO
NAT
JCT
LPA
SBA
h=5km
30s

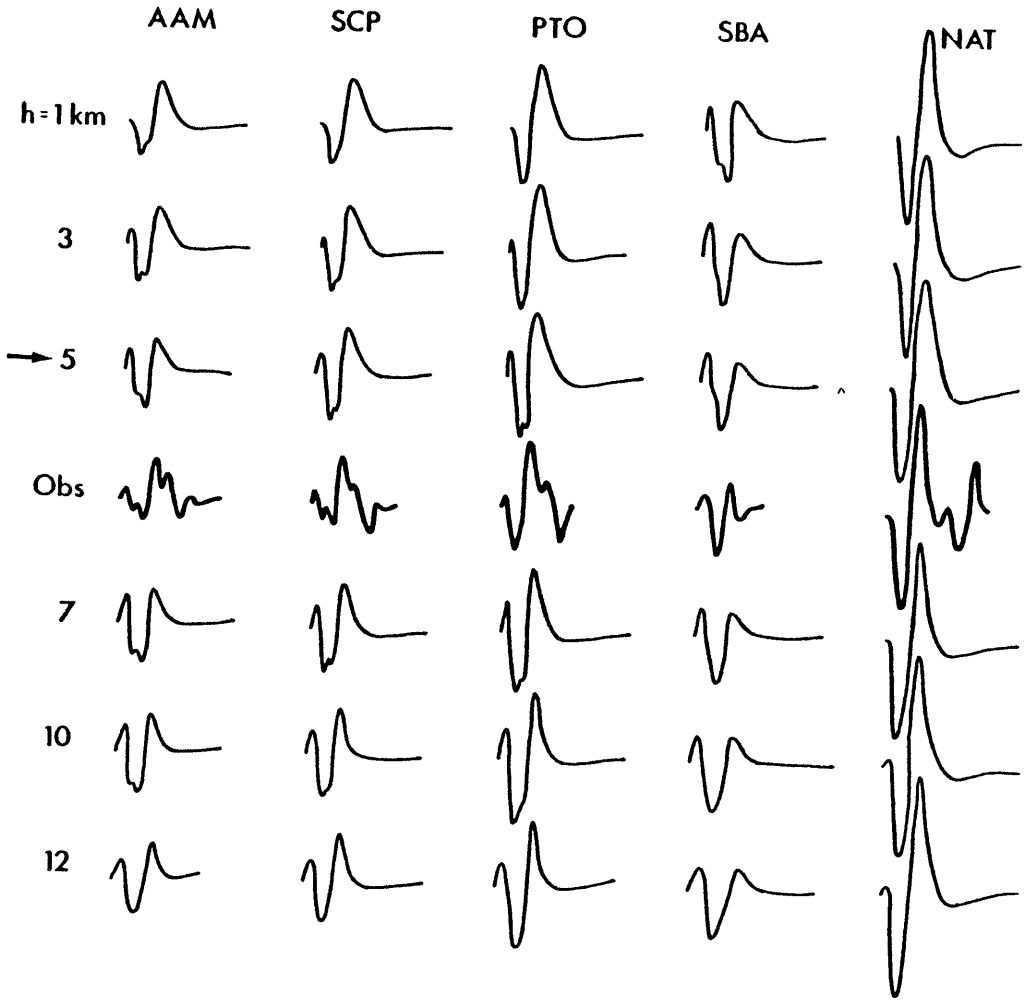
AAM
SCP
PTO
SBA
NAT
h=1km
3
5
Obs
7
10
12

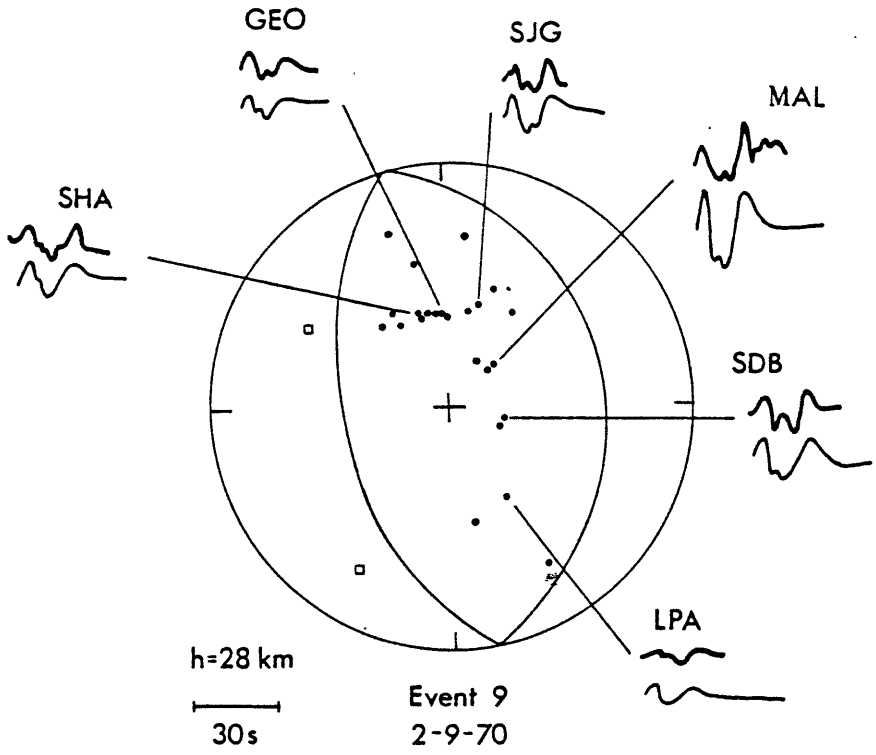
GEO
SJG
MAL
SHA
SDB
LPA
h=28 km
30s
Event 9
2-9-70

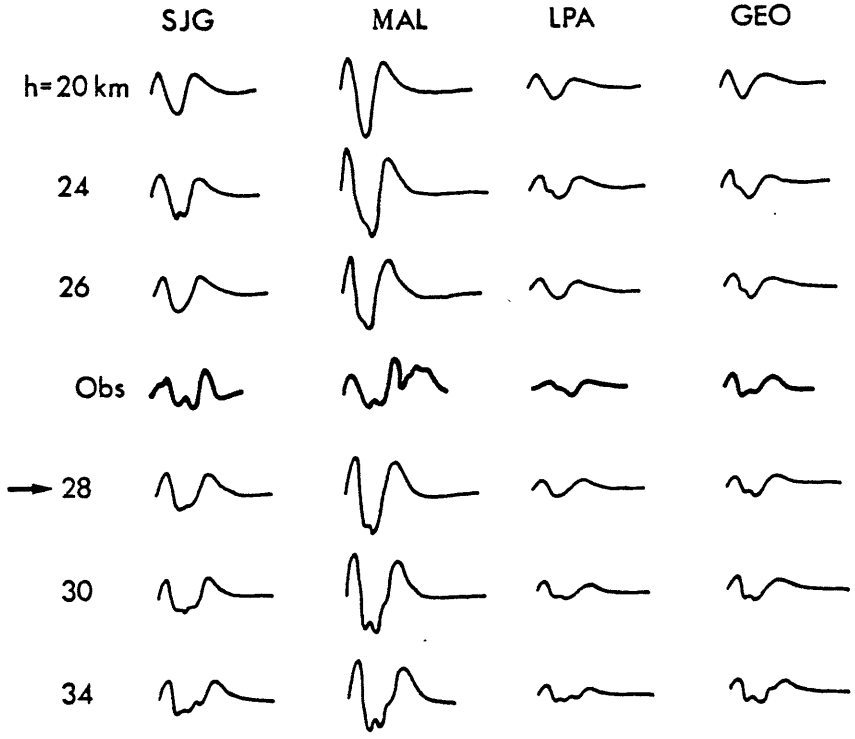
SJG
MAL
LPA
GEO
h=20 km
24
26
Obs
28
30
34

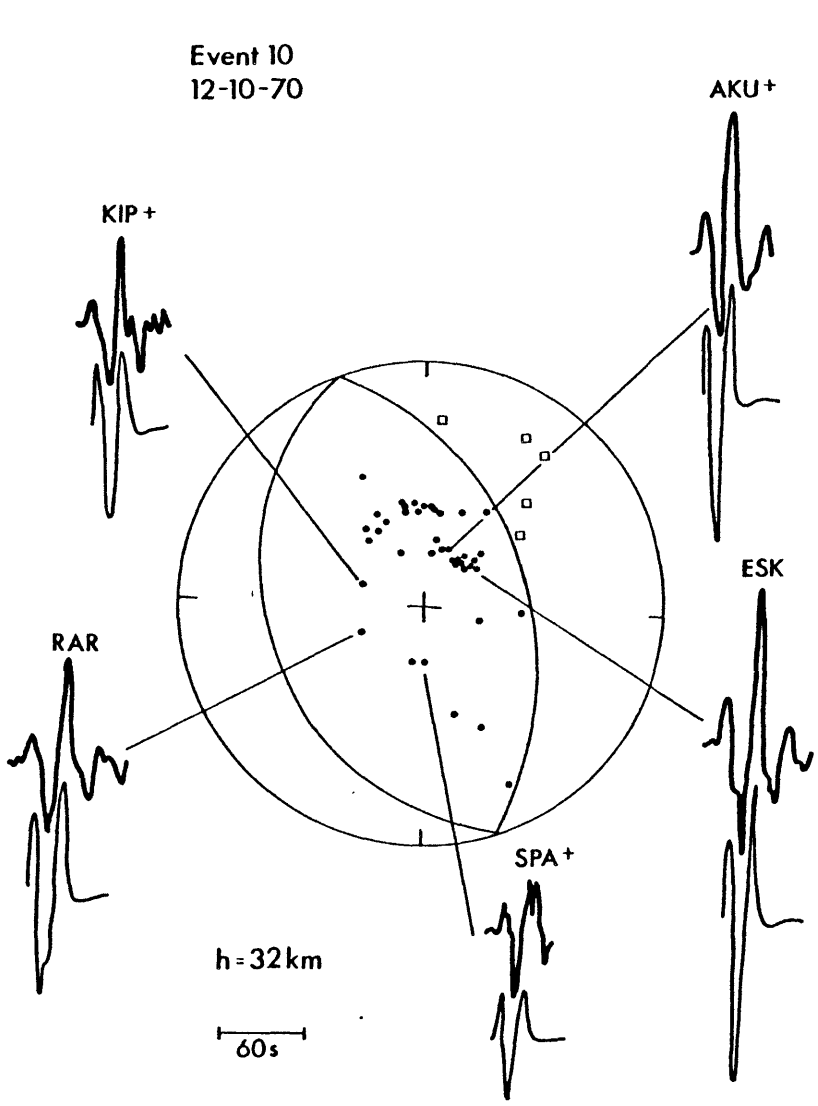
Event 10
12-10-70
AKU+
KIP+
ESK
RAR
SPA+
h=32km
60s

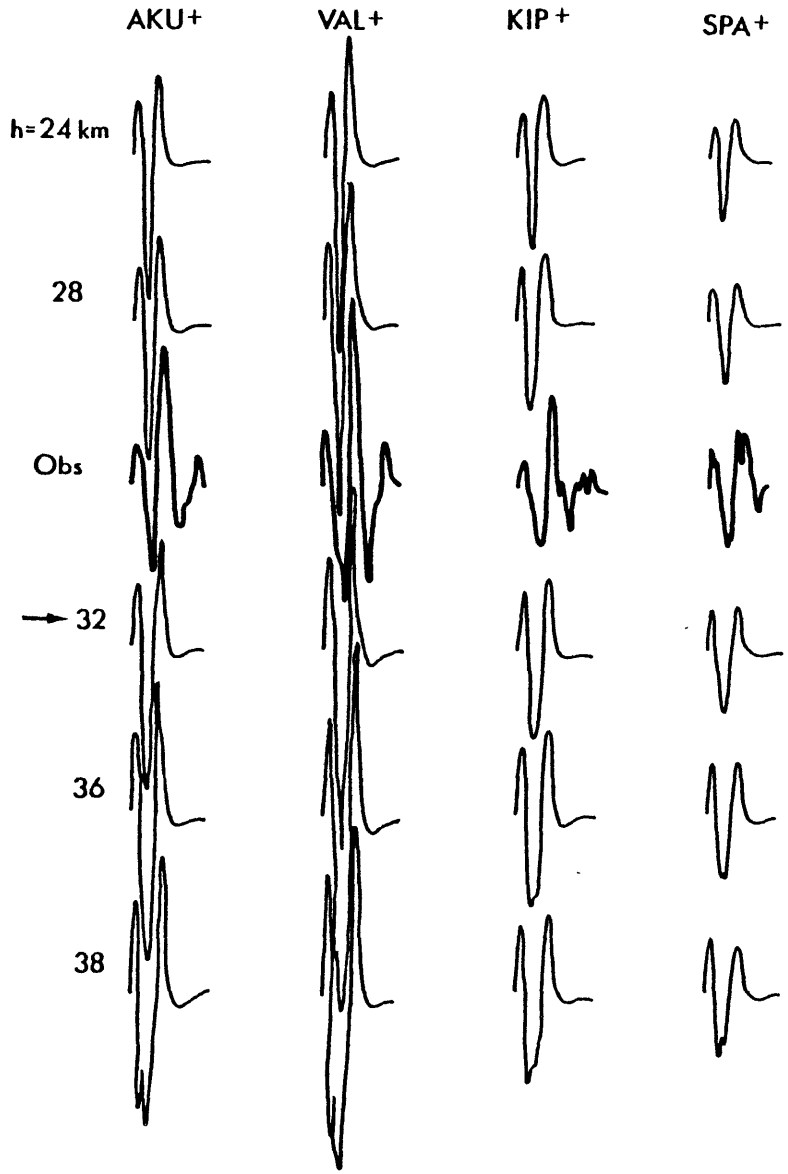
AKU+
VAL+
KIP+
SPA+
h=24 km
28
Obs
32
36
38

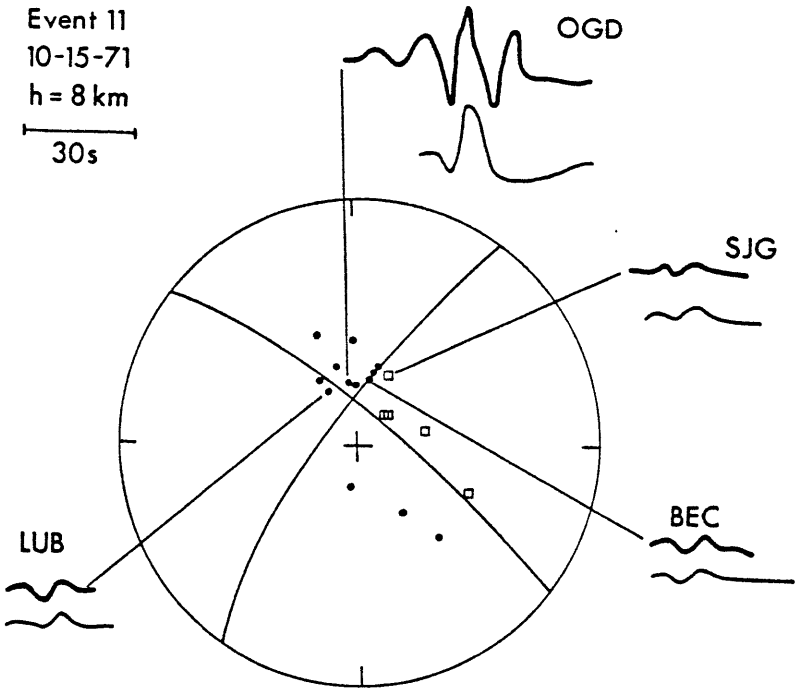
Event 11
10-15-71
h = 8 km
30s
OGD
SJG
BEC
LUB

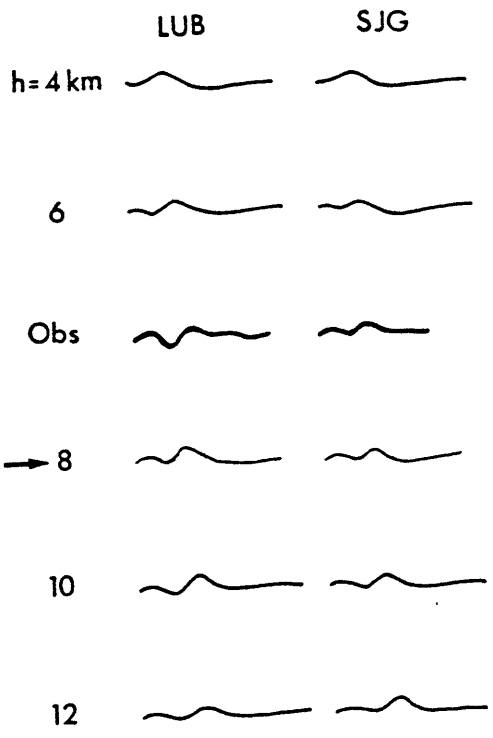
LUB
SJG
h= 4 km
6
Obs
8
10
12

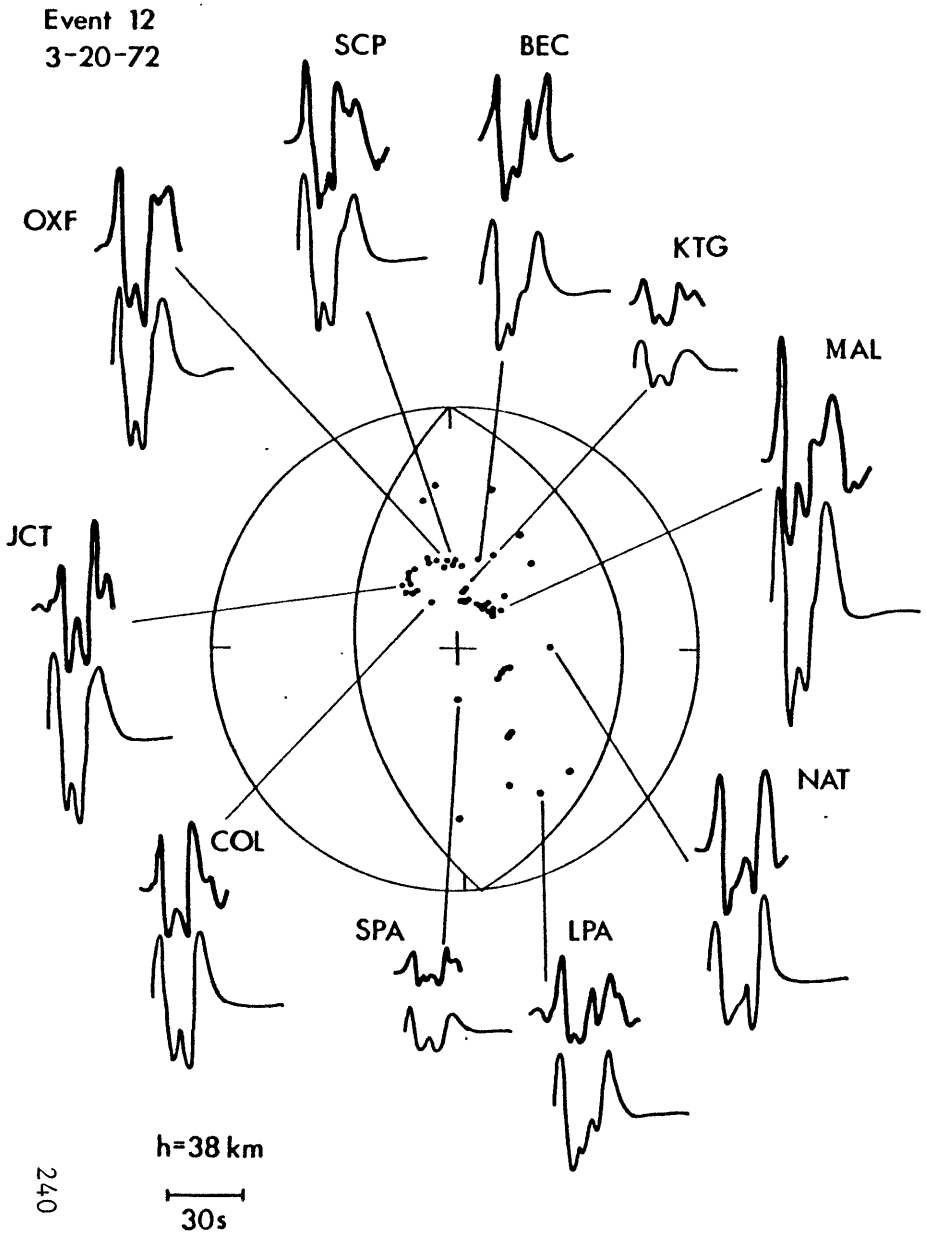
Event 12
3-20-72
SCP
BEC
OXF
KTG
MAL
JCT
NAT
COL
SPA
LPA
h=38 km
30s

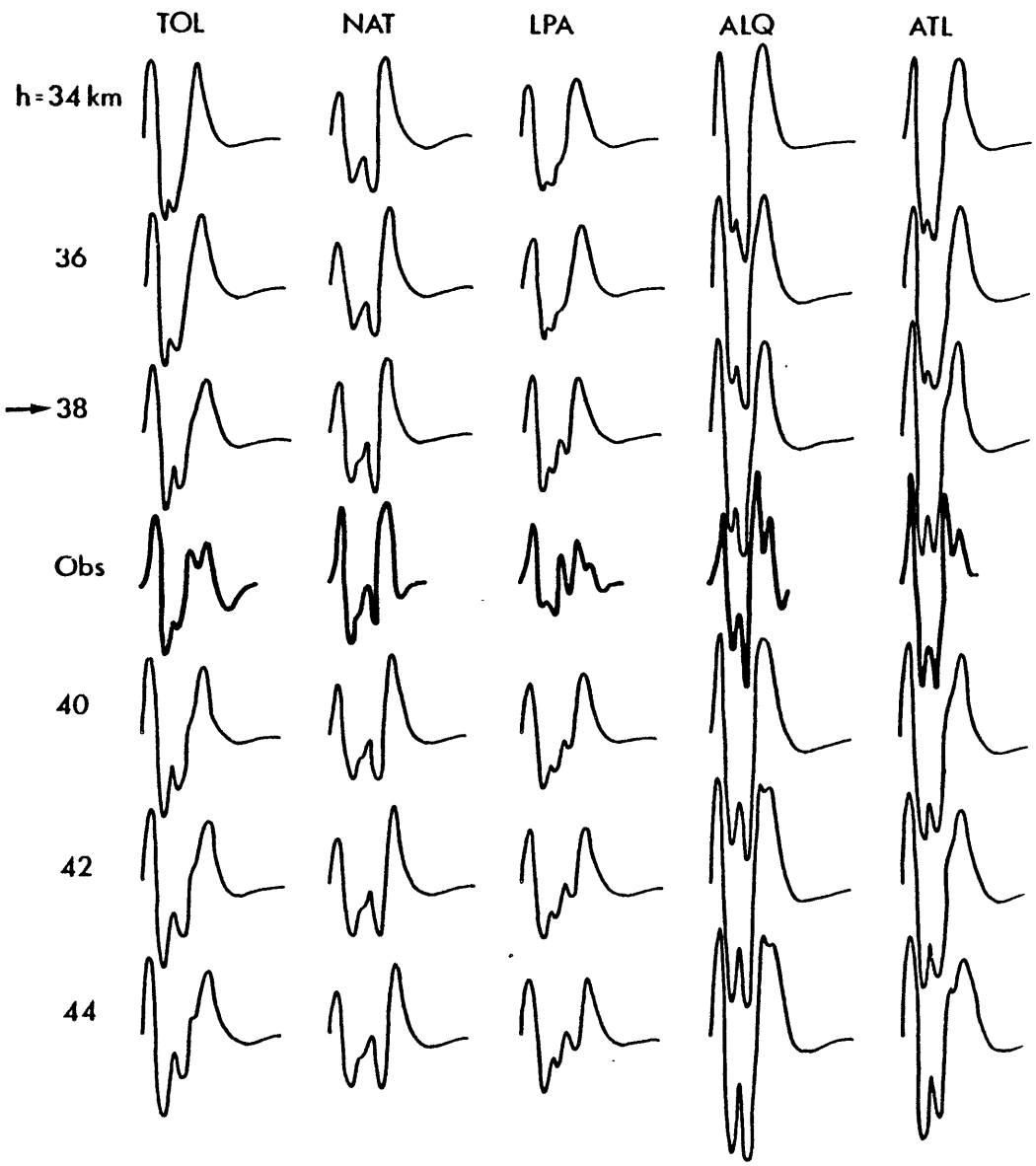
TOL
NAT
LPA
ALQ
ATL
h=34 km
36
38
Obs
40
42
44

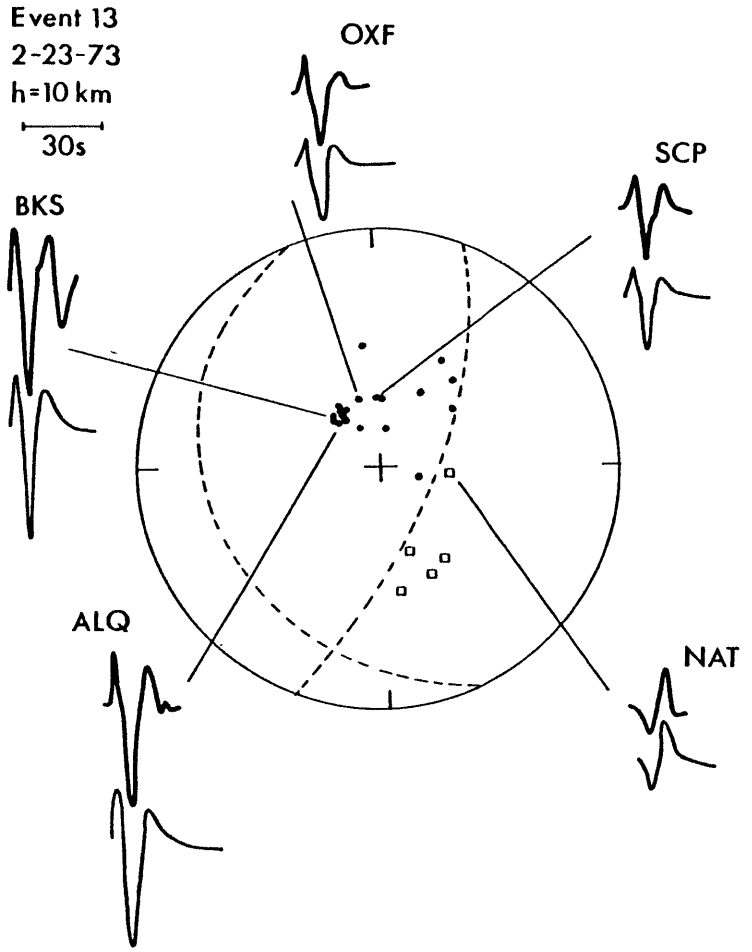
Event 13
2-23-73
h=10 km
30s
OXF
SCP
BKS
ALQ
NAT

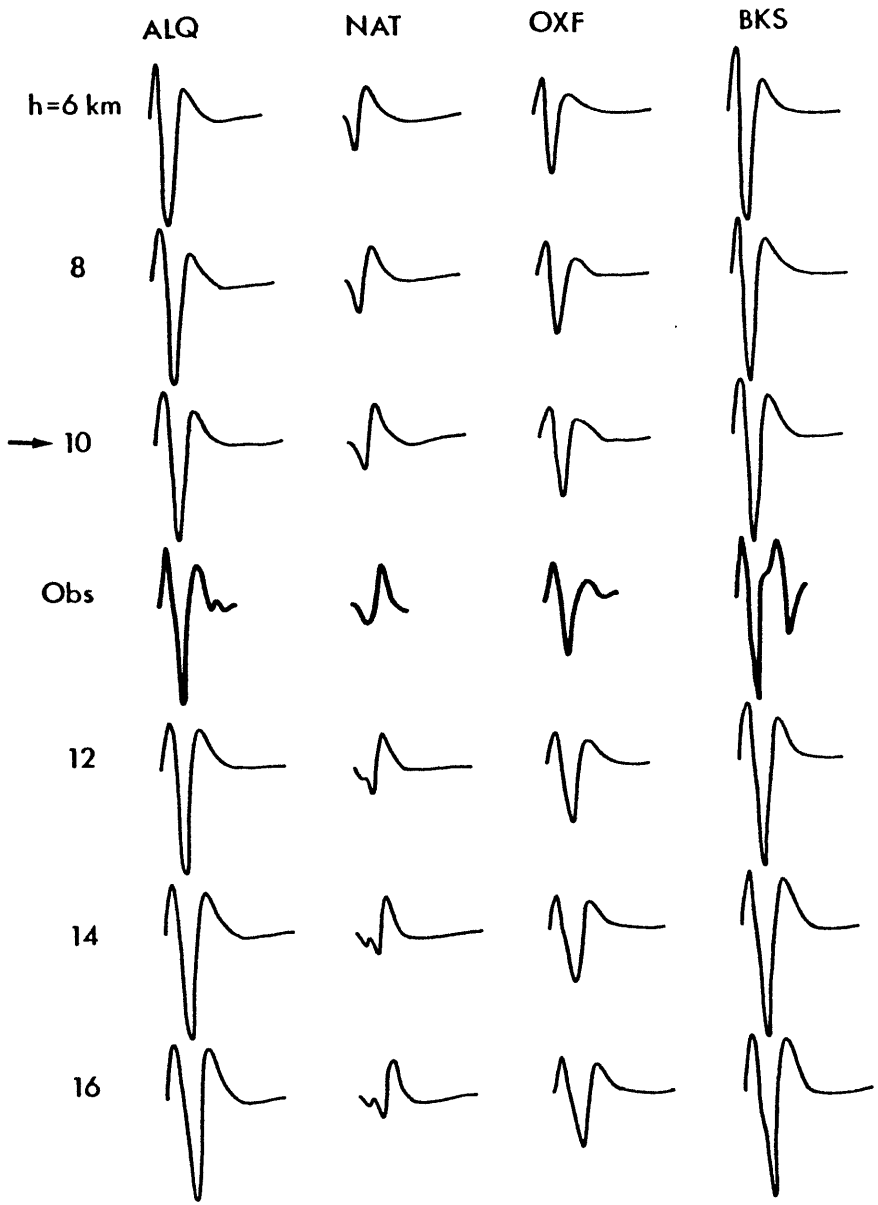
ALQ
NAT
OXF
BKS
h=6 km
8
10
Obs
12
14
16

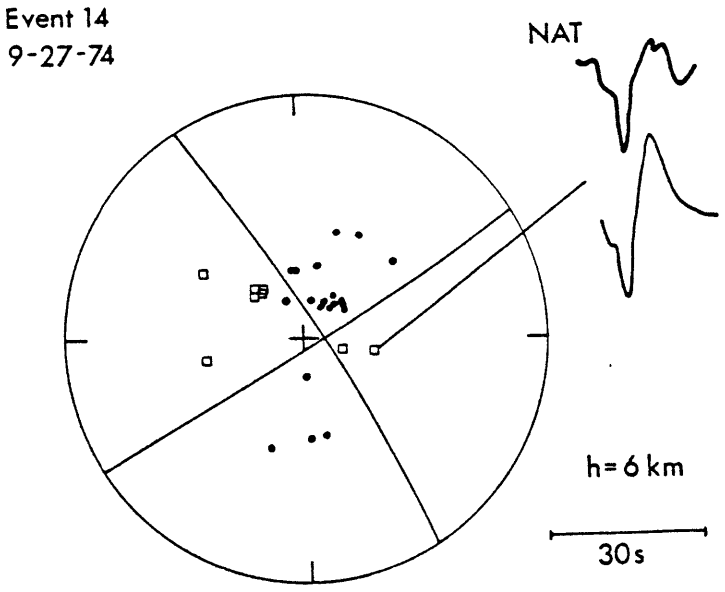
Event 14
9-27-74
NAT
h= 6 km
30 s

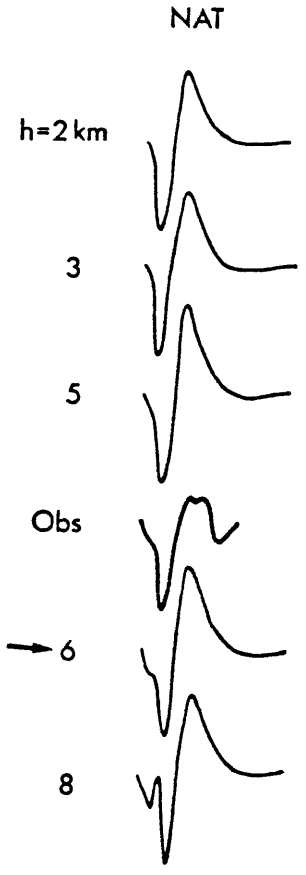
NAT
h=2 km
3
5
Obs
6
8

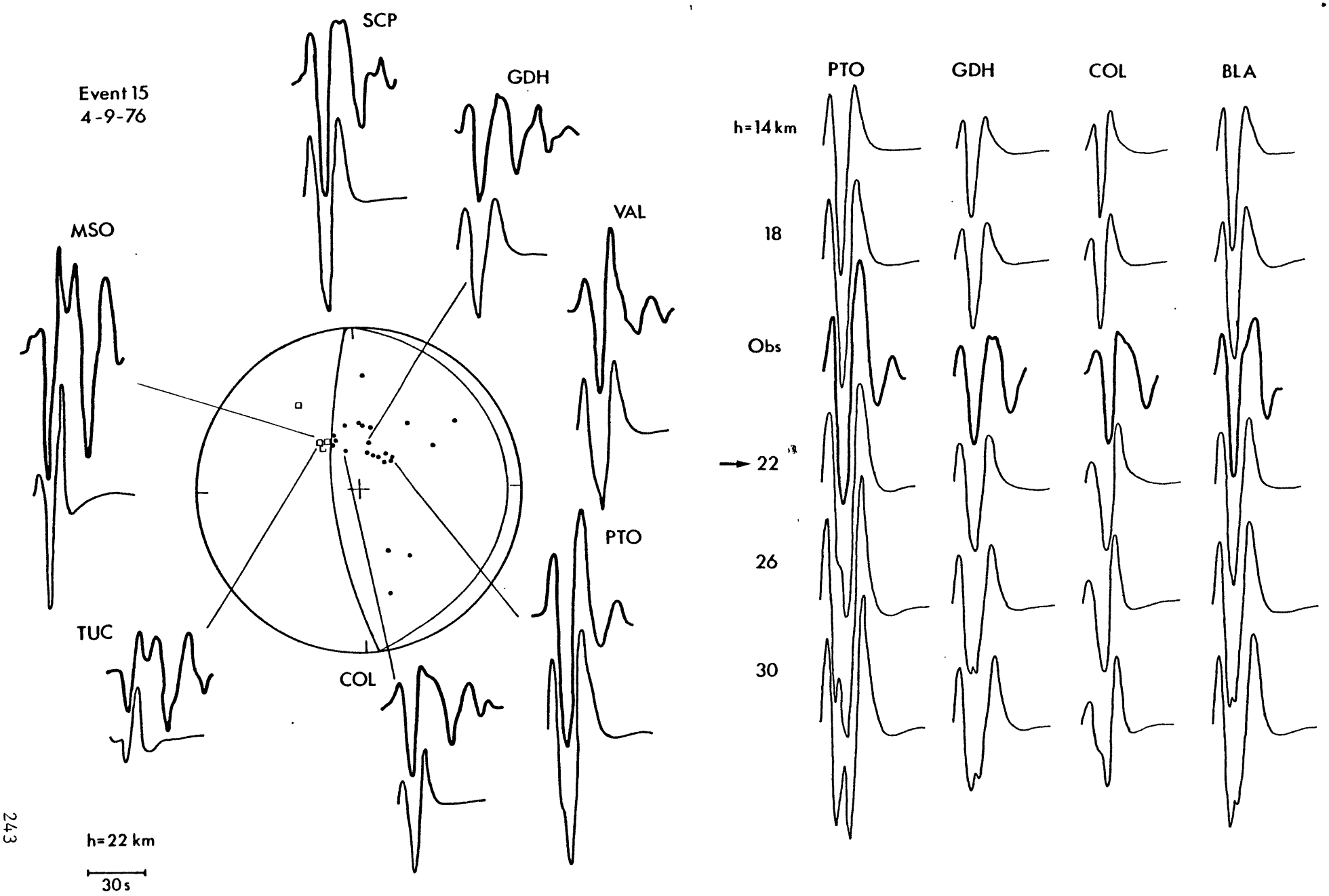
Event 15
4-9-76
SCP
GDH
VAL
MSO
PTO
TUC
COL
h=22 km
30s
PTO
GDH
COL
BLA
h=14 km
18
Obs
22
26
30

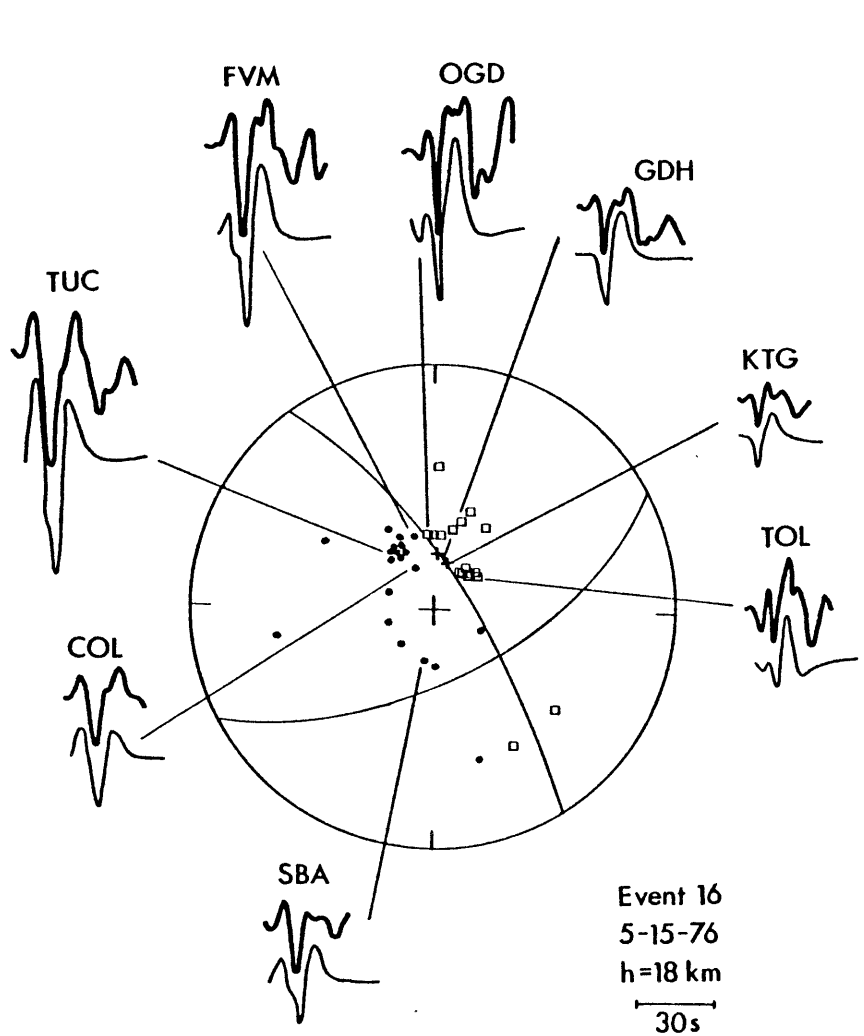
FVM
OGD
GDH
TUC
KTG
TOL
COL
SBA
Event 16
5-15-76
h=18 km
30s

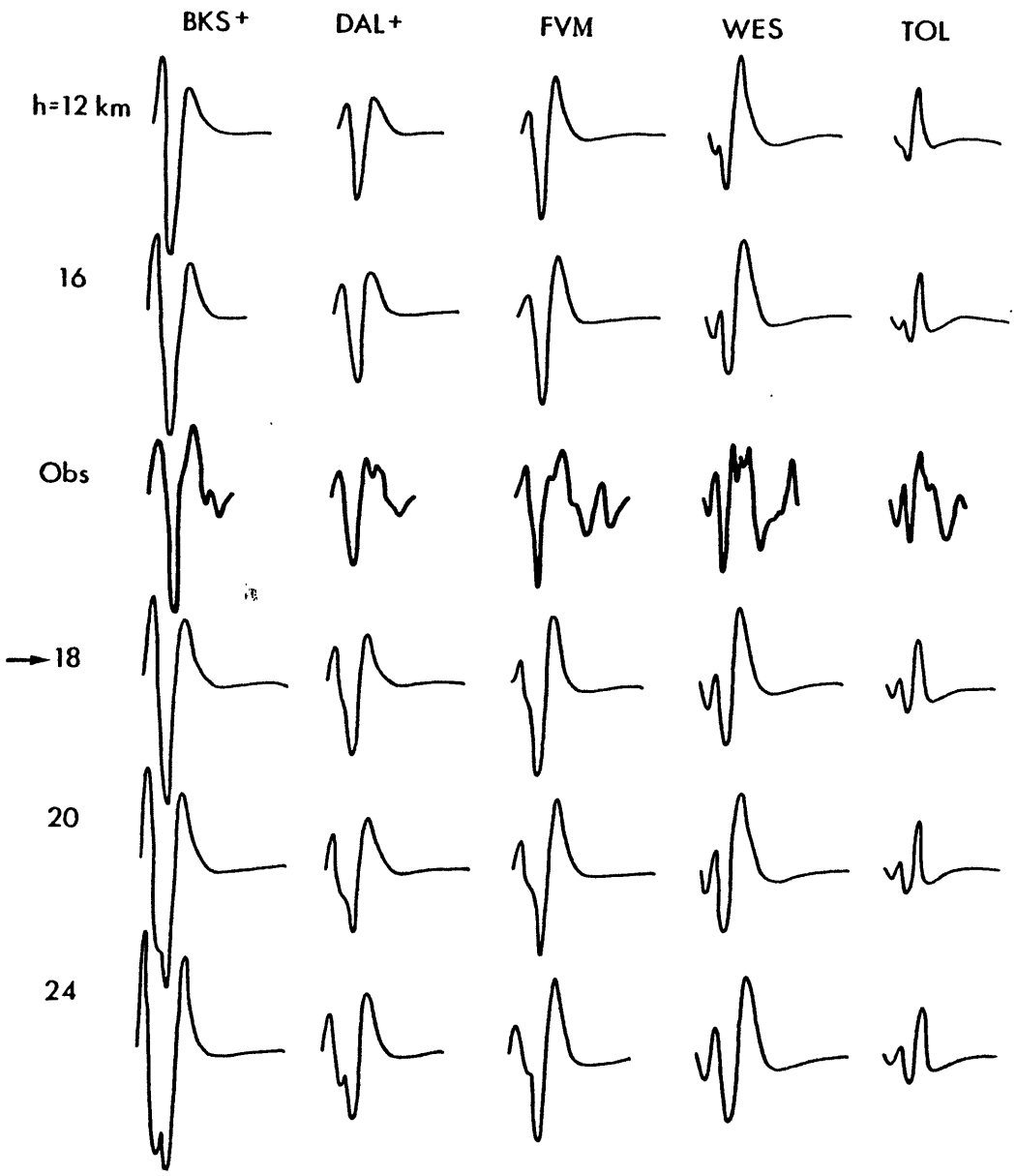
BKS+
DAL+
FVM
WES
TOL
h=12 km
16
Obs
18
20
24

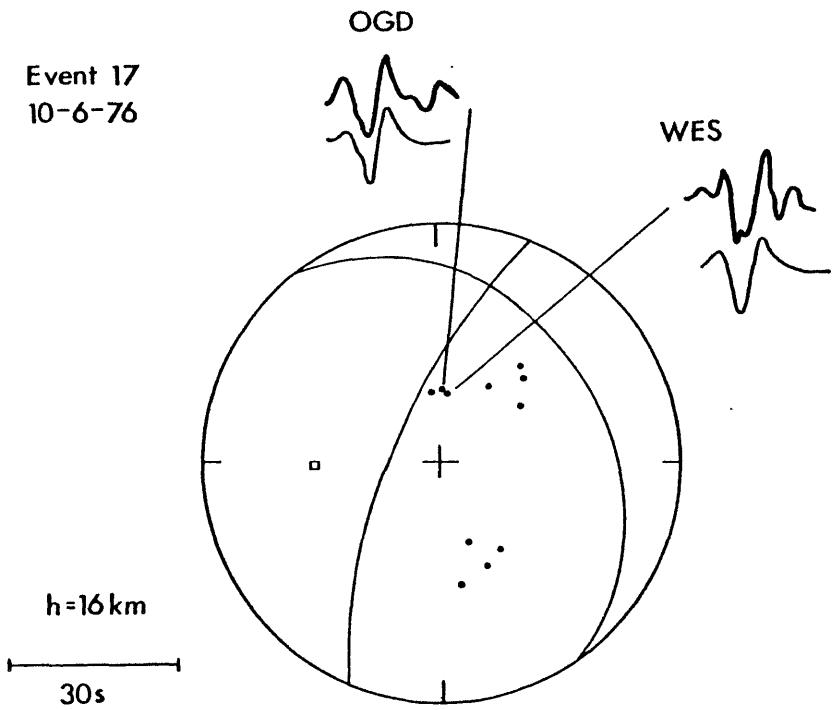
OGD
Event 17
10-6-76
WES
h=16km
30s

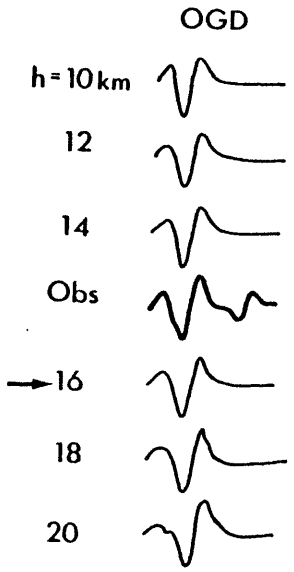
OGD
h=10km
12
14
Obs
16
18
20

Appendix 2

Phase velocities measured from the reference point to WWSSN stations around the world. Phase velocities are plotted for different stations grouped by geographical area.

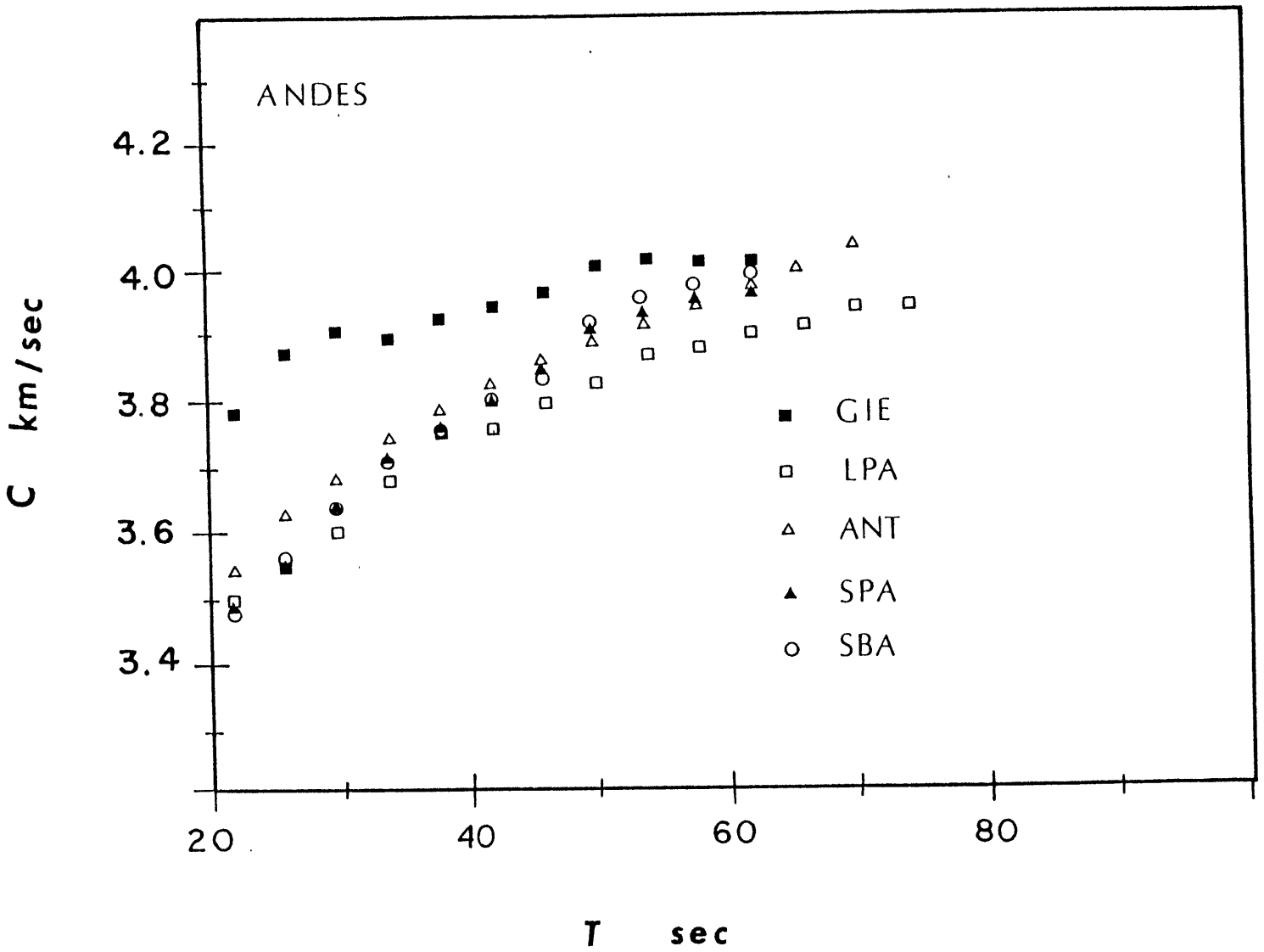
ANDES
4.2
4.0
3.8
3.6
3.4
C km/sec
20
40
60
80
T sec
GIE
LPA
ANT
SPA
SBA

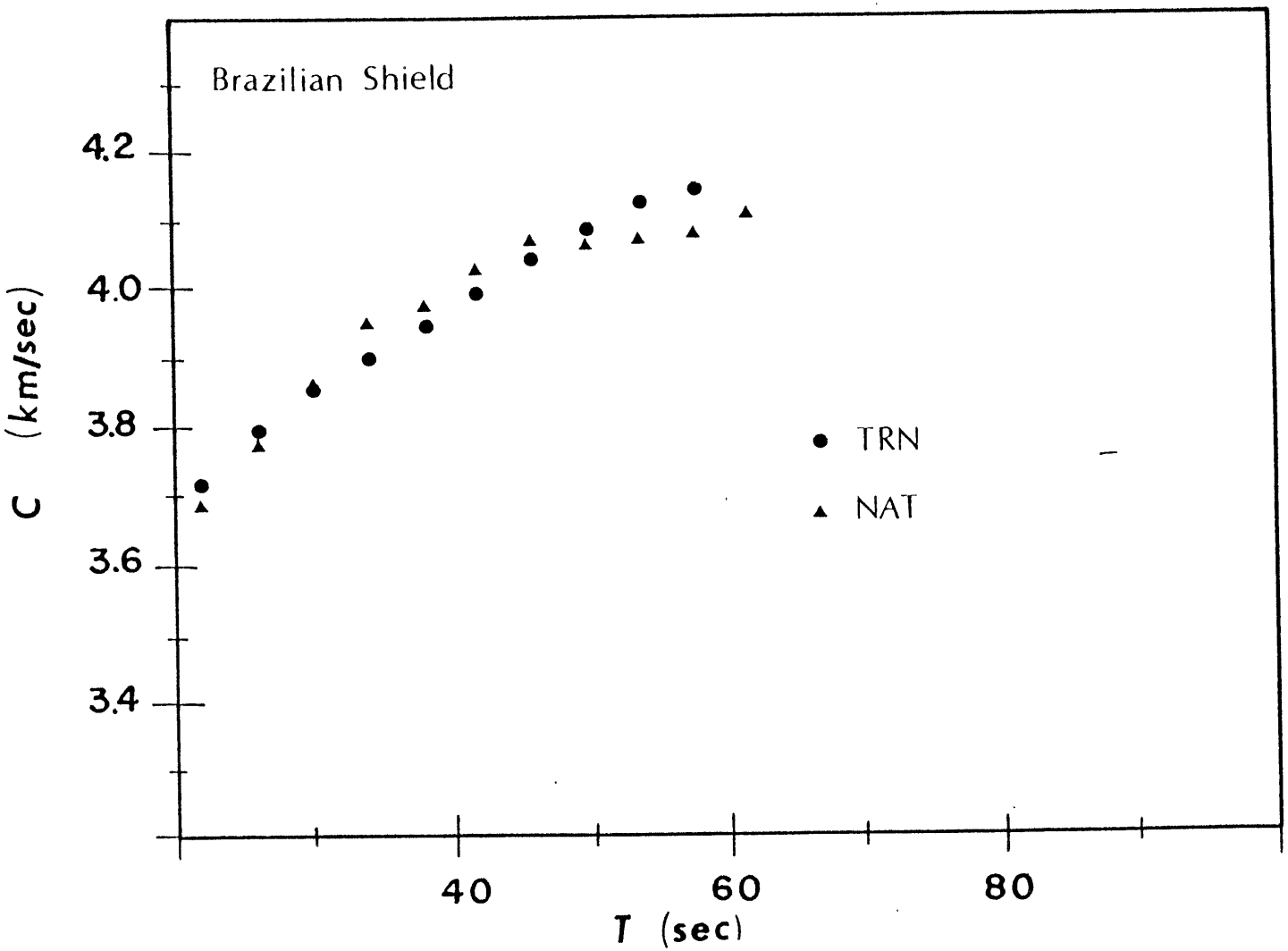
Brazilian Shield
4.2
4.0
3.8
3.6
3.4
C (km/sec)
TRN
NAT
40
60
80
T (sec)

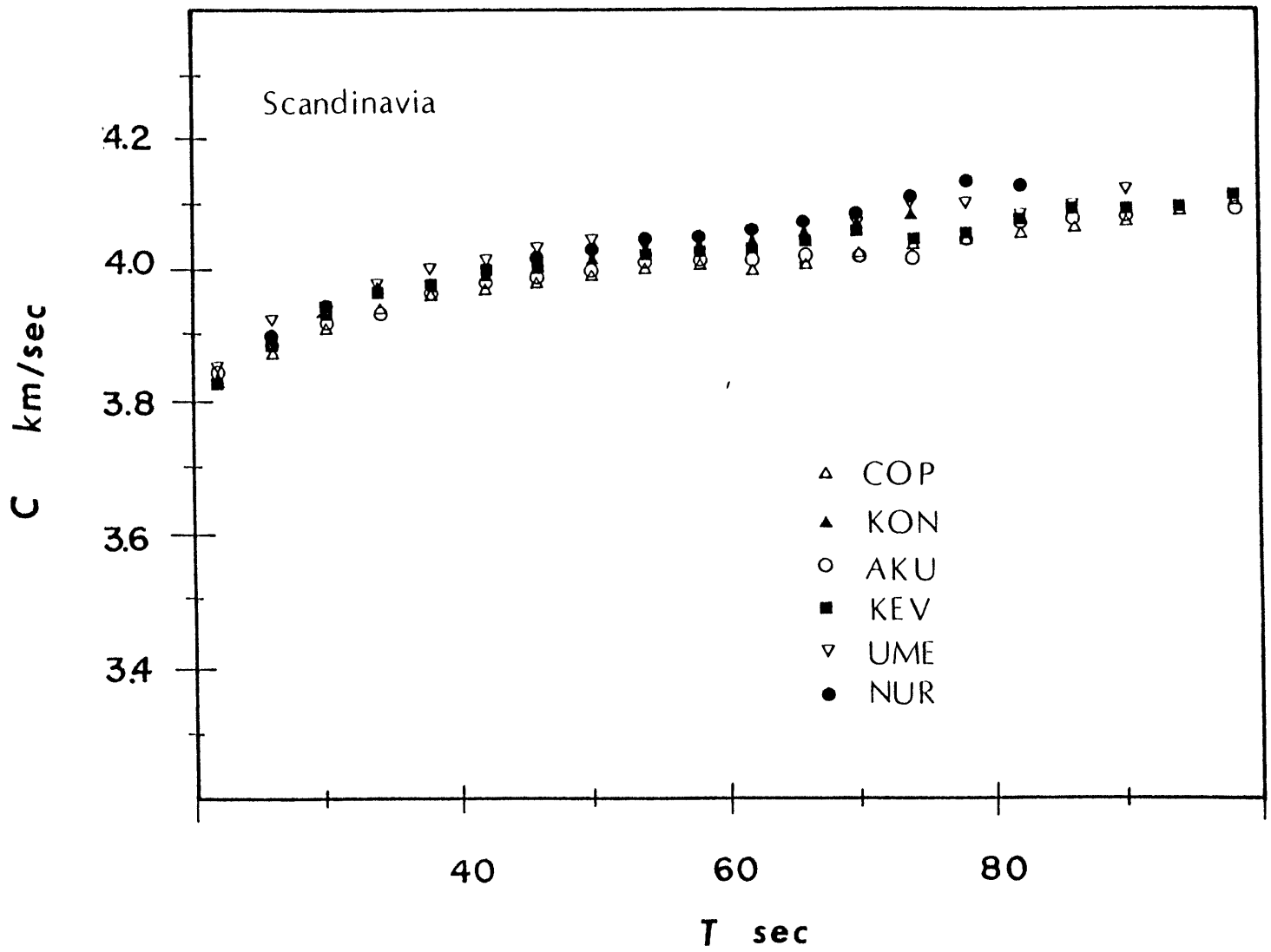
Scandinavia
4.2
4.0
3.8
3.6
3.4
C km/sec
40
60
80
T sec
COP
KON
AKU
KEV
UME
NUR

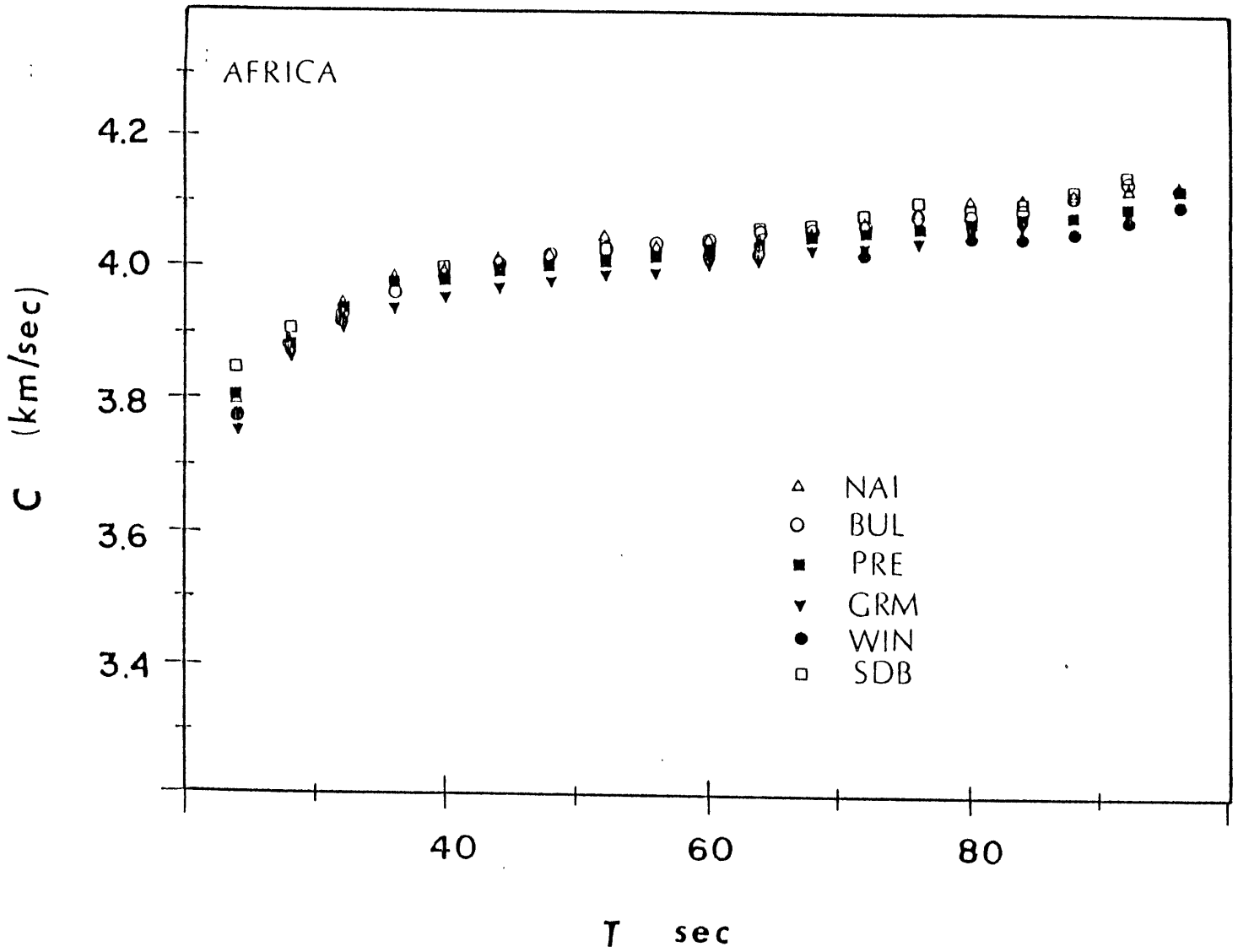
AFRICA
4.2
4.0
3.8
3.6
3.4
C (km/sec)
40
60
80
T sec
NAI
BUL
PRE
GRM
WIN
SDB

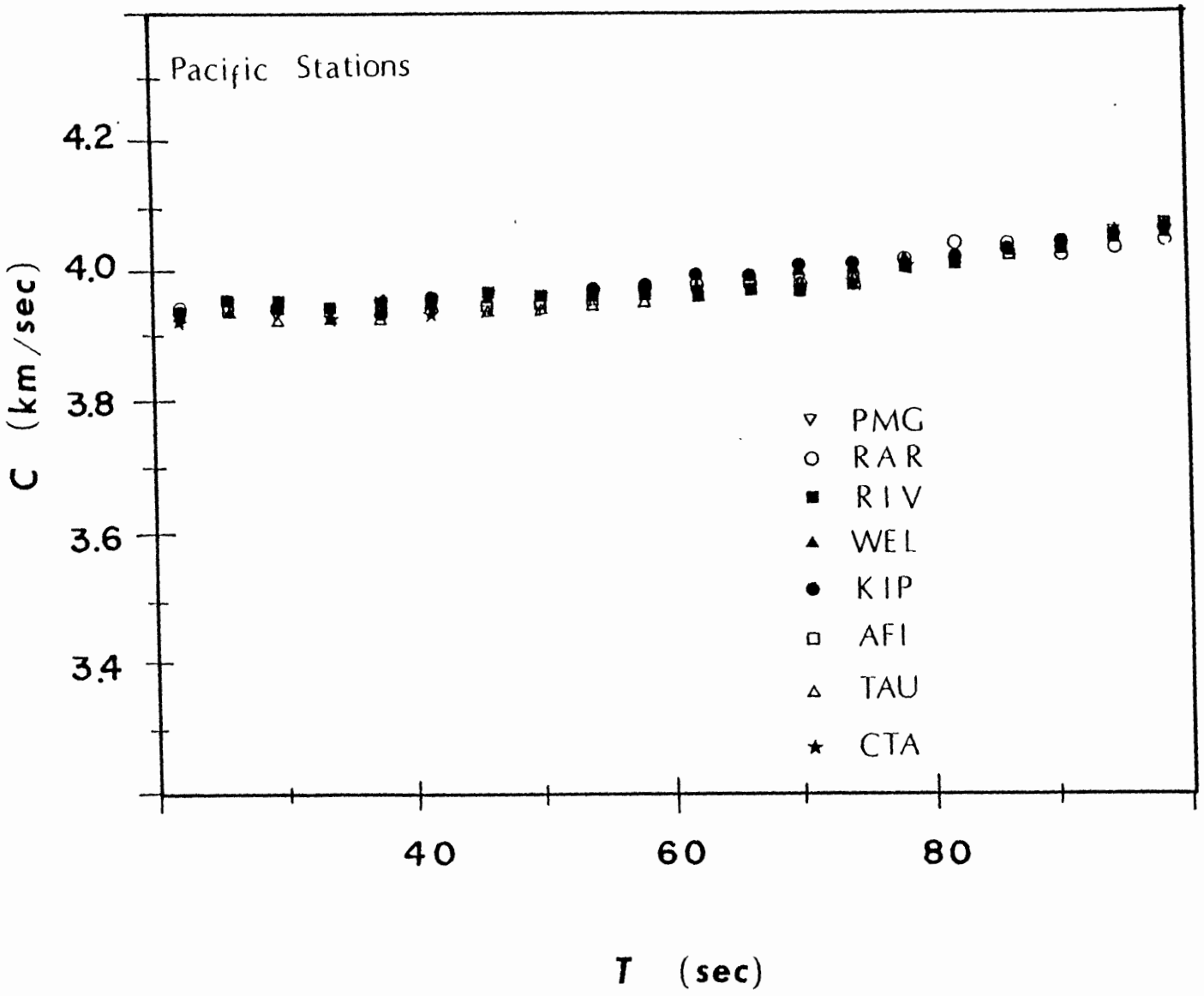
Pacific Stations
4.2
4.0
3.8
3.6
3.4
C (km/sec)
40
60
80
T (sec)
PMG
RAR
RIV
WEL
KIP
AFI
TAU
CTA

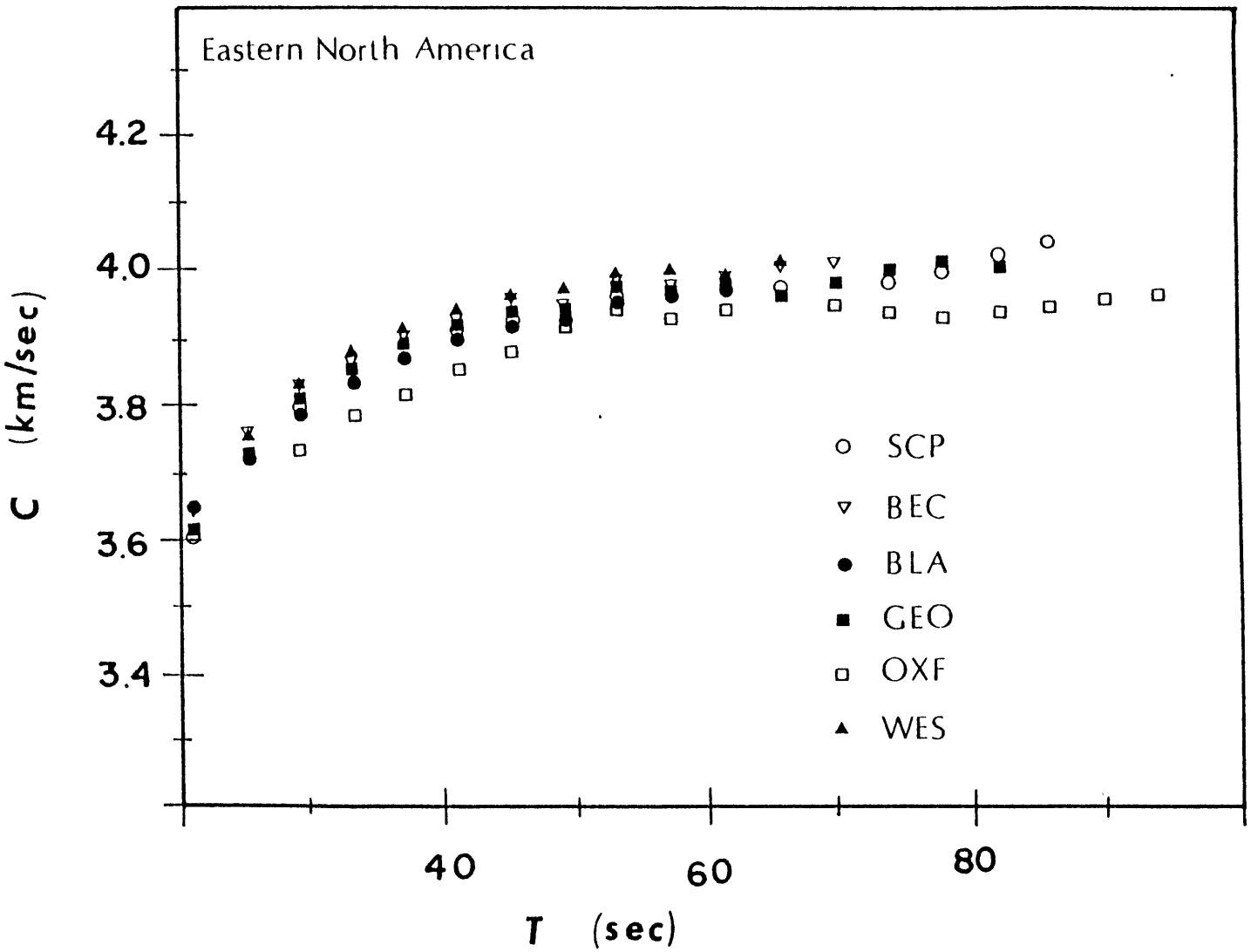
Eastern North America
4.2
4.0
3.8
3.6
3.4
C (km/sec)
40
60
80
T (sec)
SCP
BEC
BLA
GEO
OXF
WES

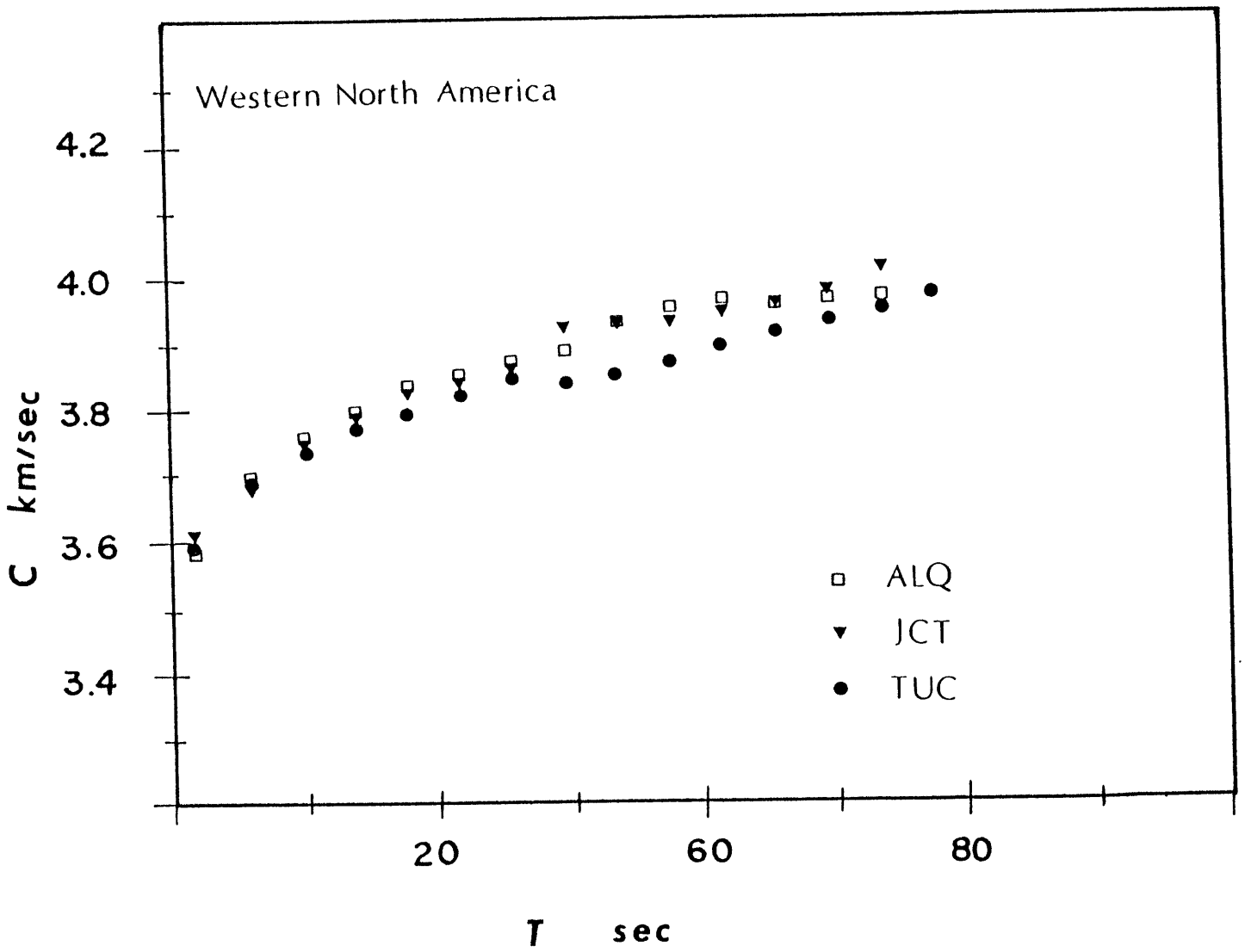
Western North America
4.2
4.0
3.8
3.6
3.4
C km/sec
20
60
80
T sec
ALQ
JCT
TUC

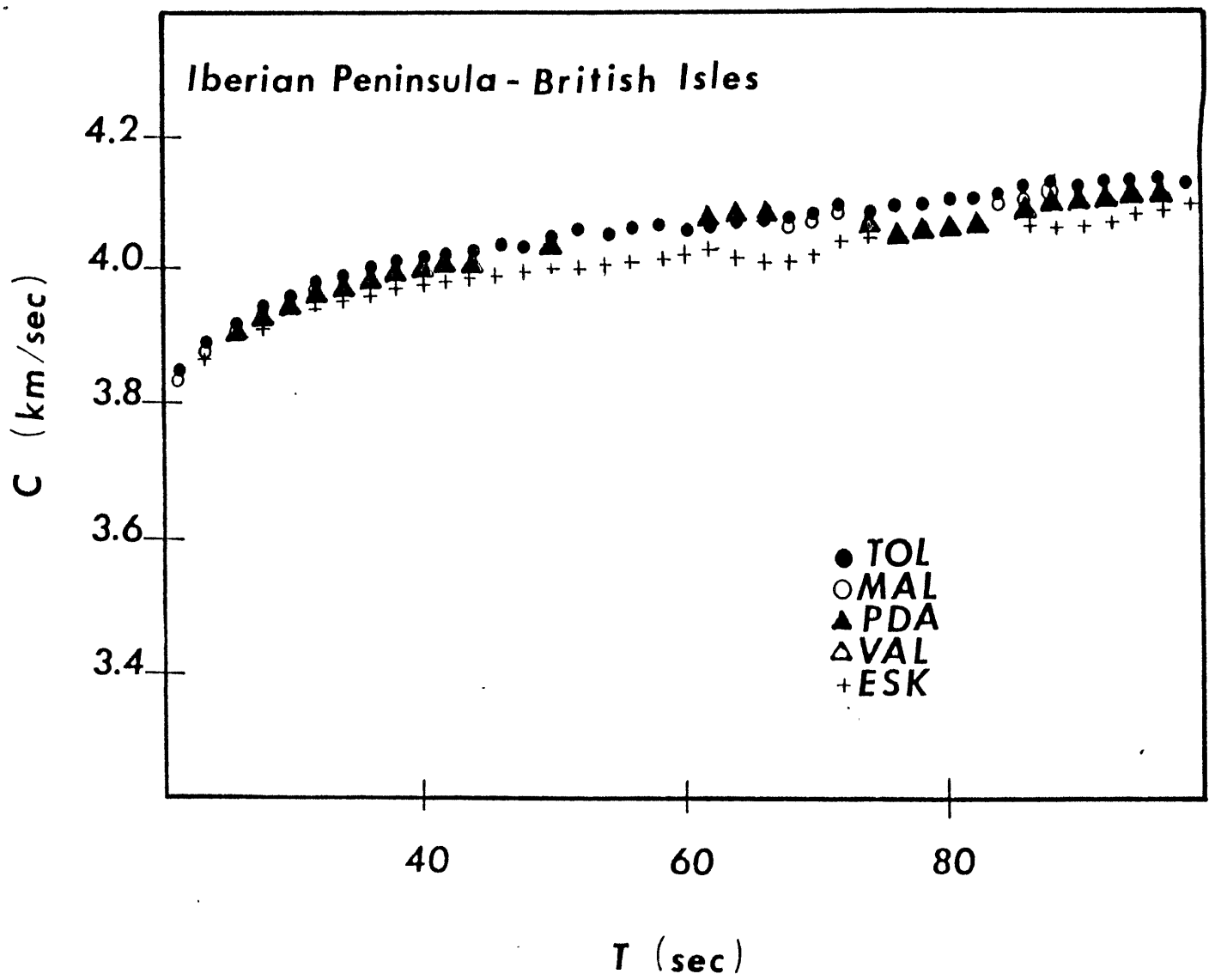
Iberian Peninsula - British Isles
4.2
4.0
3.8
3.6
3.4
C (km/sec)
40
60
80
T (sec)
TOL
MAL
PDA
VAL
ESK

Period (sec)	ADE	AFI	AKU	ALQ	ATL	BEC	BLA
100	4.075	4.082	4.094				
96	4.055	4.063	4.081				
92	4.029	4.047	4.078				
88	4.006	4.034	4.077				
84	3.994	4.023	4.070				
80	3.982	4.014	4.055				
76	3.950	4.005	4.020	3.957			
72	3.949	3.992	4.009	3.968		3.995	
68	3.992	3.982	4.025	3.952	3.968	4.013	
64	3.983	3.972	4.017	3.979	3.952	3.998	3.986
60	3.967	3.963	4.012	3.959	3.940	3.987	3.961
56	3.962	3.965	4.008	3.950	3.930	3.996	3.959
52	3.943	3.952	4.007	3.899	3.918	3.972	3.937
48	3.926	3.953	3.984	3.886	3.894	3.968	3.927
44	3.961	3.953	3.979	3.857	3.888	3.952	3.906
40	3.953	3.947	3.970	3.852	3.864	3.920	3.885
36	3.942	3.947	3.945	3.820	3.833	3.896	3.859
32	3.935	3.949	3.947	3.779	3.792	3.857	3.821
28	3.926	3.948	3.989	3.727	3.726	3.807	3.765
24	3.939	3.941	3.884	3.663	3.648	3.718	3.669
20	3.943	3.923	3.774	3.533	3.586	3.583	3.565

Period (sec)	BUL	COP	CTA	ESK	GEO	GRM	JCT
100	4.122	4.111	4.102	4.133		4.082	
96	4.120	4.097	4.084	4.124		4.063	
92	4.129	4.081	4.057	4.115		4.047	
88	4.108	4.066	4.044	4.105		4.034	
84	4.088	4.056	4.029	4.085	4.017	4.023	
80	4.077	4.048	4.006	4.060	4.003	4.014	
76	4.079	4.041	3.990	4.058	4.015	4.005	
72	4.065	4.032	3.954	4.074	3.999	3.992	3.995
68	4.059	4.017	4.002	4.088	3.959	3.982	3.970
64	4.055	3.997	3.993	4.087	3.970	3.972	3.958
60	4.042	3.999	3.974	4.066	3.974	3.963	3.939
56	4.038	4.005	3.940	4.056	3.977	3.965	3.926
52	4.027	3.997	3.959	4.046	3.962	3.952	3.941
48	4.018	3.983	3.951	4.031	3.942	3.953	3.882
44	4.005	3.975	3.955	4.018	3.931	3.953	3.860
40	3.982	3.960	3.953	4.003	3.903	3.947	3.832
36	3.959	3.952	3.951	3.982	3.874	3.947	3.816
32	3.930	3.926	3.948	3.959	3.836	3.949	3.773
28	3.879	3.891	3.939	3.929	3.770	3.948	3.713
24	3.775	3.856	3.935	3.897	3.674	3.941	3.636
20	3.668	3.785	3.928	3.794	3.559	3.923	3.565

Period (sec)	KEV	KIP	KON	MAL	NAI	NAT	NUR
100	4.125	3.905		4.134	4.136		
96	4.103	4.060		4.141	4.128		
92	4.090	3.907		4.134	4.120		
88	4.099	4.042		4.119	4.110		
84	4.089	4.024		4.103	4.015		4.134
80	4.066	3.890		4.096	4.100		4.135
76	4.049	3.895		4.101	4.082		4.126
72	4.056	3.893	4.073	4.081	4.065		4.098
68	4.051	4.006	4.059	4.067	4.051		4.082
64	4.029	3.890	4.044	4.072	4.040		4.064
60	4.033	3.988	4.035	4.062	4.044	4.086	4.055
56	4.024	3.889	4.026	4.066	4.030	4.062	4.049
52	4.020	3.970	4.018	4.047	4.048	4.069	4.037
48	4.008	3.894	4.012	4.037	4.017	4.051	4.024
44	4.009	3.961	3.999	4.029	4.013	4.051	4.005
40	3.980	3.955	3.984	4.009	3.994	3.996	3.991
36	3.993	3.901	3.939	3.997	3.985	3.967	3.961
32	3.958	3.954	3.950	3.968	3.943	3.904	3.955
28	3.914	3.951	3.920	3.927	3.889	3.811	3.921
24	3.859	3.946	3.860	3.919	3.795	3.728	3.862
20	3.791	3.925	3.777	3.825	3.676	3.614	3.778

Period (sec)	OXF	PDA	PMG	PRE	PTO	RAB	RAR
100	4.002	4.113	4.071	4.144	4.139	4.067	4.051
96	3.980	4.094	4.059	4.120	4.122	4.053	4.036
92	3.966	4.076	4.045	4.095	4.108	4.039	4.024
88	3.957	4.060	4.033	4.075	4.104	4.026	4.024
84	3.945	4.069	4.032	4.073	4.102	4.017	4.048
80	3.937	4.089	4.013	4.068	4.091	4.010	4.038
76	3.940	4.067	4.000	4.055	4.078	4.001	3.993
72	3.941	4.039	3.986	4.052	4.072	3.989	3.992
68	3.974	4.011	3.979	4.044	4.074	3.983	3.998
64	3.958	4.019	3.974	4.035	4.069	3.976	3.982
60	3.931	4.023	3.964	4.021	4.064	3.969	3.981
56	3.958	4.008	3.955	4.012	4.055	3.946	3.977
52	3.926	4.004	3.950	4.006	4.046	3.978	3.961
48	3.899	3.998	3.938	4.004	4.035	3.967	3.959
44	3.862	3.992	3.936	3.998	4.019	3.966	3.952
40	3.843	3.973	3.938	3.984	4.014	3.957	3.951
36	3.794	3.958	3.945	3.974	3.997	3.952	3.945
32	3.770	3.937	3.938	3.937	3.971	3.934	3.948
28	3.752	3.910	3.932	3.881	3.938	3.949	3.952
24	3.672	3.851	3.943	3.802	3.891	3.932	3.946
20	3.563	3.770	3.929	3.659	3.787	3.934	3.942

Period (sec)	RIV	SCP	SDB	SJG	TAU	TOL	TRN
100	4.076				4.079	4.157	
96	4.059				4.074	4.139	
92	4.042				4.070	4.127	
88	4.029				4.068	4.135	
84	4.016				4.044	4.120	
80	4.000	3.998	4.082		4.011	4.099	
76	3.991	3.981	4.098		4.001	4.090	
72	3.992	3.975	4.079		3.987	4.094	
68	3.983	3.971	4.061		3.972	4.081	
64	3.957	3.970	4.058		3.962	4.072	
60	3.967	3.981	4.042		3.957	4.063	
56	3.978	3.952	4.036		3.948	4.061	4.140
52	3.957	3.946	4.031	3.944	3.939	4.058	4.104
48	3.960	3.933	4.020	3.922	3.935	4.039	4.060
44	3.952	3.919	4.016	3.932	3.933	4.030	4.015
40	3.948	3.903	3.998	3.902	3.932	4.019	3.964
36	3.941	3.869	3.973	3.874	3.933	4.000	3.922
32	3.938	3.828	3.946	3.813	3.933	3.979	3.878
28	3.948	3.762	3.907	3.759	3.941	3.941	3.822
24	3.938	3.670	3.846	3.650	3.938	3.894	3.752
20	3.943	3.577	3.690	3.603	3.942	3.787	3.670

Period (sec)	TUC	UME	VAL	WEL	WES	WIN
100		4.226	4.106	4.071		4.113
96		4.154	4.092	4.052		4.094
92		4.134	4.078	4.044		4.073
88		4.109	4.060	4.042		4.054
84		4.089	4.039	4.027		4.047
80	3.995	4.087	4.021	4.017		4.055
76	3.960	4.105	4.016	4.005		4.040
72	3.942	4.089	4.018	3.966		4.022
68	3.929	4.056	4.008	3.998		4.042
64	3.910	4.029	3.999	3.978	3.986	4.022
60	3.879	4.029	3.984	3.964	3.972	4.011
56	3.860	4.037	3.979	3.964	3.987	4.009
52	3.984	4.062	4.027	3.964	3.991	4.011
48	3.866	4.037	4.010	3.959	3.968	3.993
44	3.832	4.024	4.000	3.954	3.945	3.983
40	3.812	4.008	3.989	3.953	3.926	3.968
36	3.785	3.985	3.964	3.951	3.896	3.946
32	3.754	3.962	3.938	3.946	3.862	3.920
28	3.714	3.962	3.899	3.944	3.797	3.870
24	3.664	3.884	3.851	3.936	3.708	3.765
20	3.584	3.790	3.759	3.944	3.585	3.640